Springer Theses
Recognizing Outstanding Ph.D. Research

Carsten Matthias Putzke

Fermi Surface and Quantum Critical Phenomena in High-Temperature Superconductors

Springer

Springer Theses

Recognizing Outstanding Ph.D. Research

Aims and Scope

The series "Springer Theses" brings together a selection of the very best Ph.D. theses from around the world and across the physical sciences. Nominated and endorsed by two recognized specialists, each published volume has been selected for its scientific excellence and the high impact of its contents for the pertinent field of research. For greater accessibility to non-specialists, the published versions include an extended introduction, as well as a foreword by the student's supervisor explaining the special relevance of the work for the field. As a whole, the series will provide a valuable resource both for newcomers to the research fields described, and for other scientists seeking detailed background information on special questions. Finally, it provides an accredited documentation of the valuable contributions made by today's younger generation of scientists.

Theses are accepted into the series by invited nomination only and must fulfill all of the following criteria

- They must be written in good English.
- The topic should fall within the confines of Chemistry, Physics, Earth Sciences, Engineering and related interdisciplinary fields such as Materials, Nanoscience, Chemical Engineering, Complex Systems and Biophysics.
- The work reported in the thesis must represent a significant scientific advance.
- If the thesis includes previously published material, permission to reproduce this must be gained from the respective copyright holder.
- They must have been examined and passed during the 12 months prior to nomination.
- Each thesis should include a foreword by the supervisor outlining the significance of its content.
- The theses should have a clearly defined structure including an introduction accessible to scientists not expert in that particular field.

More information about this series at http://www.springer.com/series/8790

Carsten Matthias Putzke

Fermi Surface and Quantum Critical Phenomena in High-Temperature Superconductors

Doctoral Thesis accepted by
the University of Bristol, Bristol, England, UK

Springer

Author
Dr. Carsten Matthias Putzke
H.H. Wills Laboratory of Physics
University of Bristol
Bristol
England, UK

Supervisor
Prof. Antony Carrington
H.H. Wills Laboratory of Physics
University of Bristol
Bristol
England, UK

ISSN 2190-5053 ISSN 2190-5061 (electronic)
Springer Theses
ISBN 978-3-319-48645-1 ISBN 978-3-319-48646-8 (eBook)
DOI 10.1007/978-3-319-48646-8

Library of Congress Control Number: 2016955800

Printed on acid-free paper

This Springer imprint is published by Springer Nature
The registered company is Springer International Publishing AG
The registered company address is: Gewerbestrasse 11, 6330 Cham, Switzerland

Supervisor's Foreword

This thesis reports experimental studies of two of the most important families of materials in condensed matter physics today: iron-pnictides and cuprate superconductors. The main experimental technique used was the de Haas-van Alphen (dHvA) effect. The work was very demanding, requiring painstaking work on very small, high purity single crystals both in our home laboratory and during several months spent in international high magnetic field facilities (Toulouse, Tallahassee, Dresden). The work has been published in several high-profile papers which are being highly cited. Results in the iron-pnictide materials revealed the details of their Fermi surfaces, the quasiparticle mass renormalisations and how these are related to the occurrence and nature of superconductivity. In the isovalently substituted series $BaFe_2(As_{1-x}P_x)_2$, a large mass enhancement close its antiferromagnetic quantum critical point was measured but this was found to affect the upper and lower critical fields in an unexpected way. These results will significantly redefine our understanding of superconductivity close to a quantum critical point. Finally, a preliminary study of the quantum oscillations in the cuprate $YBa_2Cu_4O_8$ under high pressure was made. This work has subsequently been extended revealing an unexpected inverse relationship between effective mass and T_c.

Bristol, England, UK
October 2016

Prof. Antony Carrington

Abstract

This thesis presents the results obtained from de Haas-van Alphen experiments in iron-based superconductors. Measurements of the quasiparticle mass in the quantum critical system $BaFe_2(As_{1-x}P_x)_2$ are presented, which show strong enhancement towards the critical composition $x_c = 0.3$. This is found to be in good agreement with the prediction of a diverging behaviour of the effective mass close to a quantum critical point. Further results obtained on the lower and upper superconducting critical field of this system will be presented, which are found to contradict the expectations from Ginzburg–Landau theory based on results of the quasiparticle mass and London penetration depth. However, we can reconcile the different experimental findings on superconducting and normal state properties, in this quantum critical system, by considering a significant contribution from Abrikosov vortex core states. The importance of understanding the normal state electronic structure and interactions is shown to be essential for an understanding of the superconducting ground state of a quantum critical system.

Further we will show a detailed de Haas-van Alphen study of the *111*-type iron-based superconductor LiFeP and its isovalent partner LiFeAs. To understand the formation of nodes on the superconducting gap structure in systems with little change in their Fermi surface topology, is essential for the formulation of a microscopic theory of the pairing mechanism in pnictide-superconductors. While we find both systems to be close to the geometric nesting condition, we are able to point to different possible scenarios of the origin of nodes based on quasiparticle mass enhancement.

Extending the study of quasiparticle mass and its relation to the superconducting properties to the stoichiometric high-temperature cuprate superconductor $YBa_2Cu_4O_8$, we aim to study the Fermi surface evolution under hydrostatic pressure. As the system has a very stable oxygen stoichiometry which does not allow it to be doped by oxygen ordering, we use hydrostatic pressure to tune the system unexpectedly leading to an increase in the superconducting critical temperature with almost no change to the quasiparticle mass.

Publications

Relevant for this Work

de Haas-van Alphen Study of the Fermi-Surface of Superconducting LiFeP and LiFeAs

C. Putzke, A.I. Coldea, I. Guillamon, D. Vignolles, A. McCollam, D. LeBeouf, M.D. Watson, I.I. Mazin, S. Kasahara, T. Terashima, T. Shibauchi, Y. Matsuda, A. Carrington
Physical Review Letter 108, 047002 (2012)

Quasiparticle Mass Enhancement Close to the Quantum Critical Point in $BaFe_2(As_{1-x}P_x)_2$

P. Walmsley, C. Putzke, L. Malone, I. Guillamn, D. Vignolles, C. Proust, S. Badoux, A.I. Coldea, M.D. Watson, S. Kasahara, Y. Mizukami, T. Shibauchi, Y. Matsuda, A. Carrington
Physical Review Letters 110, 257002 (2013)

Anomalous critical fields in quantum critical superconductors

C. Putzke, P. Walmsley, J.D. Fletcher, L. Malone, D. Vignolles, C. Proust, S. Badoux, P. See, H.E. Beere, D.A. Ritchie, S. Kasahara, Y. Mizukami, T. Shibauchi, Y. Matsuda, A. Carrington
Nature Communications 5, 5679 (2014)

Inverse correlation between quasiparticle mass and T_c in a cuprate high-T_c superconductor

C. Putzke, L. Malone, S. Badoux, B. Vignolle, D. Vignolles, W. Tabis, P. Walmsley, M. Bird, N.E. Hussey, C. Proust, A. Carrington
Science Advances 2, e1501657 (2016)

Other Publications

Low-temperature thermal conductivity of the noncentrosymmetric superconductor $LaRhSi_3$

N. Kurita, C.F. Miclea, C. Putzke, G. Seyfarth, C. Capan, A. Bianchi, Z. Fisk, J.D. Thompson, R. Movshovich
Journal of Physics Conference Series 273, 012077 (2011)

Fermi surface of the electron-doped cuprate superconductor $Nd_{2-x}Ce_xCuO_4$ probed by high-field transport

M.V. Kartsovnik, T. Helm, C. Putzke, F. Wolff-Fabris, I. Sheikin, S. Lepault, C. Proust, D. Vignolles, N. Bittner, W. Biberacher, A. Erb, J. Wosnitza, R. Gross
New Journal of Physics 13, 015001 (2011)

Electron-tunneling measurements of the low-T_c single-layer $Bi_{2+x}Sr_{2-y}CuO_{6+d}$: Evidence for scalling disparity between superconducting and pseudogap states

T. Jacobs, S.O. Katterwe, H. Motzkau, A. Rydh, A. Maljuk, T. Helm, C. Putzke, E. Kampert, M.V. Kartsovnik, V.M. Krasnov
Physcial Review B 86, 214506 (2012)

Vortex lock-in transition and evidence for transitions among commensurate kinked vortex configurations in single-layered Fe arsenides

G. Li, G. Grissonnanche, B.S. Conner, F. Wol-Fabris, C. Putzke, N.D. Zhigadlo, S. Katrych, Z. Bukowski, J. Karpinski, L. Balicas
Physical Review B 87, 100503 (2013)

Spear-anvil point-contact spectroscopy in pulsed magnetic fields

F. Arnold, B. Yager, E. Kampert, C. Putzke, J. Nyeki, J. Saunders
Review of Scientific Instruments 84, 113901 (2013)

Correlation between Fermi surface transformations and superconductivity in the electron-doped high-T_c superconductor $Nd_{2-x}Ce_xCuO_4$

T. Helm, M.V. Kartsovnik, C. Proust, B. Vignolle, C. Putzke, E. Kampert, I. Sheikin, E.-S. Choi, J.S. Brooks, N. Bittner, W. Biberacher, A. Erb, J. Wosnitza, R. Gross
Physcial Review B 92, 094501 (2015)

Superconducting gap structure of $BaFe_2(As_{1-x}P_x)_2$

L. Malone, Y. Mizukami, P. Walmsley, C. Putzke, S. Kasahara, T. Shibauchi, Y. Matsuda, A. Carrington
arXiv:1409.7523 (submitted 2014)

Acknowledgements

First of all, I would like to thank my supervisor Prof. Tony Carrington for giving me the opportunity to come to Bristol and work in his group. The practical advice and many scientific discussions during the last years have been invaluable. I am very thankful for so many opportunities to learn new things not just in Bristol but also at schools, workshops, placements and experiments in other groups and facilities.

Many thanks also to all members of the CES group and especially to Phil Walmsley, Dr. Nick Wakeham, Dr. Liam Malone and Dr. Isabel Guillamon who accompanied me on the way and shared the ups and downs that go along any experiment. For all the support, discussions and breaks from science I am very grateful.

I am also very thankful to Cyril Proust, David Vignolles, Baptiste Vignolle, Sven Badoux, David LeBoeuf and many more at the LNCMI Toulouse, who have supported me during many experiments in their lab. Without their effort and expertise, many of the results in this thesis would have not been possible.

Special thanks to the group of Prof. Matsuda at the University of Kyoto. Especially Shigeru Kasahara who provided great samples for the performed studies. Also to Yuta Mizukami and Tatsuya Watashige for their support in and out of the lab during my time in Kyoto.

Finally and by far most I thank my parents. Only their guidance, love and support made it possible to reach this point. I cannot thank them enough for all they have done for me.

Contents

Chapter 1
Introduction

1.1 Low Temperature Physics

In many research facilities and universities around the world you will find a group that is referred to as *quantum matter* or *strongly correlated electron* group. While those terms represent the interesting topics to study it is not so long ago that many of these groups were referred to as *low temperature physics*. Here the main technique used in the laboratory and in experiments present in this thesis is put into focus. This field experienced a boost when Kamerlingh Ones more than a hundred years first liquefied Helium. He was driven by the question: what happens to the electrical resistivity of a metal when cooled close to zero temperature. Doing so he discovered superconductivity in Mercury.

While superconductivity is maybe the most prominent low-temperature-effect there are a number of effects that require to cool samples to a few Kelvin above absolute zero. In Chap. 2 we will discuss the de Haas-van Alphen effect. This relies on the quantization of electron-states under the application of a magnetic field. At elevated temperatures these states become smeared out by the thermal energy and so unobservable. For correlated electron research low-temperatures are therefore an important tool that reveals new ground states but also enables detailed measurements on electronic correlations. A detailed summary of how to achieve low-temperatures and perform measurements under these conditions is given in Ref. [1].

Another phenomena that has been of great interest to the community are *quantum critical points* in a number of materials. These points represent the zero temperature endpoint of a continuous phase transition. At this point the only available excitations are those of the zero-point fluctuations arising from Heisenbergs uncertainty principle. The observation of such critical endpoint are not just limited by the fact that the third law of thermodynamics forbids to reach zero temperature, but also by a superconducting phase that is often found to cover these endpoints in organic, heavy fermion and iron-based superconductors. However the existence of a quantum critical point can influence the normal state of the material study even at finite

C.M. Putzke, *Fermi Surface and Quantum Critical Phenomena in High-Temperature Superconductors*, Springer Theses,
DOI 10.1007/978-3-319-48646-8_1

temperature and can lead to unconventional superconductivity as we will discuss in detailed in the context of $BaFe_2(As_{1-x}P_x)_2$.

Beyond the application of low temperatures I will utilise high magnetic fields and high pressure this thesis. Especially the application of high magnetic fields is essential to study the normal state of high temperature superconductors at low temperatures.

Most fundamental measurements at low temperatures involve determining the specific heat, resistivity and magnetisation of single crystals. In this thesis I will introduce some techniques often not or only briefly covered in undergraduate lecture courses. The main tool in studying the *bulk* Fermi surface topology are quantum oscillations. Those can be observed in a variety of properties such as the specific heat, magnetisation, resistance and other probes that are sensitive to the density of states at the Fermi level. An introduction to the theoretical background will be given in Chap. 2 and the analysis discussed in the experimental chapters.

The other technique introduced is the use of Hall-arrays to determine the lower superconducting critical field. While this is a fundamental parameter of any type-*II* superconductor that limits the Meissner-state it turns out to be one of the hardest to determine experimentally. Why this is and how we can still obtain a measure of the lower critical field I will discuss using measurements on $BaFe_2(As_{1-x}P_x)_2$ in a large range of phosphorous concentration.

1.2 Iron Based Superconductors

The discovery of superconductivity in LaFeAsO in 2008 with a critical temperature of 26 K by Hosono and co-workers [2] marked the birth of a field in condensed matter physics, soon to be known as *iron-pnictides*. Within two months of their discovery the superconducting critical temperature had been pushed to 55 K [3] by replacing lanthanum with samarium in this system. While this is the highest reported T_c for bulk superconductivity in this material class still today, the fast approach of the critical temperature to the boiling point of liquid nitrogen created much interest in the field of high-temperature superconductivity.

Numerous materials containing an iron-pnitogen layer have been found since, including large amounts of possible ways to tune the typically anti-ferromagnetic parent compounds to become superconducting. Today we divide these materials in families based on their stoichiometry, *1111*, *122*, *111* and *11*-type. In Fig. 1.1 the crystal structures are shown for the most prominent members of the relevant families. The substitution of selenium for arsenic also produces a superconducting ground state in materials like FeSe [4], thus there is a second family known as iron-chalcogenides, which share their essential physics with the iron-pnictides. Both families are known collectively as iron-pnictides.

The close proximity of superconductivity to an anti-ferromagnetic ground state is something the pnictides share with cuprates. However unlike the cuprates the iron-pnictides are multi band systems like the well studied phonon-mediated superconductor MgB_2. The research conducted in this thesis is concerned with two different

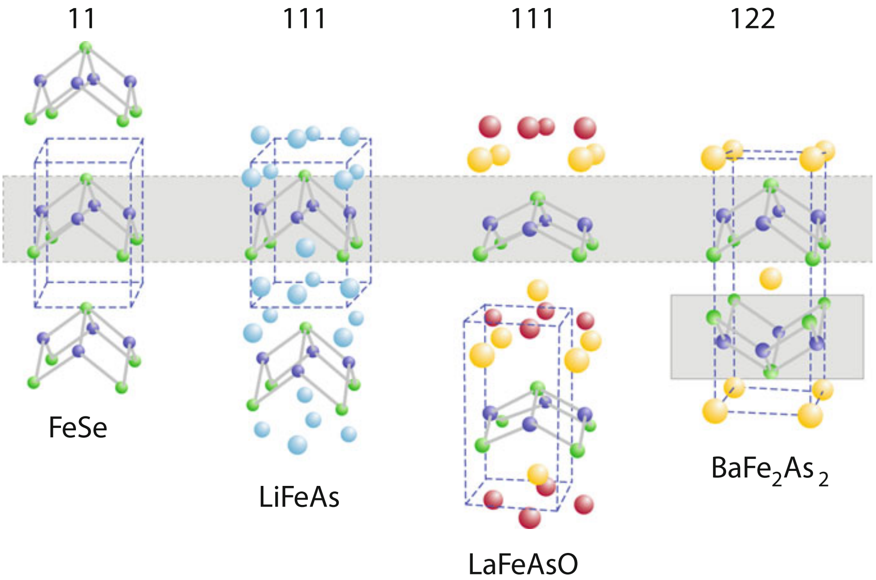

Fig. 1.1 The crystal structure of the main families of iron-based superconductors are shown. The conventional unit cell is shown as *dashed line*. The iron pnictogen layer is highlighted. After Ref. [5]

but related aspects of this material class. Experiments to determine the Fermi surface of LiFeAs and LiFeP were performed to gain insight in the origin of the nodal versus nodeless superconducting gap structures. Furthermore experiments on the band structure and especially the quasi particle mass in $BaFe_2(As_{1-x}P_x)_2$ were motivated by the possible enhancement of superconductivity due to a magnetic quantum critical point.

1.2.1 Crystal Structure and Band Structure

The common element of iron-based superconductors is the iron-pnictogen layer. Unlike the copper-oxide-layer in cuprates, which forms an almost two-dimensional plane, here the arsenic atoms take alternating positions above and below the iron-layer. While most systems crystallise in the primitive tetragonal space-group *P4/nmm* the *122*-family is special as it has a body-centred tetragonal space-group *I4/mmm*. The groups specific crystal structures are indicated in Fig. 1.1. While the *11*-type compounds only contain the iron-chalcogenide layer, the *111*-type show similar lattice parameters but have an additional element, lithium in the case of LiFeP, in their unit cell. The 122-type family in contrast has a twice as long *c*-axis parameter and contains two iron-pnictogen layers per conventional unit cell. Details on the

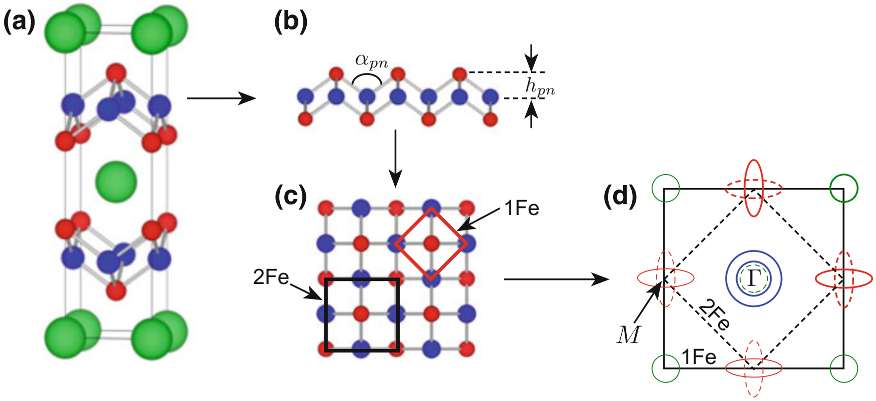

Fig. 1.2 Schematic representation of the origin of one and two-iron unit cell. Starting by the crystal structure of $BaFe_2P_2$ (**a**) the important parameter for the iron-pnictogen plane, the pnictogen height h_{pn} and pnictogen-bond-angle α_{pn}, are indicated in (**b**). In the *top view* of the pnictogen-layer (**c**) the one and two-iron unit cells are inticated. Those lead to the un-folded (*solid lines*) and folded (*dashed lines*) Brillouine zone in (**d**)

crystals structures of the *122*-family can be found in Sect. 4.1.1 in the context of $BaFe_2(As_{1-x}P_x)_2$ and for the *111*-type in Sect. 5.1.1 where we discuss LiFeAs and LiFeP.

The most important structural feature that we want to discuss here in more detail is the alternating position of the pnictogen atom above and below the iron plane. In theoretical work it was shown that the precise form of iron-pnictogen layer, characterised by the pnictogen-height h_{pn} or the pnictogen-iron-pinctogen bond angle α_{pn} shown in Fig. 1.2b, plays a crucial role for the properties of the system [6–8]. We will give a detailed discussion of this effect in the context of quasi particle mass enhancement in $BaFe_2(As_{1-x}P_x)_2$ in Sect. 4.1. Further the importance of changes in the band structure of the pnictides caused by changes in the pnictogen height and its influence on the gap structure will be cover in Sect. 5.1.3 in the context of the *111*-type LiFeP.

Here we focus on the possibly most confusing result of the alternating pnictogen position. This being the different unit cells found in literature. In the crystallographic unit cell as shown in Fig. 1.2a we find two iron atoms per layer inside the unit cell. This is the unit cell that is found in x-ray diffraction experiments. It is caused by the periodicity of the arsenic atoms. In literature this unit cell is referred to as *two-iron* (2Fe) unit cell. However the band structure of the pnictides, close to the Fermi level, is made up of all five $3d$-iron-orbitals as we will discuss in a moment. For two iron atoms we would hence need to construct a 10-orbital model to best describe the electronic properties of the system. In order to simplify this, theoretical work is sometimes carried out in a unit cell only containing one iron atom. The periodicity of iron is used in this case as shown in Fig. 1.2c (1Fe). The unit cell containing two iron atoms is $\sqrt{2}a \times \sqrt{2}a$ larger and its Brillouin zone (BZ) according smaller by the same factor.

Before we continue following this path we will have a look at the band structure that is obtained in *local density approximation* calculations using the 1Fe BZ. The typical Fermi surface found among undoped iron-pnictides holds two hole pockets at the Γ-point of the BZ and one electron pocket centred at $(\pi, 0)$ and $(0, \pi)$ respectively [9]. In some systems, depending on the pnictogen height, a third hole pocket can appear at the corner of the BZ [7]. Based on DFT calculations we find that the density of states (DOS) at the Fermi level is dominated by iron-3d-orbitals [10]. By further splitting this result in the $d_{xz,yz}$, $d_{x^2-y^2}$, d_{xy} and d_{z^2} orbital-character component it is shown that all these orbitals hold significant weight at the Fermi level, making the iron-pnictides a multiorbital system. Hence a model taking all five orbitals into account is necessary to completely describe the system as mentioned before.

In order to obtain the band structure that we would expect to find in experiments we need to transfer the 1Fe calculation into the 2Fe BZ. This is done by folding. The new BZ is shown as dashed lines in Fig. 1.2d. The folded new parts of the Fermi surface are also shown as dashed lines. We see that while the possible third hole pocket is folded to the center of the BZ the electron pockets overlap causing a degeneracy. The degeneracy is lifted by relativistic effects, spin-orbit coupling, leading to an inner and outer electron pocket at the corners of the 2Fe BZ. Due to this folding - unfolding - process between the band structures, the one and two iron BZ are also often referred to unfolded and folded BZ. A further difference is that the 1Fe and 2Fe BZ are rotated by an angle of 45 °. This leads to changes in the orbital character when comparing calculations done in the different unit cells. For example corresponds the $d_{x^2-y^2}$ orbital character in the 1Fe BZ to the d_{xy} orbital character in the 2Fe BZ and vice versa.

While in the cuprate-superconductors it took almost 20 years from their discovery to the first observation of quantum oscillations, high quality single crystals were available in the field of iron-pnictides less than a year after their discovery. A variety of experiments measuring the de Haas-van Alphen effect [11–13] showed that the *bulk* Fermi surface in iron-base superconductors was in good agreement with band structure calculations. At this point we will not extend the discussion into further detail, but will pick up on the relevant details of the band structure and their origins from the crystal structure in Sect. 4.1.2 for *122*-type and in Sect. 5.1.2 for *111*-type materials.

1.2.2 Phase Diagram

After these general remarks on the crystal structure and resulting band structure we now turn to the low temperature ground states of the materials. In their stoichiometric form only a few crystals show a superconducting ground state. One of those systems is LiFeAs with $T_c = 18\,\mathrm{K}$ and its isovalent counterpart LiFeP with $T_c = 5\,\mathrm{K}$, which we will describe in detail in Chap. 5. We typically refer to the arsenic end member as the parent compound of any given system. Those typically show an antiferromagnetic ground state that is accompanied by an orthorhombic distortion of

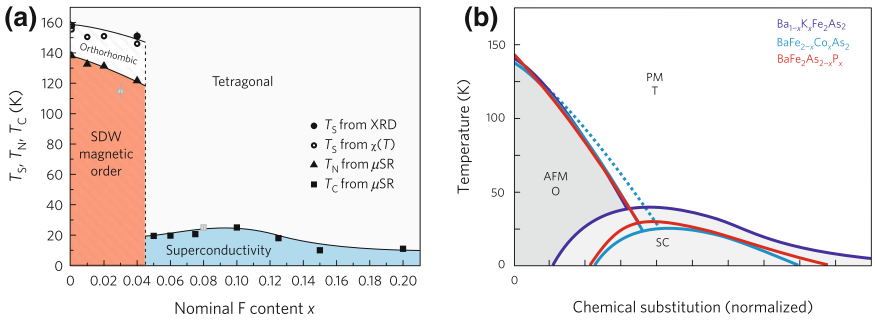

Fig. 1.3 Phase diagram of $LaFeAsO_{1-x}F_x$ (**a**) and $BaFe_2As_2$ for substitution with potassium, cobalt and phosphorous (**b**). After Ref. [14, 15]

the lattice. In Fig. 1.3 this is shown for two prominent examples of the pnictides. The phase diagram of LaFeAsO doped with fluorine is shown in Fig. 1.3a. The orthorhombic and magnetic phase-transitions are clearly separated in temperature. In the *122*-type materials this is not the case in the parent compound. Figure 1.3b shows the phase diagram of $BaFe_2As_2$ for three different chemical substitutions [14]. The chemical substitution has been normalized such that the anti-ferromagnetic (AFM) transitions overlap.

Upon chemical substitution we find first a similar result in both *1111* and *122*-systems as the structural and magnetic transitions become suppressed. In the case of $LaFeAsO_{1-x}F_x$ an abrupt change to the superconducting state is found. When substituting $BaFe_2As_2$ this transition happens more smoothly. We see that while in the potassium and phosphorous substituted system both AFM and structural transition are suppressed equally, in the cobalt doped system the two transitions can eventually clearly be separated showing the structural transition to set in at higher temperatures like in the *1111*-type parent compound. Also by extrapolating the AFM transition to zero temperature the substitution value we find is typically close or at the point where we observe the highest superconducting critical temperatures. The superconducting phase sets in well before the point where the AFM order would vanish in these systems. Up to now the question whether the two states coexist or cause a phase separation is not finally answered. By further substitution we find in all systems a decrease in the superconducting critical temperature, which in most cases leads to a non-superconducting metallic end member like in the case of $BaFe_2P_2$.

Unlike the cuprates, where an insulating AFM ground state is found for the parent compound, which then turns into a metallic behaviour towards the overdoped regime, in the pnictides we observe a metallic behaviour for the entire phase diagram. While the insulating behaviour in the cuprates is caused by strong Coulomb interaction U, best described by Mott-Hubbard physics, it was found in LDA+DFMT calculations, see Sect. 4.1 and Ref. [8, 16] for more details, that the pnictides are more susceptible to changes in the Hund's rule coupling J. This being the origin of the magnetic order, the interactions are not strong enough to completely localize the electrons, which would cause an insulating behaviour.

1.2.3 *Magnetic and Orthorhombic Ground State*

In the beginning many theories invoked that nesting driven enhancement in the Lindhard response function causes both the superconducting and the anti-ferromagnetic state [17, 18]. As time evolved it became clear that the formation of the AFM state does not necessarily require perfect nesting, shifting the view from an itinerant electron picture to a local magnetic order [18]. Density functional theory calculations by Johannes et al. [19, 20] showed that a AFM-stripe order was stabilized due to a lower ground state energy that was gained over a range of roughly 1 eV from the Fermi level concluding that the density of states at the Fermi level are only secondary. However we should point out that while DFT provides correct solutions for the ground state, in reality those calculations are carried out in the local density approximation (LDA), which also gives a much larger magnetic moment than measured experimentally [8], raising the question for the validity of the LDA results. Yin et al. [8] extended these calculations by using DFT+DMFT (dynamic mean field theory). While their results on the magnetic moment of the systems was in better agreement with the experimental results, they also found that without considering nesting a magnetic order would be possible due to localization of the electrons. However they further argued that the presence of nesting helps in stabilizing this order. For example KFe_2As_2 is a compound, where strong mass enhancement does not lead to magnetic order. We will have a closer look at those results in Sect. 4.1 in the context of $BaFe_2(As_{1-x}P_x)_2$ and focus on some of the consequences of magnetic and orthorhombic ground states that is found in many of the parent iron-pnictides at this point.

The reason why it was originally believed that the Fermi surface is driving the AFM order is the observed magnetic wave vector (π, π) in the 2Fe unit cell that would also link the hole and electron pockets [22]. In real-space the spins are aligned anti-ferromagnetically along one iron-iron direction and ferromagnetically along the other [14]. The new Fermi surface topology of the AFM state is then found by a (π, π)-reconstruction of the tetragonal band structure. In the case of perfect nesting electron and hole pockets would cancel each other and we would obtain a gap at the Fermi level leading to an insulating behaviour below the order temperature T_N. However, as we have already mentioned the material remains metallic down to low temperatures and hence this is a signature that perfect nesting is absent (see Fig. 1.5). We are rather left with small residual Fermi surface pockets that were observed for example in $BaFe_2As_2$ using Shubnikov-de Haas oscillations, see Fig. 4.6, Sect. 4.1.2 [23].

The AFM order influences the electronic properties of the system and also causes an orthorhombic distortion of the lattice. This leads not only to a modification of the band structure, as it breaks the four-fold rotational symmetry, but further causes the formation of domains within the crystal [21]. In Fig. 1.4 the x-ray diffraction pattern at temperatures above T_N and below are shown. For temperature below T_N the pattern is shown for three different uni-axial strain values in [110] direction. One can see that by applying strain the O_1 peak becomes enhanced, representing an enlargement of the respective domain. In this configuration the above mentioned observation

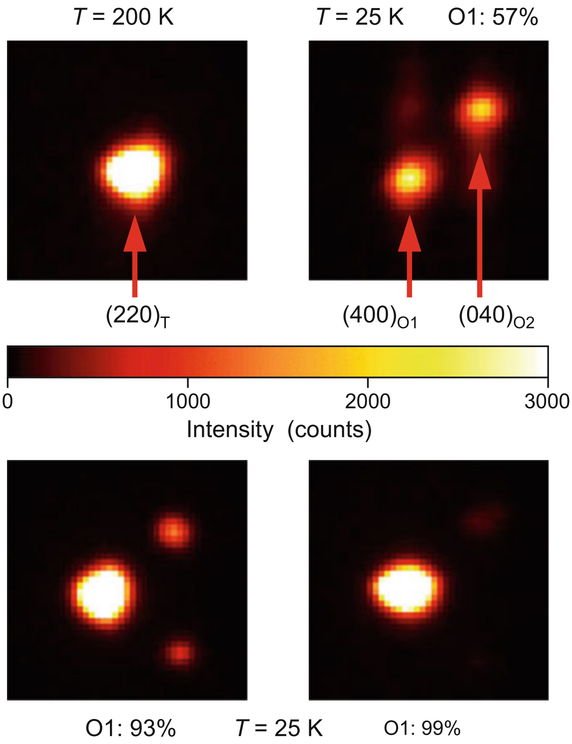

Fig. 1.4 Section of reciprocal planes around the (220)-tetragonal reflection in $BaFe_2As_2$ by x-ray diffraction. *Top left* shows the reflection above the ordering temperature T_N. Below T_N the two peaks O_1 and O_2 correspond to the different domains in the crystal. By application of uni-axial stress the intensity of O_1 grows while O_2 vanishes. This shows the formation of a single domain in the system. After Ref. [21]

of quantum oscillations was possible [23], as the mean free path is improved by increasing the domain size (Fig. 1.5).

1.2.4 Superconductivity and Gap Structure

The high critical temperature of many pnictide superconductors, ranging up to 55 K raises the question whether superconductivity in the pnictides is conventional (electron-phonon coupled) or of unconventional nature. In the case of an electron-phonon mediated superconductor one should be able to observe the *isotope effect* [25]. In the multiband system MgB_2 it was possible to show the importance of electron-phonon coupling on the superconducting critical temperature [26] via the isotope effect. That the isotope effect does not show a significant contribution to superconductivity in the iron-pnictides was concluded from measurements in

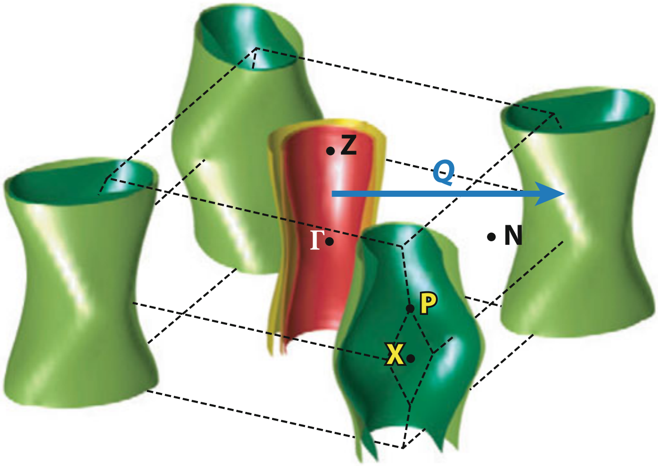

Fig. 1.5 Calculated Fermi surface of $BaFe_2As_2$ using LDA. The quasi-nesting vector $\mathbf{Q} = (\pi, \pi, 0)$ is indicated. After Ref. [24]

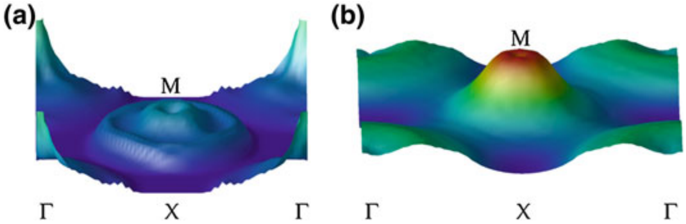

Fig. 1.6 Imaginary (**a**) and real (**b**) part of the non-interacting susceptibility $\chi_0(q, \omega \rightarrow 0)$ for LaFeAsO. After Ref. [17]

$SmFeAsO_{1-y}$ [27], where this effect was found to be absent. It was also shown theoretically by Boeri et al. [28] that the electron-phonon interaction is rather small, $\lambda \approx 0.2$. Reasonably high enhancements for the quasi particle mass were observed in quantum oscillations studies [11, 12] pointing to the presence of moderate exchange interactions.

The close proximity of the superconducting state to AFM order motivated the approach of a magnetically mediated mechanism for superconductivity. This led to a large number of theoretical works based on spin-density wave mediated superconductivity [6, 17, 29], which was originally proposed for the high-temperature cuprate superconductors [30]. Within this theory the effective coupling is proportional to the real part of the Lindhard response function $Re\chi(\mathbf{q}, \omega \rightarrow 0)$ [17], which is enhanced when nesting is present. In Fig. 1.6 the imaginary and real part of the non-interacting susceptibility $\chi(\mathbf{q}, \omega \rightarrow 0)$ are shown, calculated for $LaFeAsO_{1-x}F_x$ [17]. A peak in the real part is observed around the M point. While naturally being repulsive, spin-fluctuation can still lead to superconductivity in the case of a sign-changing

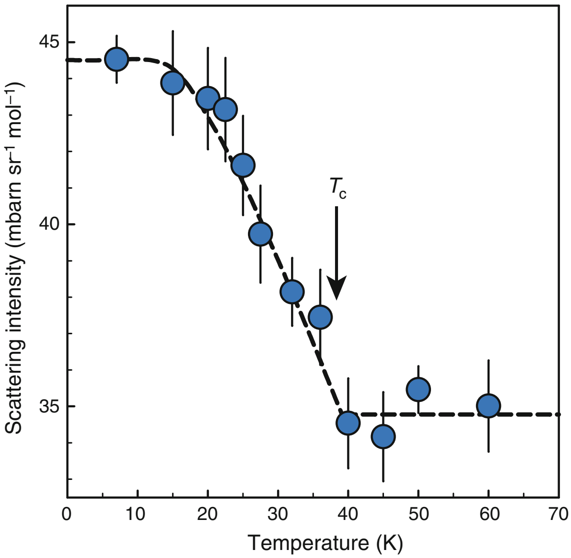

Fig. 1.7 Temperature dependence of the resonant spin excitation in $Ba_{0.6}K_{0.4}Fe_2As_2$ determined by neutron scattering. The *dashed line* is a guide to the eye and shows the strong enhancement of the resonance peak below T_c. After Ref. [22]

superconducting gap $\Delta(\mathbf{k}+\mathbf{Q}) = -\Delta(\mathbf{k})$. This concept is already well known for the single band cuprates where it causes superconductivity with $d - wave$ symmetry. In the case of the multi-band pnictides it was found that some compounds like LiFeP show a nodal gap structure as determined from magnetic penetration depth measurements [31]. This being a possible indication of a sign changing gap on one or more Fermi surface sheets, the counterpart LiFeAs was shown to be nodeless [31], while possessing a very similar band structure to LiFeP in LDA calculations. The Q-wave vector that was found in the spin-fluctuation scenario in Ref. [17], indicated in Fig. 1.5, is $(\pi/a, \pi/a)$ suggesting the sign change to occur between electron and hole pockets and hence causing a nodeless superconducting gap structure. This gap symmetry is known as $s\pm$ or extended s-wave.

It was further pointed out in Ref. [17] that it should be possible to observe the spin-fluctuation using neutron scattering. An enhancement in the intensity would be expected below T_c. One of the first reports on the existence of the predicted behaviour was in $Ba_{0.6}K_{0.4}Fe_2As_2$ [22]. In Fig. 1.7 the intensity of a resonance peak appearing for $T < T_c$ is shown which corresponds to the nesting vector predicted by Mazin et al. [17].

As mentioned, in the case of $s\pm$-symmetry of the superconducting gap we would expect a nodeless superconducting gap structure. However systems such as LiFeP [31] and $BaFe_2(As_{1-x}P_x)_2$ [32] show a nodal gap structure in magnetic penetration depth measurements, see Fig. 1.8. This raises the question of their origin. It turns out that while in the most simple case the sign of the superconducting gap changed from electron to hole pockets, it does not rule out sign changes on one or more of the pockets itself due to intra-band scattering. Theoretical work by Maier et al. [29] and Kuroki et al. [7] have early on suggested that the presence or absence of

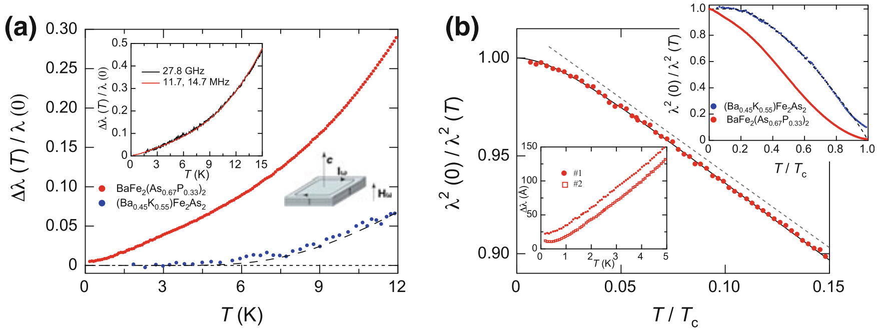

Fig. 1.8 Change in the magnetic penetration depth $\Delta\lambda(T)$ (**a**) and the superfluid density λ^2 (**b**) for $BaFe_2(As_{0.67}P_{0.33})_2$ and $Ba_{0.45}K_{0.55}Fe_2As_2$. After Ref. [32]

nodes is closely linked to the Fermi surface topology, which determines the almost degenerate scattering channels between intra and inter-band pair-scattering. Hence in order to understand the evolution of superconductivity in the iron-based materials a detailed experimental determination of the *bulk* Fermi surface topology is necessary. We will go into more detail on the possible origins of nodes in Chap. 5 where we try to understand the appearance of nodes in the isovalent systems LiFeAs and LiFeP from the perspective of Fermi surface evolution.

In the case that spin-fluctuations are the mechanism that drives superconductivity we are interested to see why some systems show critical temperatures of up to 55 K and others, even so reasonably well nested like $BaFe_2P_2$ [33], are non-superconducting.

One alternative to a purely nesting driven scenario for the difference in pairing strength is a diverging behaviour of spin-fluctuations close to a quantum critical point. When discussing the phase diagram we saw that the maximum superconducting critical temperature was reached at the point where we expected the AFM order state to be suppressed to zero. In this range studies on the nuclear magnetic resonance (NMR) [34] showed in $BaFe_2(As_{1-x}P_x)_2$ that the spin-fluctuations are maximum at a critical substitution level of $x = 0.33$. Similar results were also obtained for the cobalt doped system [35]. Further studies using magnetic penetration depth [36] and de Haas-van Alphen measurements on the effective mass [12] have shown a significant enhancement of the quasi particle mass towards the highest T_c and a strong peak in the London penetration depth at this point. All these probes are in agreement with the behaviour expected for a quantum critical system. In this work we have performed further experiments on the Fermi surface topology and quasi particle mass, which is presented in Sect. 4.2. We were also able to show direct consequences of the presence of a quantum critical point on the superconducting state in $BaFe_2(As_{1-x}P_x)_2$ which are presented in Sect. 4.3.

1.2.5 *Outline of Thesis*

As pointed out above the understanding of the Fermi surface topology and its properties are essential to tests of the suggested pairing scenarios and so gain further inside in the origin of high temperature superconductivity. In the course of this work Chap. 2 will provide the theoretical background that we need for the interpretation of our experimental results. Chapter 3 will then explain the experimental techniques used for the investigation of pnictides and cuprates in this thesis. In Chap. 4 we will show results obtained on the quantum critical superconductor $BaFe_2(As_{1-x}P_x)_2$ where Fermi surface studies and measurements on the superconducting critical fields are presented. Chapter 5 deals with the isovalent systems LiFeAs and LiFeP, where we try to gain a deeper understanding on the origin of nodes on the superconducting gap structure form the perspective of the band structure. We will then turn away from the pnictides and introduce the stoichiometric high-temperature cuprate superconductor $YBa_2Cu_4O_8$. A transport study including Shubnikov-de Haas oscillations in $YBa_2Cu_4O_8$ at ambient and under hydrostatic pressure is presented in Chap. 6.

References

1. F. Pobell, *Matter and Methods at Low Temperatures*, 3rd edn. (Springer, 2007)
2. Y. Kamihara, T. Watanabe, M. Hirano, H. Hosono, J. Am. Chem. Soc. **130**, 3296 (2008)
3. Z. Ren, G. Che, X. Dong, J. Wang, W. Lu, W. Yi, X. Shen, Z. Li, L. Sun, F. Zhou, Z. Zhao, Euro. Phys. Lett. **83**, 17002 (2008)
4. F. Hsu, J. Luo, K. Yeh, T. Chen, T. Huang, P.M. Wu, Y. Lee, Y. Haung, Y.L. Chu, D. Yan, M. Wu, PNAS **105**, 14262 (2008)
5. C. Chu, Nat. Phys. **5**, 787 (2009)
6. P. Hirschfeld, M. Korshunov, I. Mazin, Rep. Prog. Phys. **74**, 124508 (2011)
7. K. Kuroki, H. Usui, S. Onari, R. Arita, H. Aoki, Phys. Rev. B **79**, 224511 (2009)
8. Z. Yin, K. Haule, G. Kotliar, Nat. Mater. **10**, 932 (2011)
9. S. Raghu, X. Qi, C. Liu, D. Scalapino, S. Zhang, Phys. Rev. B **77**, 220503 (2008)
10. D. Singh, Phys. Rev. B **78**, 094511 (2011)
11. A. Coldea, J. Fletcher, A. Carrington, J. Analytis, A. Bangura, J. Chu, A. Erickson, I. Fisher, N. Hussey, R. McDonald, Phys. Rev. Lett. **101**, 216402 (2008)
12. H. Shishido, A. Bangura, A. Coldea, S. Tonegawa, K. Hashimoto, K. Kasahara, P. Rourke, H. Ikeda, T. Terashima, R. Settai, Y. Onuki, D. Vignolles, C. Proust, B. Vignolle, A. McCollam, Y. Matsuda, T. Shibauchi, A. Carrington, Phys. Rev. Lett. **104**, 057008 (2010)
13. J. Analytis, J.-H. Chu, R. McDonald, S. Riggs, I. Fisher, Phys. Rev. Lett. **105**, 207004 (2010)
14. J. Paglione, R. Greene, Nat. Phys. **6**, 645 (2010)
15. H. Luetkens, H. Klauss, M. Kraker, F. Litterst, T. Dellmann, R. Klingeler, C. Hess, R. Khasanov, A. Amato, C. Baines, O. Kosmala, M. Schumann, M. Braden, J. Hamann-Borrero, N. Leps, A. Kondrat, G. Behr, J. Werner, B. Bchner. Nat. Mater. **8**, 305 (2009)
16. J. Ferber, H. Jeschke, R. Valenti, Phys. Rev. Lett. **109**, 236403 (2011)
17. I. Mazin, D. Singh, M. Johannes, M. Du **101**, 057003 (2008)
18. D. Singh, Phys. C **469**, 418 (2009)
19. M. Johannes, I. Mazin, Phys. Rev. B **77**, 165135 (2008)
20. M. Johannes, I. Mazin, Phys. Rev. B **79**, 220510 (2009)
21. M. Tanatar, E. Blomberg, A. Kreyssig, M. Kim, N. Ni, A. Thaler, S. Bud'ko, P. Canfield, A. Goldman, I. Mazin, R. Prozorov, Phys. Rev. B **81**, 184508 (2010)

22. A. Christianson, E. Goremychkin, R. Osborn, S. Rosenkranz, M. Lumsden, C. Malliakas, I. Todorov, H. Claus, D. Chung, M. Kanatzidis, R. Bewley, T. Guidi, Nature **456**, 930 (2008)
23. T. Terashima, N. Kurita, M. Tomita, K. Kihou, C. Lee, Y. Tomioka, T. Ito, A. Iyo, H. Eisaki, T. Liang, N. Masamichi, S. Ishida, S. Uchida, H. Harima, S. Uji, Phys. Rev. Lett. **107**, 176402 (2011)
24. T. Shibauchi, A. Carrington, Y. Matsuda, Annu. Rev. Condens. Matter Phys. **5**, 113 (2014)
25. M. Tinkham, *Introduction to Superconductivity* (Dover Publications, 1996)
26. S. Bud'ko, G. Lapertot, C. Petrovic, C. Cunningham, N. Anderson, P. Canfield. Phys. Rev. Lett. **86**, 1877 (2001)
27. P. Shirage, K. Miyazawa, K. Kihou, H. Kito, Y. Yoshida, Y. Tanaka, H. Eisaki, A. Iyo, Phys. Rev. Lett. **105**, 037004 (2010)
28. L. Boeri, O. Dolgov, A. Golubov, Phys. (Amsterdam) C, **469**, 628 (2009)
29. T. Maier, S. Graser, D. Scalapino, P. Hirschfeld, Phys. Rev. B **79**, 224510 (2009)
30. P. Monthoux, A. Balatsky, D. Pines, Phys. Rev. Lett. **67**, 3448 (1991)
31. K. Hashimoto, S. Kasahara, R. Katsumata, Y. Mizukami, M. Yamashita, H. Ikeda, T. Terashima, A. Carrington, Y. Matsuda, T. Shibauchi, Phys. Rev. Lett. **108**, 047003 (2012)
32. K. Hashimoto, M. Yamashita, S. Kasahara, Y. Senshi, N. Nakata, S. Tonegawa, K. Ikada, A. Serafin, A. Carrington, T. Terashima, H. Ikeda, T. Shibauchi, Y. Matsuda, Phys. Rev. B **81**, 220501 (2010)
33. B. Arnold, S. Kasahara, A. Coldea, T. Terashima, Y. Matsuda, T. Shibauchi, A. Carrington, Phys. Rev. B **83**, 220504 (2011)
34. Y. Nakai, T. Iye, S. Kitagawa, K. Ishida, H. Ikeda, S. Kasahara, H. Shishido, T. Shibauchi, Y. Matsuda, T. Terashima, Phys. Rev. Lett. **105**, 107003 (2010)
35. F. Ning, K. Ahilan, T. Imai, A. Sefat, M. McGuire, B. Sales, D. Mandrus, P. Cheng, B. Shen, H. Wen, Phys. Rev. Lett. **104**, 037001 (2010)
36. K. Hashimoto, K. Cho, T. Shibauchi, S. Kasahara, Y. Mizukami, R. Katsumata, Y. Tsuruhara, T. Terashima, H. Ikeda, M. Tanatar, H. Kitano, N. Salovich, R. Giannetta, P. Walmsley, A. Carrington, R. Prozorov, and Y. Matsuda. Science **336**, 1554 (2012)

Chapter 2
Theory

This chapter will give a brief introduction to the most relevant theoretical aspects used in this thesis, with the aim of explaining the most important formulae and ideas. We will start with basic theory of electrons in metals. Moving on from free electron theory we will give the outline to a more realistic theory for our experimental results. We will then describe the theory of quantum oscillations, which is necessary to understand the main results of this thesis. We will then turn to a brief introduction to the fundamental superconducting properties that we will need in the discussion and interpretation of experimental results. One of the main aspects of this thesis is the quantum critical system $BaFe_2(As_{1-x}P_x)_2$. Also in the cuprate superconductor quantum criticality is often discussed as possible origin of high temperature superconductivity. A brief introduction to the topic of quantum criticality shall therefore be given from the starting point of classical phase transition.

2.1 From Free to Nearly Free Electrons

We begin by a brief introduction following the historical development that led to our current understanding of the behaviour of electrons in metals that will be given in the next section. While a first model proposed by Drude treated the electrons as a classical *free electron gas*, we will start by modelling the electrons in a solid as *free electron gas* in a one dimensional potential considering electrons as waves rather than particles. This *ansatz* was first proposed by Sommerfeld and Bethe. Solving the time-independent Schrödinger equation for this system we find standing waves whose energies are equivalent to those of a free electron but with discrete wavenumbers k. In three dimensions a constant energy in reciprocal space is represented by a sphere that contains a certain number of discrete k-states. The density of states can then be determined from the number of states per energy interval. This leads to the relation $D(E) \propto m^{3/2}E^{1/2}$ for the density of states in three dimensions, which holds as long as we consider a non-interacting single electron picture.

C.M. Putzke, *Fermi Surface and Quantum Critical Phenomena in High-Temperature Superconductors*, Springer Theses,
DOI 10.1007/978-3-319-48646-8_2

The distribution $f(T, E)$ of electrons among the available states is determined by the temperature of the system. The density of electrons is given by

$$n = \int_0^\infty D(E) f(T, E) dE. \tag{2.1}$$

Since electrons are Fermions (spin 1/2), we need to use the Fermi-Dirac distribution function

$$f(T, E) = \frac{1}{e^{(E-\mu)/k_{\mathrm{B}}T} + 1}, \tag{2.2}$$

with the chemical potential μ of the system and the Boltzmann-constant k_{B} and the Pauli exclusion principle. Form this we find that at $T = 0$ all electrons populate the lower energy states up to the chemical potential μ. The sphere of constant energy $E_F = \mu$ in k-space that contains all these states is known as the *Fermi-surface*, and the energy E_F as *Fermi-energy*.

This simple model of the electrons in a solid produced for the first time the correct interpretation of the heat capacity of simple metals like copper, where a linear dependence of the electronic specific heat in temperature was found. However we would not be able to understand the origin of metallic, semi-conducting or insulating behaviour in this context. Hence the assumptions made can only give a crude understanding of the system. In the further course of this work we will now try to reduce these assumptions of a constant background potential (*nearly free electron*), non-interaction (*Fermi-liquid theory*) and one-electron treatment (*density functional theory*) step by step to try to obtain a better understanding of the complex nature of electrons in solids.

2.1.1 Nearly Free Electron

A more realistic scenario for the background potential in a solid is the use of a periodic potential. The potential represents the Coulomb potential of the ionic lattice. We further include the Born-Oppenheimer approximation in our treatment. In this the electrons respond immediately to any lattice vibration as their typical velocity is orders of magnitude higher than that of the lattice. Therefore the lattice potential is given as mean field result, typically represented by the equilibrium state. The electrons in this scenario are split. While low energy electrons are bound to the ions, reducing the Coulomb potential by shielding, the so called *valence electrons* are free to move without any other interaction than those with the lattice potential. From symmetry arguments the solutions $\psi_k(r)$ of the time-independent Schrödinger equation is now represented by a plane-waves modulated by a factor $u_k(r)$ periodic on the lattice, meaning $u_k(r) = u_k(r + r_n)$, with the lattice periodicity r_n. The resulting single-electron solutions

$$\psi_k(r) = u_k(r)e^{ikr} \tag{2.3}$$

are known as *Bloch-waves*. In reciprocal space we find that the potential is periodic with the vector G, so that $\psi_{k+G}(r) = \psi_k(r)$ and hence $E(k) = E(k+G)$. This shows that the single particle energy $E(k)$ is periodic in reciprocal space and hence in further treatment we only need to consider the first Brillouin-zone (BZ).

We will now consider the dispersion $E(k)$ for a very weak potential, meaning that we first only consider the periodicity, leaving the strength of the potential negligible. In this case we find the dispersion relation $E(k)$ for a free electron periodically spaced in reciprocal space as shown in Fig. 2.1a. At the BZ boundaries the energies $E(k)$ are degenerate. In quantum mechanics this leads to the superposition of the two plane waves. Now we add the magnitude of the periodic potential. The two superimposed plane waves will have different energies resulting from a phase difference. This leads to the lifting of the degeneracy of $E(k)$ and a splitting of the energies at the crossing points. This is schematically shown in Fig. 2.1c. Therefore we find now that electrons in the presence of a periodic potential do not possess a continuous energy spectrum. This we know as the *band structure* of a solid. With this we can also understand the origin of metallic and insulating behaviour. If the Fermi energy is located in between bands then the available bands are filled and we need to overcome the energy-gap to the next band in order to excite electrons. In the case where the Fermi energy lies within a band this is not the case and a continuous increase in energy will lead immediately to excited electrons.

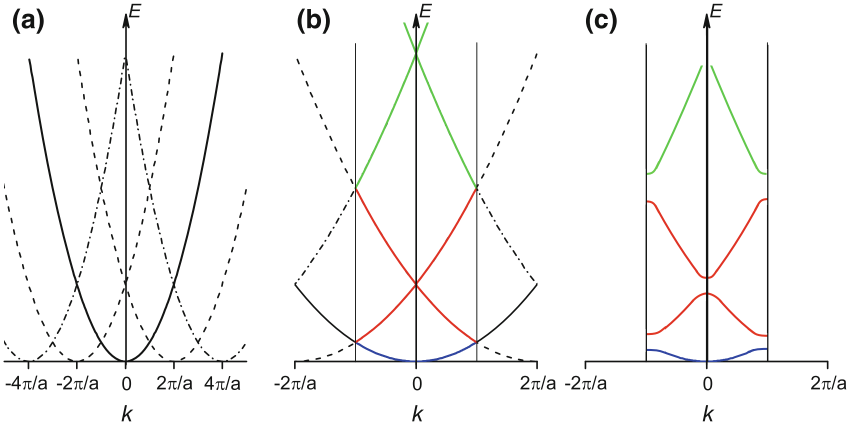

Fig. 2.1 Dispersion relation $E(k)$ for (**a**) a free electron model (**b**) for an infinitesimal small periodic potential and (**c**) a periodic background potential leading to the band structure in *solids*

2.2 Fermi-Liquid Theory

In the next step towards our understanding of electrons in metals we want to include interactions of electrons. For this we will turn to *Fermi liquid theory* (FL). This theory developed by Landau [1] for *neutral* Fermions was originally motivated to describe the rare isotope of Helium ^{3}He. Fermi liquid theory has been a powerful tool as it correctly describes properties such as the quadratic temperature dependence of the resistivity at low temperatures and the temperature dependence of the susceptibility. Today however most novel phenomena are concerned with the emergence of non-Fermi liquid like behaviour such as one-dimensional systems, or systems that are tuned close to a quantum critical point where the approximation of weak interacting Fermions does not hold any more. We find this non-Fermi liquid behaviour, typically characterized by $\rho \propto T$ in systems like the iron-pnictides and cuprates studied in this work [2–4]. However lacking a theory with the same predictive power as the Fermi liquid theory, especially close to quantum critical points, we try to understand these materials based on how they deviate from the conventional prediction by FL theory.

In order to implement interactions to the free-electron model we start by assuming the distribution function $n_0(\mathbf{k}, \sigma)$ of the non-interacting system. When introducing the interactions to this non-interacting system we have to keep in mind that any excitation will only possess a certain life-time τ after which the system will relax. However we need to turn on the excitations *adiabatically* such that the same distribution function also describes the interacting system. This leads to the limitation that the life-time τ in the system needs to be sufficiently long such that they are longer than the adiabatic introduction of excitations. This limits the theory to describe *weak* interactions that produce excited states close to the Fermi level.

As we are interested in electrons in a solid we use the Fermi distribution at T=0 for our non-interacting system. Hence all occupied states take the value $n_0(k, \sigma) = 1$ and all others are zero. The *adiabatic* introduction of interactions to the system, has two further consequences. While the distribution $n(k, \sigma)$ of the new *quasiparticle* is given by the same form as $n_0(\mathbf{k}, \sigma)$ at $T = 0$, the eigenstates are superpositions of the original non-interacting eigenstates. The difference between the distribution of free-electrons and quasiparticles and that of electrons in a Fermi liquid is shown in Fig. 2.2 [5]. While the quasiparticles, as required have the same distribution as the

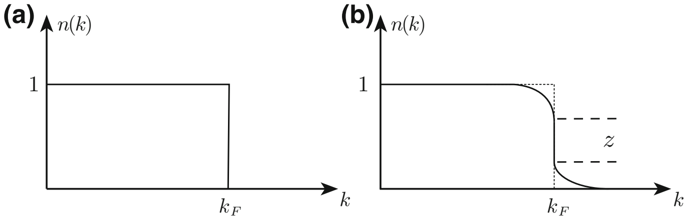

Fig. 2.2 Probability distribution n for a state k to be occupied at T=0. **a** For a non-interacting electron system, or quasiparticles in a Fermi liquid and **b** for electrons in an interacting Fermi liquid

free electron system, the interacting electrons in the Fermi liquid show a reduced step at the Fermi level. The remaining step causes the picture of a Fermi surface to remain valid in the case of an interacting system and the size of the jump Z is inversely proportional to the *effective mass* of the quasiparticles.

From the concept of quasiparticles, which form the basis of this theory, we can now understand why the *free-electron theory* was so powerful in its predictions. The quasiparticles, describing the interacting system, are thought of as non-interacting gas, where the collective interactions of the system are represented by changes in characteristic parameters such as the quasiparticle mass. This however will not change the qualitative results of the temperature dependence of for example the specific heat, but only their absolute magnitude. Further it allows us, within the approximation of a weakly interacting system, to map the problem of collective interaction on a non-interacting single particle wave-function.

We now consider what happens to the energy ε of the system when we add one quasiparticle. For weak interactions we assume a linear dispersion around ε_F, which leads to the new energy of the system [5]

$$\varepsilon_p = \varepsilon_F + \frac{p_F(\hbar k - p_F)}{2m^*}, \tag{2.4}$$

with the Fermi momentum p_F. Here we assume that the Fermi wave vector k_F is unchanged from the non-interaction system. The velocity of the quasiparticle is given by the energy-momentum derivative

$$v = \frac{d\varepsilon}{dp} = \frac{p_F}{m^*} = \frac{m}{m^*} v_F. \tag{2.5}$$

This shows that the group velocity of the quasiparticle, which is modified due to interactions, is modified by the ratio of the bare electron mass to the mass m^* known as *effective mass* or *quasiparticle mass*.

So far we have only considered a single quasiparticle neglecting any contribution of interaction to the total energy. The energy dispersion including exchange interactions is given as [6]

$$\varepsilon = \varepsilon_F + \frac{p_F(\hbar k - p_F)}{m^*} + \sum_{k,\sigma} f_{k\sigma,k'\sigma'} \delta n_{k'\sigma'}, \tag{2.6}$$

where $\delta n_{k'\sigma'}$ represent changes in the particle distribution and $f_{k\sigma,k'\sigma'}$ are a second phenomenological parameter known as *Landau interaction function*. Commonly in textbooks the properties of the Fermi-liquid are described by the so called *Landau-parameter* $F_l^{a,s}$, which can be derived from $f_{k\sigma k'\sigma'}$ [7].

Both m^* and f are not independent of each other. Using the *Landau-parameter* we can express the effective mass as [7]

$$\frac{m^*}{m} = 1 + F_1^s. \tag{2.7}$$

Here the superscript s represents *spin symmetric interaction*. From this we find that in the case where quasiparticle interaction become too strong, for example on approaching an ordered state, the effective mass will diverge. The fact that even in heavy fermion materials effective masses of $m^* \approx 1000$ were found to be in good agreement with measurements of Sommerfeld coefficient γ, shows the wide variety of possible applications.

We want to point out that the parameters m^* and $F_l^{a,s}$ are phenomenological values that need to be experimentally determined. The power of Fermi liquid theory does not rely in predicting experimental results, but rather helps finding the hallmarks of strongly correlated effects in solid state physics. It also allows further inside by linking experimental results on different properties such as heat capacity, magnetic susceptibility and quantum oscillations.

2.3 Density Functional Theory

At this point we have developed an understanding of relative behaviour of experimental values and their origin within the properties of electrons in system using the nearly free electron picture. By adding Fermi liquid theory we are further able to understand the origin of different absolute behaviour of physical properties, such as the Sommerfeld coefficient, between different materials. We have seen that we can explain the interacting Fermi liquid as Fermi gas of quasiparticles, where the interactions are taken into account by only two intertwined parameters, the quasiparticle mass m^* and the Landau parameter $F_l^{a,s}$. However these are so far of phenomenological nature and need to be experimentally determined. For a better understanding of the evolution of correlated electron systems, it would be desirable to be able to predict these values theoretically. For this the *density functional theory* is a powerful tool.

The *density functional theory* (DFT) gets its name from the Hohenberg-Kohn theorem. This states that the ground state energy is a unique functional of the ground state density [6]. So far we had assumed plane waves or in the picture of nearly free electron system Bloch-waves. However we don't know what the ground state wave-function of the real electron-system looks like. Therefore here the transition is made from the ground state wave function to the function of electron-density at place r. Using the *Ritz method* one can then write the ground state energy of the system

$$E_0 = E\{n_0(r)\} \leq \langle\psi|H|\psi\rangle, \tag{2.8}$$

with the ground state density $n_0(r)$ and the ground state of the system $|\psi\rangle$. This could theoretically be used to find the exact ground state by variation of $\delta E\{n(r)\} = 0$. DFT hence offers us the possibility to predict the ground state energy of a system and compare it to experimental findings.

In reality this is not straight forward as the functionals of the kinetic energy $T\{n(r)\}$, the potential energy $V\{n(r)\}$ and the interaction $U\{n(r)\}$, that make up E, are unknown. While $V\{n(r)\}$ can be assumed to follow the single particle potential as we used in nearly free electron theory, the kinetic functional remains unknown and the interaction functional can only be estimated to the electrostatic exchange plus a term $E_{ex}\{n(r)\}$, the exchange interaction [6].

Kohn and Sham proposed to solve the problem by writing the energy again as a functional of a single particle wave functions $\psi_i(r)$ using [6]

$$n(r) = \sum_{i=1}^{N_e} |\psi_i(r)|^2. \tag{2.9}$$

This leads to the *Kohn-Sham equations* which can be used iteratively to get a solution of the kinetic energy functional. The assumption to use a single particle wave function leads to the fact that the use of the kinetic energy and single particle potential leads still to an exact solution of the many body problem. The reason that the use of a single particle wave-function is applicable lays again in the concept of quasiparticles which we can describe in this way. The interactions are then described by their band mass, enhanced over the free electron mass. On the other hand this limits application to weakly coupled systems. All aspects of the many body problem are now contained in the exchange interaction $E_{ex}\{n(r)\}$, whose form is unknown. We therefore have the same problem as in Fermi liquid theory where the form of the Landau-parameter was not unknown.

As mentioned, the DFT formalism is theoretically exact, but in order proceed we need to make some approximations and hence the results obtained by calculations can only be as good as the validity of the approximation to the real system. The typical approaches to find $E_{ex}\{n(r)\}$ involves the *local density approximation* (LDA) where E_{ex} at place r only depends on the density n at point r or the *generalized gradient approximation* (GGA) that involves in addition to the density at point r, the gradient $\partial n/\partial r$. Both methods are limited to static exchange and correlation effects that are approximated locally. It hence leads to a band structure that lacks long range and fluctuating interactions as well as strong coupling. For this more advanced theories such as *dynamic mean field theory* (DMFT) are necessary. Typically the theoretically determined values of band structure and derived mass, *band mass*, are compared to experimental results. The comparison then holds information whether the local approximation describes the system well or if additional effects need to be taken into account.

DFT calculations have been successfully used in weakly correlated systems such as sodium. In strongly correlated systems however it has its limits, for example in the cuprate-superconductors where it predicts a metallic behaviour while experiments have found insulating behaviour in the parent compounds. The reason for this can be best described when we turn back to Fermi liquid picture. The use of a single-particle description, as present in the Kohn-Sham equations, is a good approach as long as we can define the quasiparticles as free electron gas. This treatment is correct when the spectral weight $E(k,\omega)$ is well represented by strong peaks as seen in Fig. 2.3a for a non-interacting, or (b) for a weakly interacting system as described by

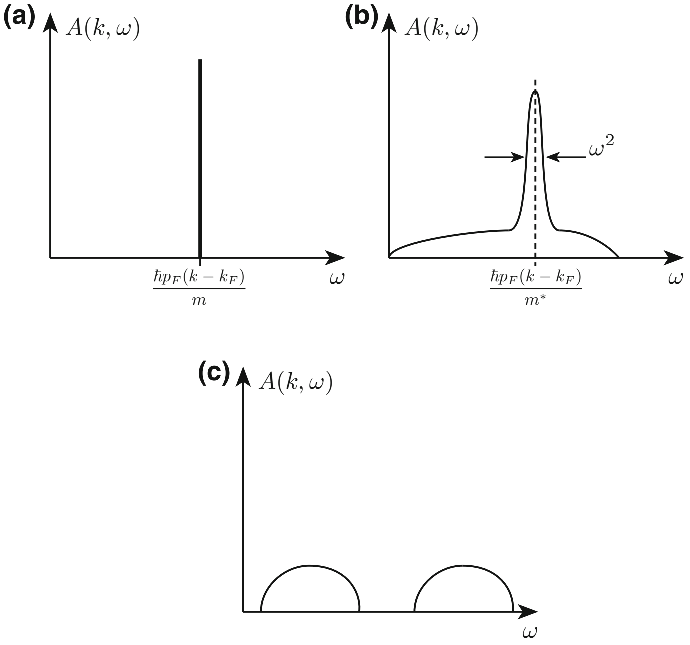

Fig. 2.3 Spectral function $A(k, \omega)$, gives the probability of an electron with momentum k to be found with a given energy ω. **a** For a non-interacting electron the probability is a delta-function, **b** for a Fermi liquid, where the quasiparticles are superimposed of non-interacting states, the peak is smeared out and **c** for a strongly correlated system, like Mott-Hubbard insulators, where the weakly coupled treatment breaks down and no quasiparticle peak is found

Fermi liquid theory. The stronger the interactions become, the more eigenstates of the non-interacting eigenstates need to be taken into account, which leads to enhanced broadening or even a shift of the spectral weight as shown in Fig. 2.3c which is typically found in Mott-Hubbard physics where strong Coulomb repulsion U needs to be taken into account. In this case the system is no longer well described by a LDA.

2.4 Bandstructure Calculations

The following section shall give a brief introduction to the basis of band structure calculations as performed in this work and the most common terms found within. The aim is to sketch the process rather than a detailed theoretical description. A more detailed treatment can be found in Ref. [6, 8].

2.4.1 LAPW

The *linear augmented plane wave* (LAPW) is a combination of the *Wigner-Seitz-method* which assumes spherical harmonics for the wave functions of the atoms and the *plane wave method* which is based on the solution of the Schrödinger equation using Bloch-functions. While the first method proves to be inaccurate in the region between atoms the second is challenging when trying to describe the atomic orbitals, as it requires higher order terms. The way around this is to split the Wigner-Seitz cell in two parts. For the inner part of radius R we assume a spherical potential, while for $r > R$ a constant potential us used. Due to its shape, the resulting potential is known as *muffin tin potential*. For the solution of the Schrödinger equation one uses linear combinations of the form

$$\psi_\varepsilon(r) = \sum_{l,m} A_{l,m} Y_{l,m}(\vartheta, \varphi)\chi_{l,\varepsilon}(r), \tag{2.10}$$

for $r < R$. $Y_{l,m}(\vartheta, \varphi)$ and $\chi_{l,\varepsilon}(r)$ are spherical and radial part of the wave functions and $A_{l,m}$ are Bloch-coefficients. In the region where $r > R$ plane-waves of the from

$$\phi_k(r) = e^{ikr} \tag{2.11}$$

are used. The dispersion relation $\varepsilon(k)$ is then achieved by the condition $\psi_\varepsilon(R) = \phi_k(R)$.

2.4.2 WIEN2k

In this work the WIEN2k package [9] was used for bandstructure calculations in the iron-based superconductors. Within this package the functions described in LAPW are used as basis set for the Kohn-Sham equations within the DFT algorithm. The calculation then follow the Ritz method to minimize the differential with respect to the linear combinations of augment plane waves. In order to estimate the exchange interaction the LDA or GGA approach can be used. The used procedure follows the outline:

1. start with a guess of the density $n_0(\mathbf{r})$
2. determine the single-particle potential from $n_i(\mathbf{r})$
3. application of LDA or GGA to determine the exchange correlation function $E_{ex}(n_i)$
4. solving the Kohn-Sham Equation $H_{KS}\psi = \varepsilon\psi$
5. determine the new density $n_{i+1}((r))$ from ψ
6. if $n_{i+1} \neq n_i$ start over with n_{i+1} as input if not we have have found ground-state density and energy

2.4.3 Dynamic Mean Field Theory

In the course of this work we will compare our experimental results to those obtained by GGA band structure calculations. However there is also a variety of studies in the field of iron-based superconductors that go beyond this approximation and incorporate *dynamic mean field theory* (DMFT) into their calculations [10–12]. DMFT is in these calculations based on LDA calculations. While in LDA we don't make any assumptions on interactions, except of limiting ourself to a local mean field effect, DMFT includes correlations due to Hubbard U and Hund's rule coupling J. These input parameters can more or less be tuned freely and are mostly limited by physical validity.

The choice of input parameter however leads to the fact that we can not see it as a first principle calculation. Also we have to take into account that while systems like the cuprates, where strong onsite Coulomb interaction can be well represented with DMFT [13], the long wave length spin interactions, likely present in the iron-based systems, are not captured in these calculations [11].

2.5 Quantum Oscillation

So far we have focused on the theoretical description of electrons in metals. In this section we will add the magnetic field to this description with the focus on quantum oscillations. In Fermi liquid theory as well as in DFT we have pointed out that we do not possess an exact knowledge of the exchange interaction of electrons in solid. However within Fermi liquid theory we know that those interactions are contained in the Landau parameters. This can be accessed experimentally using the temperature dependence of quantum oscillation amplitude and are determined as effective masses.

Using quantum oscillations in combination with LDA calculations we can further find a theoretical model of the Fermi surface topology that can help us understand electronic correlations in the system.

Within this study we will determine how the effective mass is enhanced over the free electron mass. We should bear that the band mass can refer to different theories and so we need to point out that throughout the context of this work we will use band mass m_b as the mass that has been determined by LDA calculations and hence already includes on-site interactions, at the mean-field level.

We will begin with a semi-classical treatment and then include quantum mechanics to reach the *Lifshitz-Kosevich formula* that describes the *de Haas-van Alphen effect* and lets us extract the relevant information from our experimental results.

2.5.1 Semi-classical Electron in a Magnetic Field

Lets start by considering a free electron in a uniform magnetic field. The motion of the electron will be governed by the Lorentz-force

$$\hbar \frac{\mathrm{d}\mathbf{k}}{\mathrm{d}t} = -e\mathbf{v} \times \mathbf{B}. \tag{2.12}$$

$\mathrm{d}\mathbf{k}/\mathrm{d}t$ is only non-zero perpendicular to the magnetic field $\mathbf{B}$ and the velocity of the electron $\mathbf{v}$. The energy of the electron is then constant and its velocity can be expressed as

$$\mathbf{v}(\mathbf{k}) = \frac{1}{\hbar} \nabla_{\mathbf{k}} E(\mathbf{k}). \tag{2.13}$$

From this we conclude that the electrons are bound to orbits in k-space of constant energy perpendicular to $\mathbf{B}$.

The time that is needed for one revolution t_c is given by

$$t_c = \frac{\hbar^2}{eB} \frac{\partial S(E, k_\parallel)}{\partial E}, \tag{2.14}$$

where S is the k-space area of the electron orbit. This is expressed more commonly using the *cyclotron frequency*

$$\omega_c = \frac{2\pi}{t_c} = \frac{eB}{m_c}, \tag{2.15}$$

with the cyclotron mass

$$m_c = \frac{\hbar^2}{2\pi} \frac{\partial S(E, k_\parallel)}{\partial E}. \tag{2.16}$$

In the case of a free electron system $m_c = m_e$.

2.5.2 Quantum Mechanical Description

To describe the electrons in the system in a more precise way, a quantum mechanical treatment is necessary. The motion of the electron in the magnetic field has to satisfy the Bohr-Sommerfeld-condition

$$\oint \mathbf{p} \mathrm{d}\mathbf{q} = 2\pi(r + \gamma)\hbar. \tag{2.17}$$

In this notation r is an integer value, γ a phase which still needs to be determined and $\mathbf{p}$ the canonical moment

$$\mathbf{p} = \hbar\mathbf{k} - e\mathbf{A}, \tag{2.18}$$

with the vector potential $\mathbf{A}$ defined by $\mathbf{B} = (\nabla \times \mathbf{A})$.

By substituting for $\mathbf{p}$ and solving the integral it turns out that the orbits are such, that they enclose integer values of *flux-quanta* $\phi_0 = h/e$. Transferred into k-space the area of the orbits is given by

$$S_\perp(E, k_\parallel) = (r + \gamma)\frac{2\pi B}{\phi_0}, \tag{2.19}$$

which is known as the *Onsager-relation* [14]. It is immediately clear that for constant magnetic field the area $S_\perp$ is constant for all $k_\parallel$. These tubes are the *Landau-tubes* illustrated for a free-electron system in Fig. 2.4.

We are still left to determine the phase γ. This can be done by solving the Schrödinger equation for a free electron in an applied external magnetic field. Assuming the field pointing along the z-direction we obtain for the orbital energy levels

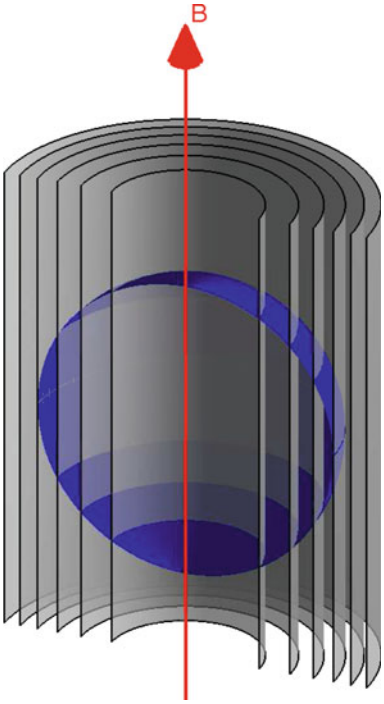

Fig. 2.4 Schematic of *Landau tubes* parallel to the applied magnetic field **B** for a free electron gas with spherical Fermi surface

$$E_n = \left(n + \frac{1}{2}\right)\hbar\omega_c + \frac{\hbar^2}{2m}k_z^2. \tag{2.20}$$

While the energy parallel to the field stays unaffected we again obtain the quantization of energy perpendicular to the magnetic field direction. Comparing this result with the previous and substituting the cyclotron frequency ω_c we obtain the phase $\gamma = 1/2$.

As the size of the orbit changes with field, the Landau-tubes will eventually cross the Fermi-level. The rate at which this happens is determined by the spacing of two consecutive orbits in field

$$\Delta\left(\frac{1}{\mathbf{B}}\right) = \frac{1}{\mathbf{B_n}} - \frac{1}{\mathbf{B_{n+1}}} = \frac{2\pi}{\phi_0 S_{extr}}. \tag{2.21}$$

Here only extremal orbits on the Fermi-surface perpendicular to $\mathbf{B}$ with area S_{extr} are taken into account. Why this is the case will be discussed later. This determines the frequency

$$F = \frac{1}{\Delta(1/\mathbf{B})} = \frac{\phi_0}{2\pi}S_{extr} \tag{2.22}$$

at which the Landau-tubes cross the Fermi-level. As we consider the non-interacting case at $T = 0$, only states up to the Fermi-level are populated. This means that as the Landau-tube crosses the Fermi-level the states empty and cause a changes to the density of states at the Fermi-level. This periodicity is reflected in the heat-capacity, magnetization and other physical properties which are related to the density of states at the Fermi-level.

2.5.3 De Haas-Van Alphen Effect

The system which we are studying is best described by the temperature T, the volume V and the chemical potential μ. Therefor to study this system in more detail we will turn to the thermodynamic potential $\mathbf{\Omega}$. The magnetic moment of the system can be derived from $\mathbf{\Omega}$ by the derivative

$$\mathbf{M} = -(\nabla_{\mathbf{H}}\mathbf{\Omega})|_{\mu=const}. \tag{2.23}$$

In order to obtain the thermodynamic potential for the Landau tubes of interest here, it is necessary to derive $\mathbf{\Omega}$ at the previously determined energy levels (Eq. 2.19) and the degeneracy of each Landau tube. A detailed derivation of this can be found in reference [15]. At this point we will focus on the resulting expression for the thermodynamic potential and its implications on the magnetic moment.

The thermodynamic potential of electrons in a magnetic field is expressed as series over all harmonics p [15]

$$\Omega = \left(\frac{e}{2\pi\hbar}\right)^{3/2} \frac{e\hbar B^{5/2}}{m^*\pi^2} \left|\frac{\partial^2 S}{\partial k_z^2}\right|^{-1/2} \sum_{p=1}^{\infty} p^{-5/2} R_T R_D R_S \cos\left[2\pi p\left(\frac{F}{B}-\frac{1}{2}\right) \pm \frac{\pi}{4}\right]. \tag{2.24}$$

Following Eq. 2.23 we obtain the parallel magnetic moment

$$M_{\parallel} = -\left(\frac{e}{2\pi\hbar}\right)^{3/2} \frac{2Fe\hbar B^{1/2}}{m^*\pi} \left|\frac{\partial^2 S}{\partial k_z^2}\right|^{-1/2} \sum_{p=1}^{\infty} p^{-3/2} R_T R_D R_S \cos\left[2\pi p\left(\frac{F}{B}-\frac{1}{2}\right) \pm \frac{\pi}{4}\right]. \tag{2.25}$$

This formula is known as the *Lifshitz-Kosevich formula*. The component perpendicular to the field direction

$$M_{\perp} = -\frac{1}{F}\frac{\partial F}{\partial \theta} M_{\parallel}, \tag{2.26}$$

will be used later in the description of the torque magnetometery and should only be mentioned for completeness.

In the *Lifshitz-Kosevich* (LK) formula we find that the amplitude of the signal is altered by the second derivative of the cross-sectional area $|\partial^2 S/\partial k_z^2|^{-1/2}$. This is known as the *curvature factor*. In the case of an almost cylindrical Fermi-surface the variation of the orbits along the k_z direction will be very small in the vicinity of the extremal orbits. This will lead to the fact that the curvature factor will get large, therefore favour the observation of quasi-2-dimensional sheets of Fermi-surface rather than spherical sheets where the change along k_z is much larger. Physically this can be understood by imagining a Landau tube crossing the Fermi-surface in the case of a cylinder and in the case of a sphere. While for the cylinder in the case of $\mathbf{B} \parallel k_z$ all state suddenly empty at the same time, the Landau-tube empties continuously in the case of the sphere only leaving a small portion of the original state to empty at the extremal orbit.

The factors R_T, R_D and R_S describe damping of the quantum oscillation due to sample and material specific parameters. While there are more influences such as mosaic effects that can reduce the oscillation amplitude we will focus on these three main factors and discuss them in the next section.

2.5.4 Damping Factors

In the following we will discuss the the main damping factors influencing the oscillation amplitude. While the LK-formula was derived for a non-interacting electron gas the origin of the damping factor comes from many-body interaction and scattering mechanisms. However it can be shown that this does not influence the form of the LK-formula [16].

2.5.4.1 Finite Temperature

In the case of finite temperature the Fermi-Dirac distribution-function becomes smeared out. This has the effect that instead of a sudden depopulation of the Landau tubes when crossing the Fermi level the depopulation becomes smooth. In the case that the Landau-level spacing is smaller than the smearing $k_{\mathrm{B}}T$ of the Fermi-dirac distribution the depopulation of Landau tubes becomes continuous. As there is no sharp energy-level of depopulation anymore, we need to consider the contribution of a range of depopulation around the Fermi-level E_F. The change of $\mathrm{d}S/d\mathrm{E}$ within $k_{\mathrm{B}}T$ of the Fermi-level will, as we have seen in the previous section (Eq. 2.22), contribute a spectrum of frequencies. The superposition of these and their individual phases will cause a reduction in the oscillation amplitude. This reduction can be expressed as [15]

$$R_T = \frac{X}{\sinh(X)}, \tag{2.27}$$

with

$$X = \frac{2\pi^2 p k_{\mathrm{B}} T m^*}{e\hbar B} \approx 14.69 p m^* \frac{T}{B}. \tag{2.28}$$

The temperature dependence at constant magnetic field is entirely determined by the effective mass m^*. The reason for this can be seen when we combine the origin of the phase smearing $\mathrm{d}S/d\mathrm{E}$ with Eq. 2.16. At finite temperature the Fermi distribution leads to the population of a states around E_F. From this we find a distribution of frequencies that due to interference lead to a reduced spectral weight of the main frequency. For flat bands crossing the Fermi-level one finds large values of $\mathrm{d}S/d\mathrm{E}$ and hence a wide spread of frequencies. In order to observe a sharp peak in the oscillation spectrum one needs to go to much lower temperatures than for bands that have small variation of S around E_F.

We should keep in mind that the mass which will be determined using the temperature dependence of the dHvA-amplitude is renormalized by many-body interaction such as electron-electron and electron-phonon interaction over the band mass m_b.

The reason for the magnetic field entering Eq. 2.27 come from the spacing of Landau-levels. In the previous section we had found (Eqs. 2.15 and 2.20) that the Landau-level spacing is $\Delta E \propto B/m_c$. Hence the effect of phase-smearing will be reduced by higher magnetic fields as the spacing of Landau tubes will become larger. An example of the temperature damping is given in Fig. 2.5 for different effective masses in the range typically found in this work, and for a constant mass at different magnetic fields used in the current study of the iron-based superconductors.

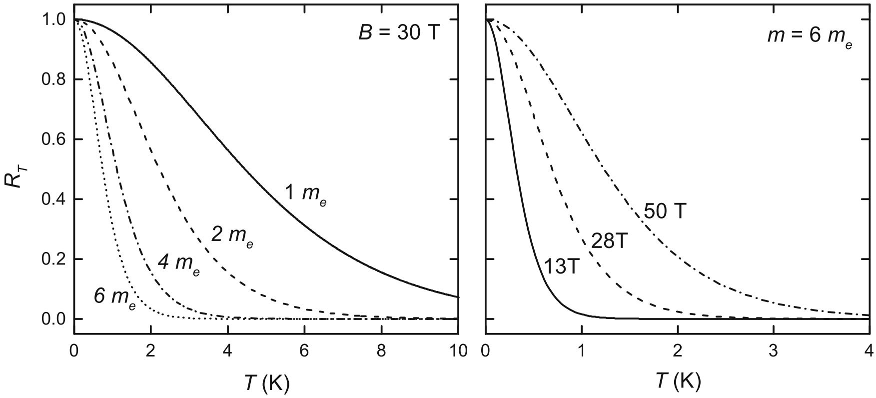

Fig. 2.5 The temperature damping term is plotted at $B = 30\,\mathrm{T}$ for different effective masses m^* (*left panel*) and for a constant effective mass $m^* = 6\,m_e$ at different magnetic fields (*right panel*)

2.5.4.2 Finite Lifetime

The effect of a finite life-time τ of the quasiparticle can be taken into account by introducing a Lorentzian broadening of the Landau-levels. The phase-smearing resulting from this effect is represented by [15]

$$R_D = \exp\left(\frac{p\pi}{\omega_c\tau}\right) \tag{2.29}$$

and is known as the *Dingle-term*. The expression in the exponent can also be expressed in terms of the mean free path l. For this we substitute ω_c using Eq. 2.15

$$\frac{\pi}{\omega_c\tau} = \frac{\pi m_c}{eB\tau}\frac{v_F}{v_F} = \frac{\pi}{eB}\frac{\hbar k_F}{l}, \tag{2.30}$$

where we used $\tau = v_F l$. By assuming a spherical orbit and Eq. 2.22 we can simplify this expression further

$$\frac{\pi}{eB}\frac{\hbar k_F}{l} = \frac{\hbar\pi}{e}\sqrt{\frac{2e}{\hbar}}\frac{\sqrt{F}}{lB} \approx \frac{1140\sqrt{F}}{lB}. \tag{2.31}$$

The mass, which enters the Dingle term, m_c, is not the renormalized mass that was found for the effective mass. It was derived theoretically by Wassermann et al. [17] and experimentally proven by Harrison et al. [18] that the mass used in the Dingle term is the band-mass m_b which can be found by band-structure calculation and only includes the renormalization due to the ionic lattice of the system [16]. We can also understand this by comparing the origin of the phase smearing in the two scenarios. While for the temperature damping term the distribution function is modified at finite temperature, in the case of a finite life time the Landau levels are broadened. Many-body effects like electron-phonon coupling, effecting the dispersion relation $E(k)$ at E_F, hence enhance the effective mass measured in R_T, but keep the Landau level spacing, determined by ω_c, constant. This holds that the field dependence and hence the mean free path is unaffected by the many body interactions.

2.5.4.3 Spin Factor

In a paramagnetic system the electron-bands originating from spin-up and spin-down electrons are degenerate in zero field. This degeneracy is lifted under the influence of a magnetic field by Zeeman-splitting with an energy-difference of $\Delta E = g\mu_B B$, with the Bohr magneton μ_B and the gyromagnetic ratio g.

This leads to a phase-smearing influenced by the spin-mass m_S of the system, which is related to the Pauli-susceptibility that is not enhanced by electron-phonon interaction. Hence it differs from the effective mass determined by the temperature dependence.

The damping-factor can be calculated as [15]

$$R_S = \cos\left(\frac{p\pi g}{2}\frac{m_s}{m_b}\right). \tag{2.32}$$

The spin factor can lead to so call *spin-zeros*. Those are regions in the angle dependence for which the field-direction causes the split energy levels to be different by one flux-quantum, which cause a destructive superposition. However one has to be careful not to mistake these spin zeros with geometric zeros in the angle dependence caused by superposition of different extremal orbits. Those effects were for example found in $\mathrm{Tl_2Ba_2CuO_{6+\delta}}$ [19].

2.5.4.4 Extremal Orbits

As mentioned before the observed quantum oscillations originate only from extreme cross-section-areas perpendicular to the applied field. This powerful tool, which allows us to map the topology of the observed quantum oscillation shall be discussed in a bit more detail, as it might not be clear at first sight why this is the case. We will assume a Fermi-surface which varies as $k_\perp = cos(k_\parallel)$, where $k_\parallel$ refers to the direction parallel to **B**. Using Eqs. 2.22 we will find a distribution of frequencies along $k_\parallel$. However, while most of these frequencies correspond to a smooth variation of the electron motion along $k_\parallel$ a strong effect in the energy of the system is observed where $\mathrm{d}F(k_\parallel)/\mathrm{d}k_\parallel$ is minimal and hence large sections of Landau tubes empty. This criteria describes the extremal orbits on the Fermi-surface.

An alternative way to find this result is to assume the frequency distribution $F(k_{\|})$ which we already introduced. The expected signal can be calculated by

$$M = \int sin\left(2\pi \frac{F(k_{\|})}{B}\right) \mathrm{d}k_{\|}. \tag{2.33}$$

The integral has to be carried out over the entire frequency distribution and phase smearing. This then gives the already known result that the signal only contains significant contributions form the extremal orbits.

2.6 Drude Model—Electronic Transport

The *Drude model*, which was the first to describe transport of electrons in metals, models the electrons as classical particles that follow Newton's law of motion

$$m\frac{d\mathbf{v}}{dt} = e\mathbf{E} - \frac{m}{\tau}\mathbf{v}, \tag{2.34}$$

for an electron of charge e in a electrical field E. The second term on the right hand side represent the friction that an electron experiences. The factor $1/\tau$ is of phenomenological nature, seen as strength of the friction whose microscopic origin is not specified. The differential equation holds two solutions. The homogeneous one $\upsilon \propto exp(-t/\tau)$, which shows that in absence of an electrical field the electron velocity decays exponentially. The factor τ is therefore seen as a mean life time. For the inhomogeneous differential equation at $t \gg \tau$ we obtain a constant velocity

$$\mathbf{v} = \frac{e\tau}{m}\mathbf{E}, \tag{2.35}$$

which is proportional to the external field E. From this we find for the current density

$$\mathbf{j} = ne\mathbf{v} = \frac{ne^2\tau}{m}\mathbf{E} = \sigma\mathbf{E}, \tag{2.36}$$

where we have used Ohms law in the last step. We see that the electrical conductivity σ of a metal is expected to be proportional to the carrier concentration and life time. The mean life time of a carrier is similar to the scattering time that we found in the description of the dHvA effect. While for the measurements of quantum oscillations samples with large τ as found from the residual resistivity $\sigma^{-1}(T = 0)$ are beneficial, the two values are not identical. The scattering rate τ in conductivity is mainly dominated by large angle scattering, while the values found in the Dingle term in dHvA include all types of scattering [15].

We will now include an external magnetic field, which alters the movement of the electrons and forces them on spherical orbits as already discussed in Sect. 2.5.1. The equation for the movement of the electrons is then given by

$$\frac{d\mathbf{v}}{dt} = \frac{e}{m}\mathbf{E} + \frac{e}{m}\mathbf{v} \times \mathbf{B} - \frac{1}{\tau}\mathbf{v}. \tag{2.37}$$

We chose to apply the magnetic field along the z-axis $\mathbf{B} = (0, 0, B_z)$. In the presence of a magnetic field the conductivity now given by a tensor as the magnetic field breaks the symmetry of the system. The conductivity tensor is given as

$$\sigma = \frac{ne^2\tau}{m}\begin{bmatrix} \frac{1}{1+\omega_c^2\tau^2} & \frac{\omega_c\tau}{1+\omega_c^2\tau^2} & 0 \\ -\frac{\omega_c\tau}{1+\omega_c^2\tau^2} & \frac{1}{1+\omega_c^2\tau^2} & 0 \\ 0 & 0 & 1 \end{bmatrix}, \tag{2.38}$$

with the cyclotron frequency $\omega_c = eB/m$. In the limit of very high magnetic field or high purity samples we find $\omega_c\tau \gg 1$, which leads to

$$\sigma_{xy} = \frac{ne}{B} \tag{2.39}$$

for the transverse conductivity known as *Hall conductivity* and

$$\sigma_{xx} = 0 \tag{2.40}$$

for the longitudinal conductivity. While the result found for the Hall effect is in agreement with experiments the vanishing conductivity is not verified in experiments.

To solve this problem we need to consider a system with two different carriers. This can be realized by assuming different effective masses, charges or scattering times. In this model one now finds that the total current $\mathbf{j}$ contains parts from both carriers

$$\mathbf{j} = \sigma_1\mathbf{E} + \sigma_2\mathbf{E}. \tag{2.41}$$

Therefore we obtain a change of resistivity due to the presence of a magnetic field [6]

$$\Delta\rho = \frac{\rho(B) - \rho(0)}{\rho(0)}. \tag{2.42}$$

For clean systems we find that where the residual resistivity $\rho(T = 0)$ becomes small the magnetoresistance increases. In a single band system this scenario can be realized by a k dependent effective mass or Fermi velocity.

2.7 Superconductivity

It took almost 50 years from the discovery of superconductivity by Kermlingh Onnes until the first microscopic understanding given by Bardeen, Cooper and Schrieffer (BCS). On the way to this theory a number of attempts for the description of this new ground state of electrons in a solid were made. In this section we will follow this path and start by the phenomenological thermodynamic treatment of the London brothers. From their work the *London penetration depth* is derived that describes the Meissner effect, where an external magnetic field is expelled from the bulk of the superconductor. We will then turn to the Ginzburg-Landau theory, which deals with the upper and lower limiting fields of superconductors based on Landaus theory of phase transitions. Finally we will end at the BCS theory which up to now is our best microscopic understanding of superconductivity. On the way we will focus and discuss those physical properties that will later be important in the analysis and understanding of experimental results.

2.7.1 London Penetration Depth

The London-penetration depth was first expressed by the London-brothers in their phenomenological work on the thermodynamics of superconductivity [20]. It describes the length-scale on which a magnetic field goes to zero inside a superconductor.

We start by assuming that for $T < T_c$ a portion of the total carrier density n has condensed to form the superconducting carrier density n_s. We can describe their motion analogue to the previous section

$$m\dot{\mathbf{v}}_\mathbf{s} = -e\mathbf{E}, \tag{2.43}$$

where we neglected the last term of the Drude-model as we assume the mean scattering of the electrons to go to infinity for a perfect conductor. By substituting $\mathbf{v}_\mathbf{s}$ with the current density $\mathbf{j}_\mathbf{s} = -n_s e\mathbf{v}_\mathbf{s}$, we come to the conclusion that unlike in Ohms-laws, where the current density $\mathbf{j}$ is proportional to the electric field $\mathbf{E}$, here the time-derivative of j_s is proportional to $\mathbf{E}$. This leads to the fact that for a direct current there will be no potential difference over the sample. By using Maxwells-equation $\nabla \times E = -\partial B/\partial t$ we can transform Eq. 2.43 to

$$\frac{\partial}{\partial t}\left(\nabla \times \mathbf{j} + \frac{n_s e^2}{m}\mathbf{B}\right) = 0. \tag{2.44}$$

While this expression is valid for all conductors with the scatting time $\tau \rightarrow 0$, in the Meissner state the flux is zero in the static case. Hence for a superconductor in the Meissner state the expression in the brackets must be zero. This then gives the *London-equation*

$$\nabla \times \mathbf{j} + \frac{n_s e^2}{m}\mathbf{B} = 0. \tag{2.45}$$

By applying this equation to find out how the magnetic field changes upon entering a superconductor we find that it decays exponentially

$$B(x) = B_0 e^{-x/\lambda_l}, \tag{2.46}$$

inside the sample, with the characteristic length-scale

$$\lambda_L = \sqrt{\frac{m^*}{\mu_0 n_s e^2}}, \tag{2.47}$$

the *London-penetration depth*. Two things are important to notice. First the value of the London penetration depth is proportional to the superconducting carrier density in the limit of $T = 0$. This means that since most metals have similar charge carrier densities they will also possess similar penetration depth values only normalised by the effective mass m^* of the relevant system. Further at the superconducting critical temperature T_c n_s goes to zero and hence the penetration depth diverges. Secondly, as mention, the penetration depth of a superconductor, even at $T = 0$, depends on the normal state property m^*.

An alternative approach to derive the London penetration depth is from the finite frequency Drude model

$$\sigma(\omega) = \frac{ne\tau^2}{m}\frac{1}{1 - i\omega\tau}. \tag{2.48}$$

The integral over all real-part frequency is conserved and gives $\omega_p^2 = \pi ne^2/m$, the *plasma-frequency* ω_p, which is independent of the scattering rate. By taking the Drude model in the limit of $\tau = \infty$ we obtain the conductivity for the ideal conductor, that we can use with $j = \sigma E$ in the above expression and obtain the same result for λ_L, which we could also write as

$$\lambda_L^2 = \frac{\pi}{\mu_0 \omega_p^2}. \tag{2.49}$$

As the conductivity σ is also given as integral over the Fermi surface $\sigma \propto \int v_x^2 v_F^{-1} dS$ [21] we can link the penetration depth to this and find $\lambda_L^{-2} \propto \int v_x^2 v_F^{-1} dS$. This shows that the London penetration depth is dominated by sections of the Fermi surface where the Fermi velocity v_F is high and hence the effective mass is low.

2.7.2 Ginzburg-Landau Theory

The Ginzburg-Landau (GL) theory is a powerful tool as a first attempt to explain new experimental results in superconductors. Its macroscopic description from a thermodynamic viewpoint provides the possibility to explain systems without an exact microscopic understanding and can therefore hold more general results than a microscopic theory.

Ginzburg and Landau based their theory on the Landau-theory of phase-transitions. It starts from the view-point of the enthalpy of a system with an order parameter ψ which is zero above a critical temperature T_c, non-zero below and one at $T = 0$. Unlike the Landau-theory of phase-transitions where the order-parameter is real and constant in space, in the GL-theory the order parameter is given by the macroscopic superconducting wave-function $\psi(r) = \psi_0(r)\exp[-i\phi(r)]$. This is of complex nature and does not necessarily need to be constant in space. As the enthalpy is real we need to take the absolute value of the complex wave-function, which represent the density of superconducting particle $|\psi|^2 = n_s$. We then develop in terms of n^2. Taking this ansatz the GL-theory is strictly only valid close to T_c where $n_s \rightarrow 0$. In the vicinity of T_c the enthalpy per unit volume g is then given by

$$g_s = g_n + \alpha|\psi(r)|^2 + \frac{1}{2}\beta|\psi(r)|^4 + \frac{1}{2\mu_0}|B_a - B_i|^2 + \frac{1}{2m_s}|(i\hbar\nabla - e_s\mathbf{A})\psi(r)|^2, \qquad (2.50)$$

with the superconducting g_s and normal-state g_n enthalpy-density and the charge e_s and mass m_s of the superconducting wave function ψ. The last therm of Eq. 2.50 represents the kinetic energy of the Cooper pair due to an external magnetic field presented by the vector-potential $\mathbf{A}$. The second last is the displacement energy need to reduce the applied magnetic field B_a to zero inside the superconductor B_i in the Meissner-state. Since derived from a purely thermodynamic standpoint without any knowledge of the microscopic origin, this is probably the most general theory we have on superconductivity. However we will see in Sect. 4.3, where we discuss the upper and lower critical field, that for quantum critical systems, even this most general form fails.

2.7.2.1 Upper Critical Field

In addition to the London penetration depth λ, the GL theory predicts a second characteristic length scale of a superconductor, the GL coherence length ξ. This is derived in the zero field limit to [22]

$$\xi = \sqrt{\frac{\hbar}{4m|\alpha|}}. \qquad (2.51)$$

While α is unknown in this phenomenological approach a more precise formulation of ξ is found in BCS theory. Ginzburg and Landau realised that for $\kappa = \lambda/\xi > 1/\sqrt{2}$ the systems can lower their energy in field by allowing additional superconducting-normal conducting interfaces. This causes the so call vortex-state between the lower and upper critical field and leads to higher critical fields were the material shows a finite resistivity. Using the GL-formalism we can determine this upper critical field H_{c2} at which the $g_s = g_n$. It can be shown [22] that this is the case for

$$\mu_0 H_{c2} = \frac{\Phi_0}{2\pi\xi^2(T)}. \tag{2.52}$$

The GL coherence-length ξ represents the length-scale at which the superconducting wave-function can vary from $\psi = 0$ to $\psi = \psi_\infty$. The criteria of $\psi = 0$ is fulfilled in the vortex core of a type-II superconductor in the mixed state. With this we can identify ξ as the vortex-core radius and H_{c2} as the field at which the normal-state vortex-cores start to overlap. Energetically speaking H_{c2} marks the magnetic field at which the kinetic energy of the screening currents exceeds the condensation energy $g_n - g_s$. This is also known as the orbital limiting effect. The Cooper pairs could also be broken due to the alignment of the spins in the applied magnetic field. This is known as the Pauli limiting field.

2.7.2.2 Lower Critical Field

The lower critical field H_{c1} of a type-II superconductor is the magnetic field at which the Gibbs-free energy of a Abrikosov vortex inside or outside the sample is equal [22]. For this we need the energy of a vortex line per unit length [22]

$$\epsilon_1 = \frac{H_{c1}\Phi_0}{4\pi}. \tag{2.53}$$

Inside the vortex the superconducting gap goes to zero and we find a normal state core. As in GL theory we describe the superconducting state with the complex function ψ, which varies at the superconducting-normal conducting interface like $|\psi| \approx \psi_\infty \tanh \frac{r}{\xi}$ [22]. In the case of a vortex we can therefore identify the parameter ξ as the core radius. The presence of a single flux $\phi_0 = h/2e$ causes screening currents that lead to a field profile [22]

$$h(r) \approx \frac{\phi_0}{2\pi\mu_0\lambda} \ln \frac{\lambda}{r}, \tag{2.54}$$

in the limit of $\lambda \gg \xi$ for $\xi \ll r \ll \lambda$. This would cause a divergent behaviour, which is cut off at $r \approx \xi$, the core radius. The vortex line energy can the also be expressed as the contribution form the field energy h and the kinetic energy of the shielding currents

$$\epsilon_1 \approx \left(\frac{\Phi_0}{2\pi\lambda}\right)^2 \ln\kappa. \tag{2.55}$$

In the derivation of this expression the core has been neglected. We find that the energy of a vortex line per unit length is inverse proportional to λ^2. By combining Eqs. 2.53 and 2.55 we obtain

$$H_{c1} \approx \frac{\Phi_0}{4\pi\mu_0\lambda^2} \ln\kappa \tag{2.56}$$

for the lower critical field. To account for the vortex core contribution that was neglected in the derivation a constant correction factor is used such that we find the result for lower critical field [22]

$$H_{c1} \approx \frac{\Phi_0}{4\pi\mu_0\lambda^2} \left(\ln\kappa + \frac{1}{2}\right) \tag{2.57}$$

2.7.3 BCS Theory

The first successful microscopic understanding of superconductivity was published by Bardeen, Cooper and Schrieffer (BCS) [23]. It had been shown by Fröhlich [24], that when electrons are placed inside a crystal most of the repulsive nature of the Coulomb interaction is screen. By assuming a simple screening model like the Thomas Fermi model we can limit the repulsive behavior to short range interactions. Further Fröhlich showed that it is possible for the electrons to develop an attractive interaction if one includes interactions with the lattice. Cooper then argued that by taking two electrons at $T = 0$ and placing them just above the Fermi level one can obtain a bound state which is energetically more favorable than having the electrons just above the Fermi-level [25]. This bound state is known as a *Cooper pair*. Built on Fröhlich's result that the electrons can interact via the lattice, only electrons of order $\hbar\omega_D$ were included (ω_D is the Debye-frequency). Using the necessary conservation of momentum one finds that the lowest energy state appears for $k_1 = -k_2$ where k_1 and k_2 are the wave-vectors of the interacting electrons. Hence the wavefunction is symmetric under spatial inversion restricting the spin part to be antisymmetric. The Cooper pairs therefore represent a singlet state.

Using the Cooper-pairs as a basis, BCS constructed a wavefunction to describe all electrons in the system. Without going into too much detail the main results of the BCS-theory shall be presented here.

Its was found that the energy of an elementary excitation can be expressed as [22]

$$E_{\mathbf{k}} = \sqrt{\epsilon_{\mathbf{k}}^2 + \Delta_{\mathbf{k}}^2} \tag{2.58}$$

with the normal state energy ϵ and the self-consistent expression for the energy gap

$$\Delta_{\mathbf{k}} = -\sum_{\mathbf{k}'} V_{\mathbf{k}\mathbf{k}'} \frac{\Delta_{\mathbf{k}'}}{2E_{\mathbf{k}'}}. \tag{2.59}$$

The BCS-theory assumes that the interaction potential V is constant and negative (attractive) for all $\mathbf{k}$ and hence results in a constant energy gap Δ. However in the *high*-T_c materials that are discussed in this thesis this is not the case and hence the more general form including the $\mathbf{k}$-dependence has been used.

Further the BCS-theory gives a result for the coherence length ξ which we had already discussed in the Ginzburg-Landau theory. Here the coherence length can be calculated as

$$\xi = \frac{\hbar v_F}{\pi \Delta}. \tag{2.60}$$

It now represents the length-scale, spacial extend, of a Cooper-pair.

The superconducting phase transition at T_c in zero field is is of second order, showing a jump of the heat capacity. The size of the anomaly in the heat capacity was determined in the BCS-theory for a s-wave superconductor in the weak coupling limit to be

$$\Delta C = 1.43 \gamma T_c, \tag{2.61}$$

where γ is the normal state Sommerfeld-coefficient which describes the electronic contribution to the heat capacity and is related to the effective mass via the density of states [26]

$$\gamma = \left(\frac{\pi k_b^2 N_A a^2}{3 \hbar^2} \right) m^*. \tag{2.62}$$

2.8 Phase Transition

Understanding the emergence of new phases and their origin has been or great interest for a long time. We can best understand phase-transitions by turning to thermodynamics. In this work the energy of a system will be described using the Gibbs-free-energy G as it depends on temperature T and magnetic field B, which are typical parameters varied in the lab. Here we hold the particle number. and hence the chemical potential, constant. We assume that a system undergoes a phase-transition as function of the external parameter T. The point at which the phase transition occurs is determined by the relation $G(T < T_c) = G(T > T_c)$, where T_c is the critical point. Within the Landau-theory of phase transitions [1] we find that the transition can be of different order n. Following the classification of Ehrenfest the order of a phase transition is given by the lowest derivative of the free energy with respect to a thermodynamic parameter that is not continuous. If the order parameter, which is the first derivative with respect to the external field, is discontinuous than the phase transition is of first order. However for a continuous order parameter the phase transition is of higher order. This classification fails in the case of divergent order parameter at the phase transition such as in ferro-magnetic materials. In modern physics we therefore distinguish between first-order phase transition, characterised by a latent heat involved in the transition, and second-order or *continuous* phase transitions which are characterized by a divergent fluctuations. In the transition that will be of interest for us and were discussed by Landau are of the second type.

In this case the phase transition is characterized by a continuous thermodynamic quantity m known as the *order parameter*, which is zero in the disordered state and then increases to reach one in the zero-temperature limit. While the average over the sample in the disordered state is zero, this does not rule out fluctuations of the order parameter. Those fluctuation possess a coherence length ξ which at T_c goes to infinity. We can express this in the form

$$\xi \propto |t|^{-\nu}, \tag{2.63}$$

with the dimensionless parameter $t = |T - T_c|/T_c$ and the critical exponent ν. While in this notation fluctuations are treated as spacial variations, when considering systems in quantum field theory, one treats them quasi-classical in d+1 dimensions, where the additional dimension is the imaginary time scale. For the fluctuation in time a typical life-time τ_c is given by

$$\tau \propto \xi^z \propto |t|^{-\nu z}. \tag{2.64}$$

Following these criteria we find for $T > T_c$ a disordered state with dynamic fluctuations of the order parameter and long-range static order of m for $T < T_c$. Hence we call ν the *correlation length critical exponent* and z the *dynamic critical exponent*.

We now considered the energy $\hbar\omega_c$ of the fluctuations, which we compare to the thermal excitation $k_\mathrm{B}T$ of the system if T_c is finite. For a finite life-time of the excitations we find that

$$\omega_c \propto \tau_c^{-1} \propto |t|^{z\nu}. \tag{2.65}$$

For the case where $\hbar\omega_c << k_\mathrm{B}T$, which can be rewritten as

$$|T - T_c| < T_c^{-z\nu} \tag{2.66}$$

the system can be treated classical [27]. However as $T_c \rightarrow 0$ this is not the case anymore and hence the description of the critical behavior close the critical point must take quantum mechanical effects into account. Therefore these phase transitions are called *quantum phase transitions* (QPT) and the point at which the order parameter goes to zero is called a *quantum critical point* (QCP). Also from the comparison of the energy levels we find that in the vicinity of a QCP a region exists where $\hbar\omega_c \geq k_\mathrm{B}T$ and hence the properties of the system are governed by the fluctuations and quantum mechanics.

Before going into detail we should point out how a continuous phase transition appears in experiments. For this we will consider the heat capacity. As mentioned before the order parameter m is zero in the disordered state and changes continuously in the ordered state from zero. Therefore we can perform a Taylor expansion at $T = T_c$ of the Gibbs-energy

$$G(m, T) - G(0, T) = \frac{1}{2}am^2 + \frac{1}{4}bm^4 + ..., \tag{2.67}$$

which is valid for small m. Also we only consider the case where $G(m) = G(-m)$, hence systems that do not break time reversal symmetry, like magnetic systems in an external field. By taking the second derivative $T\partial_T G$ we obtain the expression for the heat capacity

$$C_V(m, T) - C_V(0, T) = \begin{cases} Ta^2/b & T < T_c \\ 0 & T > T_c \end{cases}. \tag{2.68}$$

We see that for a continuous phase transition the heat capacity has a jump at T_c. Remember this is a mean-field treatment and does not include any fluctuations of the order-parameter in the disordered state. By including those fluctuations one obtains the Gibbs-energy in the form $G[m((r), \tau), T]$, which is now a functional of the order parameter. To solve this one needs to find the partition function of this ensemble. An example of this can be found in Ref. [28]. In the case of fluctuations of the order parameter the heat capacity takes the form

$$C \propto |T - T_c|^{-\alpha}. \tag{2.69}$$

Instead of a step at T_c, the heat capacity diverges when approaching the critical point. The exponent α is a characteristic *critical exponent*. Following the same derivation one can also find critical exponents for other observables which are all characteristic for a given class of phase transitions [27]. For the Gaussian approximation the exponent α can be written as $\alpha = 2 - d/2$ with the dimensionality d of the system [29]. However the Gaussian approximation only holds for not too big fluctuations. In general the form $\alpha = 2 - d\nu$ is found, known as *hyperscaling*.

2.8.1 Quantum Phase Transition

We will assume a system to have an ordered ground state below a critical temperature T_0. By tuning a non-thermal parameter g(pressure, magnetic field or chemical potential) it is possible to suppress T_0 to zero temperature (see Fig. 2.6). Following Eq. 2.66

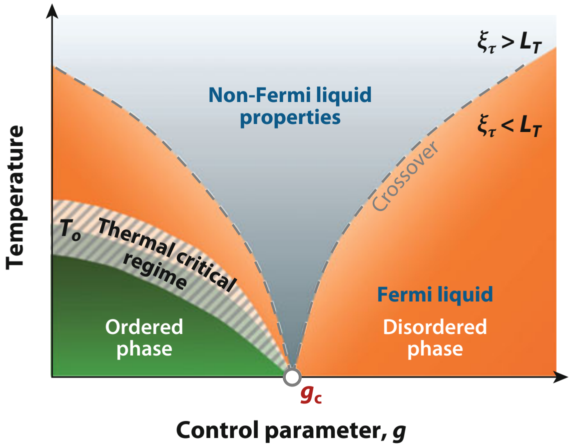

Fig. 2.6 Schematic phase diagram of a quantum critical point. Taken from Ref. [3]

we find that the region in which we can treat the critical behavior in the classical limit vanishes as we approach the QCP g_c. The only fluctuations available at this point to break the order are quantum fluctuations, resulting from Heisenberg's uncertainty principal. However, as we are experimentally not able to reach this point, we should raise the question: why is the appearance of a QCP important to the research conducted in this work? It was found in a variety of experiments that in the case of a QCP, physical properties such as transport, heat capacity and magnetic susceptibility differ from their typical behavior [3, 30]. While in most metals resistivity as a function of temperature is $\rho \propto T^2$, one finds $\rho \propto T^n$, with $n < 2$ in systems for $g = g_c$ (see for example Ref. [31, 32]). Quantum critical systems at finite temperature posses a finite length scale [33, 34]

$$L_\tau = \frac{\hbar c}{k_\mathrm{B} T} \tag{2.70}$$

which limits the imaginary time axis for thermal fluctuations in two or more dimensions. As L_τ was given in the Heisenberg model c is the spin-wave velocity, specific to magnetic phase transitions. By comparing the length-scales Eqs. 2.64 and 2.70, two regimes emerge in the phase diagram for finite temperatures. For $L_\tau > \tau_c$ conventional behaviour, as described by Landau Fermi-liquid theory, is found. For the opposite case $L_\tau < \tau_c$ a *non-Fermi liquid* behaviour, as indicated in Fig. 2.6, evolves, which is found as typical v-shape region in the phase diagram using resistivity measurements [30, 32]. Also we conclude that in the low-temperature regime the excitations from the ground state are weakly affected by thermal fluctuation but relax on the much shorter quantum-time scale. In a mean field approach the system can therefore be explained by the ground-state wave-function. However starting at $g = g_c$ and going to high temperatures an increasing range of the phase diagram is influenced by the quantum critical point, even for $g \neq g_c$. The appearance of this unusual part of the phase-diagram motivates interest in QCP and might be the reason for novel phases at finite temperature emerging from QPT.

References

1. L. Landau, Sov. Phys. JETP **3**, 920 (1957)
2. P. Coleman, A. Schofield, Nature **433**, 226 (2005)
3. T. Shibauchi, A. Carrington, Y. Matsuda, Annu. Rev. Condens. Matter Phys. **5**, 113 (2014)
4. S. Sachdev, Phys. Status Solidi B **247**, 537 (2010)
5. A. Schofield, Contemp. Phys. **40**, 95 (1999)
6. G. Czycholl, *Theoretische Festkörperphysik* (Springer-Verlag, Berlin Heidelberg, 2008)
7. G. Guiliane and G. Vignale, *Quantum Theory of the Electron Liquid*. Cambridge University Press (2005)
8. K. Capelle, Braz. J. Phys. **36**, 1318 (2006)
9. P. Blaha, K. Schwarz, G. Madsen, D. Kvasnicka, J. Luitz, *WIEN2K edited by Karl Heinz Schwarz* (Technische Universität Wien, Austria, 2001)
10. Z. Yin, K. Haule, G. Kotliar, Nat. Mater. **10**, 932 (2011)
11. J. Ferber, H. Jeschke, R. Valenti, Phys. Rev. Lett. **109**, 236403 (2011)
12. J. Ferber, K. Foyevtsova, R. Valenti, H. Jeschke, Phys. Rev. B **85**, 094505 (2012)
13. G. Kotliar, S. Savrasov, K. Haule, V. Oudovenko, O. Parcollet, C. Marianetti, Rev. Mod. Phys. **78**, 865 (2006)
14. L. Onsager, Philos. Mag. **344**, 1006 (1952)
15. D. Schoenberg, *Magnetic Oscillations in Metals* (Cambridge University Press, 1984)
16. M. Springford, *Electrons at the Fermi Surface* (Cambridge University Press, 1980)
17. A. Wasserman, M. Springford, Adv. Phys. **45**, 471 (1996)
18. N. Harrison, P. Meeson, P. Probst, M. Springford, J. Phys.: Condens. Matter **5**, 7435 (1993)
19. P. Rourke, A. Bangura, T. Benseman, M. Matusiak, J. Cooper, A. Carrington, N. Hussey, New J. Phys. **12**, 105009 (2010)
20. F. London, H. London, Proc. R. Soc. Lond. A **149**, 71 (1935)
21. M. French, Angle dependent magnetoresistance in $tl_2ba_2cuo_{6+\delta}$. Ph.D. dissertation, University of Bristol, 2009
22. M. Tinkham, *Introduction to Superconductivity* (Dover Publications, 1996)
23. J. Bardeen, L. Cooper, J. Schrieffer, Phys. Rev. **108**, 1175 (1957)
24. H. Fröhlich, Phys. Rev. **79**, 845 (1950)
25. L. Cooper, Phys. Rev. **104**, 1189 (1956)
26. N.W. Ashcroft, N.D. Mermin, *Solid State Physics*, 3rd edn. (Oldenbourg, 2007)
27. M. Vojta, Rep. Prog. Phys. **66**, 2069 (2003)
28. J. Annett, *Superconductivity* (Oxford University Press, Superfluids and Condensates, 2004)
29. S.-K. Ma, *Modern Theory of Critical Phenomena* (W.A. Benjamin Inc., 1976)
30. S. Sachdev, B. Keimer, Phys. Today **64**, 29 (2011)
31. S. Kasahara, K. Shibauchi, K. Hashimoto, K. Ikada, S. Tonegawa, R. Okazaki, H. Shishido, H. Ikeda, H. Takeya, K. Kirata, T. Terashima, Y. Matsuda, Phys. Rev. B **81**, 184519 (2010)
32. J. Custer, P. Gegenwart, H. Wilhelm, K. Neumaier, Y. Tokiwa, O. Trovarelli, C. Geibel, F. Steglich, C. Pepin, P. Coleman, Nature **424**, 524 (2003)
33. S. Sachdev, J. Ye, Phys. Rev. Lett. **69**, 2411 (1992)
34. A. Chubukov, S. Sachdev, J. Ye, Phys. Rev. B **49**, 11919 (1994)

Chapter 3
Experimental Setup

In this chapter will turn to the experimental procedures used in this work. We will start by looking at the external parameters temperature, magnetic field and hydrostatic pressure which were used to tune the properties of the measured materials, reach the ground state at low temperature or suppress the superconducting ground state. For this we will focus on the mostly used systems, such as a bath-cryostat for temperatures between 0.3 and 300 K and the generation of magnetic field from a few milli Tesla to several tens of Tesla. Further we will discuss the procedures used to grow high quality single crystals for the study of Fermi surface topology and quantum critical phenomena in iron pnictides. The further course of this chapter will then introduce the measurement techniques that were used and developed for the detailed studies of electronic and magnetic properties of the systems studied in this work.

3.1 Low Temperature

Like Kamerlingh Onne's discovery of superconductivity many new phenomena are often revealed by cooling samples close to zero temperature. While ferromagnetic phases can have ordering temperatures well above room temperature, like in NdFe-alloys, a lot of interest today lays in novel ground states that emerge close to QCP. In this work the temperature range of 0.3–300 K was used.

3.1.1 ^{4}He-System

Helium is the only element that does not solidify at ambient pressure at any temperature. When referring to helium we mean the more common isotope ^{4}He. The boiling point of helium is 4.2 K. When reducing the vapour pressure above a liquid helium

C.M. Putzke, *Fermi Surface and Quantum Critical Phenomena in High-Temperature Superconductors*, Springer Theses,
DOI 10.1007/978-3-319-48646-8_3

bath the boiling point drops, following closely the behaviour expected for an ideal gas

$$p \cdot V = \mathrm{Nk_B}T. \tag{3.1}$$

We can see that at constant volume the pressure is proportional to the temperatures of the system. The phase transition from liquid to gas is of first order and is described by the *Clausius-Clapeyron-equation* [2]

$$\frac{dp}{dT} = \frac{L}{\Delta VT}, \tag{3.2}$$

with the latent heat L of the material. By combining the two equations we find that

$$p(T) = p_0 \mathrm{e}^{-L/RT}, \tag{3.3}$$

which shows that it will become exponentially more difficult to reach lower temperatures with lower pressure. At 2.17 K helium changes into a new phase known as the superfluid phase, which is the chargeless counterpart to a superconductor. The transition temperature is known as the λ-point of helium. The base temperature reached in pumped cryostats is typically around 1.2–1.5 K, depending on the system. We have used this technique mainly at the pulsed field facility in Toulouse. The used cryostat is shown in Fig. 3.1. In this system the upper-reservoir is filled with helium. The needle valve can be open or closed during the filling, depending whether the desired temperature for measurements is below or above 4.2 K. For temperatures $T \leq 4.2$ K the needle valve is kept open to allow both upper and lower reservoir to be filled. For temperatures below 4.2 K the needle valve is then closed and the pressure above the lower reservoir is decreased via the pumping port. This allows to reach temperatures down to 1.4 K at the sample position. During this process the helium level drops until it reaches the sample position in which case a sudden increase in sample temperature is observed. In order to increase the hold-time at base temperature, the pressure above the bath was reduced slowly, maintaining a temperature decrease of 0.1–0.2 K/min. For temperatures between 1.5 and 4.2 K the pressure above the lower reservoir was varied to achieve the desired temperature. Before carrying out the experiment the temperature was held constant for at least 5 min allowing for a good thermalisation. After each high field experiment the valve to the pump was closed and the lower reservoir pressurised to atmospheric pressure by opening the needle valve. For experiments at base temperature typically three experiments could be carried out before refilling the system. Also by leaving the needle valve open a hold time of 12 h or more, depending on the quality of the vacuum in the isolating chamber, was achieved, such that the sample could be held at 4.2 K over night.

The system could also be used to reach temperatures above 4.2 K or to allow for constant temperature sweeps from or to room temperature. For this the needle valve was kept closed and a heater, wrapped around the inner tail, was used. The upper reservoir, attached to the sample space, as shown in Fig. 3.1 allows for cooling via

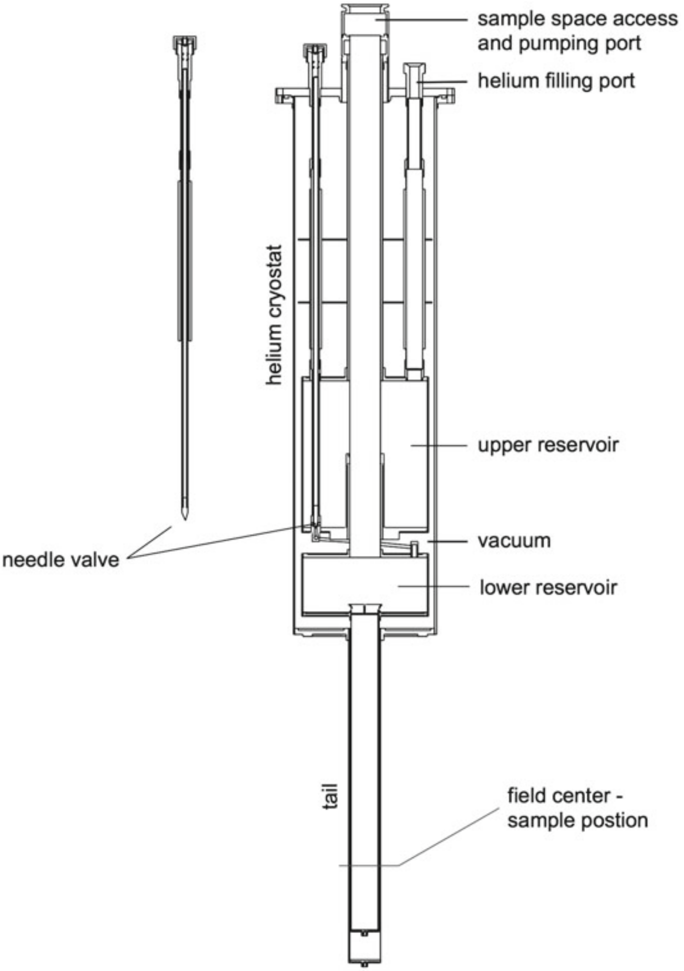

Fig. 3.1 Technical drawing of the ^{4}He cryostat used at the LNCMI Toulouse [1]. See text for detailed explanation

the exchange gas in the sample reservoir. In order to stabalise temperatures above 4.2 K the pressure in the sample space was typically reduced to $p\ \approx 600\,$mbar to reduce convection and reach a more stable condition.

Care needs to be taken when using the heater to bring the sample to room temperature before taking it out, as the cryostat will have a strong temperature gradient from room temperature in the tail to low temperature, 4.2–77 K depending on the fill level, at the upper reservoir back to room temperature at the top of the cryostat. In order to prevent thermal shock, especially for fragile samples, we lower and raised the probe stepwise, while monitoring the temperature at the sample position, so obtaining an average cooling rate of ≈3 K/min, instead of using the heater.

As the pulsed field experiments are carried out in less than 1 s a long hold time at the desired temperature is not necessary. In contrast the experiments that we carried out on H_{c1} or also the heat capacity a longer hold time at temperatures between 1.5 and 300 K is desired. For this a different system was used. The sample in these systems are no longer submerged in the liquid, but rather sit in vacuum. Similar to the lower reservoir a so called *1K-pot* is connected to the main bath via a capillary. By using a thin, long capillary or a needle-valve the flow to the lower reservoir can be limited, allowing to hold it constantly at base temperature, even during the refill of the main bath. The sample platform is then attached to the 1K-pot using a weak link. This is typically done using non-metallic materials like fibreglass-composites together with a metallic wire (typically cooper or silver) whose cross-section can be varied to achieve the desired thermal link. By attaching a heater and a thermometer to the sample stage, these systems allow to reach continuous temperatures from 300 K to based temperature of $\approx$1.5 K.

3.1.2 ^{3}He-System

For temperatures below 1 K one needs to use ^{3}He, which is a rare isotope of helium. It has a boiling point of 3.2 K, which is lower than the more common Helium-4. As ^{3}He has a nuclear magnetic moment of S = 1/2 and including the electrons is considered a Fermion. As it is the only material with such a low boiling point at ambient pressure it can be produced very clean and hence is the most clean system to study Fermi liquid theory.

The form in which ^{3}He is used is very similar to that just described for ^{4}He. However the fact that it is very rare and hence more expensive raise the need for a contained system to minimize losses. Within this thesis a ^{3}He-system was used at the National High Magnetic Field Laboratory (NHFML) Tallahassee inside the Hybrid Magnet. A schematic of the system used is shown in Fig. 3.2. Unlike ^{4}He, ^{3}He is stored in gas form in a so called dump at room temperature. To prevent losses the pressure inside the dump is kept below atmospheric pressure. In order to condense the gas a ^{3}He-insert, built as double-wall system for thermal isolation at the sample position, is placed inside a ^{4}He bath. As the boiling point of ^{3}He is lower than that of ^{4}He, the temperature in the main bath is reduced, like described in the previous section. We will then open the condensing valve to allow ^{3}He to flow into the sample space. If the main bath was only cooled to 3.2 K, the boiling point of ^{3}He we would not be able to condense any liquid, as the vapour pressure above the liquid would be one atmosphere, but the gas is stored at reduced pressure. We therefore always use the base temperature of the bath to condense the maximum amount of ^{3}He for a longer hold time. During this process we monitor the pressure inside the sample space. Once the pressure becomes stable the maximum amount of gas has been condensed. We then close the condensing valve and open the pumping valve. With this we can just like in the ^{4}He system set temperatures between the bath temperature and typically

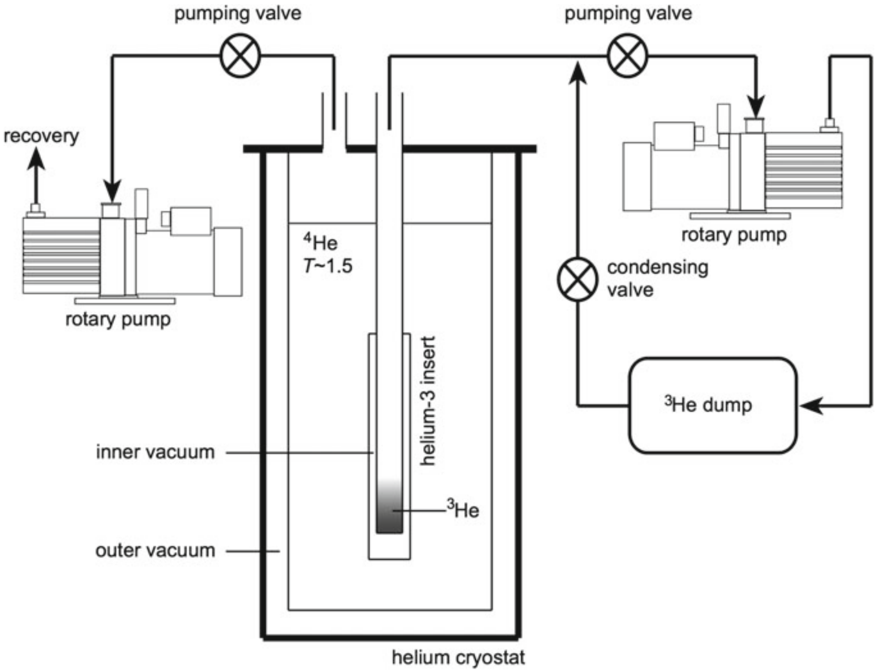

Fig. 3.2 Schematic drawing of the ^{3}He system used at the NHMFL Tallahassee to reach temperature below 1 K. See text for detailed explanation

0.3 K by reducing the pressure above the ^{3}He. The evaporated ^{3}He is pumped back into the dump. When the liquid level drops below the sample we repeat the procedure.

It should here also be mentioned that ^{3}He systems can also be used for measurements in the temperature range of 1.5 and 2.5 K, which could be reached by ^{4}He. However as ^{4}He changes into the superfluid state at 2.17 K it is pointed out in Ref. [3] that the Kapiza-resistance between the sample and the bath change unfavourably. To prevent this the sample was placed inside a ^{3}He bath which allows for a better thermal coupling, specially important in pulsed field measurements, as metallic samples can experience significant heating due to eddy currents.

3.2 Magnetic Field—Gauss to MegaGauss

When trying to understand high temperature superconductors it is desired to probe superconducting and normal state properties of these materials at low temperatures. While the measurement of the lower critical field requires high resolution field sweeps in the range up to a few hundred Gauss, the normal state at low temperatures can often only be reached in fields above 50 T. In the presented work a variety of different magnet systems, including resistive, superconducting, hybrid and pulsed field were used, covering almost six orders of magnitude in magnetic field strength. While commercial superconducting magnets were used for calibration of Hall-sensors and reference measurements, the main results of this work were obtained in the hybrid magnet at NHMFL in Tallahassee, the pulsed field facility in Toulouse and in a low field resistive magnet built by the author in Bristol, which we will explain in more detail in this section.

3.2.1 Superconducting Magnet

Superconducting magnets provide the opportunity to carry out research at low energy consumption in fields up to 21 T. The magnet typically made of Nb_3Sn or NbTi wires needs to be cooled to low temperatures to become superconducting. They are therefore submerged in liquid helium. As the critical current density rises upon cooling, one can gain maximum field by further cooling the system to the λ-point of helium as described before. Due to the wire being superconducting, low sweep-rates are possible at low energy consumption. Superconducting magnets are typically equipped with superconducting switches, allowing to created a closed superconducting loop, which enables these systems to run for long time without loss and the need of a constant power supply. Commercial systems are available in the laboratory in Bristol enabling measurements up to 20.5 T.

3.2.2 Hybrid Magnet

For fields beyond 20 T we turn first to the high field resistive and hybrid magnet systems. These systems are available at a variety of facilities around the world. The magnets are made of low ohmic resistive conductors. The energy necessary to provide the field up to 35 T is dissipated as heat which needs to be compensated by cooling with large amounts of water. This has two effects. First the cooling system adds to the total energy consumption, but further more it causes significant vibrations that can cause enhanced noise in these systems. Currently the highest dc magnetic field is available at the NHMFL Tallahassee. Here a 34 T resistive magnet is place inside a large 11 T superconducting magnet. So the system is able to provide a dc field of up to 45 T, known as *Hybrid*. While the 11 T superconducting magnet is used as constant background field the resistive magnet is used to sweep the magnetic field between 11 and 45 T with a maximum sweep-rate of 7 T/min. In order for the superconducting magnet to be operated up to 11 T it needs to be cooled below 4.2 K. For this the system has a dedicated liquefier providing a constant supply of superfluid ^{4}He. Owing to the complexity of the system there is currently only one of these systems in the world. For this reason the time allocated to any user is very limited. We have therefore used samples that were already measured in pulsed magnetic field to take high resolution angle dependence measurements and effective masses on various crystals.

3.2.3 *Pulsed Field Magnet*

For optimally doped high temperature superconductors often fields beyond 45 T are necessary to access the normal state at low temperatures. For this so call *pulsed magnets* are used. The setup of the pulsed field system used at the LNCMI-Toulouse is shown in Fig. 3.3. A resistive magnet, reinforced with fibreglass composites, is cooled to 77 K using liquid nitrogen. The cryostat including the sample is fixed inside the bore of the magnet. Different approaches can be used in mounting the cryostat. While in one case the cryostat is hanging freely inside the magnet, this is only found

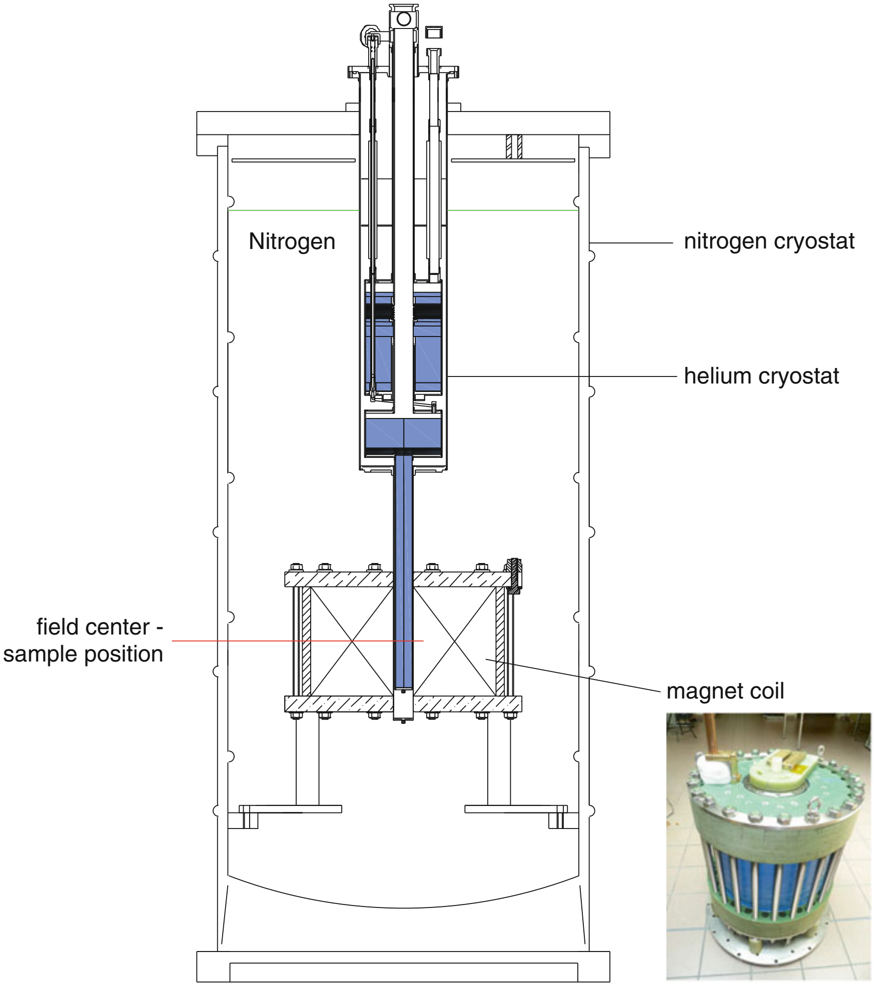

Fig. 3.3 Drawing of the pulsed field setup used at the LNCMI Toulouse. The pulsed field coil (see picture) is placed inside a liquid nitrogen cryostat. Taken from Ref. [1]

effective for a completely decoupled system. As this is typically difficult to achieve, the cryostat, in the work conducted as part of this thesis, was always tightly coupled to the magnet. In order to carry out a magnetic field sweep, capacitors are charged with several megajoules of energy, depending on the desired maximum field and then discharged into the magnet. The resulting field profile is shown in Fig. 3.4. While line (a) and (b) show field profiles of a 60 T and 70 T magnet respectively, line (c) shows the profile obtained from a dual-coil configuration. In these systems field up to 100 T (1 MGauss) are possible now at the NHMFL Los Alamos, by discharging part of the energy into a separate inner coil once the outer coil has reached its maximum field value.

During the discharge of the capacitors into the coil part of the energy is dissipated in the coil as heat causing its temperature to raise close to room temperature. In order prevent damage to the coil the system is allowed to cool back down to liquid nitrogen temperature prior to a new pulse. As the cooling will be proportional to the difference in temperature between the bath and the coil, the cooling process would slow down ones getting close to the boiling temperature of liquid nitrogen, 77 K. In order to cut down on cooling time the vapour pressure above the liquid nitrogen bath is decreased to reduce the temperature of liquid nitrogen bath. Due to this it is possible to carry out an experiment every 80 min.

The biggest limitation on the available maximum field is the strong constrain that available materials set to the coil design. As the field is rapidly increased the Lorenz-force that acts between individual layers of the magnet cause an internal pressure. This pressure can cause damage to the conductor. In order to prevent the coil from breaking a special fibreglass known as *Zylon* is used. However as the pressure inside

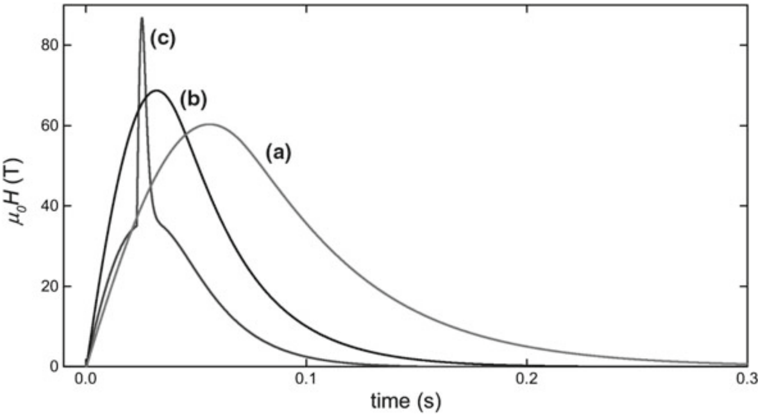

Fig. 3.4 Magnetic field versus time for different coils commonly used in pulsed magnetic field facilities. Profile (a) and (b) were obtained from a 60 and 70 T coil at the LNCMI-Toulouse, while profile (c) was taken from a *90+x* T coil at the High Magnetic Field Laboratory Dresden. While coils (a) and (b) are single-coil designs, coil (c) is a coil-in-coil design. Here the inner coil is triggered shortly before the maximum field of the outer coil

the coil grows like the square of the maximum field, limits of available materials are reached typically around 100 T making this the practical limit for current applications.

We have used this technique to screen and study a variety of crystals using dHvA at the LNMCI Toulouse. Also electrical transport experiments and transport under pressure was carried out in these systems using fields up to 70 T.

3.2.4 *Resistive Magnet*

Superconducting magnets typically exhibit a strong remanent field due to flux trapping in the solenoid. These fields can be up to several milli-Tesla strong, depending on the maximum field used and can hence hinder the possibility of zero field cool-downs. For some experiments like the measurement of magnetization this is a significant limitation. In order to overcome this problem, the measurements on the lower critical field, have been carried out in a home made resistive magnet cooled to helium temperature. An aluminium coil-former was used. This has the advantage of a natural low pass filter in the applied magnetic field due to the skin depth. The coil-former was chosen to have a wall thickness of 5 mm. The skin depth can be calculated by [4]

$$\delta_0 = \sqrt{\frac{2\rho}{\mu_0 \pi f}}. \tag{3.4}$$

with the cutoff frequency f, the resistivity ρ and the vacuum permeability μ_0. The resistivity of the former is estimated to $\rho = 5 \times 10^{-10} \Omega \mathrm{m}^{-1}$ using the values of aluminium with a residual resistivity ration of 110 [3]. Then the cut-off frequency is determined to $f = 5\,\mathrm{Hz}$, damping any high frequency noise in the applied field.

The magnetic field is controlled by a 16bit digital-to-analog converter (DAC), built by the author, followed by a voltage-to-current converter. The settings for the sweep are preloaded to a micro-controller, which then performs the field-sweep independently. The sweep-rate is set by a delay in milliseconds after which the controller changes the output-voltage of the DAC by 5bit (0.763 mV). As it is desired to have a continuous changing field a low pass filter is added to smoothen these steps. The low-pass filter property of the coil-former mentioned above adds to this effect to produce an even better result.

The field strength versus applied current was determined by using a Hall-sensor which had been calibrated in a commercial 14 T-magnet system before. The profile of the magnet, shown in Fig. 3.5, was determined by varying the position of the Hall-sensor. For this and for all subsequent measurements the current through the magnet was monitored using a Keithley 2000 and used in further experiments as measure of the applied field with a conversion factor of 20.6 mT/A.

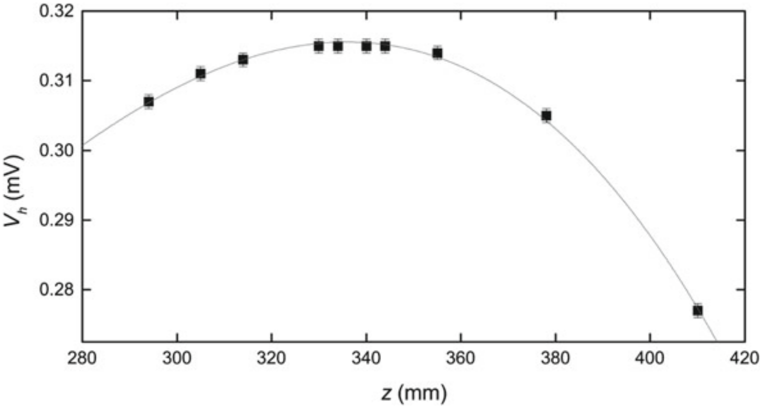

Fig. 3.5 Magnetic field profile of home built resistive magnet. The Hall-voltage of the sensor is plotted at various positions of the magnet. A constant current of 0.5 A was applied to the magnet for all positions

3.3 Hydrostatic Pressure

Pressure is a powerful tool to reveal new exotic ground states in solid state physics. In the field of iron-based superconductor it is believed that hydrostatic and chemical pressure (doping, isovalent substitution) lead to the same effects [5–7]. This is particularly useful for systems where clean single crystals are not available throughout the phase diagram. In this work hydrostatic pressure was used to investigate the quasi particle mass and Fermi-surface topology of $YBa_2Cu_4O_8$. For this a CuBe-pressure cell was built to carry out zero-field transport in Bristol. A non-magnetic pressure cell available at the facility in Toulouse was used for the quantum oscillation study. We will briefly introduce these techniques in the following section.

3.3.1 Pressure Cell for Zero Field

In order to test samples of $YBa_2Cu_4O_8$ under pressure prior to experiments in high magnetic fields a pressure cell was built for zero field measurements. For this we have followed the design by Walker [8]. The piston cylinder cell shown in Fig. 3.6 was made of copper-beryllium and all parts were annealed for 2 h at 315 °C prior to first use.

For the transport measurements 25 μm copper twisted pairs were glued inside the feedthrough using Stycast 2850. At the edge of the Stycast the wires are likely to break and are therefore stabilized by an additional layer of soft UHU two component epoxy.

Fig. 3.6 Pressure cell used for zero field measurements. The cell has a sample space of 3.6 mm and was successfully used up to 10 kbar. Except of the inner cylinder and the gasket the cell is entirely machined from copper-beryllium

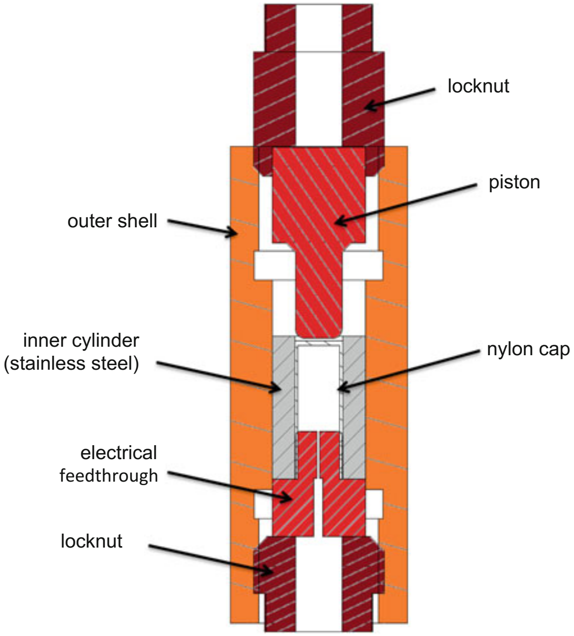

When loading the cell, a nylon cup with a inner diameter of 3.6 mm and an outer diameter of 5 mm was pressed inside the stainless steel cylinder. This is then filled with Daphne 7373 used as pressure medium. In order to prevent a collapse of the nylon gasket under pressure one needs to make sure that no air is trapped when filling the pressure medium. The stainless steel cylinder and the feedthrough have the same outer diameter. They were placed inside a guiding cylinder to have good alignment. In this configuration the feedthrough is pressed inside the nylon cup, sealing it. The assembly is then pressed inside the cell and fixed with the locknut. In the last step the piston and top-locknut are fixed. Pressure is applied using an additional piston placed inside the top locknut. At the same time the sample signal is monitored to exclude sudden changes that could point to sample imperfection or changes in the electrical contacts. When the desired pressure is reached, the top locknut is tightened until the a reduction of pressure on the press is observed.

3.3.2 Pressure Cell for Pulsed Field

When working in pulsed magnetic field the heating due to eddy-currents limits the choice of materials to those having high resistances or being insulators. At the LNCMI-Toulouse a pressure cell consisting of Timetal64 with Yttrium stabilized Zirconia pistons is available [9] that can be used at fields up to 60 T without signatures of heating. $YBa_2Cu_4O_8$ samples of about $200 \times 200 \times 50\,\mu m^3$ were contacted with Dupont 6838 silver paint, which was cured at 450 °C under high purity oxygen. The samples were then place inside the pressure cell where the contact to the leads was made using Dupont 4929 silver paint. The sample space has been filled with silicon oil, used as pressure medium and then covered with a 300 μm thick plastic cover used as gasket (see Fig. 3.7 for details). As the gasket gets deformed into the sample space, this setup is best suited for thin single crystals. In the present work the setup was successfully used for measurements up to 10 kbar. As the leads running into the pressure cell are also exposed to the applied pressure, they are protect by a two-component epoxy. This way they are only thermalized to the bath further away from the sample. Tests on the cooling power inside the pressure cell were carried out. For this a resistive wire (heater) with a resistance of $R = 3\Omega$ was placed inside the pressure cell together with a germanium-gold-thermometer (see Sect. 3.9). Various currents have been applied to the heater and and the thermometer while monitoring the temperature inside the cell using the GeAu-thermometer. The results are shown in Fig. 3.8. In panel (a) the temperature inside the cell is plotted versus the applied power for the two different cases. A clear difference in the onset of a static ΔT can be seen. From this and the low value of cooling power for the case of the GeAu-thermometer, we conclude that the cooling is mainly provided via the wires. As these are only coupled outside the cell this reduces the cooling significantly. The difference between the thermometer and the heater onset might be caused by a low thermal conduction of the pressure medium. This can also be seen in Fig. 3.8b where the onset power for heating is plotted versus the bath temperature. While little variation is found for the heater, the thermometer cooling power changes by two orders of magnitude. These findings are relevant, especially in the case, when very low resistive contacts are not possible. Therefore when working inside the pressure cell we need to assume the sample to be in weak contact with the cold reservoir and chose the measurement current accordingly.

3.3.3 Determination of Pressure

Knowing the precise pressure applied to the sample is essential. The thermal contraction of the used materials can cause the pressure inside the cell to change with temperature. Therefore it is desired to measure the pressure inside the cell at least in the two limits of room temperature and low temperature. As space is limited a manganin wire was place inside the cell prior to the measurement and the change of resistance with pressure applied was monitored. This process has been reproduced several times. The data obtained is shown in Fig. 3.9. The observed change in resistance was converted using

$$p_{cell} = \left(\frac{R}{R_0} - 1\right) \times 2.37 \times 10^{-3}\,\text{kbar}, \tag{3.5}$$

which was found for $T = 25\,^{\circ}\mathrm{C}$ [10]. In the low temperature limit the pressure has been determined by using the superconducting transition of lead. As the variation in the superconducting transition of lead is only $\Delta T_c/\Delta p = -(4.2 \pm 0.5) \times 10^{-2}$ K/kbar [11], great care on the determination of temperature has to be taken. This has been achieved by stabilizing the temperature every 5 mK and holding for several minutes before reading the resistance value.

3.4 Crystal Growth

As discussed previously, the observation of quantum oscillations relies on samples with long mean free paths, hence high quality. High quality single crystals of the *111*- and *122*-family were grown by the author, while samples used in the quantum oscillations studies where grown by collaborators from the group of Prof. Y. Matsuda at the University of Kyoto. The procedures used shall be discuss in this section.

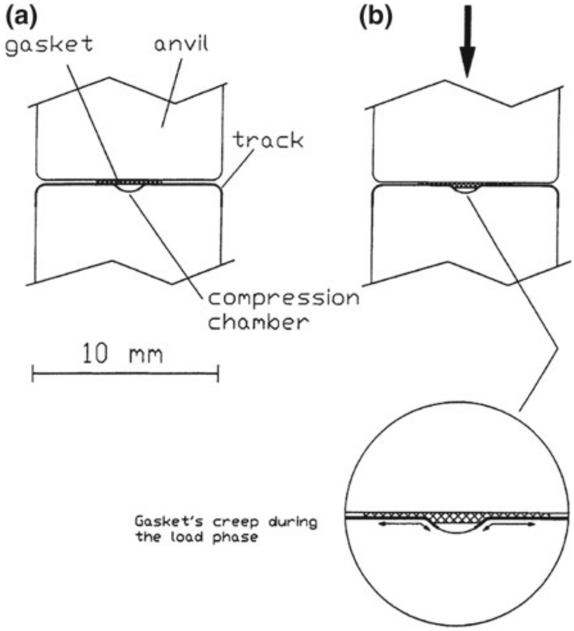

Fig. 3.7 Cross-section of the sample region for the pressure cell used in pulsed magnetic field. The cell is shown before (**a**) and after (**b**) applying pressure. The deformation of the plastic gasket is shown in **b**. Figure taken from Ref. [9]

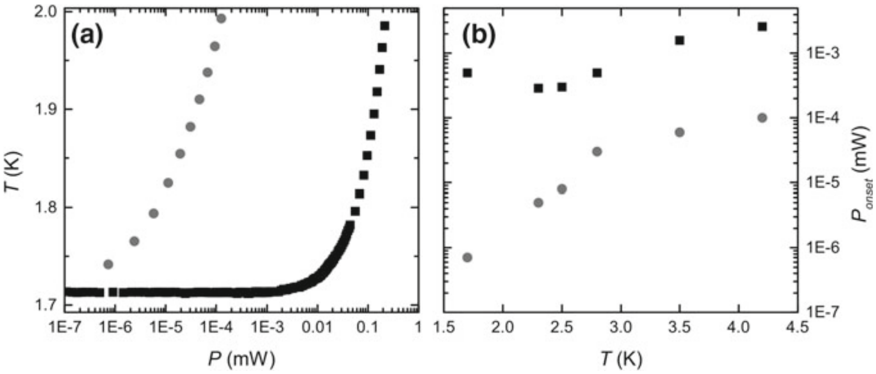

Fig. 3.8 Thermalization test inside a non-magnetic Zirconia pressure cell. **a** Shows the temperature versus applied power to a 3Ω heater (*squares*) and to the thermometer itself (*circles*). **b** Shows the onset power of heating versus the temperature of the surrounding bath

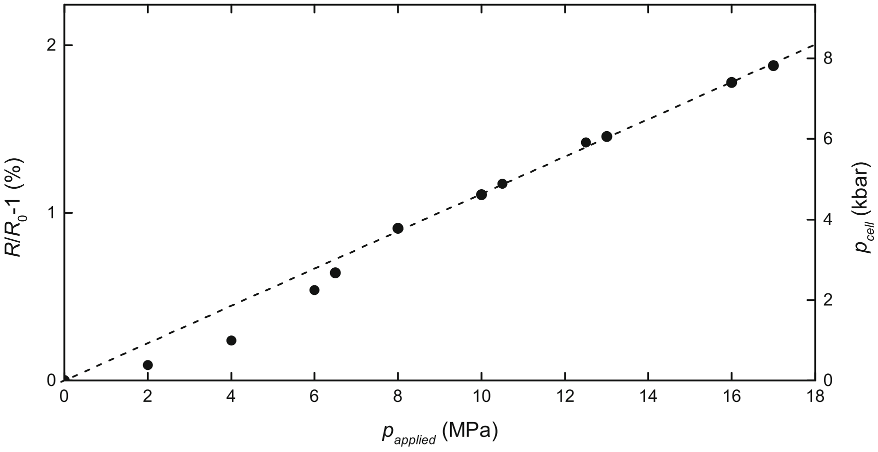

Fig. 3.9 Change in resistance of annealed manganin wire versus applied pressure to the cell. On the right axis the corresponding internal pressure is shown

3.4.1 LiFeAs and LiFeP

The growth of LiFeP and LiFeAs is analogous and therefore only the latter will be discussed here.

For the growth of LiFeAs it is necessary to produce the precursor Li_3As. This is done by mixing Li(99.9 %):As(99.9999 %) in the ration 3:1 in a boron-nitride crucible. This is sealed under high-vacuum in a quartz tube. The thermal cycle for the reaction is shown in Fig. 3.10a. Boron-nitride crucibles are necessary as lithium is highly reactive and would destroy commonly used alumina crucibles. After the first part of the cycle the material was removed from the crucible and grinded before

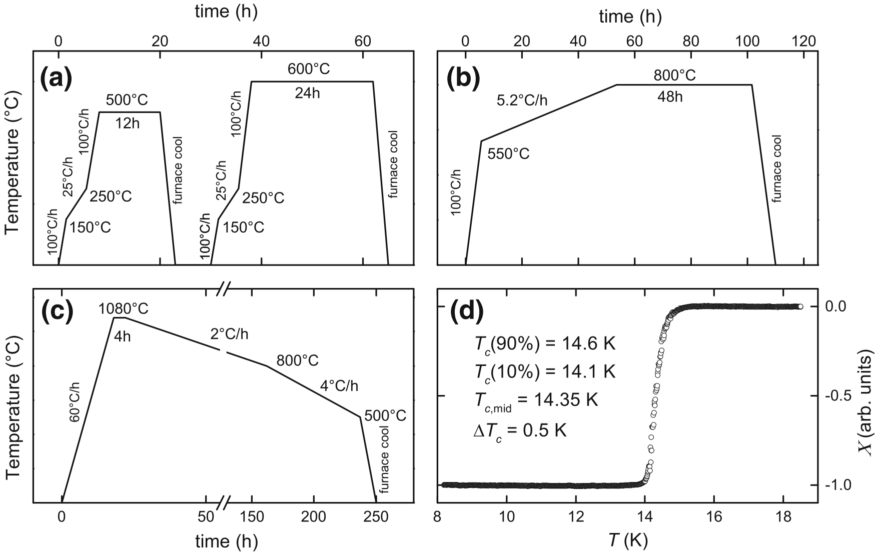

Fig. 3.10 Thermal profile used for the growth of Li_3As (**a**), Fe_3As (**b**) and LiFeAs (**c**). Panel (**d**) shows the susceptibility measured on a sample grown by procedure in [12] and exposed to air for several days

continuing. This procedure is commonly used in solid state reactions to produce a homogeneous mixture. As lithium has the lowest melting point of the three elements involved, we chose this as a flux. Hence a lithium-rich ratio of 1:2 for Li_3As:FeAs was chosen. The iron-arsenide (FeAs) is commercial available. The mixture was again placed in a boron-nitride crucible and sealed under vacuum in a quartz tube. Figure 3.10c shows the temperature settings that were used to grow the single crystals from the lithium-flux. Clean single crystals of several cubic millimeter could be extracted under high-purity argon atmosphere.

Recently an alternative synthesis has been carried out for LiFeAs, which was proposed by Juza and Langer [12]. In this synthesis the starting materials are Li_3As and Fe_3As_2. The advantage of this procedure is that the valance of iron does not change during the single-crystal growth. The temperature settings used for the solid state reaction of iron and arsenide are shown in Fig. 3.10b. For the single crystal growth the same temperature settings as previously described have been used. From this growth small single crystals of typically $500 \times 500 \times 100\,\mu\mathrm{m}^3$ where extracted. The crystals where measured by ac-susceptibility. A sharp superconducting transition was observed in the range of 14–16 K. While previously superconducting transition at T_c=18 K were reported [13], superconductivity vanished when exposing the samples to air for a short amount of time. The data shown in Fig. 3.10d however was taken after exposing the sample to air for several days. This proves to be a promising result for further investigations.

3.4.2 $BaFe_2(As_{1-x}P_x)_2$

Single crystals of $BaFe_2(As_{1-x}P_x)_2$ are grown by self flux technique from Ba (purity 99.9 %), FeAs (99.5 %) and FeP(99.5 %). The materials are mixed according to the reaction formula

$$Ba + 2(1 - x)\,FeAs + 2x\,FeP \rightarrow BaFe_2(As_{1-x}P_x)_2. \tag{3.6}$$

The materials were mixed under argon atmosphere to the desired stoichiometry and a typical mass of 1.5 g was placed in an alumina crucible. This was then sealed under vacuum of $p \approx 1 \times 10^{-6}$ mbar in a quartz tube. As the growth requires temperatures up to 1200 °C [14], we are working close to the melting point of the quartz tube. The quartz tube is therefore placed inside a stainless steel tube which is sealed on both ends under partial argon pressure. This has two advantages. First it is a safety procedure that prevents contamination with arsenic or phosphor in case the quartz tube fails. Further, if the quartz tube becomes soft it will expand due to the vapour pressure inside. This expansion will be limited by the stainless steel tube. This increases the chance of a successful growth.

The thermal cycle used is shown in Fig. 3.11a. $BaFe_2(As_{1-x}P_x)_2$ is not found to be highly air sensitive when exposed to air. This causes any unreacted material to oxidize and we find small shiny single crystals like shown in Fig. 3.11b. The crystals are analysed using x-ray diffraction. Crystals exhibit the expected space group $I4/mmm$. However by comparing different crystals from the same growth using x-ray diffraction, energy dispersive x-ray diffraction and the superconducting critical temperature, we find that x can vary up to 10 % from the nominal value.

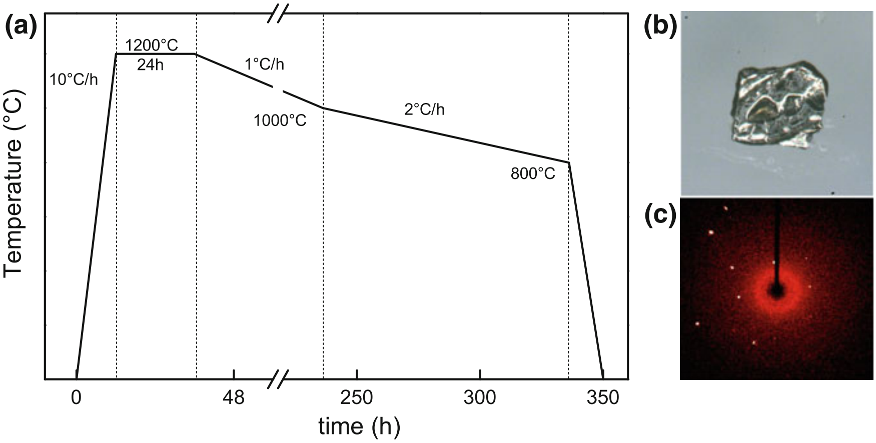

Fig. 3.11 Panel (**a**) shows the temperature profile used during the growth of $BaFe_2(As_{1-x}P_x)_2$. Panel (**b**) a resulting crystal with $x = 0.3$ and a frame of the x-ray diffraction taken on this crystal (**c**)

3.5 Measurement of H_{c1}

3.5.1 Setup and Characterization

The measurement of the lower critical field of a type-II superconductor can be challenging. When carrying out global measurements using *vibrating sample magnetometers* or *superconducting quantum interference devices* one can only determine changes in the overall magnetization. However in the case of strong pinning this can lead to an overestimated lower critical field H_{c1}. A better way is therefore a local probe that allows to investigate the flux penetrating field H_p on the edge and in the center of the crystal. Without surface pinning the entering vortex moves straight to the center of the crystal leading to the same H_p at the edge and in the center (Fig. 3.16).

We have chosen to use micro-Hall arrays to measure the local magnetic field on different places on the sample surface. This technique has already been used successfully in the past [15, 16]. The Hall voltage that is generated by applying a magnetic field is

$$V_h = -\frac{IB}{nde}. \tag{3.7}$$

The magnetic field B is the perpendicular component of the applied field with respect to the active Hall area of thickness d. The current I runs perpendicular to the field. e is the electron charge and n is the carrier density which is dependent of the used materials. The highest sensitivity to the applied field is achieved for low carrier densities and thin active areas. For this reason mostly 2D electron gases (2DEG) in GaAs/AlGaAs hetero-structures are used [15]. In the present study different types

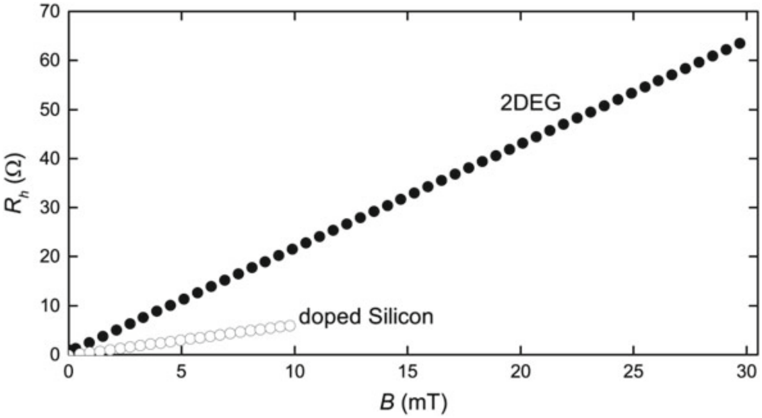

Fig. 3.12 Hall resistance versus applied field for a 2DEG and a doped silicon Hall array measured at $T = 10$ K

of materials were used. While first 2DEG systems were used, we found that doped-silicon with carrier concentrations of $n = 1 \times 10^{16}\,\mathrm{cm}^{-3}$ gave a factor $\approx$10 lower response, see Fig. 3.12, but higher reliability for repeated cool down. The used Hall sensors were produced by J. Fletcher and P. See at the National Physics Laboratory and clean rooms at the University of Cambridge. In Fig. 3.13b, c two different sensors are shown. One can clearly see eight different active Hall areas, the first marked by a cross. The sample is place on the Hall-array using a thin film of grease to hold it in place and as thermal link. The Hall-arrays are then placed on the sample holder shown in Fig. 3.13a using GE vanish. Contacts to the Hall array were made using Epotech H20E silver epoxy that was current for 5 min at 150 °C. The platform can be rotated and locked in two different orientations, parallel and perpendicular to the applied field. The setup is connected to a probe with 1 K-pot. By weakly coupling the body of the stage to the 1K-pot the probe can be used in the temperature range of 300–1.5 K.

The sensitivity of two doped silicon Hall-arrays with different carrier concentrations were compared in a wide temperature range. The results are shown in Fig. 3.12. While the solid squares show the results obtained on a doped silicon waver W745 with $n = 1 \times 10^{16}\,\mathrm{cm}^{-3}$ the open circle are obtained on a structure with $n = 1 \times 10^{18}\,\mathrm{cm}^{-3}$. The sensitivity is in agreement with the nominal difference of a factor 100 in the carrier concentration of the used wafer. The W745 wafer is on the limit of the available

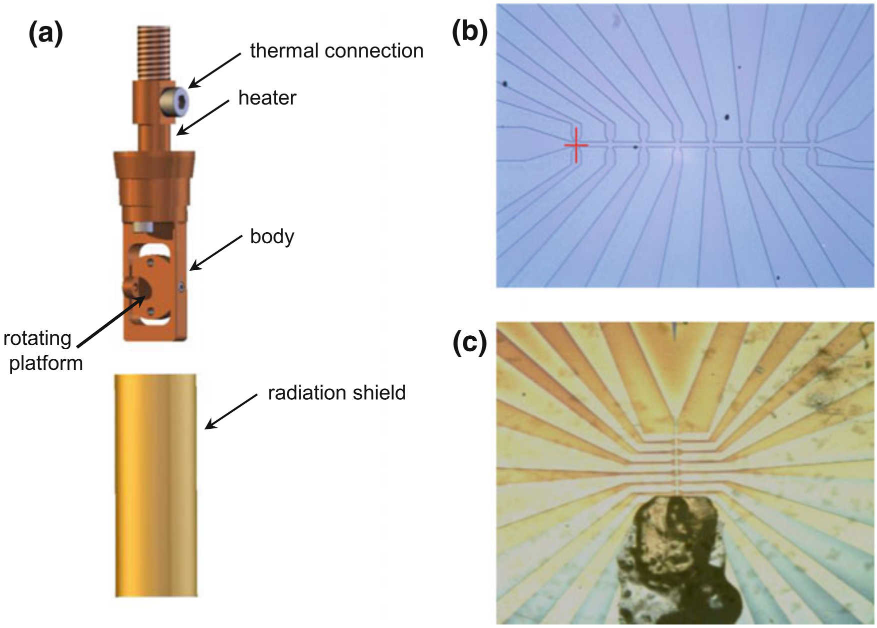

Fig. 3.13 Stage used for the measurement of H_{c1} (**a**). Different Hall arrays are shown in **b** and (**c**). In **b** the first active area is marked by a cross for clarity. Samples are mounted using grease as shown in **c**

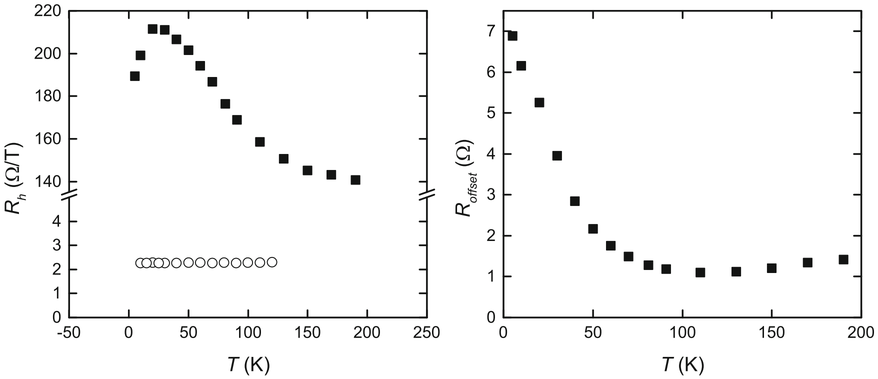

Fig. 3.14 Hall coefficient for different Hall arrays made from doped silicon with $n = 1 \times 10^{16}\,\text{cm}^{-3}$ (*squares*) and $n = 1 \times 10^{18}\,\text{cm}^{-3}$ (*circles*) are shown in the *left panel*. The *right panel* shows the longitudinal voltage for one active area for $n = 1 \times 10^{16}\,\text{cm}^{-3}$

concentrations of doped silicon wafer. While a clear change in Hall value is found at low temperature the sensitivity change still allows it to be used for the measurements. In the right panel of Fig. 3.14 the longitudinal part of the resistance is shown. This is caused mainly by the offset of the Hall-contacts. By comparing this resistance to that found over the structure we find an alignment miss match of only ≈20 nm. This high precision is essential for high resolution measurements using Hall-arrays. In the case of a high spacial offset the zero-field signal could exceed the Hall signal by orders of magnitude leading to high sensitivity of the sensor to small temperature changes. In the present case we can compare the two effects by taking a linear fit to the low temperature part of Fig. 3.14b. This gives a change of $\Delta R = -0.11\,\Omega/\text{K}$. The sensor can typically be stabilized to better than $\Delta T = 5\,\text{mK}$. This corresponds to a noise of $\Delta B_{sensor} \approx 3 \times 10^{-3}\,\text{mT}$, much smaller than the earths magnetic field. As we expect H_{c1} for most materials to be on the order of 10 mT or more we can neglect this contribution in our case.

3.5.2 *Signal from Superconductor*

In the presence of a superconductor on top of the Hall-array the effective field seen by the sensor will be reduced due to the Meissner effect. This is schematically shown in Fig. 3.15. While the field inside the superconductor is zero in the Meissner state one does not necessarily observe zero response by the Hall-sensor. The effective field measure

$$H_{eff} = H_{app} - \alpha N M, \tag{3.8}$$

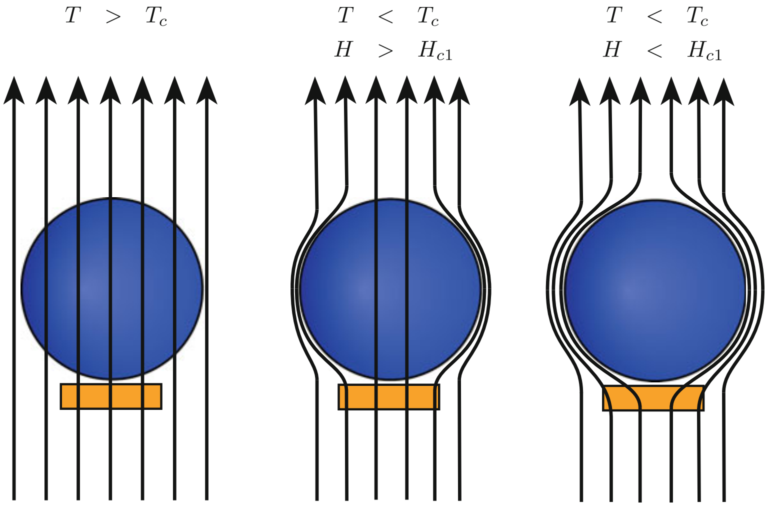

Fig. 3.15 Schematic drawing, field penetrating a superconductor and the respective change in field profile in the underlying Hall sensor

depends on the sample specific parameter α and the demagnetizing factor N. It reflects the position of the sensor with respect to the sample. Assuming a homogenous external magnetic field and a long thin sample parallel to the applied field ($N = 1$), we would find that $\alpha = 1$ inside the sample while $\alpha \rightarrow 0$ if the sensor is placed far away from the sample. As the sensor in the present setup is place a few nanometer away from the sample surface α will be close to one for those placed in the center of the sample, while the ones on the edge will have an $\alpha \ll 1$. We assume α to be purely dependent on the sample geometry and hence can assume $\alpha(H_{app})$ to be constant. This means we can correct for the *field leakage* (shown schematically in Fig. 3.15) by subtracting a linear fit to the low field part of the up and the down sweep. In Fig. 3.16a the signal form a sensor on the edge (squares) and the center of the sample (circles) are shown. As mentioned the initial slope, indicated as dashed lines) changes depending on the sensor position. By subtracting this slope we obtain the curve in Fig. 3.16b for the sensor at the edge. The field of first flux penetration is identified as the field where the magnetization deviates from a linear behavior. As any barrier effects will cause the deviation to follow a B^2 dependence one typically plots the square-root of the sensor field [16–18]. Further in the case of weak surface barrier effects one expects a change in slope in the down-sweep to occur at the same field position H_p [18]. This is indicated in the Fig. 3.16b by a linear fit to the low field part of the down sweep. The data clearly starts to deviate form the linear fit at $H = H_p$.

In the analysis so far we have only taken the sensor position into account. To determine the lower critical field from H_p we need to find the demagnetizing factor N. This has been done by taking a picture of the sample using a digital camera. With

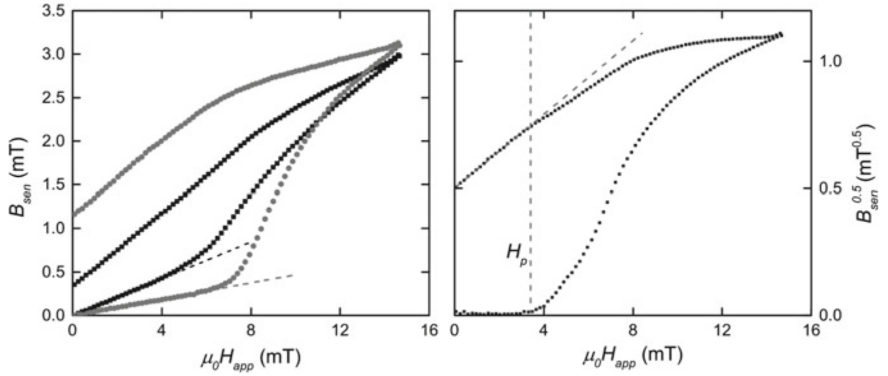

Fig. 3.16 Data taken on $BaFe_2(As_{0.62}P_{0.38})_2$ at $T = 18$ K at the center (*squares*) and at the edge (*circles*) of the sample. *Dashed lines* represent linear fits to the low field region. The *right panel* shows the data on the edge corrected for the *field leakage*. The field of first flux penetration H_p is marked

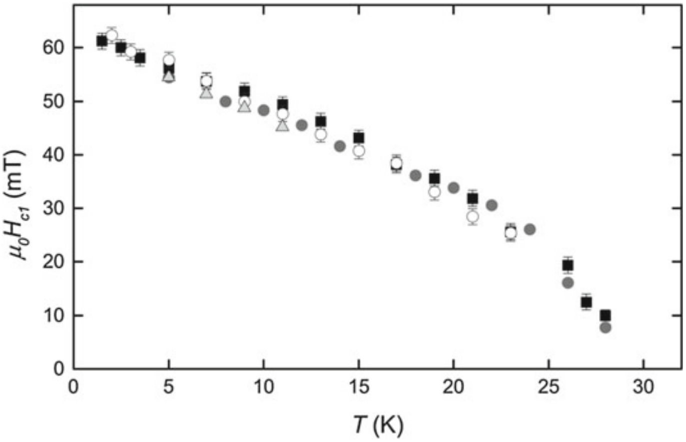

Fig. 3.17 Lower critical field H_{c1} versus temperature for $BaFe_2(As_{0.7}P_{0.3})_2$ with various thickness to width to width ratios

this it was possible to determine the thickness and width of the sample. These values can then be used in Eq. 3.12 to obtain H_{c1} from H_p.

As Eq. 3.12 was obtained numerically we shall test its validity in the parameter range used in this work. For this we have measured the same sample repeatedly with different aspect ratios. The result of $H_{c1}(T)$ are shown in Fig. 3.17. Two things are important to mention. First all the data for different aspect ration b/a are in good agreement which means that Eq. 3.12 is consistent for the used samples. Secondly we find a linear dependence of $H_{c1}(T)$ at low temperatures. Previously it was found that samples with strong pinning deviate from this behavior and exhibit an upturn of H_{c1} at low temperatures [19].

3.5.3 Measurement Procedure

The measurements were performed by first taking a field-sweep above the superconducting critical temperature for each new run. This was done to rule out any loss of sensitivity in the Hall sensor over time. The sensor and sample were then cooled to the desired temperature with a constant sweep rate of 1 K/min and the magnet connected to ground. Once the temperature was reached and stabilized to $\Delta T \leq 5\,\mathrm{mK}$ the program was set to hold for thermalization. The hold time was typically set to 5 min. After this the magnet was automatically reconnected to the power supply and the field-sweep was carried out. Finally the magnet was again disconnected from the power supply and grounded. The sample was heated above T_c and held there for at least 5 min before starting a new run. For each temperature a positive and negative field sweep were carried out and the pure Hall-contribution determined from both measurements.

3.5.4 Demagnetizing Factor

When applying an external magnetic field H_a to an arbitrary shaped sample the internal magnetic field H_i is modified by the magnetization M of the sample. The magnetization however depends on geometric and material specific parameter. Considering these effect the internal magnetic field is given by

$$H_i = H_a + \chi N M(H_a, N), \tag{3.9}$$

with the susceptibility χ and the demagnetizing factor N. Here only superconductors in the Meissner-state will be considered. Hence we set $\chi = -1$. In the used notation the magnetization of the sample $M = M(H_a, N) = M(H_i, 0)$ [20]. As for the Meissner-state the internal magnetic field $H_i = 0$, the magnetization of the sample can be written as

$$M(H_a, N) = -\frac{H_a}{1 - N}. \tag{3.10}$$

At the lower critical field $H_{c1} = -M$. Therefore we can substitute M in Eq. 3.10 for H_a giving

$$H_a = (1 - N) H_{c1}. \tag{3.11}$$

This shows that for any sample with $N > 0$ the applied field where flux entrance will be observed is suppressed over the real lower critical field. To determine the effective field seen by the sample a precise knowledge of the demagnetization factor is necessary.

The samples that have been measured in this work where all of plate-like shape. A numerical estimate for the demagnetization factor for such sample was given by Brandt [20]. In the limit of a thin plate-like sample the field of first entrance H_p can be converted to H_{c1} using

$$H_{c1} = \frac{H_p}{\tanh \sqrt{0.36b/a}}, \tag{3.12}$$

with the thickness b and the length a of the sample.

3.6 Arduino Based Phase-Sensitive Detector

Phase sensitive detectors are widely used among scientists as they allow to measure signals smaller than the surrounding noise floor. They are based on the mathematical solution of multiplying two sinusoidal signals. While this technique is used in different applications like optics and ESR, here the method will be described in the context of transport measurements as this is how is was used in this study. In the measurement of the lower critical field it is necessary to probe multiple hall sensors at the same time. For this a number of commercial *lock-in amplifiers* would be necessary. In order to reduce the cost and technical demand for this experiment the development of a low-cost alternative was done by the author as part of this thesis.

To start, lets recap the mathematical solution for the multiplication of two sine-waves

$$V_{DSP} = V_{ref} \sin(\omega_{ref} t + \phi_{ref}) \cdot \sum_i V_i \sin(\omega_i t + \phi_i) \tag{3.13}$$

with V_{ref}, ω_{ref} and ϕ_{ref} being the excitation voltage, frequency and phase of transport measurement. The signal coming back from the sample is usually of the sample response and noise coming from the setup and the surrounding, presented by a sum over discrete noise sources i. In the early days of the technique the multiplication was done by mixing the two signals in an analog way, while it is done numerically in most modern instruments.

The result of the multiplications and substitution gives

$$\begin{aligned} V_{DSP} = \quad & \frac{1}{2} V_{ref} \sum_i V_i \sin([\omega_{ref} - \omega_i]t + [\phi_{ref} - \phi_i]) + \\ & \frac{1}{2} V_{ref} \sum_i V_i \sin([\omega_{ref} + \omega_i]t + [\phi_{ref} + \phi_i]) \end{aligned} \tag{3.14}$$

consisting of two parts, with the sum and difference between excitation and response frequency. For the response of the sample, which we are interested in, the condition

$\omega_{ref} = \omega_i$ can be used. This means we are only interested in the DC part of V_{DSP}, which can be achieved by a low pass filter. Numerically the low pass filter of order o is achieved iteratively by

$$y_n^o = A y_n^{o-1} + B y_{n-1}^o. \tag{3.15}$$

The parameter A and B are dependent on the desired time constant and sampling time. They are connected by $B = 1 - A$. The value y_n^0 represents the new input value at a given time. This description follows the behavior found in RC-lowpass filter. The filter constant A is given by [21]

$$A = \frac{\Delta t}{\tau + \Delta t}, \tag{3.16}$$

with the sampling time Δt and the filter time constant τ.

3.6.1 24bit Analog to Digital Converter

The procedure described above was implemented on an Arduino Uno [22] that controlled an analog to digital converter (ADC). The chosen ADC is a Analog Devices AD7764 that has 24bit precision [23]. The circuit design was done using the design guidelines within Ref. [23] and the design of the evaluation board in Ref. [24] (Fig. 3.18). The Arduino environment has the benefit that comes as single-board microcontroller including a built in USB interface. This allows to focus on the data acquisition and the development of the digital signal processing (DSP) code.

The AD7764 was chosen, as it provides the possibility for 24bit full precision in the used sampling range, which allows a higher precision on signals with large background. Further it comes with an input filter that limits high frequency noise and a full differential input with ±5 V input tolerance. The ADC is controlled by the Arduino board using *serial peripheral interface* (SPI) connection. This four-wire interface has two wires for the communication, the master-clock which is provided by the Arduino and a channel for chip selection. The ADC was calibrated in DC mode. In this configuration constant voltages are applied to the ADC and a Keithley Digital Multimeter in parallel as reference. The Arduino reads the 24bit binary number from the ADC and returns it to the computer via the USB port. This way a calibration as shown in Fig. 3.19a are achieved. We have further taken measurements with the input of the ADC grounded. The data is shown in Fig. 3.19b. This hold an rms-noise level of $V_{rms} = 3.9\,\mu$V, which corresponds to a useful resolution of 21bit.

For the DSP the Arduino uses one external triggered clock as interrupt. This is connected with the trigger-out of the excitation, typical a Stanford Research SR830. This way the Arduino measures the time between two rising edges of the trigger signal and determines so the reference frequency. A second clock is used as sampling time. It was found that good low noise results are obtained using 10 samples per oscillation

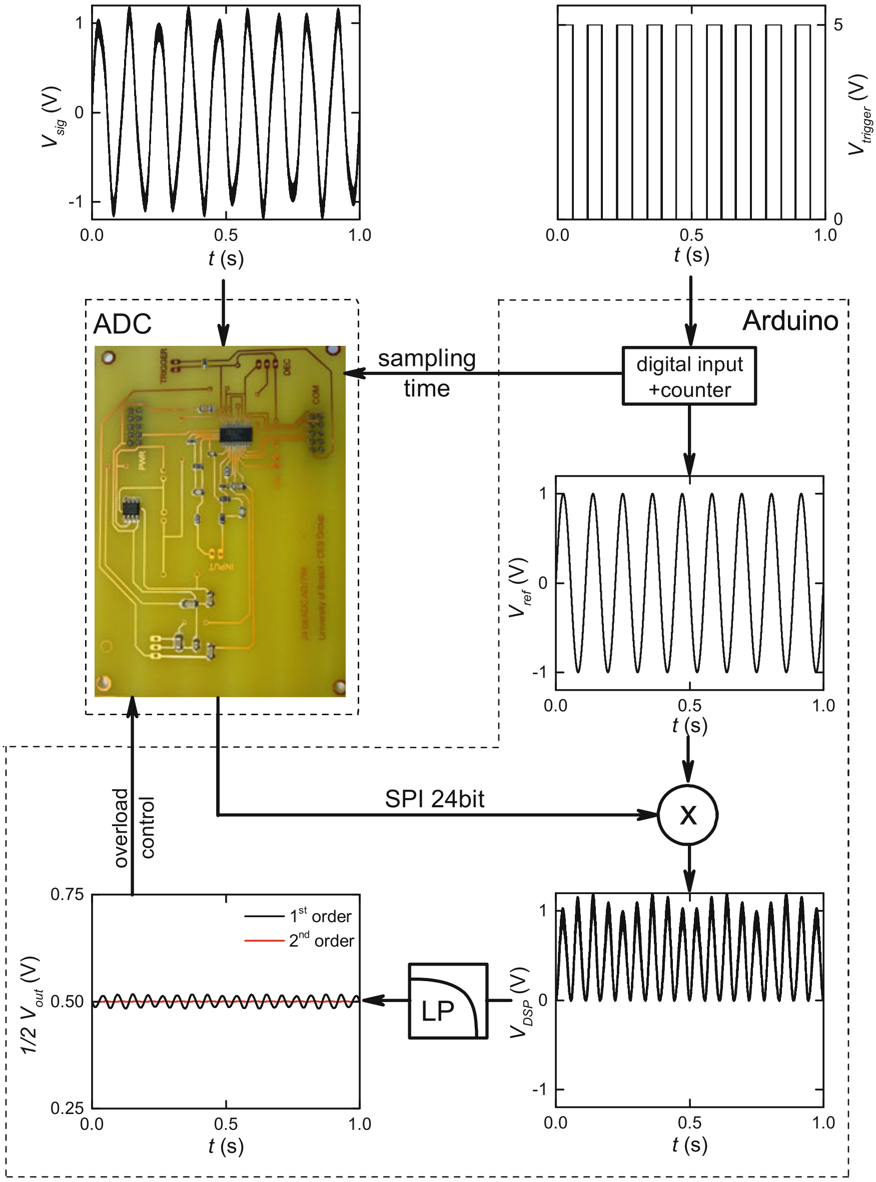

Fig. 3.18 Schematic outline of the Arduino controlled ADC and the programmed DSP procedure. Starting by a signal including noise (*top left*) and the trigger signal as reference (*top right*) the work flow is presented. See text for more information

period. The internal clock is configured such that it causes an interrupt after one-tenth of the oscillation period. At this point the Arduino waits for the ADC to convert the current voltage. This is then transferred to the microcontroller. This procedure is also

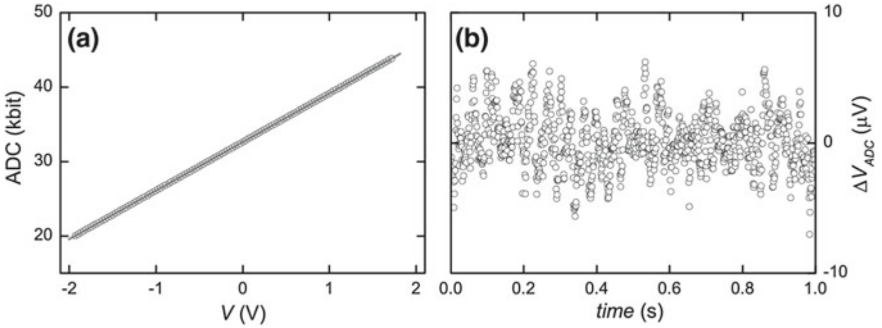

Fig. 3.19 **a** Calibration for the analogue to digital converter. The integer value of the chip, representing the 24bit response, is plotted versus the applied voltage. **b** Noise contribution from one of the ADC channels described in the text. An offset of 200 μV was removed

illustrated in Fig. 3.18. Further the microcontroller determines the reference point by calculating the sine and cosine, for in- and out-of-phase component, at the present time. By multiplying the reference with the data from the ADC we obtain V_{dsp}. In the present work a fourth order low pass filter, as described before, was used to get the $\omega_{ref} - \omega_i = 0$ component that we are interested in.

This setup was successfully used in measuring H_{c1}. As we could measure up to eight sensors in parallel the use of Lockin amplifier would exceed the available instruments in the laboratory. The procedure presented here provides a cheap alternative when working in the low frequency range $f \leq 50$ Hz. In this configuration eight identical channels were produced. These were then connected to an additional Arduino using a two wire *inter-integrated circuit* (I^2C) bus. This reduces the overall communication time as the opening and closing of the communication-port takes most time.

3.7 Transport Measurement in Pulsed Magnetic Field

While in the zero- and static-field measurements commercial Lock-in amplifier allow to measure signals down to a few nanovolt, these devices are not suited for the use in pulsed magnetic field. The update rate at which they operate is not high enough to meat the desired resolution necessary to observe quantum oscillation of several kilo-Tesla. While in superconducting magnets sweep-rates of 2 T/min or less are used, in pulsed magnetic field we find sweep-rates of up to 2000 T/s. Therefore it is desired to record the signal with a high sampling rate, which is done by using scopecorder or as in the present case data-acquisition(DAQ)-cards NI PXI-5922. We follow the same idea as already described in Sect. 3.6. An ac-signal with a typical frequency of 50 to 60 kHz and amplitude of V_{exc} is generated by an Stanford Research SR830. This signal is applied to the sample with two series resistors (see Fig. 3.20). The first

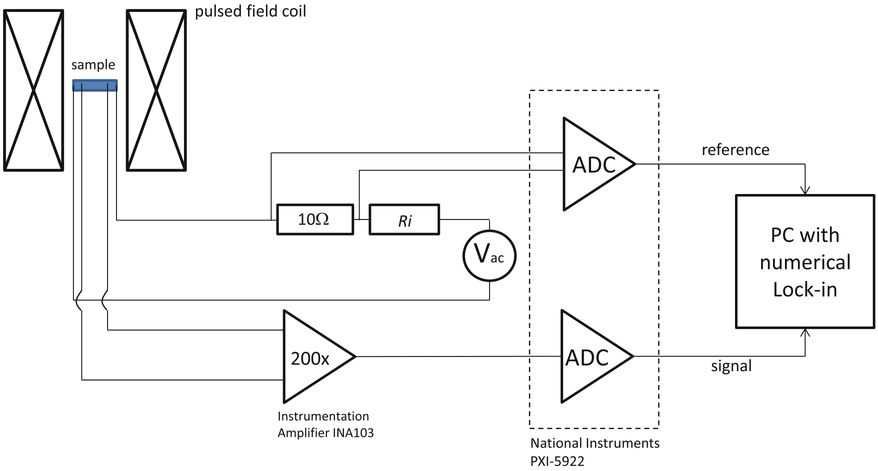

Fig. 3.20 Schematic of setup used to measure transport in pulsed magnetic field at the LNCMI-Toulouse. The resistor Ri is the current limiting resistor. The reference signal is measured as voltage-drop over a $10\,\Omega$ resistor

resistor Ri is the current-limiting resistor. It ensures that the current applied to the sample I_s does not exceed V_{exc}/Ri. The second resistor is a calibrated reference. The voltage over this resistor is measured and digitized. This signal will be used as V_{ref} (see Sect. 3.6). In the case of the sample resistance being close to Ri it is also used to determine the correct current used. As the DAQ system has a fixed input-range of ±5 V we typically need to amplify our signal to increase the used voltage range. For the measurements carried out here INA103 instrumentation amplifiers were used with a fixed gain of 200. For samples with small signals a different amplifier (SSM2019) was used with a gain up to 1000. The signal was then also digitized using the same time-base as the reference signal. In order to analyse the data obtained a Matlab-code was developed which performs the numerical-phase sensitive detection that was described previously. The used code can be found in Appendix A.

3.8 Torque Measurements

The magnetization **M** of a sample in an external magnetic field **B** can be measured using torque magnetometry. The torque density τ (torque per unit volume) can be written as $\tau = \mathbf{M} \times \mathbf{B}$. In the case that the applied field lies in an arbitrary direction with respect to the symmetry axis of the sample the component $M_\perp$ perpendicular to **B** becomes none zero.

If the Fermi-surface of the system is anisotropic the contribution $M_\perp$ can be written as [25]

$$M_{\perp} = -\frac{1}{F}\frac{\mathrm{d}F}{\mathrm{d}\theta}M_{\parallel}. \tag{3.17}$$

The angle θ represents the angle of **B** in the plane perpendicular to $M_{\perp}$ and F is related to the extremal cross-section of the Fermi-surface via the Onsager-relation (Eq. 2.22). The resulting torque density can hence be written as

$$\tau = -\frac{1}{F}\frac{\mathrm{d}F}{\mathrm{d}\theta}M_{\parallel}\mathbf{B}. \tag{3.18}$$

This results shows some limitations that need to be taken into account when performing measurements using torque magnetometers. The torque signal will vanish when the applied field **B** lies within a high symmetry axis of the investigated sample. This will cause 'blind spots'. It should also be mentioned that the observed torque will be $\tau \cdot V$, V beeing the sample volume. While in the ideal case the entire sample can give rise to quantum oscillation, in reality only a fraction of the of the sample volume might contribute. Most importantly we notice that the signal amplitude observed will be proportional to the applied magnetic field.

For the application of torque magnetometry in the field of iron-based superconductors it is essential to be able to measure microscopic crystals on the order of $100 \times 100 \times 100\,\mu\mathrm{m}$ or smaller. This is possible by using piezo-resistive micro-cantilever. In this work self sensing micro-cantilevers originally designed for atomic force microscopy where use. Each device contains a signal lever and a reference. The reference is used to minimize contributions coming from magnetoresistance.

Samples were attached to the leaver using grease, giving the possibility to reuse the cantilever. The produced torque in field cause the leaver to bend and results in a change in resistance of the piezo-element. By using a Wheatstone-bridge setup it is possible to detect small changes in between the reference and sensor resistance which correspond to a change in angle of the leaver.

As the technique relies on a bending of the leaver there occurs a subsequent displacement of the the original angle between the crystallographic axis of the sample and the applied magnetic field. This leads to a change of the extremal cross-section perpendicular to field and in the case of large quantum oscillations to the appearance of new frequencies. This effect is known as *torque interaction*.

3.8.1 Torque Interaction

As torque interactions can lead to the observation of new frequencies, it is important to find a way to distinguish between true quantum oscillations and artefacts. In order to do this data taken by Dr. I. Guillamon on high quality single crystals of MgB_2 have been analyzed. Lets start by taking a look at the reason for new frequencies in the case of torque interaction. Assuming the signal contains quantum oscillations of the form

$$\tau_i = A_i B^{1/2} e^{-\alpha_i/B} \sin\left(2\pi \frac{F_i}{B\cos(c(\theta-\theta_0))}\right), \tag{3.19}$$

with A_i, α_i and F_i being the amplitude, dingle-factor and frequency of the different extremal orbits i. The total observed torque is

$$\tau = \sum_i \tau_i. \tag{3.20}$$

The condition for the observation of quantum oscillations using torque magnetometry was that our sample exhibits an anisotropic Fermi-surface. Hence $F = F(\theta)$. The form of the angular frequency-dependence has been studied in detail for MgB_2 [26]. For the further steps we assume $F(\theta)$ to vary as $F_0/cos(\theta)$ for small changes around the angle of interest. Also we neglect the fact that there will be a change in oscillation amplitude when changing the angle. The main frequencies F_1, F_2 and F_3 (see Fig. 3.21) where filtered and fitted using Eq. 3.19. Afterwards we can use the obtained parameters which will be fixed in the following steps. The effect of torque interaction is described by

$$\tau = \sum_{\substack{i,j\\ i\neq j}} A_i B^{1/2} e^{-\alpha_i/B} \sin\left(2\pi \frac{F_i}{B\cos(c(\theta-\theta_0)-\gamma\tau_j)}\right). \tag{3.21}$$

The parameter c is fixed by knowing the angular dependence of F. This leaves one free parameter γ which converts the measured change in resistance into the angle of

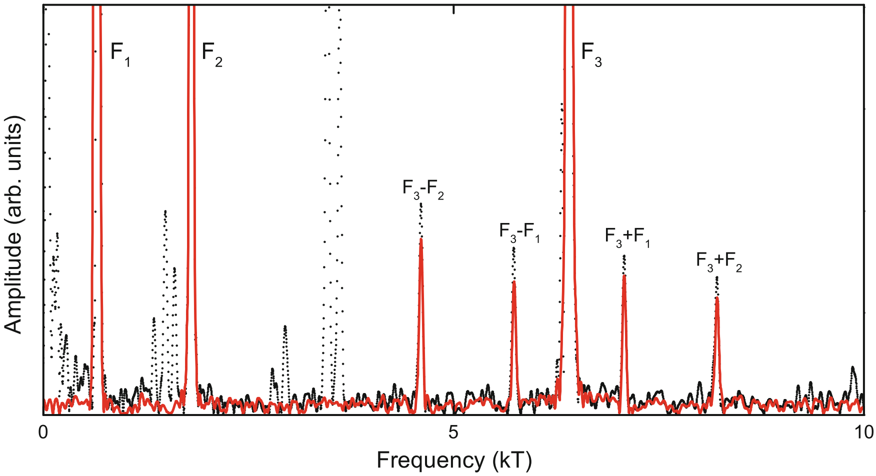

Fig. 3.21 FFT taken on high quality on dHvA-signal of MgB_2 by Dr. I. Guillamon (*black dots*). The data was taken at $T = 0.3$ K in the field range of 10 to 18 T. The *red line* shows the fit to the data using Eq. 3.21 and the procedure described in the text

displacement. As the torque interaction is typically much smaller then the quantum oscillations, higher accuracy was found by fitting the data in frequency space. The resulting fit is shown in Fig. 3.21. Good agreement between the data and the fit was found for $\gamma = 0.18\,^\circ/\Omega$. This factor can now be taken as calibration for the used SEIKO PRC120 micro-cantilever.

3.9 Germanium-Gold-Thermometer

Germanium-gold thermometers have been know to work in the range of low temperatures up to room temperatures for many years [27]. Germanium-gold thin films have been produced by sputtering alternating layers of germanium and gold with a molar ratio of Ge:Au of 0.83:0.17. The thin films were post annealed at 450° for 1 h. The resulting thin film resistors were found to be sensitive over the temperature range of 1.5–300 K, shown in Fig. 3.22. By varying the gold concentration used, the sensitivity of the produced films can be tuned. By lowering the gold concentration the system becomes more sensitive at elevated temperature, while a higher gold concentration makes the system more useful for lower temperatures.

The used procedure was further used to built a new calorimeter for measurements of small single crystals. During this procedure calibration under magnetic field have been performed by Dr. L. Malone. Results of magnetoresistance versus applied field are shown in Fig. 3.23. The results are compared to those obtained by Brandt et al. [20] for Cernox thin film thermometers.

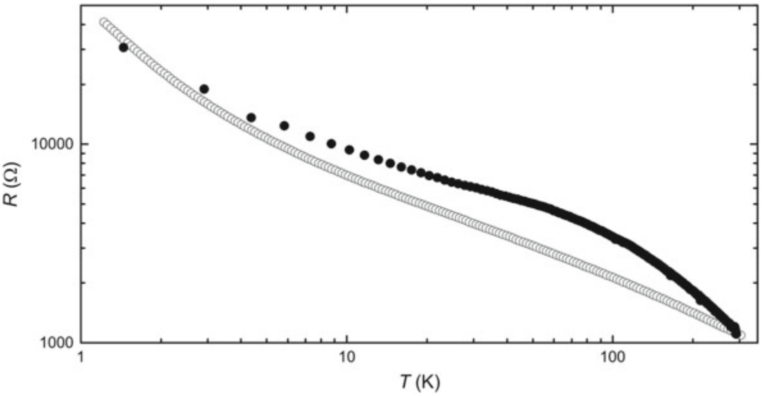

Fig. 3.22 Resistance versus temperature of a germanium-gold thin-film on silcon (*solid circles*) compared to a cernox CX1050 (*empty circles*)

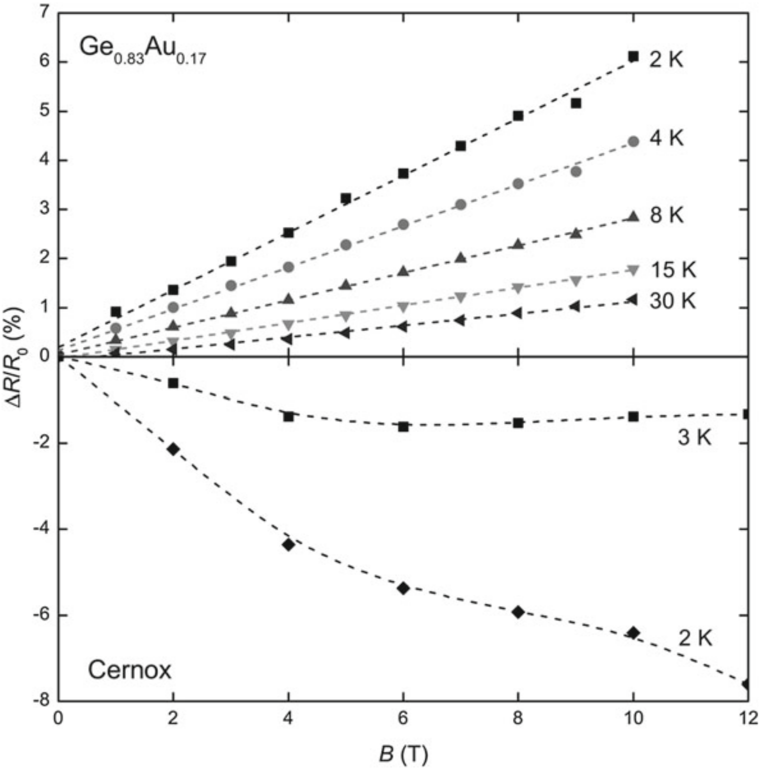

Fig. 3.23 Magnetoresistance of a germanium-gold thin film thermometer, manufactured as described in the text, compared to a Cernox resistor as specified in Ref. [20]. While a linear field dependence with increasing sensitivity is found for the germanium-gold film, a more complex behaviour is found in the Cernox resistor. Courtesy of L. Malone

3.10 Rotator for High Magnetic Field

In the field of high-temperature superconductors it is often not possible to suppress superconductivity with superconducting magnets. In this case all experiments, including sample screening for quantum oscillations need to be carried out at user facilities. In order to increase productivity a rotator capable of holding four micro-cantilever was built thereby enabling us to screen twice as many samples in a day as before. The decision to built a rotator rather than a static probe was made as the angle-dependence of the oscillation amplitude is not constant and hence requires to check different field directions with respect to the crystal axis. The bottom part of the rotator is entirely built from *hysol* to prevent eddy current heating (see Fig. 3.24). The rotating *ball* contains three levels. The bottom level holding a Cernox thermometer and an angle-pickup coil or Hall sensor for angle determination. The top two layers can fit two cantilevers each. In order to access the middle layer the top level can

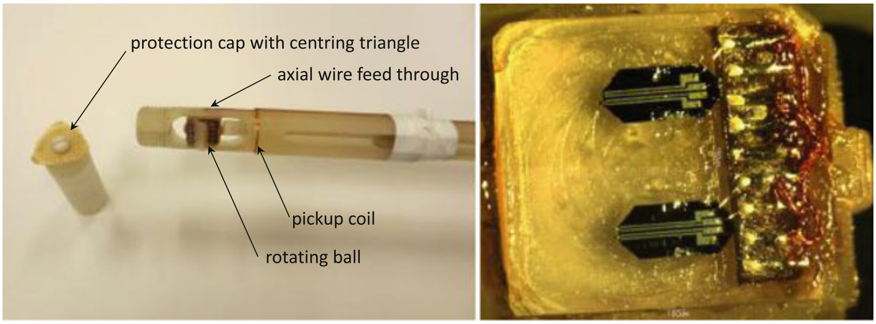

Fig. 3.24 Rotator used for dHvA measurements at the LNCMI-Toulouse and the NHMFL Tallahassee. The rotator is constructed as swedish rotator from plastic (*left panel*). Inside the rotating *ball* three platforms are mounted. The lowest platform holds the thermometer and angle-pickup coil. The top two platforms can hold 2 cantilever each, as seen in the right panel

be folded back and is held in place by GE vanish. To protect the sensitive micro-cantilever, a protection cap is screwed on the end of the probe. This cap includes a semi-flexible plastic triangle which centers the probe and reduces vibration during the measurement.

To determine the angle two different approaches are used depending on the used magnetic field. For pulsed magnetic field a second pickup-coil was placed perpendicular to the cantilever. The rapid change in magnetic field induces a voltage that is proportional to the area of the pickup coil perpendicular to the applied field and the change of field in time,

$$V \propto \frac{\mathrm{d}B}{\mathrm{d}t} \sin\theta. \tag{3.22}$$

θ is the angle between the applied field $\mathbf{B}$ and the sample. The same technique is used to determine the magnetic field strength in pulsed field systems. When plotting the voltage of the angle-pickup coil versus the voltage of the field-pickup coil one finds a linear correlation where the slope is related to $\sin\theta$. For the calibration of the system, one only needs to find the maximum value of the slope.

In static magnetic field this technique is not useful as the sweep rates used are too small to obtain a significant induced voltage. We therefore have used Hall sensors to obtain the angle. The sensor was again placed on the rotating platform and we find that the Hall voltage V_h is again proportional to $\sin\theta$ when placed perpendicular to the sample. As most commercial Hall sensors are used in the limit of low magnetic fields, they are made with low carrier densities to obtain maximum sensitivity in the range of a few milli-Tesla. In the limit of high fields up to 45 T they typically show quantum-hall-plateaus. We have therefore used a home-built alternative made of thin-film silver-gold alloy. It had been shown that the Hall coefficient increases when adding silver to pure gold in thin films [28].

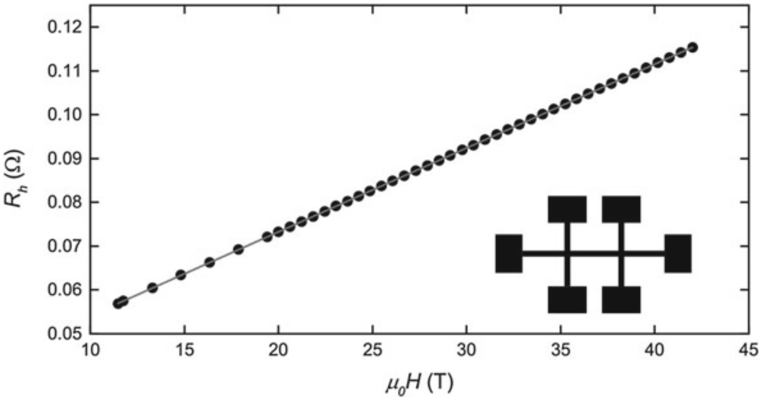

Fig. 3.25 Field dependence found for the Hall resistance of a silver-gold alloy, thin film at $T = 0.5\,\mathrm{K}$ in static field at the NHMFL Tallahassee. The layout of the deposited material is shown as inset. Two active areas per substrate were performed

3.10.1 Silver-Gold Hall Sensor

For the determination of the angle in high static field we use a Hall-sensor. As commercial available Hall-sensors have good sensitivity at low field and high high temperature they are not suited for the use in fields up to 45 T and temperatures down to 0.3 K. For this reason Hall-sensors from silver-gold alloy were produced on glass. The mask for the deposited pattern, shown as inset in Fig. 3.25, are laser-cut from aluminium film. Silver and gold were taken in molar ratio of 1:1. Both materials were simultaneously deposited by evaporation using a home-built thermal evaporator. Afterwards the mask was removed and the thin film was place in the furnace at 200 °C for 20 min. In the next step the resulting pattern was contacted using Dupont 6838 conductive paint. This was further annealed for 45 min at 200 °C and then for 1 h at 400 °C. The Hall sensor was used in high dc magnetic field at the NHMFL Tallahassee. Data obtained for the field perpendicular to the substrate is shown in Fig. 3.25. A Hall-coefficient of 35 mΩ/T was found for the used substrate.

3.11 Energy-Dispersive X-Ray Spectroscopy

The determination of the exact composition is essential when probing different chemical substitutions such as in $\mathrm{BaFe_2(As_{1-x}P_x)_2}$. In the present work this has been done in two ways, x-ray diffraction (XRD) and *energy-dispersive x-ray spectroscopy* (EDX). X-ray diffraction on single crystals was used to determine the crystal structure and the lattice parameters. In the $\mathrm{BaFe_2(As_{1-x}P_x)_2}$ series the lattice parameters

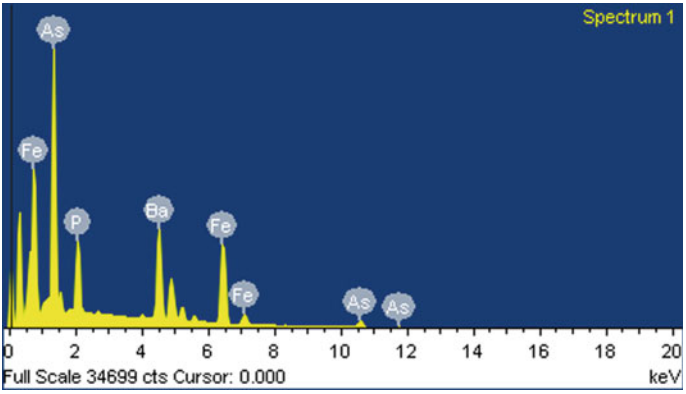

Fig. 3.26 Typical EDX spectrum obtained on $BaFe_2(As_{1-x}P_x)_2$ with $x = 0.30$. Several of these were taken at different positions on the sample surface

are sensitive to substitution of As for P [14]. As the single crystals of interest are typically very small the diffraction pattern as already shown in Fig. 3.11c was not sensitive enough to determine the distribution to better than ±5 %. Further the composition obtained from the lattice parameters a and c using Ref. [14] held different substitution levels. Hence in the quantum oscillation study of $BaFe_2(As_{1-x}P_x)_2$ XRD was used only to estimate the composition prior to the experiment in order to find crystals in the desired range of x. The composition of the crystal was then determined more accurately by the linear dependence of the dHvA frequencies [29] as will be discussed later.

For the study of H_{c1} in $BaFe_2(As_{1-x}P_x)_2$ different samples to those of the dHvA study were measured making it necessary to find another way to obtain the composition more accurately. For this we have used *electron-dispersive x-ray spectroscopy* (EDX). In this technique the sample is bombarded with primary electrons which interact with electrons on the inner shell of the atoms. Thereby created holes are filled with electrons 'falling' from a higher shell. During this process a photon of energy $E = \hbar\omega$ with a characteristic wavelength $\lambda = 2\pi c/\omega$ is emitted. These energies/wavelength are characteristic for all elements as the allowed energy-levels in an atom are $E_n \propto Z^2$, with the the atomic number Z. By analyzing the emitted x-ray photon for its energy it is possible to assign it to a specific transition in a specific atom. The count of the occurring photons for a given transition can then be used to evaluate the ratio of different atoms in a system. Such a spectrum is shown in Fig. 3.26 for a $BaFe_2(As_{0.7}P_{0.3})_2$ sample.

Several spectra were taken for each sample at different positions on the sample surface.

References

1. G. Scheerer, High-magnetic-field study of the heavy fermion system uru$_2$si$_2$, Ph.D. dissertation, LUniversite de Toulouse (2013)
2. C. Enss, S. Hunklinger, *Tieftemperaturphysik* (Springer, 2000)
3. F. Pobell, *Matter and Methods at Low Temperatures*, 3rd edn. (Springer, 2007)
4. N.W. Ashcroft, N.D. Mermin, *Solid State Physics*, 3rd edn. (Oldenbourg, 2007)
5. L. Klintberg, S. Goh, S. Kasahara, Y. Nakai, K. Ishida, T. Sutherland, M. ad Shibauchi, Y. Matsuda, T. Terashima, J. Phys. Soc. Jpn. **79**, 123706 (2010)
6. T. Yamazaki, N. Takeshita, R. Kobayashi, H. Fukazawa, Y. Kohori, K. Kihou, C. Lee, H. Kito, A. Iyo, H. Eisaki, Phys. Rev. B **81**, 224511 (2010)
7. E. Colombier, S. Bud'ko, C. P.C., Phys. Rev. B **79**, 224518 (2009)
8. I. Walker, Rev. Sci. Instrum. **70**, 3402 (1999)
9. M. Nardonne, A. Audouard, D. Vignolles, L. Brossard, Cryogenics **41**, 175 (2001)
10. C.-Y. Wang, Rev. Sci. Instrum. **38**, 24 (1967)
11. D. Bowen, G. Jones, Proc. R. Soc. Lond. A **254**, 522 (1960)
12. R. Juza, K. Langer, Ternäre phosphide und arsenide des lithiums mit eisen, kobalt oder chrom im cu$_2$sb-typ. Zeitschr. für anorg. und allg. Chemie **361**, 58–73 (1968)
13. Z. Deng, X. Wang, Q. Liu, S. Zhang, Y. Lv, J. Zhu, R. Yu, C. Jin, EPL **87**, 37004 (2009)
14. S. Kasahara, K. Shibauchi, K. Hashimoto, K. Ikada, S. Tonegawa, R. Okazaki, H. Shishido, H. Ikeda, H. Takeya, K. Kirata, T. Terashima, Y. Matsuda, Phys. Rev. B **81**, 184519 (2010)
15. J. Lefebvre, M. Hilke, Z. Altounian, K. West, L. Pfeiffer, Phys. Rev. B **79**, 124524 (2009)
16. R. Okazaki, M. Konczykowski, C. van der Beek, T. Kato, K. Hashimoto, M. Shimozawa, H. Shishido, M. Ishikado, H. Kito, A. Iyo, H. Eisaki, S. Shamoto, T. Shibauchi, Y. Matsuda, Phys. Rev. B **79**, 064520 (2009)
17. R. Liang, P. Dosanjh, D. Bonn, W. Hardy, A. Berlinsky, Phys. Rev. B **50**, 4212 (1994)
18. R. Liang, D. Bonn, W. Hardy, D. Broun, Phys. Rev. Lett. **94**, 117001 (2005)
19. M. Nideröst, R. Frassanito, M. Saalfrank, A. Mota, G. Blatter, V. Zavaritsky, T. Li, P. Kes, Phys. Rev. Lett. **81**, 3231 (1998)
20. B. Brandt, D. Liu, L. Rubin, Rev. Sci. Instrum. **70**, 104 (1999)
21. W. Press, S. Teukolsky, W. Vetterling, B. Flannery, *Numerical Recipes* (Cambridge University Press, 2007)
22. Arduino SA (2014) Open source platform. http://arduino.cc
23. Analog Devices AD7764 (2009) Datasheet. http://www.analog.com/static/imported-files/data_sheets/AD7764.pdf
24. Analog Devices AD7764EV (2008) Datasheet evaluation board. http://www.analog.com/static/imported-files/eval_boards/EVAL-AD7764_AD7765EBZ.pdf
25. D. Schoenberg, *Magnetic Oscillations in Metals* (Cambridge University Press, 1984)
26. A. Carrington, P. Meeson, J. Cooper, L. Balicas, N. Hussey, E. Yelland, S. Lee, A. Yamamoto, S. Tajima, S. Kzakov, J. Karpinski, Phys. Rev. Lett. **91**, 037003 (2003)
27. S. Sahling, O. Bethoux, J. Lasjaunias, R. Brusetti, Phys. B **219–220**, 754 (1996)
28. I. Bhattacharya, D. Bhattacharya, Int. J. Electron. **41**, 258 (1976)
29. H. Shishido, A. Bangura, A. Coldea, S. Tonegawa, K. Hashimoto, K. Kasahara, P. Rourke, H. Ikeda, T. Terashima, R. Settai, Y. Onuki, D. Vignolles, C. Proust, B. Vignolle, A. McCollam, Y. Matsuda, T. Shibauchi, A. Carrington, Phys. Rev. Lett. **104**, 057008 (2010)

Chapter 4
$BaFe_2(As_{1-x}P_x)_2$—A Quantum Critical Superconductor

4.1 Introduction

Among the large variety of iron-based superconductors the $BaFe_2(As_{1-x}P_x)_2$ series is special. The isovalent substitution allows changes in the electronic structure to be linked to the crystal structure rather than additional doping and high quality single crystals are available throughout the phase diagram, which allows the study of a variety of properties with high precision.

We begin by introducing the parent compound $BaFe_2As_2$. Upon cooling, the material undergoes a structural (from tetragonal to orthorhombic) and magnetic transition at $T = 137\,\mathrm{K}$ [1, 2]. While for $x > 0$ transition-temperatures of the structural and anti-ferromagnetic transition can be separated, in the parent compound they can not. Shortly after its discovery, the origin of the anti-ferromagnetism was believed to be a spin-density-wave (SDW) instability of the Fermi surface, which is caused by Fermi surface nesting and reflected as a peak in the Lindhard dielectric response function [3]. Further theoretical investigations using DFT calculations [4] changed this view and suggested, that the magnetic order is driven by Hund's rule coupling, onsite interaction. It was shown that the energy gain for a stripe like anti-ferromagnetic order in $BaFe_2As_2$ was achieved over a wide range of 1 eV from the Fermi surface, making the energy gain at E_F a minor effect. This is supported by the band-structure of $BaFe_2P_2$ [5], which we will discuss in more detail later. Here good nesting but no magnetic ground state was found. Also it was discussed in Ref. [6], in the context of charge density wave formation, that the nesting criteria, described in the Peierls theory, is not a sufficient factor in systems with two or more dimensions. DFT+DMFT studies by Yin et al. [7] as well argued the importance of the Hund's rule coupling on these system, but they point out that a DFT based calculation has its limitations to predict the real system as it neglects long-wavelength fluctuations and strongly overestimates the magnetic moment in these systems. They propose to treat the system using DFT+DMFT, which strictly speaking also neglects long wave length spin fluctuations [8], but it can incorporate the Hund's rule coupling J. They

C.M. Putzke, *Fermi Surface and Quantum Critical Phenomena in High-Temperature Superconductors*, Springer Theses,
DOI 10.1007/978-3-319-48646-8_4

find a correlation of the quasi particle mass with magnetic moment which is in good agreement with experimental results. They were able to further link changes in the effective mass to structural parameters, whose origins we will discuss in the next section. These structural changes cause a change in the iron-iron interaction but at the same time modify the band structure, leading to changes in the effective mass. Yin et al. [7] further point out that the development of magnetic order not necessarily needs nesting and can be understood in a local picture of the iron-iron interaction, similar to the DFT prediction, in systems like KFe_2As_2 where the mass enhancement is substantial but nesting is absent and only a small magnetic moment exists. So we must conclude that while DFT calculations show correctly, that the formation of magnetic order is possible without nesting, a theory including interactions, not captured by DFT, might find nesting as an enhancing but not a causal effect.

In the system considered here arsenide has been replaced by phosphorous, which is isovalent. As the Fermi surface mainly contains iron d-orbitals which are hybridised with the pnictogen orbitals we find that this substitution changes the overlap of atomic orbitals but we would not expect any changes to the charge balance in or out of the iron-pnictogen layer. In Fig. 4.1 the resulting phase diagram is shown in comparison to that of $Ba_{1-x}K_xFe_2As_2$ for which the system becomes hole doped and $Ba(Fe_{1-x}Co_x)_2As_2$ which is electron doped. While in the case of cobalt or potassium substitution the electron-hole-balance changes to the point where for example only hole-pockets are observed in the case of KFe_2As_2 [9], in the arsenide-phosphor series the electron-hole balance stays constant.

As can be seen in Fig. 4.1 the anti-ferromagnetic, orthorhombic phase is suppressed when substituting phosphorous for arsenide and a new, superconducting, phase emerges. The maximum critical temperature in $BaFe_2(As_{1-x}P_x)_2$ was found

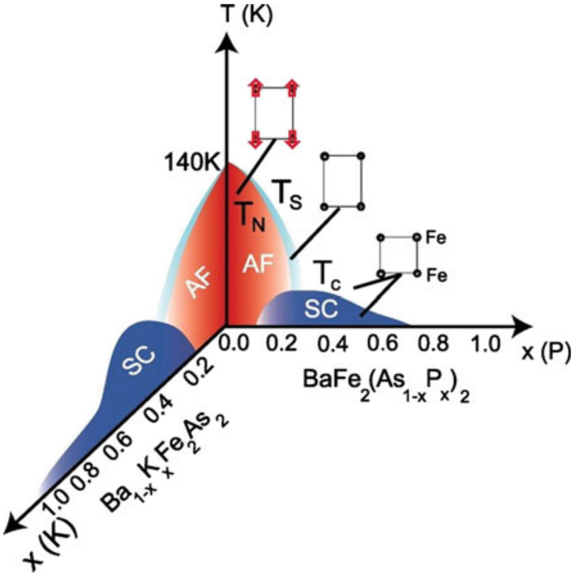

Fig. 4.1 Schematic phase diagram of $BaFe_2(As_{1-x}P_x)_2$ and $Ba_{1-x}K_xFe_2As_2$ as taken from Ref. [10]. The temperature T_N and T_S represent the anti-ferromagnetic and structural transition respectively

for $x = 0.3$ with $T_c = 30\,\mathrm{K}$ and is located at the composition where T_N extrapolates to zero. By further substitution the superconducting state eventually vanishes at $x = 0.71$ [1] and the $BaFe_2P_2$ end member is a paramagnetic metal.

It should be mentioned here shortly that the suppression of anti-ferromagnetism and the appearance of superconductivity was also observed under high pressure [11–13]. Klintberg et al. [11] showed that the achievable maximum T_c is comparable to that of isovalent substitution. Due to the analogous behaviour, the substitution of phosphorous for arsenide is often referred to as *chemical pressure*.

Besides the evolution of the ground state it is found that the temperature dependence of the resistivity changes across the phase-diagram from T^2 at $x = 0$, to T-linear at $x = 0.3$ back to T^2 at $x = 1$ [1, 14]. As discussed in Sect. 2.8.1 this region of non-Fermi liquid behaviour is believed to be a possible indication for quantum critical behaviour.

4.1.1 Crystal Structure

To describe the crystal structure of $BaFe_2(As_{1-x}P_x)_2$ we will start with the body-centred tetragonal ($a = b$) system, space group $I4/mmm$, as it can be found in $BaFe_2P_2$, most of the superconducting compositions and temperatures above T_s in Fig. 4.1 in the arsenic rich region. In these parts of the phase diagram the system has tetragonal body-centred symmetry, shown in Fig. 4.2.

We will again start with $BaFe_2As_2$ and discuss changes due to the substitution with phosphorous. As both elements are in the same column in the periodic table, but phosphorous being one row above arsenic we can expect phosphorous to have a smaller atomic radius but similar oxidisation state. Hence the number of electrons per unit cell will stay constant but the lattice parameter will change as shown in Fig. 4.3 [1]. The lattice parameter a and c shrink, as will the pnictogen height h_{pn} with increasing x. Due to the reduced pnictogen height the iron-pnictogen distance becomes shorter, leading to a stronger hybridization of the atomic orbitals. This has consequences for electronic properties. As the hybridisation of iron-d-orbitals increases valence electrons become more de-localized leading to a larger bandwidth and hence a reduction in effective mass. As described earlier this might be the origin for the suppression of the anti-ferromagnetic phase with increasing x. We can possibly better understand this by the opposite approach. When increasing the pnictogen height the electrons become more localized. By following the first Hunds's rule they populate available states such that the magnetic moment becomes maximum. The lowest energy configuration for this magnetic ordering in $BaFe_2(As_{1-x}P_x)_2$ is the AFM stripe order. Further these changes in the crystal structure effect the band structure of the system. The importance of these effects was pointed out early on by Kuroki et al. [15], where changes in the superconducting gap structure where linked to Fermi surface caused by modifications in the pnictogen height.

As mention previously, the ground state of the arsenic end member is different from the so far discussed crystal structure as it experiences a structural transition to

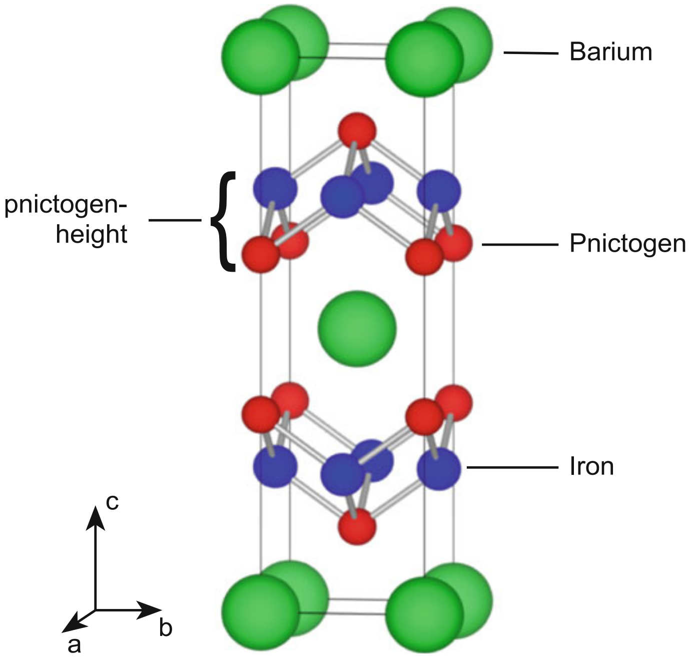

Fig. 4.2 Crystal structure of BaFe$_2$(As$_{1-x}$P$_x$)$_2$

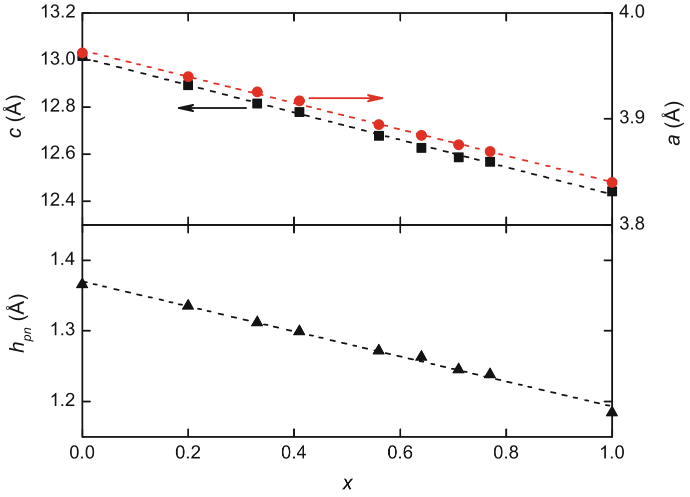

Fig. 4.3 Lattice parameters a and c for the tetragonal phase of BaFe$_2$(As$_{1-x}$P$_x$)$_2$, as well as the pnictogen height h_{pn} as determined in Ref. [1]

an orthorhombic phase (space group $Fmmm$). In this phase $a \neq b$ and the formation of anti-ferromagnetism causes a doubling of the unit cell. Both effects have important consequences for the bandstructure of the system which will be discussed in the next section.

4.1.2 Bandstructure of $BaFe_2(As_{1-x}P_x)_2$

In this section we wish to introduce the bandstructure of $BaFe_2(As_{1-x}P_x)_2$ by discussing in more detail how it is linked to the crystal structure. We will then turn to review results obtained prior to the present study. In contrast to the previous section will start from the $BaFe_2P_2$ side, as our interest lies in the evolution of the non-reconstructed Fermi surface. As pointed out in the introduction it is believed that the nesting of the tetragonal band structure causes SDW fluctuations that lead to superconductivity. The reconstructed Fermi surface will be briefly discussed at the end of the section for completion.

The crystal structure being body-centred tetragonal has immediate consequences for the band structure expected. The Brillouin-zone (BZ) for the $I4/mmm$ space group is shown in Fig. 4.4a. The staggered form of the BZ causes a difference in symmetry between the Γ-line, four-fold symmetry, and the X-line, two-fold staggered symmetry [16]. DFT calculations, performed using the WIEN2K package [17], show how this affects the Fermi surface topology shown in Fig. 4.4b. While the hole-pockets found at the center of the BZ show four-fold symmetry, the electron pockets, at the corners of the BZ, possess a staggered two-fold symmetry. While the two-fold staggered symmetry causes the electron-pockets to appear rather warped, dispersive in k_z, the observed dHvA frequencies show good quasi-two dimensional behaviour as will see when we review the results. This can be understood when we recall what is

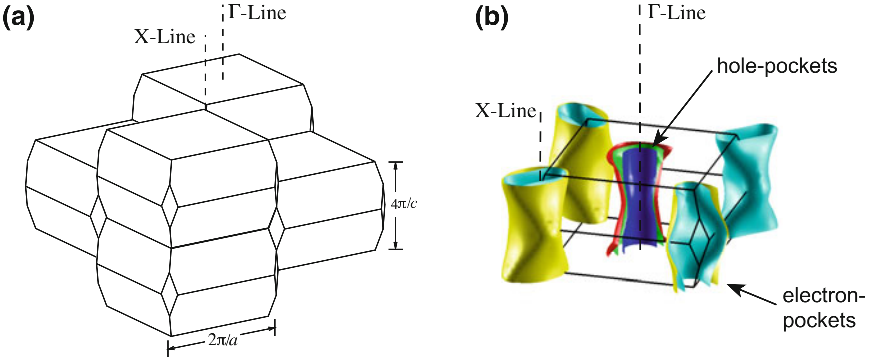

Fig. 4.4 **a** Brillouin zone of the tetragonal body centred space group (after Ref. [16]). **b** Fermi surface topology of $BaFe_2As_2$ as calculated in WIEN2k [17]. Symmetry axis and pocket type have been labelled for clarity

observed in the dHvA effect. We only observe extremal orbits but not their position or exact shape, $k_z = 0$ and $k_z = 2\pi/c$ will show the same oscillation frequency as they have the same extremal area. The range in k_z between the planes will cause additional frequencies but the area of those will not vary strongly from those already mentioned. In contrast, we find that warping of the hole pockets located in the centre of the BZ will lead to significantly different extremal orbits at the $k_z = 0$ and $k_z = 2\pi/c$.

The variation of x and its changes in the lattice parameter has direct consequences for the hybridization, as already mentioned. This does not just affect the bandwidth, but also the Fermi surface topology and orbital content at the Fermi level. As the Fermi surface is mainly caused by iron-d-orbitals their relative hybridization with pnictogen orbitals will cause changes in the Fermi surface topology and relative orbital weight distribution. A more detailed discussion of the effects of the crystal structure on DFT results will be given in the context of LiFeP, see Sect. 5.4, where we will find that increasing the unit cell, as observed in the case of reducing x (see Fig. 4.3), the k_z dispersion gets reduced. Therefore we expect the band structure of the arsenic end member having cylindrical hole-pockets, while the phosphorous end member shows stronger warping which is caused by a substantial contribution of d_{z^2}-iron-orbital at the Fermi level. The appearance of this orbital character on the Fermi surface was discussed by Kemper et al. [18] to be a disadvantage for the formation of an isotropic superconducting gap. Hence we would expect the formation of a superconducting gap to become more beneficial when moving from phosphorous to arsenic.

After these remarks lets have a look at the experimental observations prior to the study present in this work. There had been a variety of reports on the non-reconstructed Fermi surface of $\mathrm{BaFe_2(As_{1-x}P_x)_2}$ in the past [5, 19, 20]. As mentioned we will begin by looking at the end member $\mathrm{BaFe_2P_2}$, for which a detailed study of almost the entire Fermi-surface is available [5]. The observed Fermi-surface is found to contain four pockets, see Fig. 4.5, for $x = 1$. By comparison of the observed angle dependence of dHvA-frequencies with DFT predictions it was found that the observed orbits result from two electron and 2 hole pockets. Significant dispersion of the outer hole-pocket was found which reduces the nesting of the Fermi surface at top and bottom of the BZ, in contrast to the good geometrical nesting found for the inner hole- and electron-pocket. For the many-body mass-enhancement it was found that $\lambda = m^*/m_b - 1$ is in the range of 0.59 to 0.88. Compared to the expected enhancement of electron-phonon interaction $\lambda = 0.2$ [21] this is a factor 3 to 4 higher. This points to interactions that go beyond the local mean field approximation.

While the experimental values and DFT calculations can be brought in good agreement with small rigid band shifts for $\mathrm{BaFe_2P_2}$, the trend of Fermi surface evolution with x can not be correctly predicted using DFT [19]. We can understand this when considering that the substitution of arsenic for phosphorous follows a statistical distribution on the pnictogen sites. Hence a calculation using one unit cell by adjusting the lattice parameters can not correctly reproduce this effect. We therefore rely on experimental data to correctly describe the evolution of the system. The observation of hole-pockets by quantum oscillations has been limited to one composition $x = 0.64$ where the observation of the minimal orbit of the outer hole-

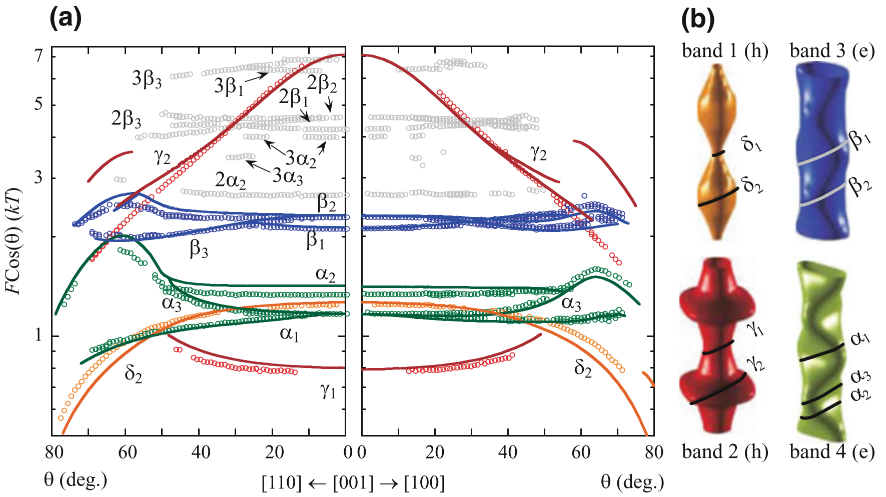

Fig. 4.5 dHvA frequencies multiplied by the rotation angle versus angle for $BaFe_2P_2$ taken from Ref. [5]. Experimental values (*circles*) and bandstructure calculations (*solid lines*) are shown in panel (**a**). The corresponding orbits are pointed out in panel (**b**) where (**e**) represent electron pockets and (**h**) hole pockets

pocket γ_1 was reported [20]. Beyond this the trend of extremal orbits of the electron pockets was given by [19, 20]. By combining the results it was found that the extremal orbits of the electron pockets shrink linearly when reducing x. This is accompanied by a strong enhancement of the effective mass on the electron orbits (see Fig. 4.7b) when entering the superconducting state and approaching optimal doping [19]. This enhancement is on one side in agreement with the localization expected for the increased iron-pnictogen bond length [7], on the other hand it does not follow a linear dependency in x, but rather seems to diverge towards $x = 0.3$ [19].

For $x < 0.3$ the anti-ferromagnetic ground state causes a doubling of the unit cell and hence a reconstruction of the Fermi surface. This reconstructed Fermi surface has been observed for $BaFe_2As_2$ [22], by Shubnikov-de Haas (SdH) measurements, shown in Fig. 4.6.

In the case of perfect nesting the reconstruction would lead to the formation of a gap at the Fermi level and hence an insulator. Due to imperfection of nesting the resulting Fermi surface contains small residual three-dimensional pockets. The observation of quantum oscillations originating from these pockets using SdH was only possible when applying uni-axial pressure to the system [22]. This is necessary as the orthorhombic distortion in this phase leads to the formation of domains and hence a reduction in mean free path to the domain size. By applying uni-axial stress in the [110] direction a single domain can be achieved [23].

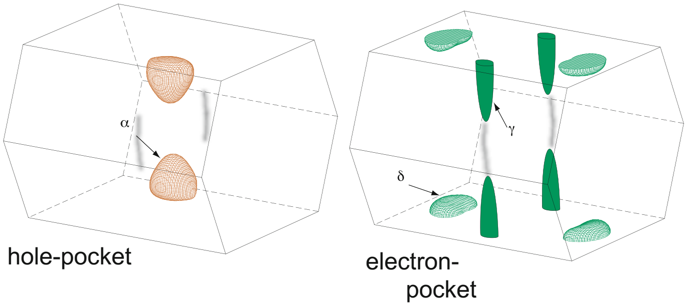

Fig. 4.6 Reconstructed Fermi surface of $BaFe_2As_2$ as observed by SdH in Ref. [22]

4.1.3 *Quantum Critical Point*

Like in the cuprates or some heavy fermion compounds superconductivity in the iron-pnictides appears in close proximity to an antiferromagnetic ordered state. As the anti-ferromagnetic order is suppressed in $BaFe_2(As_{1-x}P_x)_2$ by chemical pressure, one would expect to find a QCP at $x = 0.3$. Instead a new phase, superconductivity, emerges. As discussed in Sect. 2.8, we are limited to the finite temperature range to look for evidence to the quantum critical behaviour. One is the linear resistivity in temperature as observed by Kasahara et al. [1]. A v-shaped non-Fermi liquid regime is found, see Fig. 4.7b, which resembles that predicted by a limited life-time of thermal excitations as described in Sect. 2.8 and illustrated in Fig. 4.7a.

Measurements of the nuclear magnetic resonance (NMR) were performed on $BaFe_2(As_{1-x}P_x)_2$ with various P concentrations [24]. In their experiment Nakai and coworkers measured the Knight shift K and spin-lattice relaxation rate $1/TT_1$. They found that at high temperature K is almost independent of temperature and concluded from this that the density of states is almost constant as a function of temperature. Further they compared their results of T_1 with the so called Korringa relation TT_1K^2 = const. The Korringa relation should hold for all metals in the Fermi liquid regime. Nakai et al. [24] found that this is the case for samples $x = 0.64$ but can not be used at optimal doping where a Curie-Weiss behaviour is found. The Curie-Weiss temperature θ, shown in Fig. 4.7c, is then extracted. θ crosses zero around $x = 0.33$ which shows that the dynamical susceptibility diverges, in the zero temperature limit at this composition [24]. As this divergence happens simultaneously to the increase in the superconducting critical temperature and the former observation of the effective mass [19, 24] Nakai et al. [24] suggested that the observed enhancement of the quasi-particle mass might be caused by enhanced AFM fluctuations.

While in most cases the normal state quasi-particles are probed to investigate any non-Fermi liquid like behaviour it is also possible to measure superconducting properties such as the London-penetration depth, which is linked to the quasi-particle mass via Eq. 2.47 in the case where the superconducting carrier density is constant. This experiment has been carried out using different probes to determine the London

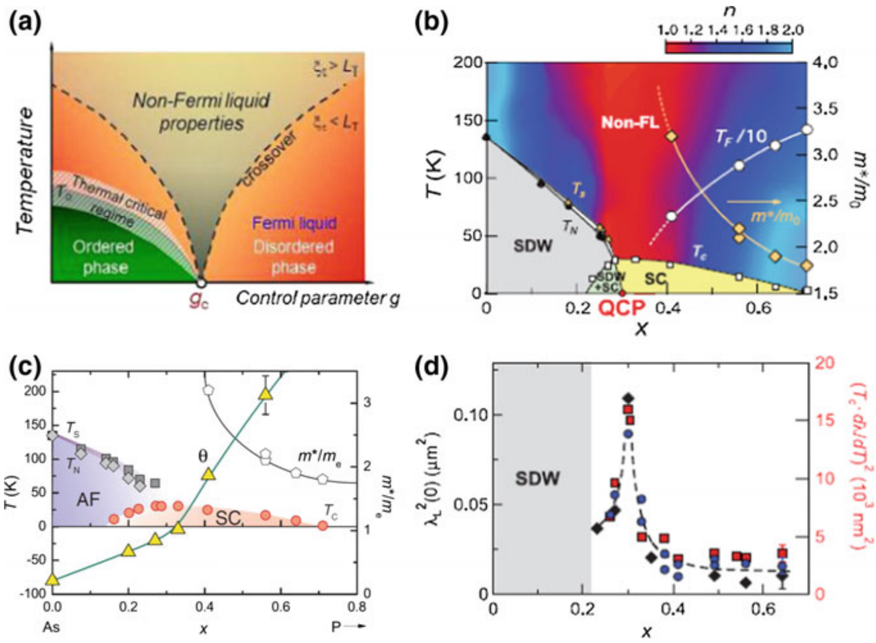

Fig. 4.7 Panel (**a**) shows a general phase diagram near a quantum critical point. A non-thermal control parameter g tunes the ordered phase to a disordered phase [25]. Panel (**b**) shows previous data taken on the normal state properties of $BaFe_2(As_{1-x}P_x)_2$. A linear dependence in resistivity is observedabove the superconducting dome around $x = 0.3$. Also the previously reported results on the effective mass are shown, pointing to a divergence in the effective mass at the QCP. In panel (**c**) data on the Curie-Weiss temperature obtained by NMR is shown [24]. The crossing of the Curie-Weiss temperature around $x = 0.3$ indicates a divergent behaviour of the susceptibility. Panel (**d**) presents data on the London penetration depth. A strong peak at the QCP is observed by different techniques. Panel (**b**) and (**c**) are taken form Ref. [14]

penetration depth λ_L [14]. They discovered a strong peak in λ_L^2 in the zero temperature limit. These measurements therefore suggested the existence of a QCP underneath the superconducting dome at $x = 0.3$, directly influencing the superconducting properties in the $T = 0$ limit.

4.2 Quasi-particle Mass Enhancement

The observation of a strong peak in λ_L [14] has motivated a further investigation of the effective mass by dHvA close to the quantum critical point of $BaFe_2(As_{1-x}P_x)_2$. One can see in Fig. 4.7d that a significant part of the enhancement is within 0.1 of $x_c = 0.3$. As most of the previous data was taken on samples with T_c up to 15 K the prediction of a diverging mass relied on the data point at $x = 0.4$ for the outer electron pocket. In order to improve our understanding of the evolution of the effective mass in $BaFe_2(As_{1-x}P_x)_2$ more than 40 samples were measured in static and pulsed magnetic fields up to 70 T using micro-cantilever. It was possible to observe quantum oscillation using the dHvA effect in samples with substitutions ranging from $x = 0.38$ to $x = 0.76$ (see Fig. 4.11), thereby adding significant detail to the evolution of the mass enhancement. Further oscillations originating from the the inner electron pockets were observed, which were strong enough to follow their mass evolution far into the superconducting dome. However as the signal from quantum oscillations is fading away when approaching the QCP due to an enhanced upper critical field H_{c2} and a shorter mean free path, we will start the discussion of the results on the phosphorous rich end and work our way towards the QCP.

4.2.1 On the Edge of Superconductivity

The superconducting critical temperature in $BaFe_2(As_{1-x}P_x)_2$ goes to zero temperature at $x = 0.71$ [1]. Therefore we have started our investigation just outside of this range where high quality single crystals are available. In Fig. 4.8 the oscillatory part of the torque signal from a crystal with $x = 0.76$ at $T = 0.5$ K in the field range of 18 to 42 T is shown. The data was taken at the NHMFL Tallahassee using a helium-3 cryostat inside the Hybrid magnet. A smooth background was subtracted from the data to account for the paramagnetic response of the sample. In the right panel of Fig. 4.8 the Fast Fourier Transformation (FFT) of the data in the range of 24 to 42 T is shown. Two dominant frequencies originating from the inner (α) and outer (β) electron pockets can be identified in the frequency spectrum by comparing the

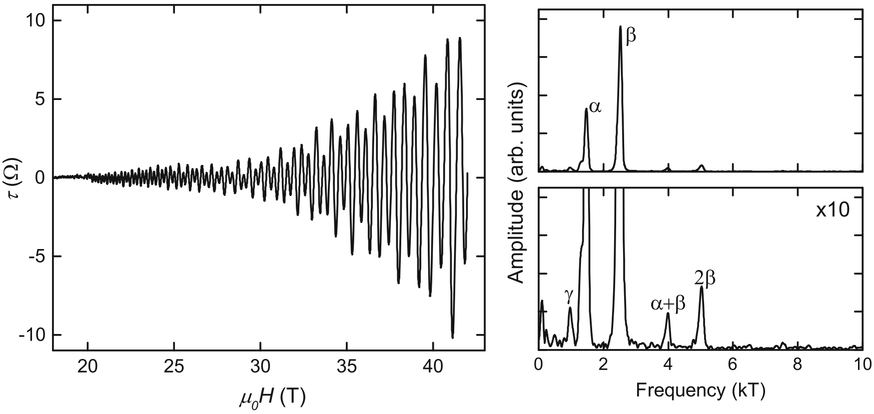

Fig. 4.8 Torque versus magnetic field for a sample of $BaFe_2(As_{1-x}P_x)_2$ with $x = 0.76$. The *left panel* shows the data after subtraction of a smooth background. The *right hand panels* show the FFT in the range of 24 to 42 T (*top*) and a zoomed view of the low peaks (*bottom*)

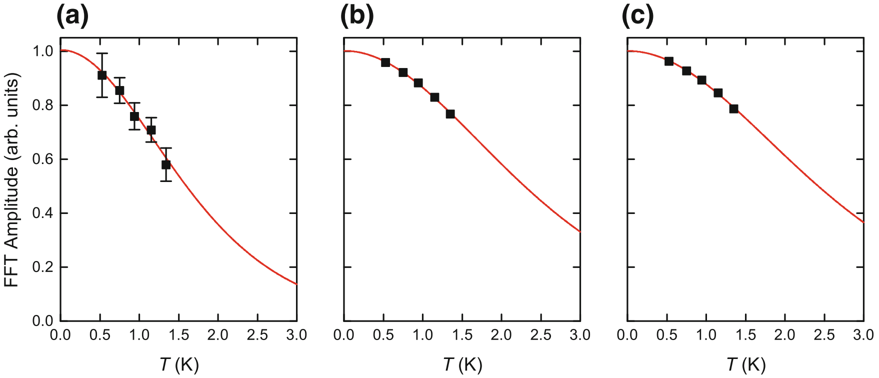

Fig. 4.9 Amplitude versus temperature for the γ-orbit (**a**), the α-orbit (**b**) and the β-orbit (**c**). Data was taken in a helium-3 cryostat at the NHMFL-Tallahassee. The FFTs were perform on a field window of 20 to 42 T after subtracting a smooth background. *Solid lines* are fits to of the temperature damping term R_T contained in the LK-formula

angular dependence of the frequency to that found in DFT calculations. By increasing the scale we find further peaks well above the noise level. The first, we believe, originates from the minimal orbit of the outer hole-pocket (γ), as it shows very similar angle dependence and frequency to γ_1 found in the end member $BaFe_2P_2$ [5]. The second peak is identified as torque interaction, explained earlier in Sect. 3.8.1, and the third represents the second harmonic of the most dominant frequency β. The amplitude of the first harmonics were measured at different temperatures. By fitting the temperature damping term R_T of the LK-formula (Eq. 2.27), as shown in Fig. 4.9, the effective masses of the individual Fermi surface sheets were extracted. We obtained $m_\gamma = (2.6 \pm 0.4) m_e$ for the outer hole pocket and $m_{\alpha,\beta} = (1.8 \pm 0.1) m_e$ for the electron sheets.. These values are comparable to those found for the end member $BaFe_2P_2$ [5]. The determination of the mean free path of each individual orbit proves to be difficult for systems with multiple frequencies. In order to disentangle the contributions from different extremal oscillation frequencies, we need to separate them by filtering in Fourier space. In Fig. 4.10 the outline of the procedure is shown, which shall now be discussed in more detail. Starting from the FFT of the oscillatory component in Fig. 4.10a the data is multiplied by a filter-function

$$F = \frac{1}{2}\left[\tanh\left(\frac{f - f_{min}}{s}\right) - \tanh\left(\frac{f - f_{max}}{s}\right)\right], \qquad (4.1)$$

with the lower and upper boundary of the filter f_{min} and f_{max} and the smoothing parameter s (shown in Fig. 4.10b dash-dotted line). The benefit of the chosen filter-window over a rectangular shape lays in the side-effects. These will affect the amplitude in a field range at the beginning and the end of the chosen window that is the smaller the larger the transition range from 1 to 0 in the filter-window is. The

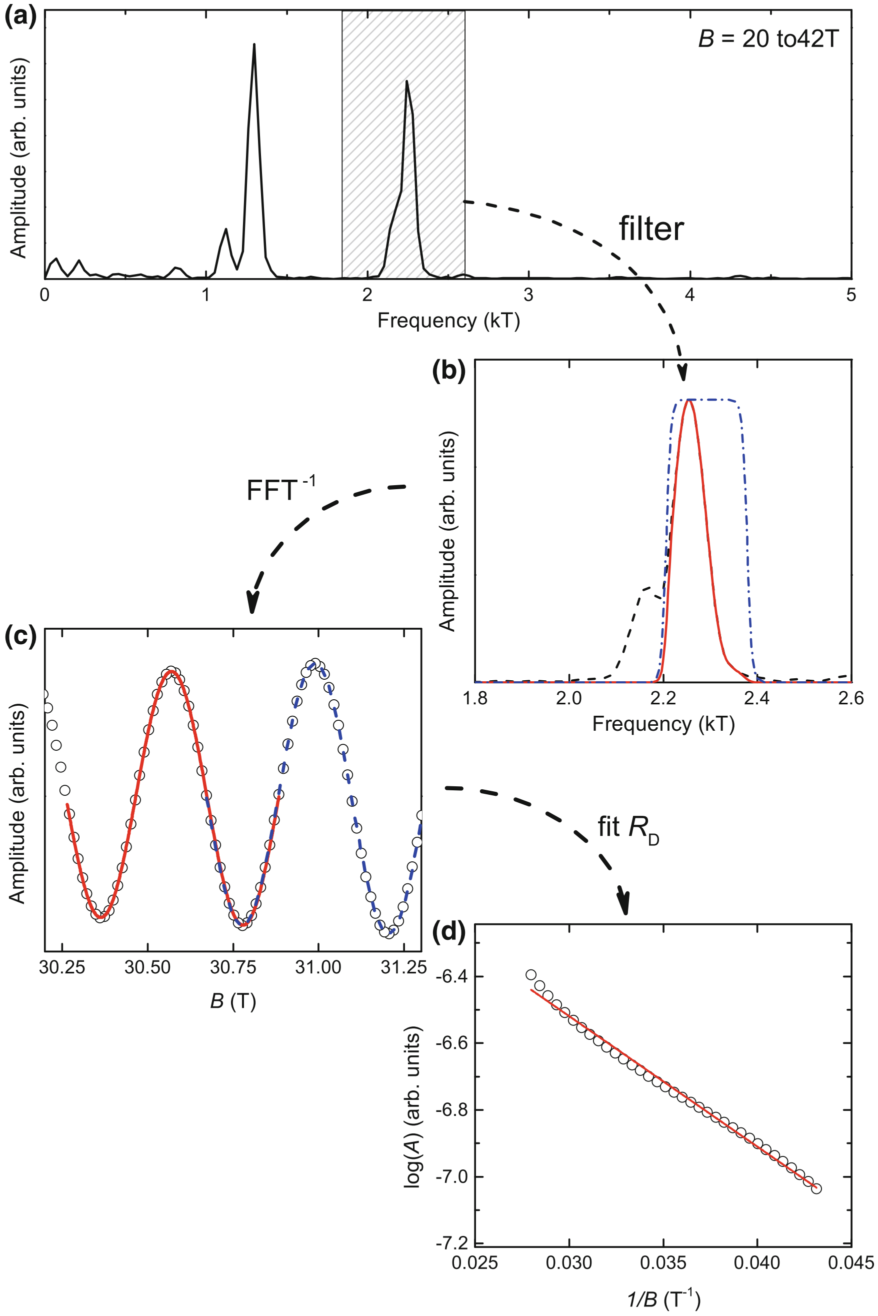

Fig. 4.10 Procedure used to determine Dingle-damping factor in LK formula from multi-frequency spectrum. **a** FFT taken on a sample with $x = 0.76$ at $T = 0.3$ K in the field range of 20 to 40 T. **b** FFT of unfiltered (*dashed*) and filtered data (*solid*). **c** Inverse FFT of the filtered data. The lines present fits to the LK formula. **d** Logarithm of the Amplitude obtained from fit in (**c**) versus inverse field. The *solid line* represents a linear fit to the data. See text for more details

folded data is then transferred using the inverse FFT. The result is shown in Fig. 4.10c together with fits of the LK-formula. Those fits are performed over typically 'one-and-a-half' periods and repeated in steps of one period, giving the result shown in Fig. 4.10d. Here it should be mentioned that data at low and high fields are left out as they are affected by the shape of the used filter window. As mentioned the amount of field unaffected depends on the smoothing factor s. Plotting the data as the logarithm of the amplitude versus the inverse field represents the data best in accordance to the dingle-damping term (Eq. 2.29). The increase in oscillation amplitude in field can now be evaluated by a linear fit to the data. Using this procedure rather than fitting an exponential term to the amplitude versus field has the advantage that the result is less influenced by remaining beats in the signal due to closely spaced frequencies. The slope α of the linear fit is related to the mean free path of the extremal orbit

$$l = \frac{1140\sqrt{F}}{\alpha}. \tag{4.2}$$

We obtain $l_\alpha = 66.5\,\text{nm}$, $l_\beta = 55.7\,\text{nm}$ and $l_\gamma = 27.4\,\text{nm}$. Compared to the mean free paths observed in Ref. [5] those values are significantly reduced. This is consistent with the observation of Shishido et al. [19] where a similar reduction was observed with reduced x. While the mean free path is mainly a measure of sample quality, the observation of a reduction in the mean free path upon approaching the highest T_c in a variety of samples suggests an intrinsic property of the system. For substitution from $x = 1$ to $x = 0.5$ this is expected as the statistical distribution of arsenic and phosphor atoms will have similar effect as impurities. For $x < 0.5$ the close proximity to the magnetically order, orthorhombic state can cause a strong fluctuation between the reconstructed and non reconstructed Fermi surface in parts of the sample, which leads to a frequency distribution and will hence be seen as low mean free path. In the case of a strong increase of the oscillation amplitude in magnetic field due to a short mean free path and a wide field window used for the FFT, the result of the effective mass can be influenced by the Dingle term. In order to rule this out the obtained parameter are used to simulate the result and check for self consistency. In the present case no significant deviations were found, but we will come back to this and have a look at an alternative procedure when discussing LiFeAs.

4.2.2 Electron Pockets Inside the Superconducting Dome

We will now turn to the data obtained on superconducting samples (see Fig. 4.11). Following the same procedure as previously we have determined the effective mass and mean free path of the samples. We were able to observe quantum oscillations originating from the outer electron pocket for samples with $x = 0.38$ to $x = 0.65$. The data of amplitude versus temperature and corresponding fits of the LK-formula are shown in Fig. 4.12. Frequency dependences on applied field direction of the β-orbits were determined for all samples around $B \parallel c$ from the angular dependence

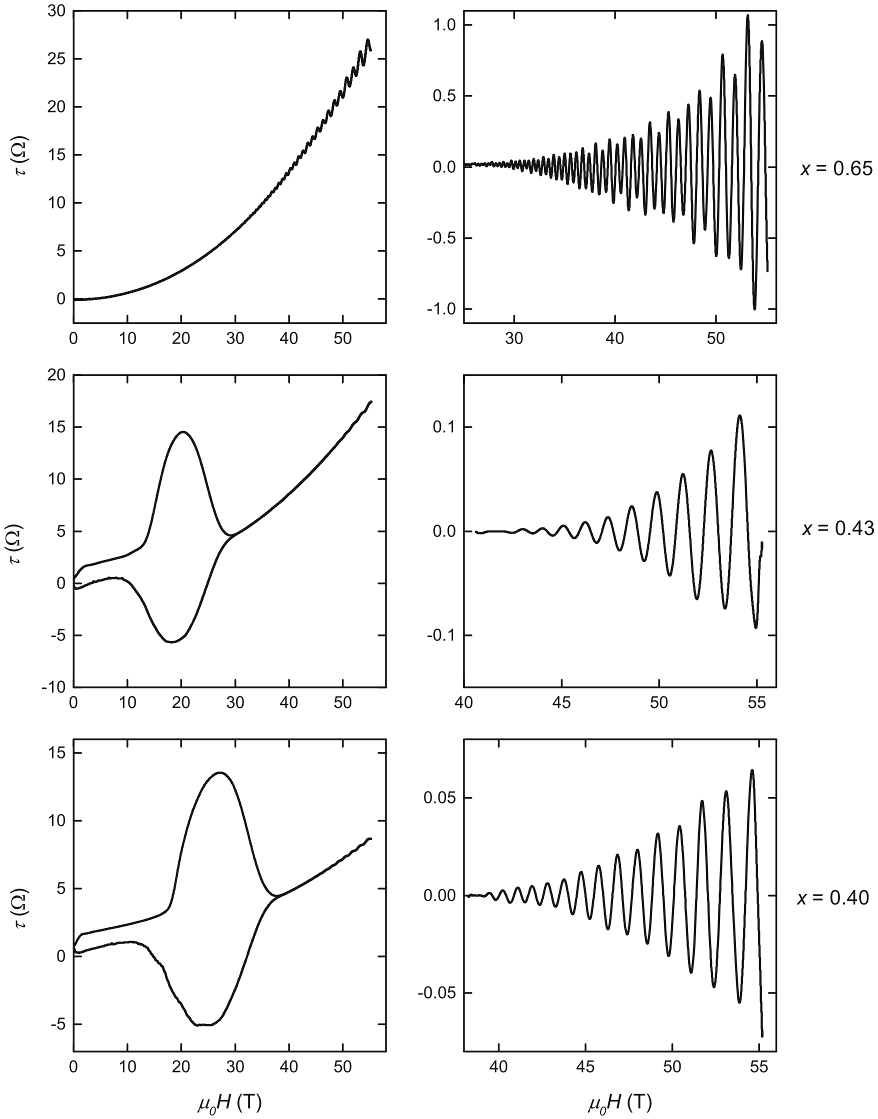

Fig. 4.11 Torque signal for different compositions of $BaFe_2(As_{1-x}P_x)_2$ with superconducting ground state. The *left panels* show the raw data obtained in pulsed magnetic field at the LNCMI-Toulouse. A smooth background has been removed to obtain the oscillatory part of the signal shown in the *right panels*. The relevant phosphor concentration x has been indicated for each row

of the oscillation frequency. From this the minimum frequency F_0^β was extracted by a polynomial fit. The linear decrease of pocket size, found in Ref. [19], was then used to determined the sample composition. Also the superconducting transition temperature

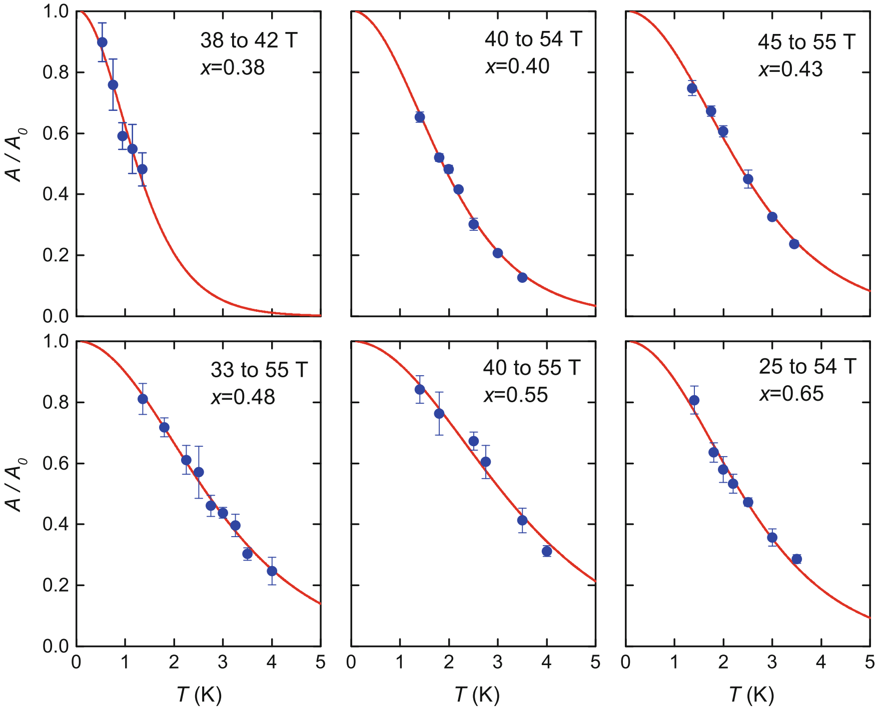

Fig. 4.12 Temperature dependence of the FFT amplitude of the dHvA signal for the β orbits in several $BaFe_2(As_{1-x}P_x)_2$ samples with different x. The *lines* are fits to the temperature dependent part of the LK formula. The respective x and field range used are indicated in the plots

was measured using a tunnel-diode oscillator. This was used to check the composition values x by comparison to previous reports [1]. The obtained transitions for 2 samples with $x = 0.65$ and 0.40 are shown in Fig. 4.13.

As T_c rises in these materials so does the upper critical field H_{c2}. For $x = 0.3$, which shows the highest superconducting transition temperature $T_c = 30$ K, we estimated H_{c2} by determining the irreversibility field (see Sect. 4.3 for more information) to be 50 T. As these fields can currently only be reached by using pulsed magnetic field, the major part of this study has been carried out at the LNCMI-Toulouse. During the fast increase in magnetic field the sample can experience heating due to eddy currents induced by the large dB/dt. In order to rule out any systematic error in the presented data, the sample with the highest mass determined in pulsed field ($x = 0.4$) was remeasured at the NHMFL Tallahassee using the hybrid magnet up to 42 T. The masses obtained in static and pulsed magnetic fields were in good agreement. As all other samples were of similar shape and size we can therefore rule out any effect of eddy current heating on the obtained results.

In Fig. 4.14a the results for the outer electron pocket, β-orbit, are shown as enhancement over the bare electron mass. The data is superimposed on the

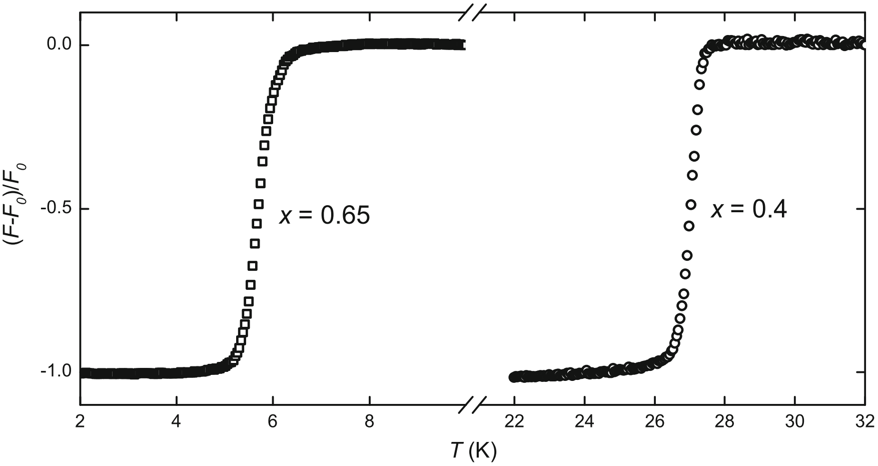

Fig. 4.13 Superconducting transition for samples with x = 0.65 and x = 0.4. A tunnel diode oscillator was used. The shift of resonance frequency in the tank circuit is plotted vs temperature

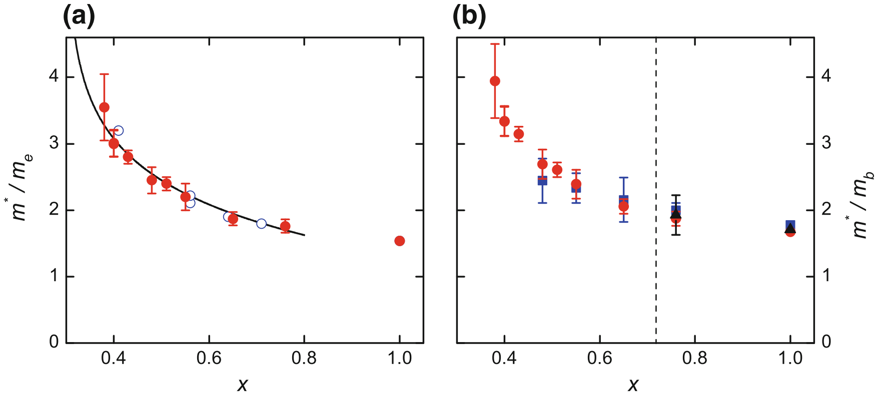

Fig. 4.14 Panel (**a**) shows the dependence of the measured quasiparticle mass from dHvA on x for the β orbits. The data obtained in the present study (*solid dots*) is in good agreement with previous reports [19] (*open circles*). In panel (**b**) the renormalization of the measures quasiparticle mass over the bandmass is plotted for β orbit (*solid dots*), α orbit (*solid squares*) and γ orbit (*triangles*). The *dashed line* marks the edge of the superconducting dome [1]. Data at x = 1 in this figure was taken from Ref. [5]

previous results of Shishido et al. [19], which shows good agreement. The solid line presents a fit to the data using $y = 1 - a\ln(x - x_c)$ as expected for the effective mass close to a QCP [26]. We have fixed the critical composition $x_c = 0.3$, which was found in London penetration depth [14]. The factor $a = 0.91$ represents a measure of the critical exponent. As we do not have data close enough to the quantum critical point an exact determination is not possible. The agreement of the data with the fit shows that the effective mass does follow the expectations for a quantum critical point and hence supports this scenario.

4.2.2.1 Comparison to DFT

Bandstructure calculations have been performed using the WIEN2K package [17]. The observed shift in frequency as a function of x for the β and α orbits are not reproduced in band structure calculations as pointed out by Shishido et al. [19]. As rigid band shifts are required to bring the DFT calculation into agreement with experimental results, we decided to use the same band structure calculation as starting point for these rigid band shifts. This is further justified, as the evolution of the electron pockets in DFT (see Ref. [19]) is rather smooth. A significant change in the band structure predicted by DFT happens on the hole pockets where a third hole pocket is found in calculations for $x = 0.3$. Since the only composition at which a hole pocket is observed in this study is $x = 0.76$ we used the lattice parameter of this compound $a = b = 3.8693$ Å and $c = 12.5691$ Å and the pnictogen height of $h_{pn} =$ 1.2489 Å for the DFT calculations. The space group *I4/mmm* of $BaFe_2P_2$ was used as the crystals possess body-centred tetragonal crystal structure.

In order to perform the rigid band shifts the first step was to calculate the dependence of dHvA frequencies of energy shifts $F(E_F - \Delta E)$ to obtain the necessary shift $\Delta E(x)$. Second the band masses and density of states (DOS) for the individual pockets were calculated. Results are presented in Tables 4.1, 4.2 and 4.3. The enhancement of the individual orbits over the band mass are plotted in Fig. 4.14b, also including data from Ref. [5] for $x = 1$. The dashed line marks the onset of superconductivity as determined in Ref. [1]. One can clearly see the an enhancement upon entering the superconducting dome for the β-orbit. We were able to trace the mass evolution of the inner electron pocket inside the superconducting dome as well. This, within error bars, shows the same behaviour as that of the outer electron pockets.

Table 4.1 Parameter obtained by experiment and band structure calculation of $BaFe_2(As_{1-x}P_x)_2$ for the extremal orbit γ on the outer hole pocket. m_b and γ_b are taken from brandstructure calculations all other values are obtained from experiment

Name	x	F_0	ΔE	m_b	m^*	λ	γ_b	γ
Arnold [5]	1.00	812	62	–1.35	2.3	0.70	0.885	1.51
No38	0.76	750	67	1.35	2.6	0.93	–0.885	1.70
Analytis [20]	0.63	450	–92	1.34	4.5	2.36	0.767	2.58
		T	meV	m_e	m_e		mJ $K^{-2}mol^{-1}$	mJ $K^{-2}mol^{-1}$

Table 4.2 Parameter obtained by experiment and band structure calculation of $BaFe_2(As_{1-x}P_x)_2$ for the extremal orbit α on the inner electron pocket. m_b and γ_b are taken from brandstructure calculations all other values are obtained from experiment

Name	x	F_0	ΔE	m_b	m^*	λ	γ_b	γ
Arnold [5]	1.00	1169	–57	0.9	1.6	0.78	0.87	1.54
No38	0.76	1000	–77	0.9	1.8	1.00	0.84	1.67
No33	0.65	1043	–71	0.9	1.94	1.16	0.85	1.83
Analytis [20]	0.63	1060	–70	1.0	2.3	1.23	0.85	1.90
No7	0.55	860	–93	0.9	2.1	1.33	0.83	1.93
No1	0.48	840	–96	0.9	2.2	1.44	0.82	2.01
		T	meV	m_e	m_e		$mJ\ K^{-2}mol^{-1}$	$mJ\ K^{-2}mol^{-1}$

Table 4.3 Parameter obtained by experiment and band structure calculation of $BaFe_2(As_{1-x}P_x)_2$ for the extremal orbit β on the outer electron pocket. m_b and γ_b are taken from brandstructure calculations all other values are obtained from experiment

Name	x	F_0	ΔE	m_b	m^*	λ	γ_b	γ
Arnold [5]	1.00	2277	–20	0.92	1.54	0.67	0.91	1.52
No38	0.76	2000	–50	0.94	1.8	0.87	0.89	1.66
No33	0.65	1869	–67	0.91	1.9	1.06	0.88	1.81
Analytis [20]	0.63	1800	–75	0.96	2.1	1.19	0.87	1.91
No7	0.55	1758	–80	0.92	2.2	1.39	0.87	2.08
No25	0.51	1712	–86	0.92	2.4	1.61	0.87	2.26
No1	0.48	1677	–91	0.91	2.5	1.69	0.86	2.33
No23	0.43	1619	–98	0.89	2.8	2.15	0.86	2.71
No27	0.40	1585	–102	0.90	3.0	2.33	0.86	2.87
No34	0.40	1780	–102	0.90	3.0	2.33	0.86	2.87
Talla	0.38	1562	–105	0.90	3.6	2.95	0.86	3.40
		T	meV	m_e	m_e		$mJ\ K^{-2}mol^{-1}$	$mJ\ K^{-2}mol^{-1}$

4.2.3 Evolution of Fermi Surface Topology

As mentioned above the composition of the measured samples was determined by the minimal frequency F_0^{β} of the beta orbits, using the linear dependency found in Ref. [19]. The good linear dependency shown in Fig. 4.16 is hence a result of this procedure. In addition to the dHvA frequencies found in bulk measurements (solid symbols) the results from ARPES measurements in $x = 0.38$ [27], see Fig. 4.15, are shown (open symbols). We find the frequencies extracted from the extremal orbits of the electron pockets in good agreement with the fits to the dHvA data, shown as dashed lines. Here we make the assumption that the obtained hole pocket topologies in Ref. [27] is be in similarly good agreement with the *bulk* Fermi surface. However we should point out that the hole pocket mean-free path was more affected

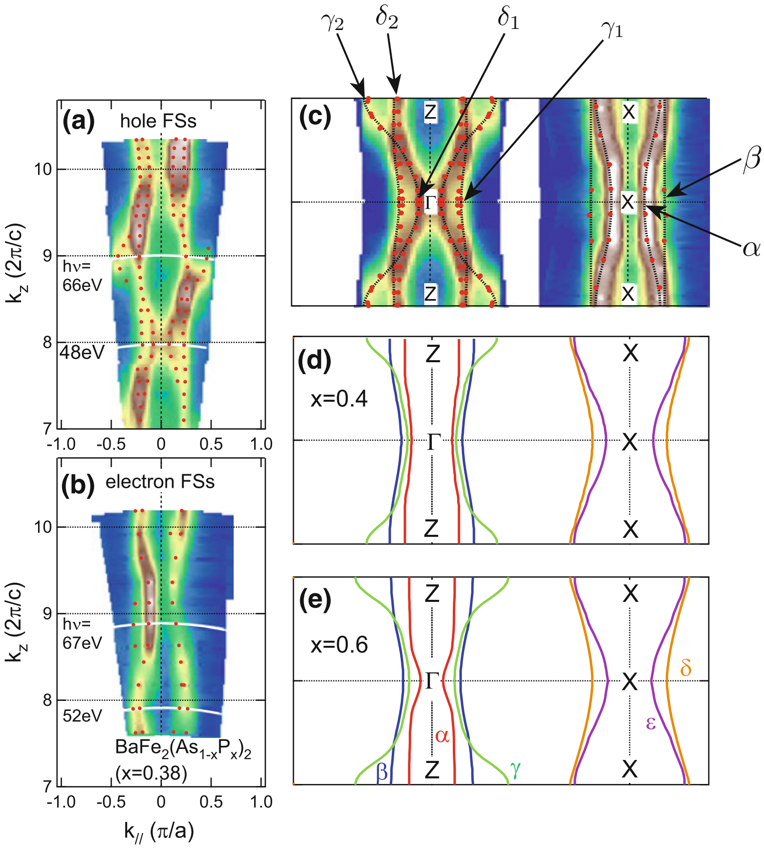

Fig. 4.15 ARPES data obtained by Yoshida et al. [27]

by substitution, which suggests that the hole pockets are more susceptible to small changes in the lattice potential. We use this data in combination with dHvA by Analytis et al. [20] and Arnold et al. [5] to investigate the evolution of the Fermi surface topology.

While DFT calculation shown in Fig. 4.15d, e predict three hole pockets for $x = 0.4$ and $x = 0.6$ the data shown in Fig. 4.15a, c only allows for the identification of two of those bands. The extremal orbit areas, given in Ref. [27], were transferred to the expected frequencies using the Onsager relation (Eq. 2.22). For clarity the identified orbits where labelled in Fig. 4.15c according to the labelling found in Ref. [5] and is also used in this work. We will in the following focus on the orbits that have previously been observed in *bulk* dHvA measurements as we can only predict a trend for those.

In Fig. 4.16a the interpretation of Fermi surface evolution as found in Ref. [5, 20, 28] is shown. In those reports the authors state that the Fermi surface experiences an

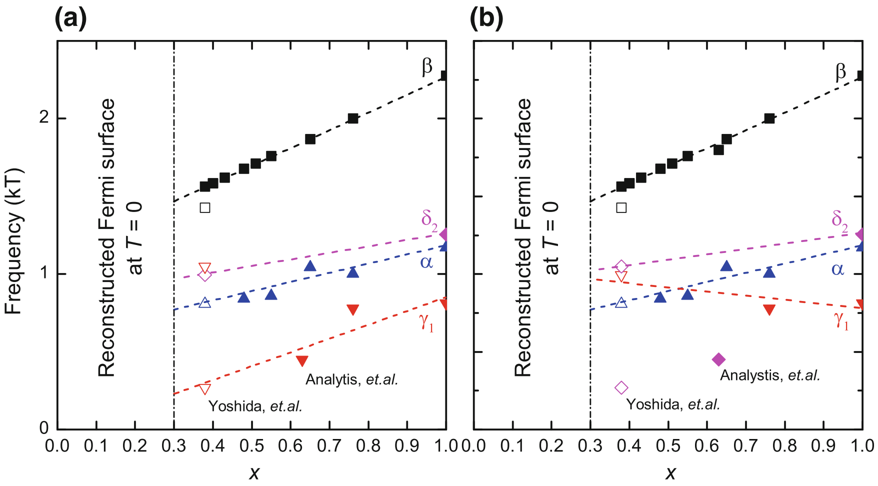

Fig. 4.16 dHvA frequency versus x for β orbits (*squares*), α orbits (*triangles top*) and γ orbits (*triangles bottom*). Open symbols are taken from data taken by Yoshida et al. [27] using ARPES and data at $x = 0.63$ was taken by Analytis et al. [20] and Arnold et al. [5] for $x = 1.0$ using dHvA. Panel (**a**) shows the identified orbits as found in Ref. [20, 28] while panel (**b**) contains the interpretation of the change in extremal orbits present in this work. *Dashed lines* are fits to the data selected according to the respective interpretation. The inner hole pockets which could not be observed in this work are shown as *diamonds*

overall shrinkage with reducing x. In contrast our interpretation of the data suggests a different scenario for the Fermi surface evolution with x shown in Fig. 4.16b. Instead of a monotonic decrease of the outer hole pocket the extremal orbit γ_1 stays almost constant while the large orbit γ_2, not shown in the figure, at $k_z = 2\pi/c$ reduces in size from $F_0^{\gamma_2} \approx 7000\,\mathrm{T}$ at $x = 1$ [5] to $F_0^{\gamma_2} \approx 4390\,\mathrm{T}$ at $x = 0.38$ [27]. While this still represents a significant k_z dispersion, the reduction in extremal orbit size by almost 40 % shows the trend towards a quasi two dimensional Fermi surface topology as argued in the introduction. The decrease in k_z dispersion is accompanied by a loss in d_{z^2} orbital character which was suggested to be beneficial for a SDW mediated superconducting pairing scenario [18].

A further consequence of this scenario is that the observed orbit γ in Ref. [20] does not originate from the outer but rather from the inner hole pocket. In the current model we would suggest to assign this orbit to δ_1, which was missing in the study of the end member $BaFe_2P_2$ [5]. We believe that the trend towards more cylindrical Fermi surface sheets would cause this orbit to show a similar angle dependence of the frequency as observed for γ_1 at $x = 1$. As the measured composition of $x = 0.63$ in Ref. [20] is close to the point where the interpolation in Fig. 4.16b suggests the bands α and γ_1 to have similar F_0, the assigned orbit α might therefore contain contributions from different orbits.

The small extremal orbit assigned to δ_1 in Fig. 4.15c seems to have a rather low value as compared to that found by Analytis et al. [20] and would therefore not be captured by our interpretation. However as the data in Ref. [27] is taken by a surface sensitive technique we need to point out that this could cause variations to the chemical potential. While the electron pockets, as we argued, are in good agreement, the bands most affected by such a change are those that are close to localization as it is the case for the δ_1 orbit. Therefore an underestimation of the orbital size of δ_1 can not be ruled out, which would bring it in good agreement with the proposed evolution of the Fermi surface topology.

4.2.4 Discussion

In summary quantum oscillations originating from the electron pockets in $\mathrm{BaFe_2(As_{1-x}P_x)_2}$ were measured over a large part of the phase diagram. By measuring multiple samples in the range of $x = 0.38$ to 0.76 a smooth upturn of the effective mass was observed. This upturn was fitted using the logarithmic divergence suggested in Ref. [26, 29] to describe the evolution of the effective mass close to a quantum critical point. However as we were not able to observe quantum oscillations close enough to the critical composition $x_c = 0.3$ we can only show a qualitative agreement with the proposed form while the extraction of the critical exponent was not possible.

The presented study of the mass enhancement was further refined by a study of the heat capacity [30]. In this study the jump of $C(T)$ at the superconducting transition temperature T_c was used to determine the Sommerfeld-coefficient γ. As γ depends on the density of states at the Fermi level the same way as the effective mass, we can use $\gamma/\gamma_b = m^*/m_b$. In Fig. 4.17 a comparison of the data from dHvA, heat capacity

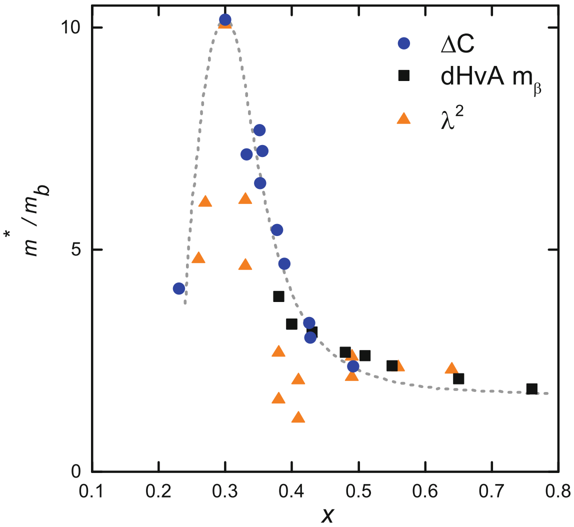

Fig. 4.17 Renormalization of the quasiparticle mass over the bandmass as derived from heat capacity [30], dHvA (presented in this work) and microwave magnetic penetration depth measurements [14]. The *dashed line* presents a quide to the eye

and penetration depth is shown. The band structure values for the enhancement of the heat capacity and penetration depth are based on the results found in this work. One can see that the two-fold enhancement measured by quantum oscillations is only the beginning of the divergent behaviour. The quantitative agreement between the different probes shows that the peak in the London penetration depth is caused by a strong increase in the normal state quasi particle mass. Here the assumption was made that all pockets contribute equally to the heat capacity data [30]. This is justified with the results obtained by dHvA for the electron pockets and also for the outer hole-pocket γ, where the renormalization was found to agree within errors. Further it should be mentioned that as dHvA measures the effective mass as an average of the observed extremal orbit and heat capacity measures the enhancement as sum over all Fermi surface sheets, one can not rule out *hot spots*, local parts of the Fermi surface with higher enhancements. This might be of importance taking into account that the gap-structure found to contain nodes [31]. From this argument the interaction potential in the expression for the gap in the BCS-theory (Eq. 2.59) will depend on k and hence the quasi-particle mass might depend on k.

Recent theoretical work based on a two-band model found that the best fit of the heat capacity data is obtained by including an additional term to the logarithmic divergence [32]. In their work the authors fitted the data using

$$\frac{\Delta C}{T_c} = \alpha + \beta \ln(x - x_c) + \gamma (x - x_c)^{-1}. \tag{4.3}$$

While the first two terms correspond to the form we used to fit the effective mass, showing a strong increase in the quasi particle mass due to quantum critical fluctuations, the third term incorporates the thermal fluctuations of the SDW order. The authors in Ref. [32] suggest from the resulting fit close to x_c that the SDW fluctuations become more important than the quantum fluctuation, which could explain the slight difference in the diverging behaviour between dHvA and heat capacity data shown in Fig. 4.17. However from the present data a small field dependence of the effective mass close to the QCP can not be ruled out to cause the difference in the obtained values of m^*/m_b using dHvA and heat capacity results. As data close to x_c is not available from dHvA experiments the precise determination of the contribution of the two functional forms is so far not possible. This was also pointed out by Analytis et al. [33], where resistivity measurements were performed to obtain the electronic behaviour close to the quantum critical point. They pointed out that for $x_c = 0.3$ their resulting coefficient β was in good agreement with the results presented here. However they found a somewhat lower value when using $x_c = 0.32$ which also held a good agreement with their obtained data. This shows that while we can confirm the trend of the quasi particle mass to be in good agreement with that predicted for a QCP the precise determination of the critical exponent, characterizing the phase transition, would require even more detailed studies.

By combining data of the extremal orbits on the Fermi surface obtained in this work with those found previously [5, 20, 27] we argued that the Fermi surface topology become better nested and less dispersive in k_z when approaching $x = 0.3$.

The presented data is in good agreement with the calculations by Yin et al. [7] presented in the introduction. When reducing x the overall size of the Fermi surface shrinks as best seen by the electron pockets, which leads to a higher localization as also seen by the divergence in the effective mass. This makes the system more susceptible to critical long-wave length fluctuation that can cause superconductivity but further lead to magnetic order. While the system even at $x = 0.3$ is not perfectly nested as shown in Fig. 4.16b, the trend towards nesting might help stabilise the anti-ferromagnetic order as proposed in Ref. [7].

4.3 Anomalous Behaviour of the Critical Fields

The work which will be presented in this section was motivated by previous results on the London penetration depth [14] and the quasiparticle mass enhancement [30] in $BaFe_2(As_{1-x}P_x)_2$. We will start by presenting the data obtained on the upper critical field, before we show and discuss data on the lower critical field.

4.3.1 Upper Critical Field H_{c2}

The upper critical field in single crystals of $BaFe_2(As_{1-x}P_x)_2$ was determined by two different techniques, heat capacity at T_c and torque magnetometry at low T. The upper critical field, for orbital limiting, is given in the Ginzburg-Landau theory as

$$H_{c2} = \frac{\phi_0}{2\pi\mu_0\xi_{GL}^2}. \tag{4.4}$$

The coherence length ξ_{GL} can typically be approximated with the BCS-value [34]

$$\xi = \frac{\hbar v_F}{\pi\Delta}, \tag{4.5}$$

which leads to the expression $H_{c2} \propto (m^*\Delta/k_F)^2$. As the variation of T_c close to x_c is rather small [1], as well as the change of k_F which we will assume to be roughly constant in this range, we see that the upper critical field H_{c2} should vary as m^{*2}.

The upper critical field $H_{c2}(T = 0)$ can be evaluated in different ways. First we have used data taken by P. Walmsley using heat capacity measurements at static field close to T_c (see Fig. 4.18). The obtained slope $\mathrm{d}H_{c2}/\mathrm{d}T$, shown in Fig. 4.19, can then be extrapolated to zero temperature using the Werthamer-Helfand-Hohenberg (WHH) relation [35]

$$H_{c2}(0) = -0.73\left(\frac{\mathrm{d}H_{c2}}{\mathrm{d}T}\right)_{T_c} T_c. \tag{4.6}$$

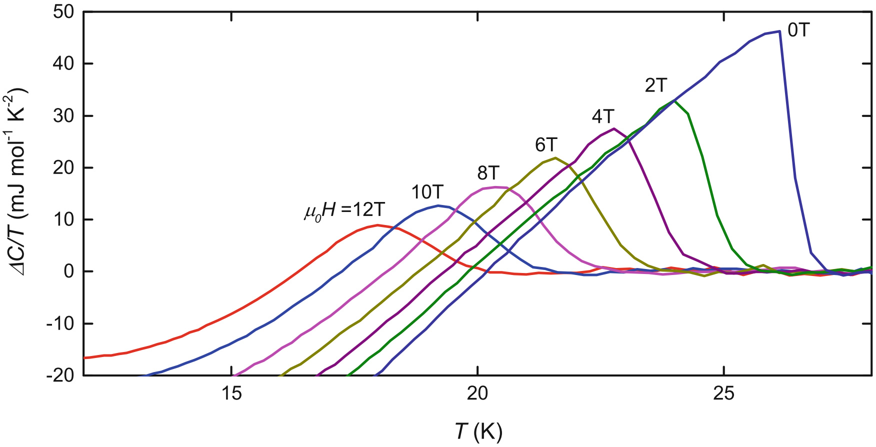

Fig. 4.18 Heat capacity $\Delta C/T$ as a function of temperature for a sample of BaFe$_2$(As$_{1-x}$P$_x$)$_2$ with $x = 0.35$. Temperature sweeps were performed at various constant magnetic fields. A smooth background has been subtracted to account for the phonon contribution to the specific heat. Courtesy of P. Walmsley

Fig. 4.19 Upper critical field of BaFe$_2$(As$_{1-x}$P$_x$)$_2$ as function of temperature normalized to T_c for different concentration x. The *solid lines* represent linear fits to the data. The data is based on heat capacity measurements taken by P. Walmsley

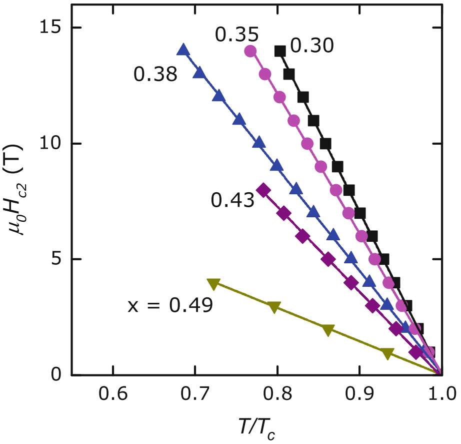

As the data obtained by this technique represent the critical field at $T = 0$ by extrapolation, is it desired to compare these values with data taken at low temperatures. For this we use torque magnetometry. Although using this technique we determine the irreversibility field H_{irr}, which does not directly correspond to H_{c2}, for systems with low anisotropy, as it is the case in BaFe$_2$(As$_{1-x}$P$_x$)$_2$ [36], it can be used as a good estimate. H_{irr} was determined from the data taking the difference of up and the down sweep as shown in Fig. 4.20. In the normal state the magnetization for a paramagnet gives the same result independent of dH/dt, while in the superconducting state a hysteresis opens. The onset of the hysteresis is identified as H_{irr}.

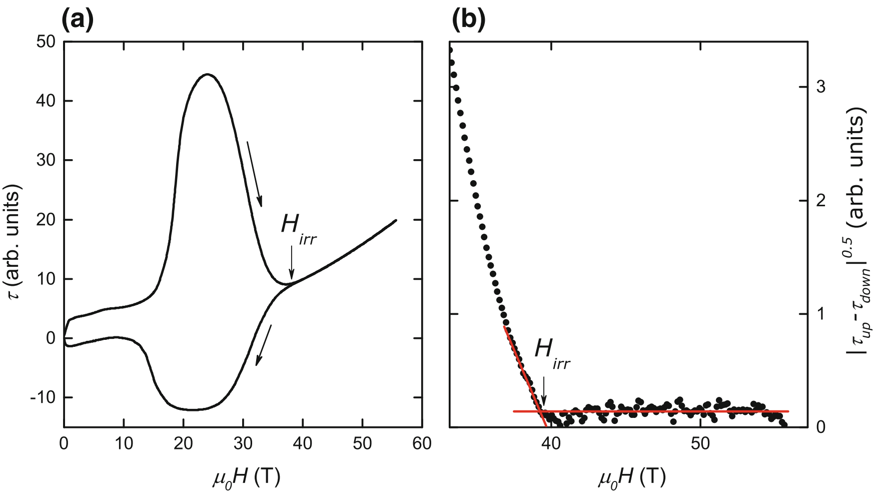

Fig. 4.20 Magnetic torque taken on a sample of $BaFe_2(As_{1-x}P_x)_2$ with $x = 0.4$ at $T = 1.5$ K. Panel **a** raw data taken in pulsed magnetic field up to 58 T at an angle of 14°. The sweep direction are indicated by *arrows*. Panel **b** difference between up and down sweep. The square root has been plotted as the signal starts to deviate smoothly. The determined irreversible field was indicated

For both experiments the field direction $H \parallel c$ was chosen. For selected samples the results of H_{c2} at T_c and the low temperature data are compared in Fig. 4.21. The extrapolation of the heat capacity data, using the WHH theory, is shown as dashed line, which is in good agreement with the torque magnetometry data at low temperatures. It should be mentioned that the measured samples in both cases where not identical. While the sample composition in the heat capacity study was determined by x-ray diffraction [30], the composition in torque magnetometry was determined by the observed frequency of the β-orbit, as discussed in the previous section. Also we have assumed the WHH theory in the dirty limit as we can not make direct statements of their mean free path. Samples of the torque magnetometry study were identical, down to $x = 0.38$, to those where quantum oscillations were observed. For these crystals we know that the superconducting coherence length ξ is not limited by the mean free path l and hence we could assume the clean limit which would increase the values obtained from WHH at $T = 0$ for even better agreement between values obtained from ΔC and τ.

The results for all measured compositions in the low temperature limit from heat capacity data and the torque magnetometry are combined in the inset in Fig. 4.22.

While so far we have only discussed the expression for H_{c2} in the frame work of GL theory this only accounts for orbital limiting effects while neglecting that the energy difference due to Zeeman splitting in field is unfavourable for the formation of singlet cooper pairs. The critical field that leads to the pair breaking due to the Zeeman effect is known as *Pauli-limiting field* H^p given by [37, 38]

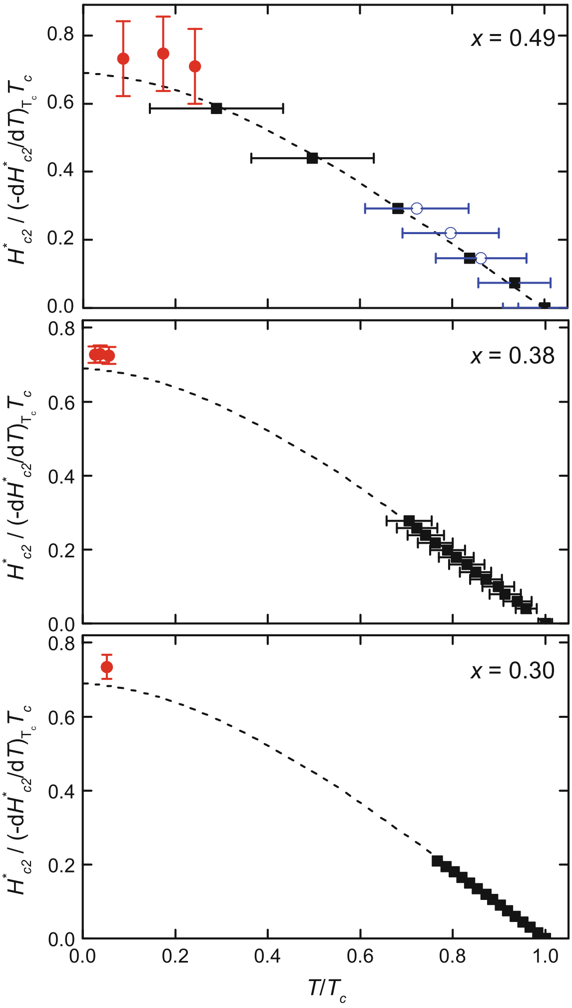

Fig. 4.21 Upper critical field H_{c2} of BaFe$_2$(As$_{1-x}$P$_x$)$_2$ as determined by heat capacity measurements (*squares*, *empty circles*) and from torque magnetometry (*solid circles*). The data is shown for different compositions $x = 0.5$, $x = 0.38$ and $x = 0.3$. As different samples were used the samples where matched by their superconducting critical temperature. The *dashed lines* are predicted behaviour by the Werthamer-Helfand-Hohenberg theory (WHH) [35]. Heat capacity measurements were taken by P. Walmsley and L. Malone

$$H^p_{c2}(0) = \chi^{-0.5}\Delta N(E_F), \tag{4.7}$$

with the normal state susceptibility χ, density of states at the Fermi level $N(E_F)$ and the superconducting gap Δ. Comparing the temperature dependence of the two pair breaking fields we find $H^p_{c2}(T) \propto \Delta(T)/\Delta(0)\chi^{-0.5}$ for the Pauli limiting field and $H^{orb}_{c2}(T) \propto (\Delta(T)/\Delta(0))^2 m^{*2}$ for the orbital limiting field as described in BCS theory. Therefore we see that for temperatures close to T_c $H^{orb}_{c2} < H^p_{c2}$. Only at low temperatures where Δ becomes approximately temperature independent both values can reach similar values. The dominating pair breaking mechanism at low temperatures then depends on the electron-phonon coupling which effects the effective mass m^* but not the susceptibility χ [39]. Since in our case $H_{c2}(0)$ as determined close

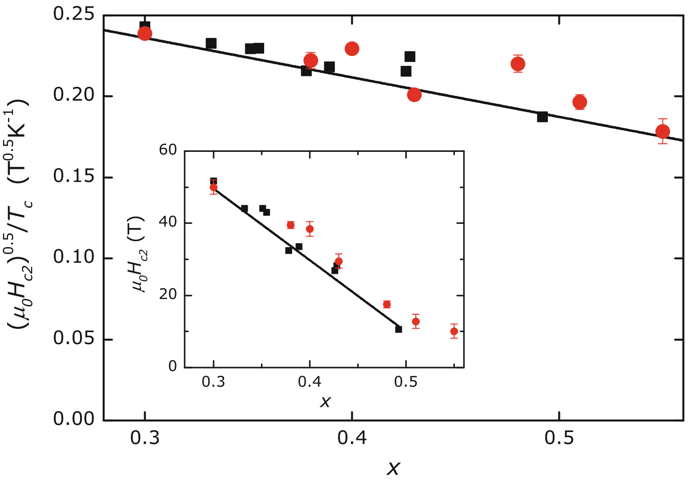

Fig. 4.22 Upper critical field H_{c2} of $BaFe_2(As_{1-x}P_x)_2$ as function of phosphorous concentration x. The *dots* show the data obtained by torque measurements while the square show the values of H_{c2} estimated from the heat capacity data close to T_c. The main panel shows $\sqrt{\mu_0 H_{c2}}/T_c$ which is expected to be proportional to m^* as described in the text

to T_c and at low temperatures show good agreement we can conclude that both are caused by the same mechanism letting us rule out a Pauli limiting mechanism at low temperatures that could cause a cut off of the critical divergence.

By plotting the data in the from $\sqrt{\mu_0 H_{c2}}/T_c$ we expect to find a behaviour that is proportional to the quasi particle mass enhancement as argued in the beginning. Instead we found a linear change over the main part of the superconducting region. From this we suggest that the change in the upper critical field is mainly explained by the increase in T_c rather than the dominant change in the quasi particle mass as can be seen in Fig. 4.23.

This being in contrast to the expectation by GL theory we want to point out that similar results were found in $CeRhIn_5$ [40] shown in Fig. 4.24. In this compound a QCP appears under pressure and a clear peak is observed in the effective mass at this point. The estimate of the effective mass from H_{c2} however shows a similar behaviour as found in the present study of $BaFe_2(As_{1-x}P_x)_2$. A possible explanation for the missing peak in H_{c2} could be given by a low mean free path that limits the upper critical field close to x_c, which we had already ruled out. Another scenario that could explain the observation, would be a field dependent effective mass. In the case that the strong divergence of the quasi particle mass would be suppressed in field we could expect an upper critical field H_{c2} that would not be affected by the QCP. However the mass enhancement by a factor 2 from $x = 0.7$ to 0.38, as studied by dHvA, as well as low temperature transport studies by Analytis et al. [33] were performed in fields well above H_{c2}, observing a similar enhancement in quasi particle mass. While the results in both experiments where slightly reduced from those in zero-field heat capacity studies, this difference can not account for the

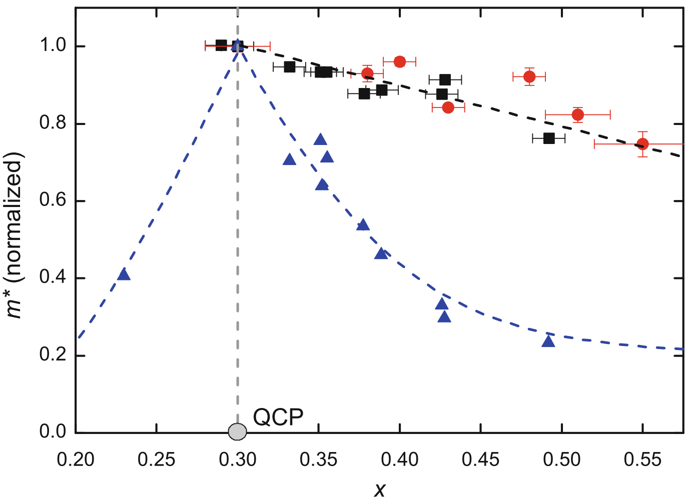

Fig. 4.23 The effective mass of $BaFe_2(As_{1-x}P_x)_2$ as function of x close to the QCP as derived from the upper critical field H_{c2} (*squares*, *circles*) and from the heat capacity measurements in Ref. [30]. The values were normalized to those found at x = 0.3 for better comparison

Fig. 4.24 The effective mass of $CeRhIn_5$ as derived from dHvA, H_{c2} and the A coefficient in transport. The conversions $m \propto \sqrt{H_{c2}}/T_c$ and $m \propto \sqrt{A}$ were used. The figure was taken from Ref. [40]

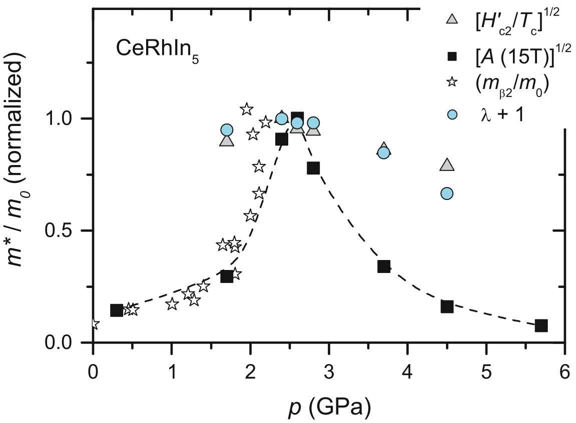

strong deviation from the expected values in H_{c2}. Also, we have determined H_{c2} close to T_c which should be directly affected disregarding a possible cut off at low temperatures and high magnetic fields. Last but not least the fact that we are here dealing with a multi-band system might cause additional complications. In the well understood multi-band system MgB_2 the upper critical field is entirely determined by the σ-band at $T = 0$, as the superconducting gap Δ is largest in this band. As shown above $H_{c2} \propto \Delta^2 m^2$, from which we conclude the possibility to construct a gap Δ which would cancel the divergence of m. However as Δ, according to BCS theory, depends on the density of states at the Fermi level and the interactions in

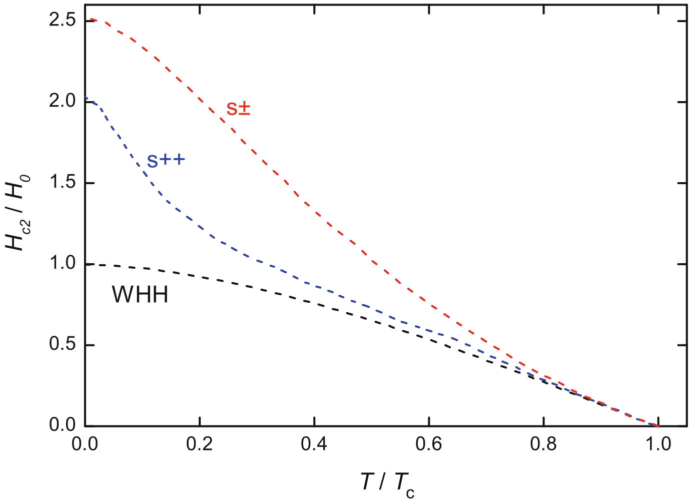

Fig. 4.25 Temperature dependence of the upper critical field H_{c2} in the single and multi band scenarios. The different models are scaled to posses the same slope dH_{c2}/dT at T_c. After Ref. [35, 41]

the system, as does m in the framework of Fermi liquid theory, this scenario is not possible.

We will further consider the possibility of multi band scenarios based on calculation by Gurevich [41]. The numerical results obtained for the temperature dependence in the $s++$ and $s\pm$ case are shown in Fig. 4.25. The results are normalized to posses the same slope dH_{c2}/dT at T_c. We find that the extrapolated values for $H_{c2}(0)$ deviate quite dramatically from each other. It was shown in Ref. [41], that in the case of a multi band scenario H_{c2} follows the expression

$$H_{c2}(T) \propto \frac{T_c(T_c - T)}{v_1^2 + v_2^2}. \tag{4.8}$$

From this one could argue that in the presence of a light band, with $v_1 \ll v_2$, which is not enhance, the expected peak in the upper critical field would be absent as H_{c2} is then dominated by v_2. However the strong peak in the London penetration depth [14], which probes light carriers, was found to be in good agreement with heavy quasi particles probed by specific heat [30], we can conclude that in the case of $\mathrm{BaFe_2(As_{1-x}P_x)_2}$ $v_1 \approx v_2$. Due to this argument the expression takes the form as that of a single band model. However as the model in Ref. [41] was based on 2 identical spherical Fermi surface sheets, a more sophisticated model including the quasi two-dimensional topology of the Fermi surface and anisotropy of v_F could change these predictions, but has so far not been done.

4.3.2 Lower Critical Field H_{c1}

The lower critical field of a type two superconductor is connected to the London penetration depth in the GL-theory by

$$\mu_0 H_{c1} = \frac{\phi_0}{4\pi\lambda^2} \ln\left(\kappa + \frac{1}{2}\right), \tag{4.9}$$

with the Ginzburg-Landau parameter $\kappa = \lambda/\xi_{GL}$ which is assumed to be large. The factor 1/2 is a correction term for the vortex core contribution that is neglected in the original derivation. In the high-temperature superconductors such as $BaFe_2(As_{1-x}P_x)_2$ we find $\kappa \approx 100$ [14] and hence the above formula should be valid. From the peak in the penetration depth [14] we would expect to find a dip in H_{c1} close to the quantum critical point.

We have determined the lower critical field using micro-hall arrays. Those allow us to determine the field of first flux penetration H_p at the center and at the edge of the sample simultaneously as illustrated in Fig. 4.26. This method is important as to rule out an overestimation of the lower critical field due to surface pinning or surface barrier effects. In the case where surface pinning can be neglected the vortices entering will move straight to the center of the sample and both sensors will detect a change in effective field in the sensor area at the same applied field.

Also we would expect a hysteresis upon entering and leaving the sample in the case of pinning. To check that this is not the case we have compared up and down sweeps of the applied magnetic field and determined the critical fields respectively. Figure 4.26 shows data taken on a sample with x = 0.38 and at T = 18 K. One

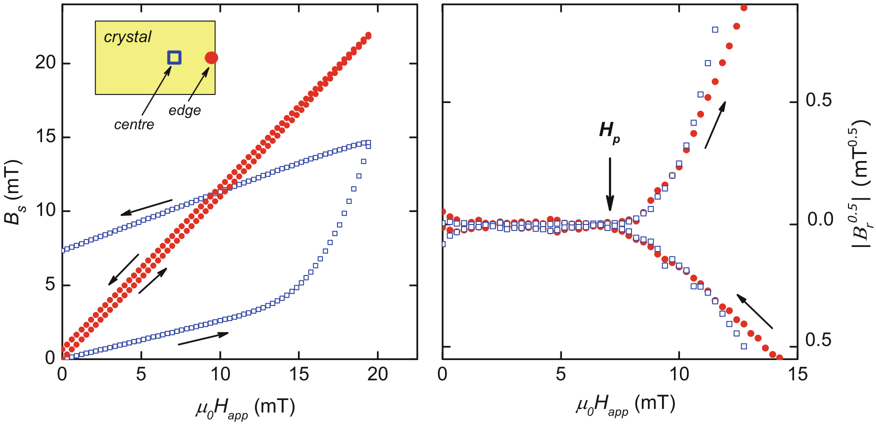

Fig. 4.26 Panel (**a**) shows the magnetic flux density measured by the micro Hall array versus the applied field H_{app} for $BaFe_2(As_{1-x}P_x)_2$ with x = 0.38 at T = 18 K. Different positions at the edge and the center of the crystal are shown (see schematic inset). In panel (**b**) the remanent field after subtraction of a linear fit to the low field data is plotted versus the applied field

can see that both criteria are fulfilled. Throughout the experiment we have used this method to check for contributions of surface pinning and have only considered samples were the above mentioned criteria were obeyed. By comparing the data taken for the lower critical field with data taken on the same sample using heat capacity, we found a correlation between the superconducting transition width and whether or not a sample fulfilled the criteria. A threshold of $\Delta T_c \leq 1$ K was found for the used samples. As measurements of heat capacity were less time consuming we then started by screening a variety of samples selecting those below the threshold for magnetisation measurements. Best results were found for samples where the edges of the sample were cleaved off. A typical transition found is shown in Fig. 4.27. The size of the heat capacity anomaly in $\Delta C/T_c$ was used as additional quality and consistency check, and was found to be in good agreement with previous measurements [30], as shown in Fig. 4.28.

The critical fields of the selected single crystals were determined from the fields of first flux penetration using the demagnetizing factor given by Brandt [42] (see Eq. 3.12). For a list of the used dimensions see Table 4.4.

At low temperatures we found a linear behaviour of H_{c1} in temperature as displayed in Fig. 4.29, which is a further indication of the absence of surface pinning in our systems. As pinning typically becomes enhanced at lower temperatures a strong upturn in H_{c1} would then be expected. This upturn, in the case of pinning, was observed for example in $YBa_2Cu_3O_{7-\delta}$ [43]. Using a linear fit to extrapolate the

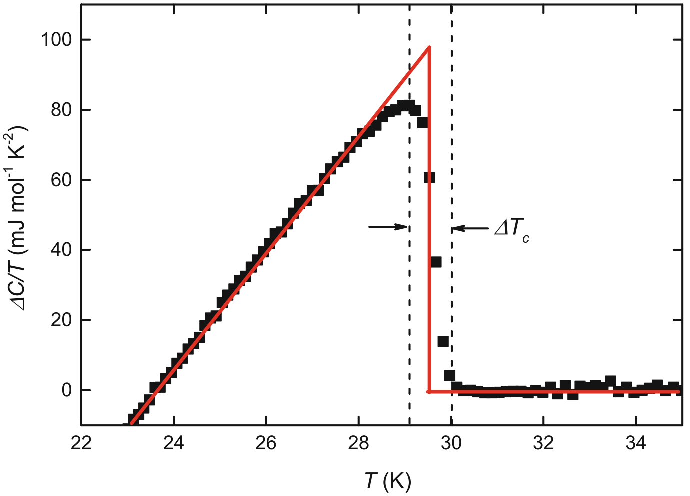

Fig. 4.27 Electronic specific heat for a $BaFe_2(As_{1-x}P_x)_2$ sample with $x = 0.3$. Contributions from phonons have been removed by a fit to the data. The determination of the transition width ΔT_c is illustrated by *dashed lines*. The *solid line* represents a construction of the ideal case, used to obtain the size of the discontinuity $\Delta C/T_c$. The onset of the superconducting transition coincides with the values reported previously by Kasahara et al. [1]

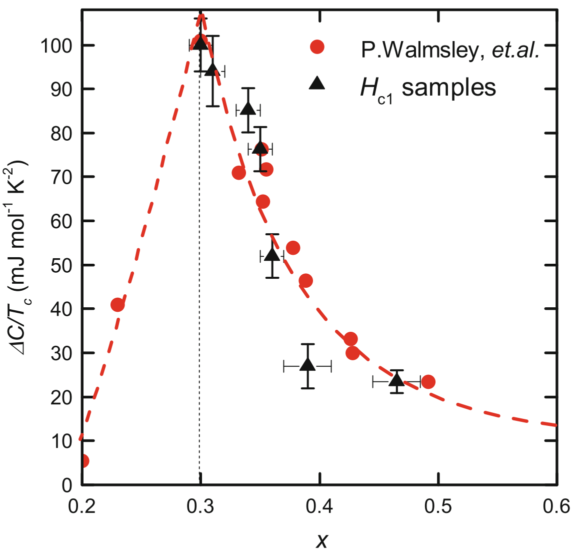

Fig. 4.28 Measurements of the jump in heat capacity $\Delta C/T_c$ at the superconducting critical temperature T_c (*triangles*). The obtained data is in good agreement with previous results reported in Ref. [30] (*circles*)

Table 4.4 List of sample dimensions for study of lower critical field in BaFe$_2$(As$_{1-x}$P$_x$)$_2$

Sample	x	Δx	l_c (μm)	l_a (μm)
C19	0.29	0.01	11	149
C24a	0.30	0.01	27	360
C24b	0.30	0.01	18	360
C24c	0.30	0.01	18	170
C2a	0.31	0.01	28	300
C21	0.34	0.01	20	255
0p3B	0.35	0.01	48	115
C1	0.36	0.01	35	269
C7a	0.39	0.02	17	260
C9	0.47	0.02	40	300
0p6a	0.55	0.02	48	240

data we obtain the zero-temperature lower critical field $H_{c1}(0)$. The extracted values are shown in Fig. 4.30.

Surprisingly, instead of a dip at the critical composition $x_c = 0.3$ we find a strong peak in strong contrast to the prediction based on the penetration depth values [14]. As this violates the expectation from GL-theory we need to take a step back to compare the two results. The expression for H_{c1} is obtained by comparing the Gibbs-free energy of vortex inside and outside the sample. The lower critical field is identified

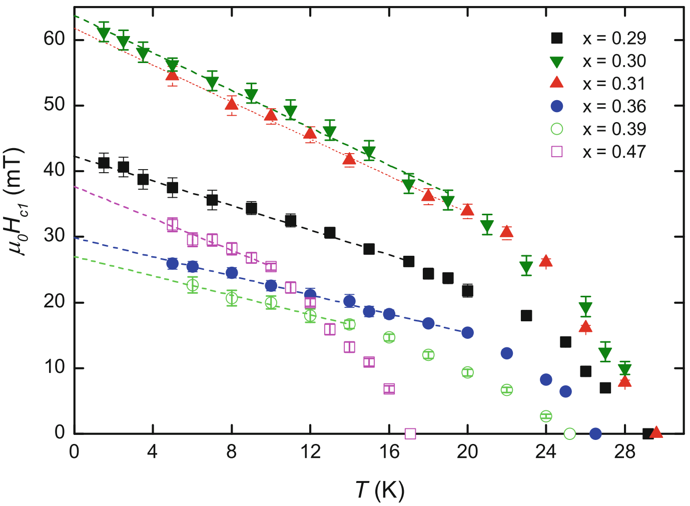

Fig. 4.29 Temperature dependence of the lower critical field H_{c1} for $BaFe_2(As_{1-x}P_x)_2$ samples with different x indicated in the legend. The *dashed lines* are fits to the linear part at low temperature to extract $H_{c1}(T = 0)$

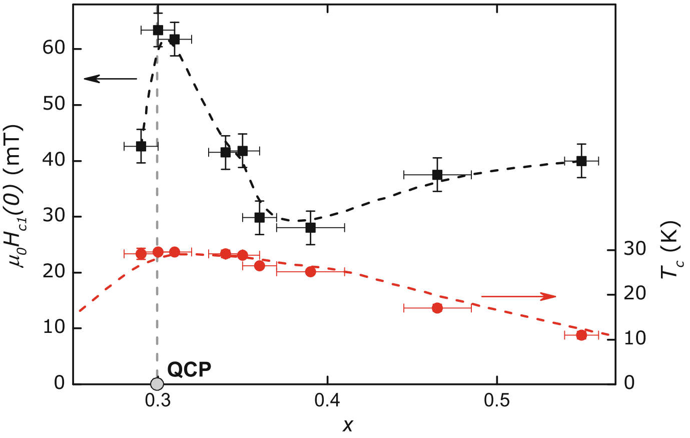

Fig. 4.30 Lower critical field $H_{c1}(T = 0)$ (*squares*) and the superconducting critical temperature T_c of $BaFe_2(As_{1-x}P_x)_2$ versus x. The *dashed lines* are guides to the eye

as the field where the energy levels are equal. The total energy of the vortex per unit length is given by [34]

$$E_{\text{line}} = \frac{H_{c1}\phi_0}{4\pi\mu_0}. \tag{4.10}$$

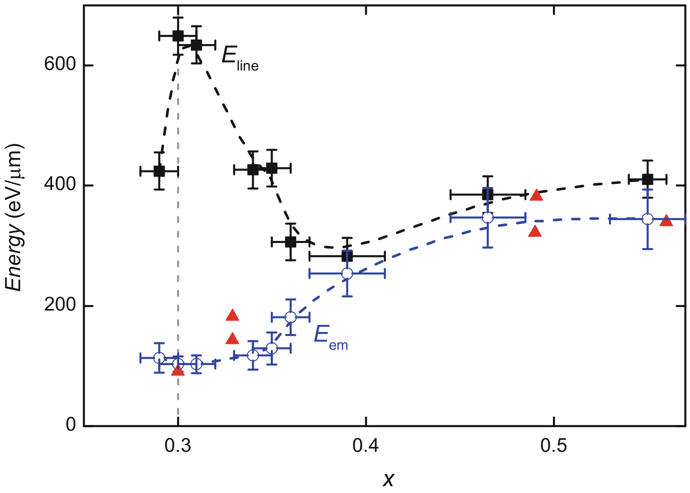

Fig. 4.31 Vortex line energy E_{line} (*squares*) determined from H_{c1} and electromagnetic energy E_{em} determined from heat capacity (*open circles*) and microwave magnetic penetration depth (*triangles*) of $\mathrm{BaFe_2(As_{1-x}P_x)_2}$. For derivation see the text. *Dashed lines* are guides to the eye

In order to create a vortex inside a superconductor a screening current is created which contributes the electro-magnetic energy

$$E_{\mathrm{em}} = \left(\frac{\phi_0^2}{4\pi\mu_0\lambda^2}\right)\ln\kappa. \tag{4.11}$$

This now allows us to compare the results obtained from H_{c1} and the London penetration depth [14] on a more phenomenological level. The results are shown in Fig. 4.31. Due to the higher scattering of penetration depth data and the good numerical agreement of the enhancement between λ and γ shown in the previous section and Ref. [30] we have determine the electromagnetic energy more precisely using $\lambda(x)/\lambda(x = 0.3) = \gamma(x)/\gamma(x = 0.3)$. For this we have used the measured values of the used samples, shown in Fig. 4.28. Based on this analysis we find good agreement between the energy levels of the two probes far away from the QCP, in contrast to compositions $x_c \leq x \leq 0.4$ where a strong upturn is observed. While the difference between the two sets of data can not be understood in the conventional formulation of the GL theory, we will argue that it originates from the vortex core contribution, that is typically seen as small correction.

The contribution of the vortex core had been neglected in the derivation of Eq. 4.9. It only entered as constant 1/2 in the logarithm. However the vortex core corresponds to a normal state region with the radius ξ_e which is commonly estimated by the Ginzburg-Landau coherence length ξ_{GL}. In the case of an enhanced normal state energy this simple picture is not necessarily true. Therefore we will calculate the vortex core energy in the following way.

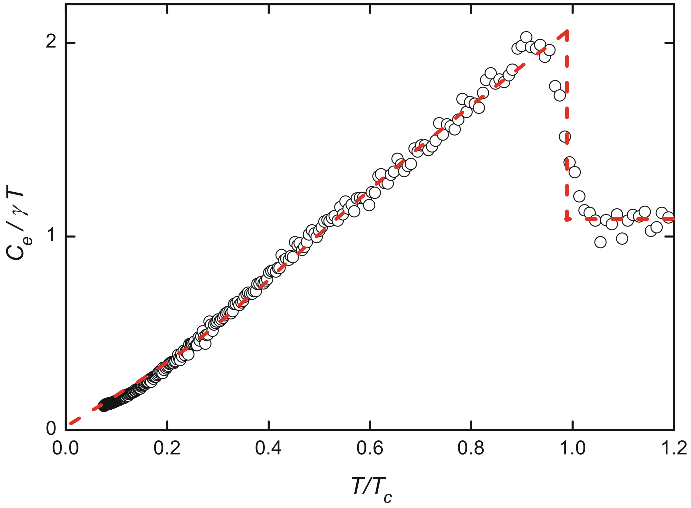

Fig. 4.32 Electronic part of the heat capacity of $BaFe_2(As_{1-x}P_x)_2$ at $x = 0.43$. The *dashed line* presents fit to the data using a single band *d-wave* model. Courtesy of L. Malone

Starting from an alpha-model fit to the heat-capacity of a sample with $x = 0.43$ (see Fig. 4.32), this model is then multiplied by the strong enhancement of the heat capacity that was found previously [30]. From this we can derive the condensation energy density using

$$\varepsilon_{\text{cond}} = \int_0^\infty [C_s(T) - C_n(T)]\, \mathrm{d}T, \tag{4.12}$$

where C_s and C_n are the heat capacity in the superconducting and normal state respectively. Thus we obtain the condensation energy per unit length of a cylinder with the effective radius ξ_e. This energy corresponds in first approximation to the energy necessary to create a normal state region of size $\pi\xi_e^2$ inside a superconductor. As this corresponds to the common definition of the vortex core, we can write

$$E_{\text{core}} = \varepsilon_{\text{cond}} \pi \xi_e^2. \tag{4.13}$$

As mentioned previously the core size can be estimated by the GL coherence length, determined from the upper critical field H_{c2}. We find that for $\xi_e(x) \approx 4\xi_{GL}(x)$ the residual energy is in good agreement with our estimate of the core energy E_{core} as shown in Fig. 4.33. While a scaling factor is needed to bring the experimental data in agreement with our calculation, the extracted value is in good comparison to other techniques probing the effective vortex size. Typical values in the range of 3 to 4 ξ_{GL} are found for systems such as MgB_2 [44, 45], LiFeAs [46] and 2H-$NbSe_2$ [47].

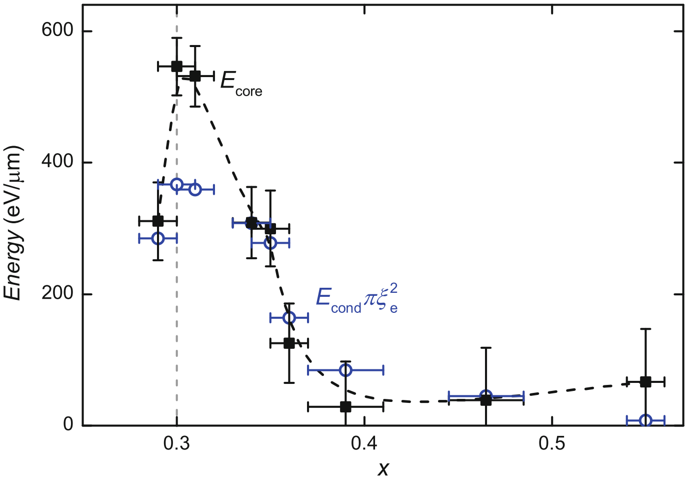

Fig. 4.33 Core energy E_{core} (*squares*) of BaFe$_2$(As$_{1-x}$P$_x$)$_2$ as determined from the difference between H_{c1} and λ and the condensation energy E_{cond} (*open circles*) for a vortex with the effective radius ξ_e

4.3.3 Conclusion

In conclusion we have determined the lower and upper superconducting critical field in BaFe$_2$(As$_{1-x}$P$_x$)$_2$ over a wide range of the superconducting dome. We have found that despite the strong enhancement in the quasi particle mass we did not find any unusual increase in the upper critical field as expected from GL and BCS theory. Our data suggests that the increase in H_{c2} throughout the superconducting range of the phase diagram is almost entirely described by the increase in T_c. Furthermore this results is obtained by probing H_{c2} close to T_c and at low temperatures. As H_{c2} is not limited by Pauli-pair breaking close to T_c and both probes show good agreement in the zero temperature limit, we believe that Pauli-limiting effects are not causing a cut-off of the enhancement at low temperatures. This behaviour is in agreement with that found in other quantum critical materials such as CeRhIn$_5$ [40]. Since a deeper theoretical understanding is missing up to date, we would like to stress that the universality of this behaviour could possibly help identify the unconventional nature of quantum critical superconductors, as it violates not just the quantitative but also qualitative predictions from BCS and GL theory.

Further we have found striking results on the lower critical field. Unlike the prediction from GL theory based on the London penetration depth results [14], H_{c1} showed a strong peak rather than a dip at the critical composition x_c. While GL theory is valid far from the QCP is does not hold at the the critical composition. We were able to show convincing evidence that this result is caused by an unusually high normal state energy close to the quantum critical point. This high normal state energy, which is caused by an enhanced normal state quasiparticle mass close to the QCP makes the superconducting state energetically more favourable, leading to a strong peak in the condensation energy. To our knowledge this has been the first doping dependent study of H_{c1}. A similar differences between measurements of H_{c1} and London penetration depth was found in the field of cuprates [48]. While no doping dependence was carried out in this study the deviation from GL theory might be a general property of high-temperature superconductors and especially quantum critical systems.

In the interpretation of our results we have so far followed the chain causality of our results. As we were able to show that the quasi particle mass effects the lower superconducting critical field, we take a closer look at the vortex core that is the place of origin. The vortex core typically holds low laying Andreev bound states with energy levels spaced by $\Delta/k_B T_F$ [49]. As pointed out in Ref. [14] the Fermi temperature $T_F = \frac{\hbar e^2}{2\pi k_B m^*} S_k$ is strongly suppressed at the QCP while the superconducting gap Δ is strongest at this point. Therefore we expect a larger than usual energy-level spacing which leads to higher populated energy states. These not only make the vortex core energy more important in the treatment in GL theory but also lead to an extension of the effective core size [50]. In this way the effect of a strong quasi particle mass enhancement on H_{c2} as predicted by GL theory could be reduced by the enhancement of the effective vortex core size. While we have assume a constant scaling of the effective core size with x, in this scenario the scaling variable would be proportional to T_c/T_F and hence vary with x. The variation between $x = 0.38$ to $x = 0.3$, where we found the strong increase in the core energy, for the effective core radius by a factor 4, could hence compensate the approximately 5 fold enhancement of the effective mass.

References

1. S. Kasahara, K. Shibauchi, K. Hashimoto, K. Ikada, S. Tonegawa, R. Okazaki, H. Shishido, H. Ikeda, H. Takeya, K. Kirata, T. Terashima, Y. Matsuda, Phys. Rev. B **81**, 184519 (2010)
2. Y. Huang, Q. Qui, W. Bao, M. Green, J. Lynn, Y. Gasparovic, X. Chen, Phys. Rev. Lett. **101**, 257003 (2008)
3. A. Carrington, Rep. Prog. Phys. **74**, 124507 (2011)
4. M. Johannes, I. Mazin, Phys. Rev. B **79**, 220510 (2009)
5. B. Arnold, S. Kasahara, A. Coldea, T. Terashima, Y. Matsuda, T. Shibauchi, A. Carrington, Phys. Rev. B **83**, 220504 (2011)
6. M. Johannes, I. Mazin, Phys. Rev. B **77**, 165135 (2008)
7. Z. Yin, K. Haule, G. Kotliar, Nat. Mater. **10**, 932 (2011)
8. J. Ferber, H. Jeschke, R. Valenti, Phys. Rev. Lett. **109**, 236403 (2011)
9. T. Terashima, N. Kurita, M. Kimata, M. Tomita, S. Tsuchiya, M. Imai, A. Sato, K. Kihou, C.H. Lee, H. Kito, H. Eisaki, A. Iyo, T. Saito, H. Fikazawa, Y. Kohori, H. Harima, S. Uji, Phys. Rev. B **87**, 224512 (2013)
10. T. Shimojima, F. Sakaguchi, K. Ishizaka, Y. Ishida, W. Malaeb, T. Yoshida, S. Ideta, A. Fujimori, T. Kiss, M. Okawa, T. Togashi, C. Chen, S. Watanabe, Y. Nakashima, A. Ino, H. Anzai, M. Arita, K. Shimada, H. Namatame, M. Taniguchi, S. Kasahara, T. Terashima, T. Shibauchi, Y. Matsuda, M. Nakajima, S. Uchida, K. Kihou, C. Lee, A. Iyo, H. Eisaki, A. Chainani, S. Shin, Science **332**, 6029 (2011)

11. L. Klintberg, S. Goh, S. Kasahara, Y. Nakai, K. Ishida, T. Sutherland, M. ad Shibauchi, Y. Matsuda, T. Terashima, J. Phys. Soc. Jpn. **79**, 123706 (2010)
12. T. Yamazaki, N. Takeshita, R. Kobayashi, H. Fukazawa, Y. Kohori, K. Kihou, C. Lee, H. Kito, A. Iyo, H. Eisaki, Phys. Rev. B **81**, 224511 (2010)
13. E. Colombier, S. Bud'ko, P.C. Canfield, Phys. Rev. B **79**, 224518 (2009)
14. K. Hashimoto, C.K., T. Shibauchi, S. Kasahara, Y. Mizukami, R. Katsumata, Y. Tsuruhara, T. Terashima, H. Ikeda, M. Tanatar, H. Kitano, N. Salovich, R. Giannetta, P. Walmsley, A. Carrington, R. Prozorov, Y. Matsuda, Science **336**, 1554 (2012)
15. K. Kuroki, H. Usui, S. Onari, R. Arita, H. Aoki, Phys. Rev. B **79**, 224511 (2009)
16. C. Bergemann, A. Mackenzie, S. Julian, D. Forsythe, E. Omichi, Adv. Phys. **52**, 639 (2003)
17. P. Blaha, K. Schwarz, G. Madsen, D. Kvasnicka, J. Luitz, *WIEN2K edited by Karl Heinz Schwarz* (Technische Universität Wien, Austria, 2001)
18. A. Kemper, T. Maier, S. Graser, H. Cheng, P. Hirschfeld, D. Scalapino, New J. Phys. **12**, 073030 (2010)
19. H. Shishido, A. Bangura, A. Coldea, S. Tonegawa, K. Hashimoto, K. Kasahara, P. Rourke, H. Ikeda, T. Terashima, R. Settai, Y. Onuki, D. Vignolles, C. Proust, B. Vignolle, A. McCollam, Y. Matsuda, T. Shibauchi, A. Carrington, Phys. Rev. Lett. **104**, 057008 (2010)
20. J. Analytis, J.-H. Chu, R. McDonald, S. Riggs, I. Fisher, Phys. Rev. Lett. **105**, 207004 (2010)
21. L. Boeri, O. Dolgov, A. Golubov, *Physica (Amsterdam) C***469**, 628 (2009)
22. T. Terashima, N. Kurita, M. Tomita, K. Kihou, C. Lee, Y. Tomioka, T. Ito, A. Iyo, H. Eisaki, T. Liang, N. Masamichi, S. Ishida, S. Uchida, H. Harima, S. Uji, Phys. Rev. Lett. **107**, 176402 (2011)
23. M. Tanatar, E. Blomberg, A. Kreyssig, M. Kim, N. Ni, A. Thaler, S. Bud'ko, P. Canfield, A. Goldman, I. Mazin, R. Prozorov, Phys. Rev. B **81**, 184508 (2010)
24. Y. Nakai, T. Iye, S. Kitagawa, K. Ishida, H. Ikeda, S. Kasahara, H. Shishido, T. Shibauchi, Y. Matsuda, T. Terashima, Phys. Rev. Lett. **105**, 107003 (2010)
25. T. Shibauchi, A. Carrington, Y. Matsuda, Annu. Rev. Condens. Matter Phys. **5**, 113 (2014)
26. E. Abrahams, Q. Si, J. Phys.: Condens. Matter **23**, 223201 (2011)
27. T. Yoshida, I. Nishi, S. Ideta, A. Fujimori, M. Kubota, K. Ono, S. Kasahara, T. Shibauchi, T. Terashima, Y. Matsuda, H. Ikeda, R. Arita, Phys. Rev. Lett. **106**, 117001 (2011)
28. B. Arnold, *High Field Invesitigation into the Electronic State of Unconventional Superconductors* (Ph.D. Dissertation, University of Bristol, 2013)
29. A. Levchenko, M. Vavilov, M. Khodas, A. Chubukov, Phys. Rev. Lett. **110**, 177003 (2013)
30. P. Walmsley, C. Putzke, L. Malone, I. Guillamon, D. Vignolles, C. Proust, S. Badoux, A. Coldea, M. Watson, S. Kasahara, Y. Mizukami, T. Shibauchi, Y. Matsuda, A. Carrington, Phys. Rev. Lett. **110**, 257002 (2013)
31. K. Hashimoto, M. Yamashita, S. Kasahara, Y. Senshi, N. Nakata, S. Tonegawa, K. Ikada, A. Serafin, A. Carrington, T. Terashima, H. Ikeda, T. Shibauchi, Y. Matsuda, Phys. Rev. B **81**, 220501 (2010)
32. D.D. Kuzmanovski, A. Levchenko, M. Khodas, M. Vavilov, arXiv:1401.1118 (2014)
33. J. Analytis, H. Kuo, R. McDonald, M. Wartenbe, P. Rourke, N. Hussey, I. Fisher, Nat. Phys. **10**, 194 (2014)
34. M. Tinkham, *Introduction to Superconductivity* (Dover Publications, 1996)
35. N. Werthamer, E. Helfand, P. Hohenberg, Phys. Rev. **147**, 295 (1966)
36. M. Tanatar, K. Hashimoto, S. Kasahara, T. Shibauchi, Y. Matsuda, R. Prosorov, Phys. Rev. B **87**, 104506 (2013)
37. A. Clogston, Phys. Rev. Lett. **9**, 266 (1962)
38. B. Chandrasekhar, Appl. Phys. Lett. **1**, 7 (1962)
39. M. Springford, *Electrons at the Fermi Surface* (Cambridge University Press, 1980)
40. G. Knebel, D. Aoki, J. Brison, J. Flouquet, J. Phys. Soc. Jpn. **77**, 114704 (2008)
41. A. Gurevich, Phys. Rev. B **82**, 184504 (2010)
42. B. Brandt, D. Liu, L. Rubin, Rev. Sci. Instr. **70**, 104 (1999)
43. D. Chen, R. Goldfarb, R. Cross, A. Sanchez, Phys. Rev. B **48**, 6426 (1993)
44. A. Koshelev, A. Golubov, Phys. Rev. Lett. **90**, 177002 (2003)

45. M. Eskildsen, M. Kugler, S. Tanaka, J. Jun, S. Kazakov, J. Karpinski, O. Fisher, Phys. Rev. Lett. **89**, 187003 (2002)
46. Z. Zakharchuk, P. Belova, M. Safonchik, K. Traito, E. Lahderanta, J. Appl. Phys. **113**, 013906 (2010)
47. U. Hartmann, A. Glubov, T. Drechsler, M. Kupriyanov, C. Heiden, Phys. B **194–195**, 387 (1994)
48. R. Liang, P. Dosanjh, D. Bonn, W. Hardy, A. Berlinsky, Phys. Rev. B **50**, 4212 (1994)
49. C. Caroli, P. de Gennes, J. Matricon, Phys. Lett. **9**, 307 (1964)
50. L. Kramer, W. Pesch, Z. Phys. **269**, 59 (1974)

Chapter 5
LiFeAs and LiFeP—Stoichiometric Superconductors

5.1 Introduction

The 122-type superconductor $BaFe_2(As_{1-x}P_x)_2$, discussed in the previous chapter, is a good example of the typical phase diagram found in iron-pnictide superconductors. The parent compound can be tuned from an anti-ferromagnetic ground state to superconductivity by a variety of parameters. The challenging aspect of this procedure is that the parameter used to suppress the magnetic order typically also introduces disorder in the system. Further it is difficult to find a theoretical model for a non-stoichiometric system where the location of 'substitutes' follows statistical distributions on the corresponding lattices sites.

111-type pnictide LiFeAs and its counterpart LiFeP do not have these difficulties. Both materials superconduct in the stoichiometric form with $T_c \approx 18\,\mathrm{K}$ [1, 2] and $\approx 5\,\mathrm{K}$ [3] respectively. Above the superconducting critical temperature both show metallic, non-magnetic behaviour [4]. Hence, we do not expect to find any reconstruction of the Fermi surface which allows for a direct comparison of the Fermi surface topologies of the end members. While in other pnictides the maximum T_c is achieved in a mixed composition in the phase diagram, requesting the use of super-cell DFT calculations we here have the possibility to compare experimental values and DFT calculations on stoichiometric systems with an almost 4 fold enhancement in T_c, minimizing the assumptions made for the crystals structure as starting point of theoretical models.

One of the open question remains the driving mechanism for the appearance of nodal and nodeless superconducting gap structures in iron based superconductors. The framework, that models the gap structure, might also give a microscopic understanding of the superconducting pairing mechanism. For LiFeAs a nodeless superconducting gap was found using magnetic penetration depth measurements, while LiFeP was shown to possess nodes on the superconducting gap [4]. As the appearance of these nodes has been closely linked to details in the band structure of these materials the isovalent systems LiFeAs and LiFeP are truly unique for combination of experimental and theoretical investigations.

C.M. Putzke, *Fermi Surface and Quantum Critical Phenomena in High-Temperature Superconductors*, Springer Theses,
DOI 10.1007/978-3-319-48646-8_5

Fig. 5.1 Crystals structure of LiFeP

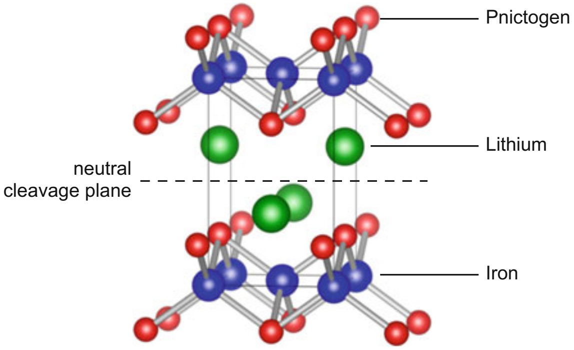

5.1.1 Crystal Structure

The crystal structures of LiFeP and LiFeAs possess tetragonal symmetry and crystallises in the $P4/nmm$ space group, shown in Fig. 5.1. As discussed in the case of $BaFe_2(As_{1-x}P_x)_2$ the lattice parameter shrink when replacing arsenic with phosphorous. In LiFeAs we find $a = 3.7924$ Å and $c = 6.3639$ Å [1] and $a = 3.6955$ Å and $c = 6.0411$ Å in LiFeP [5]. The pnictogen height change from $h_{pn} = 1.505$ Å in LiFeAs [1] to $h_{pn} = 1.327$ Å in LiFeP [5], presents an $\approx$13 % change compared to an $\approx$15 % change between $BaFe_2As_2$ and $BaFe_2P_2$ [6]. As this substitution is isovalent, meaning the system should not change its charge balance, any difference between LiFeAs and LiFeP can be linked in first approximation to the presented changes in the lattice parameter and the resulting changes in hybridization between iron and pnictogen atomic orbitals.

Not only from its electronic properties, but also from its crystal structure LiFeP and LiFeAs are interesting for experiments as they possess a neutral cleavage plan. The double layer of lithium atoms allows to obtain neutral surfaces which are important to reduce surface effects in surface sensitive techniques like ARPES and STM.

Up to know no single crystals for the intermediate region $LiFeAs_{1-x}P_x$ could be grown. In attempts to grown these phase-separated crystals were found. Also while crystals available for LiFeAs are typically several square-millimetre big, LiFeP could so far only be grown up to $150 \times 150 \times 50\,\mu m^3$. This has great impact on the possible measurement techniques to study these systems. While LiFeAs has gotten great attention over the last few years, LiFeP is poorly studied even though its nodal superconducting gap structure in the stoichiometric form had been very interesting.

5.1.2 Bandstructure

The band structure obtained by DFT calculations using LDA in the WIEN2K package [7] for LiFeP is shown in Fig. 5.2. The typical result obtained in iron-pnictide superconductors of hole-pockets in the centre of the BZ and electron pockets at the

Fig. 5.2 Band structure of LiFeP determined by DFT calculations using the lattice parameter specified in the text

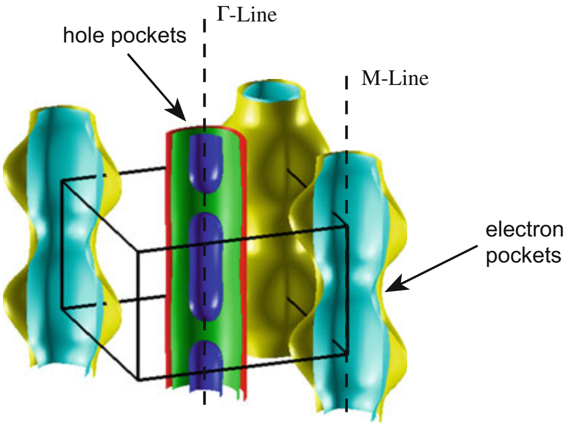

zone corner is found. While all pockets possess four-fold symmetry the inner hole-pocket is special as it has a peanut-shaped topology. We have already discussed in the context of $BaFe_2(As_{1-x}P_x)_2$ that such strong difference from a quasi-2D Fermi surface is caused by the iron-d_{z^2}-orbital. A significant warping is also found on the outer electron pocket at the top and bottom of the BZ. While the warping on the electron pockets in $BaFe_2P_2$ was caused by the body centred space group, here the warping is also caused by significant d_{z^2}-orbital weight on the hole pockets.

The first experiments on determining the band structure of LiFeAs were performed using ARPES [8]. In this work the authors confirmed the Fermi surface having the typical shape of at least two hole pockets in the center of the BZ and two electron pockets at the zone corners. Borisenko and co-workers [8] attributed the absence of a magnetic ground state with the absence of good nesting in the system as shown in Fig. 5.3. They also suggested that superconductivity in LiFeAs is independent of the nesting criteria in the system which was believed to be a key ingredient for superconductivity in the pnictides. However we want to remind the reader of the discussion on the origin of the magnetic ground state in Sect. 4.1, where we argued that the emergence of a magnetic ground state is not necessarily caused by Fermi surface nesting but rather localization effects due to hybridization.

5.1.3 Third Hole Pocket Scenario

Much theoretical and experimental effort was made trying to solve the origin of the nodes in iron pnictide superconductors. One of the first proposals for their origin was made by Kuroki et al. [9] only shortly after their discovery. Based on calculations done on the band structure of LaFeAsO and LaFePO they propose that the driving mechanism, that switches between a nodal and nodeless gap structure, is the pnictogen height [9]. In their model they find that the obtained band structure is

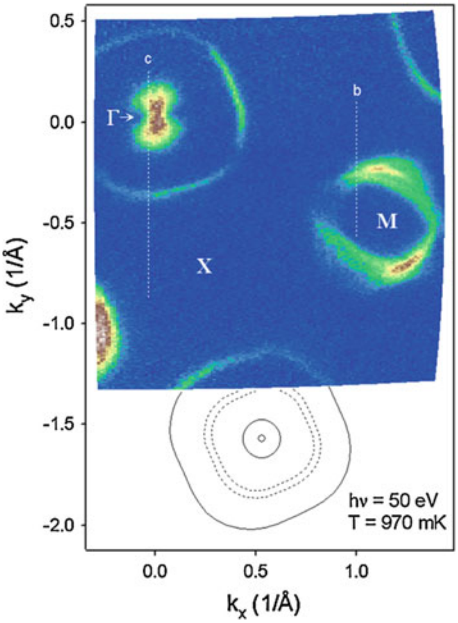

Fig. 5.3 Momentum distribution map of the Fermi surface shape of LiFeAs measured by ARPES and taken from Ref. [8]. *Solid lines* represent Γ centered Fermi surface sheets, while *dashed line* are from *M* center Fermi surface

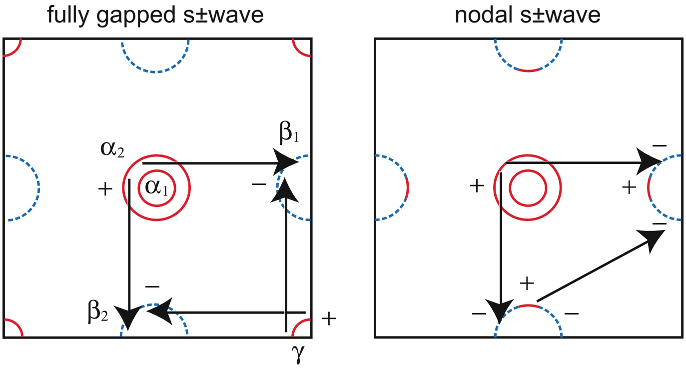

Fig. 5.4 Schematic representation of fully gapped $s \pm$ wave (*left*) and nodal $s \pm$ wave gap structure. The *solid red* and *dashed blue curves* represent positive and negative sign of the superconducting gap respectively. Dominant interaction due to nesting are indicated by *arrows*. The figure was modified from that found in Ref. [9]

highly sensitive to these changes. Upon reducing the pnictogen height in LaFeAsO the hole pocket at the corner of the unfolded BZ (see Fig. 5.4a) disappears leaving the system with two hole pockets at the Γ-point and two electron pockets at

$(\pi, 0)$ and $(0, \pi)$. Since this procedure mimics the substitution of arsenide with phosphorous, Kuroki et al. [9] tried to understand how the disappearance of this pocket effects superconductivity in the system. As we had discussed in the introduction, the repulsive pair-scattering by SDW fluctuations can still lead to a superconducting ground state. For this the sign of the superconducting energy gap needs to change sign, $\Delta(\mathbf{k}+\mathbf{Q}) = -\Delta(\mathbf{k})$, for parts of the Fermi surface connected by the nesting vector $\mathbf{Q}$. In an ideal theoretical formulation pair-scattering would only be allowed for sections of the Fermi surface with equal orbital character, as transition in angular momentum would be forbidden. So in absence of the third hole pocket the d_{xy} pairing channel between electron and hole pockets would be absent, as the other hole pockets contain mainly $d_{xz,yz}$-orbital character, reducing the superconducting gap on these parts of the Fermi surface. We are then left with an intra-band scattering of d_{xy}-character parts of the electron pockets, that favours the sign changing within the electron-pocket. This scenario is indicated in the nodal $s\pm$ schematic in Fig. 5.4. In real systems such a strict distinction is not applicable. The orbital character acts not as an *on-off* switch, but more as a weighting parameter for the Lindhard-response function as it enters the exchange potential [10]. In this both the inter-band interactions, leading to nodeless superconducting gap with changing sign between electron and hole pockets, as well as the intra-band interactions leading to nodes are present. Details on the Fermi surface, such as the nesting criteria and distribution of orbital weight determine which of the two, almost degenerate mechanisms, is dominant leading to a nodal or nodeless superconducting gap structure. To determine whether this scenario correctly describes the superconducting pairing mechanism in the iron-pnictides, a detailed determination of the Fermi surface is needed for a realistic theoretical model.

Lets consider this scenario now for LiFeAs. Platt et al. [11] have calculated the expected superconducting gap for LiFeAs. Their results are shown in Fig. 5.5. A strongly anisotropic gap for the electron pockets was found at $k_z = 0$. The dominant orbital characters are shown as different colors. The *third hole pocket* discussed by Kuroki et al. [9] is shown to possess dominantly d_{xy}-orbital character (green Fig. 5.5). As indicated in the figure the inter-band pair-scattering of parts of electron and hole Fermi surface with equal dominant orbital character favours a sign change of the superconducting gap. The intra-band scattering on the electron pockets between parts with different orbital character favours an anisotropic gap. As seen in the left panel Fig. 5.5 the superconducting form factor on the parts of Fermi surface with d_{xy} orbital character have small gap-values at $k_z = 0$. We could imagine that small changes in the Fermi surface topology or orbital content could lead to a further reduction of the pair-interaction and hence of the superconducting form factor at these points, leading to *accidental nodes*.

To determine whether the third hole pocket scenario correctly describes the formation of nodes on the superconducting gap structure, a detailed study of the *bulk* Fermi surface in LiFeAs and LiFeP is desired, which could lead to a more realistic theoretical treatment.

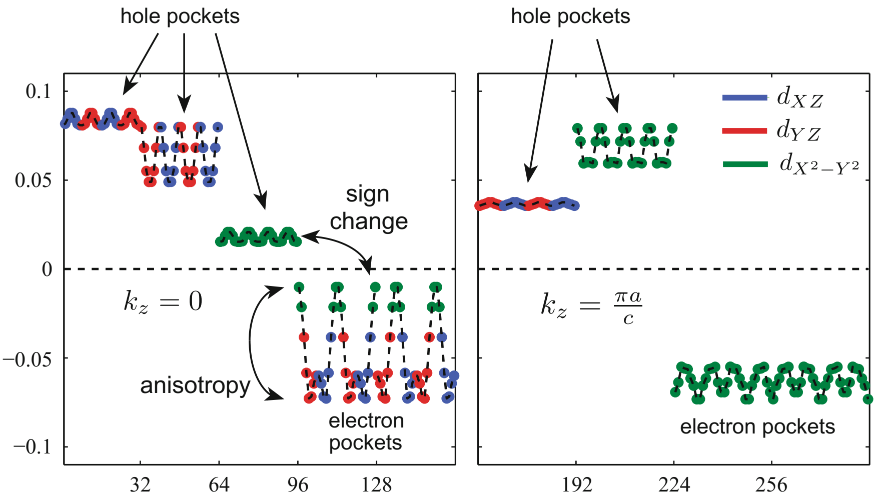

Fig. 5.5 Leading superconducting form factor for LiFeAs calculated by Platt et al. [11] along cuts on the Fermi surface at $k_z = 0$ and $k_z = \pi a/c$. Orbital weights are indicated in colors. Since these calculations were performed in the unfolded BZ the orbital characters are rotated by 45°. Hence the indicated $d_{x^2-y^2}$ orbital character corresponds to d_{xy} in the text. Figure was taken from Ref. [11]

5.2 Fermi Surface of LiFeAs

De Haas-van Alphen measurements in pulsed and high static magnetic fields have been carried out to determine the Fermi surface properties of LiFeAs. As the material is highly sensitive to air the single crystals were stored in sealed quartz tubes under vacuum and were only taken out at the user facilities right before the experiment. The ampoules were opened inside a glove bag under argon atmosphere to minimize the contact to air and were then covered in *degassed grease*. For this we have used Apiezon N grease, which was heated to 150 °C and then pumped repeatedly until the formation of bubbles in the grease vanished. With this procedure it was possible to increase the lifetime of the crystals to several days. By storing the samples at liquid nitrogen temperatures we were able to detect superconductivity in the samples even after several months. Torque measurements were first carried out in pulsed magnetic field at the LNCMI-Toulouse and later in static fields at the NHMFL-Tallahassee. In Fig. 5.6 the raw signal obtained in pulsed field at $T = 1.5\,\text{K}$ is shown. By removing a smooth background and performing a FFT we obtained the spectrum shown in Fig. 5.6. Three different peaks can be observed. While we would expect five pockets from band structure calculations, leading to possibly ten different extremal orbits, the fact that oscillations can only be observed in high magnetic fields above 30 T suggests that the observation of the predicted higher frequency orbits is limited by the samples having insufficiently long mean-free-path.

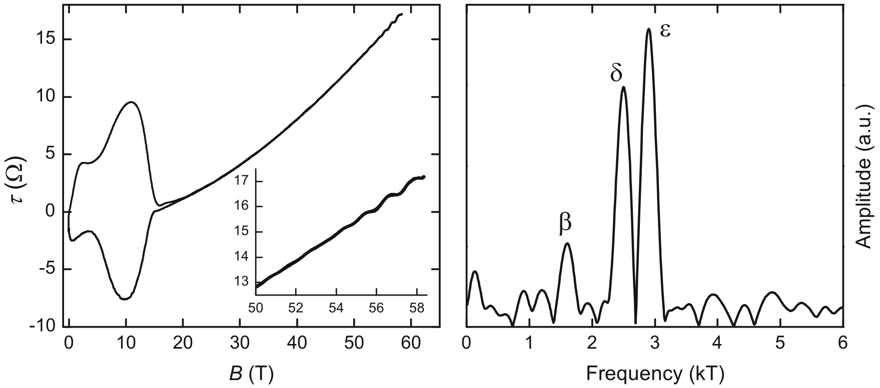

Fig. 5.6 Torque signal obtained in pulsed field at the LNCMI-Toulouse for LiFeAs (*left panel*). In the *right panel* the FFT after subtracting a smooth background is shown

A first angle dependence of the observed frequencies was taken in pulsed magnetic field, while a more detailed set of data was obtained at the NHMFL Tallahassee using static fields up to 45 T and temperatures down to 0.3 K. These low temperatures are beneficial for LiFeAs as the masses found were up to six times the free electron mass. Moreover unlike in $BaFe_2(As_{1-x}P_x)_2$ where we found the same mass in pulsed and static fields LiFeAs was very sensitive to eddy current heating present in pulsed field. We found that the effective mass determined in pulsed field was significantly lower than that in dc fields. During the fast increase in magnetic field in the pulsed magnet system, the sample experiences heating caused by eddy currents. This leads to the fact that the real temperature of the sample at the point where quantum oscillations are observed is higher than the surrounding bath temperature. This causes a lower oscillation amplitude at the desired temperature and hence an underestimation of the effective mass. We found that while data taken between 2.2 and 4.2 K was roughly in agreement between pulsed and dc fields, the data below the lambda-point of helium showed strong variation between the two magnet-systems. This is believed to be caused by a strong reduction in Kapitza-resistance below the lambda point, causing a lower thermal conductivity between the sample and the bath [12, 13].

The reason for this to affect LiFeAs but not the experimental values on $BaFe_2(As_{1-x}P_x)_2$ might be due to the sample geometry. The samples used for LiFeAs were cleaved, thin plate-like pieces. Therefore the ratio of cross section in field compared to the total volume was much larger than the samples measured in the $BaFe_2(As_{1-x}P_x)_2$ study. Due to this observation all masses which are stated in Table 5.1 where taken in static fields.

The mean free path of LiFeAs was found to be as low as 10 nm causing an underestimation of the effective mass when taking a large field window of 30–45 T. This was first checked by simulating the data with the obtained results from the LK-fit to the amplitude and field dependence. Generating data with a mean free path of $l = 10\,\text{nm}$, a frequency of $F = 3000\,\text{T}$ and a mass of $m^* = 6\,m_e$ and then using the same

Table 5.1 Measured values for LiFeAs for the dHvA frequencies extrapolated to $\theta = 0$. The effective masses and bandmasses are given in units of the bare electron mass. Values marked with $\sharp$ are taken on data that might possibly include contributions form different orbits

Orbit	$F_0(T)$	m_b	m^*	λ
δ	2400(25)	+1.22	5.2(4)	3.3(3)
$\beta^\sharp$	1590(10)	+1.54	$6.0(4)^\sharp$	2.9(3)
ε	2800(40)	+1.02	5.2(4)	4.2(4)

analysis as for the data, we find an effective mass $m^* = 5.5m_e$. In order to correct for this behaviour we have hence carried out fits to the complete data set including the oscillatory part of the signal between 30 and 45 T at all measured temperature. For this the frequencies were fixed to the values found in the FFT and the Dingle term using data at base temperature. Then the magnetic field was parametrized to include the temperature $B' = T(B)$ and substituted in the LK formula. In this way the Dingle term and effective mass can be fitted at the same time as the torque signal is only a function of temperature but not field any more. Any influence on the results obtained and presented in Table 5.1 from the Dingle term can thus be ruled out. The oscillation frequencies were determined at various angles of the applied field with respect to the c-axis of the sample. The results are shown as $F \cos\theta$ in Fig. 5.7. While a perfect cylindrical Fermi surface would give a constant value in this representation we find that orbits β and δ bend upwards while orbit ε shows a downwards bending. Further we can see the ε has a more constant dependence around $\theta = 0$. Form this behaviour we can compare the observed frequencies with the angle dependence obtained from band structure calculations. We find that the evolution of F versus θ for ε is best described by that found for the maximum orbit of the inner electron pocket and β by the minimum of the same pocket. The orbit marked as δ shows good agreement with that calculated for the minimum of the outer electron pocket. The band structure could be brought into good agreement with the experimental values by rigid band-shifts of −5 meV for band 4 and +18 meV for band 5. These shifts are small compared to those needed in other compounds [14, 15]. The necessity of these shifts is believed to originate from many-body corrections to the DFT band structure [16]. In Ref. [16] the authors show that different bands require different shifts to their chemical potential, as the shift is proportional to the inter-band interaction strength. As this varies due to for example nesting criteria, a non-uniform shift is justified (Fig. 5.8).

While the main identification of the observed frequencies can be done by only considering the electron pockets of the system, we can make some predictions on the hole pockets. For the β orbit a significant scattering in frequency was observed in pulsed magnetic field. This could originate from a difference in the mean free path of different orbits at different angles and hence could be interpreted as originating from the middle hole pocket found in calculations. As already mentioned the mean free path in these crystals was lower than we will see in LiFeP, but in the case of a significant reduction in orbit size of band 2, as found in ARPES, we would

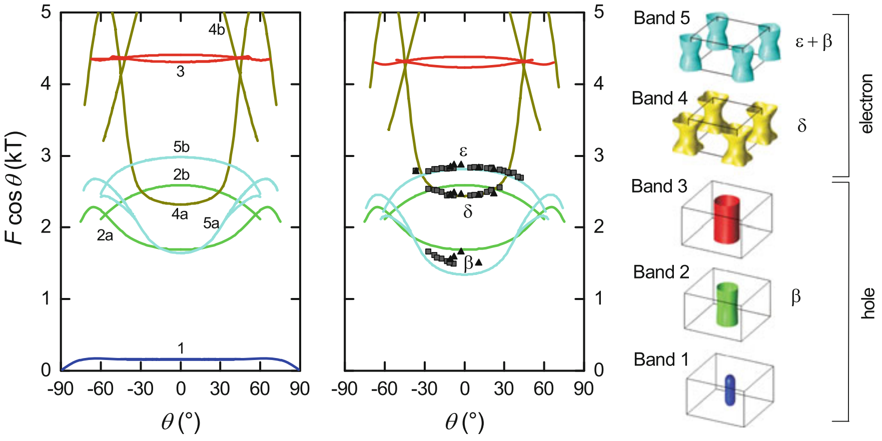

Fig. 5.7 Angle dependence of LiFeAs. *Right panel* shows the results from bandstructure calculations. The *middle panel* has data measurements in static (*squares*) and pulsed (*triangles*) magnetic field. The bandstrcuture has been brought into agreement with the observed extremal orbits using rigid bandshifts. The pockets found in bandstructure calculations are shown on the *right* as guide

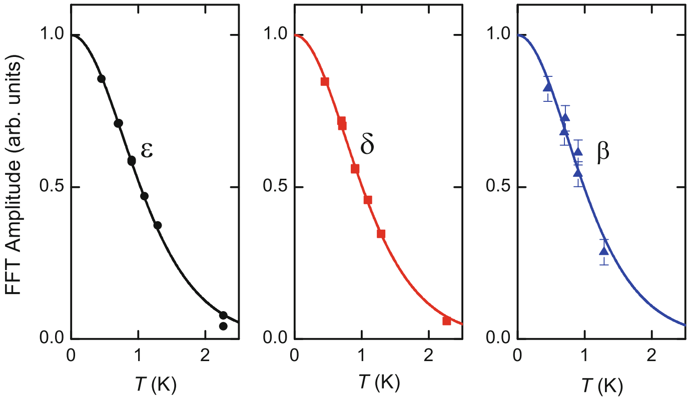

Fig. 5.8 Temperature dependence of the FFT amplitude of LiFeAs for the observed extremal orbits. The data was taken in a field range of 30–45 T. *Solid lines* represent fits to the temperature dependent part of the LK formula

still expect to see this in the experimental results. We therefore believe that band 2 experiences similarly small rigid band shifts, causing a good nesting with the electron pockets and hence in the available angle range no distinction can be made between the observed frequencies. Hence δ and β likely contain contributions from different extremal orbits. For the inner most hole pocket, that is predicted to have a very small extremal orbit, we would expect to find a strong peak in the frequency spectrum as we will see later is the case in LiFeP. The absence of this peak suggests that this band does not cross the Fermi level. As argued in the Ref. [17], the arsenic end member should show more localized bands caused by the longer iron-pnictogen distance. In order to suppress this band below the Fermi level we would require a rigid band shift of only 40 meV. The absence of this pocket would also account for the change in ratio between electron and hole-volume in the BZ that needs be consistent before and after rigid band shifts. In order to prove these suggestions samples with a longer mean-free-path are required to be able to study band 3 or increase the range in $1/B$ where oscillations are observed such that a differentiation between frequencies from band 2, 4 and 5 are possible in the FFT.

The identification of the frequencies as mainly originating form the electron pockets can now be used to compare the determined effective masses with the band masses of the individual orbits. We find renormalization values $\lambda = m^*/m_b - 1$ of 3–4 (see Table 5.1) showing a significant enhancement over the value expected for electron-phonon coupling $\lambda = 0.2$ [18].

5.3 Fermi Surface LiFeP

For measurements in LiFeP the same procedure was used as for LiFeAs. It should be pointed out that the available single crystals were however much smaller than those of LiFeAs. In order to determine the superconducting critical temperature we have therefore used a tunnel-diode oscillator which has high sensitivity for small changes of the inductance of the coil. With this technique we were able to determine the superconducting transition of a single crystal of $50 \times 50 \times 10\,\mu\text{m}^3$ shown in Fig. 5.9. The result is in good agreement with previous reports [3]. For this size of crystals the SEIKO PRC400 micro-cantilever were used in high static fields in Tallahassee to study quantum oscillations. Data obtained from torque magnetometry in pulsed field using SEIKO PRC120 is shown in Fig. 5.10a. One can see that the observed signal is an order or magnitude lower than that of LiFeAs which is caused by smaller sample size. The oscillation amplitude is about 20 % of the paramagnetic

Fig. 5.9 High frequency susceptibility measurements of the superconducting transition of LiFeP obtained after dHvA measurements in the same crystal. The observed onset of superconductivity is in good agreement with previous reports [3], showing that the sample had not degraded during the experiment

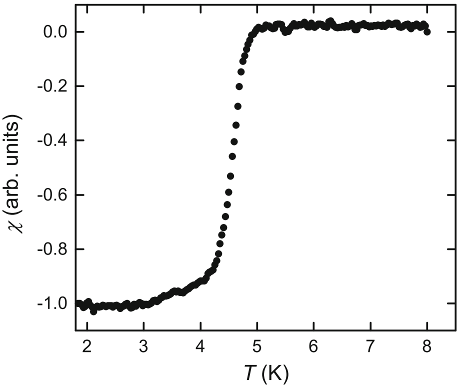

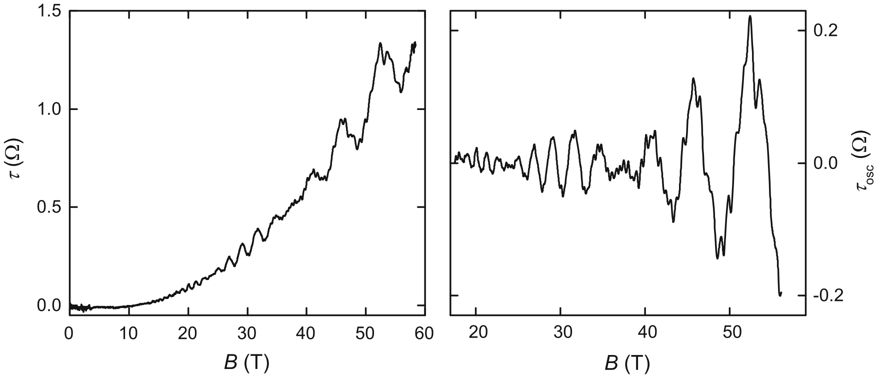

Fig. 5.10 Torque signal obtained on LiFeP in pulsed magnetic field at $T = 1.5\,\mathrm{K}$ (*left panel*). By subtracting a smooth background the oscillatory part of the torque signal remains (*right panel*)

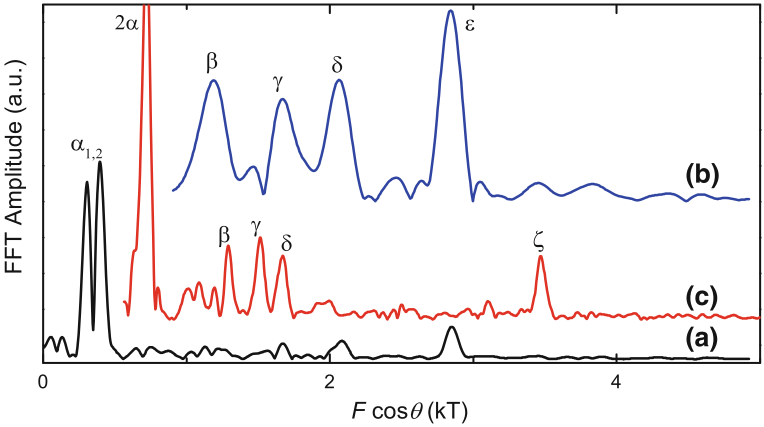

Fig. 5.11 FFT taken on the oscillatory troque signal of LiFeP in different field ranges. **a** 25–58 T: showing the split in the extremal orbits of α, **b** 40–58 T: better signal to noise ration for high frequency peaks and **c** 33–45 T: taken at in dc field at $\theta = 51°$

background and we start to observe oscillations below a field of 20 T. The FFT of the data, shown in Fig. 5.10b, contains a variety of peaks, Fig. 5.11. While the spectrum is mainly dominated by a low frequency contribution, further small peaks, clearly above the noise-level can be observed at high Frequency.

A detailed angular dependence of the oscillation frequency was taken at the NHMFL Tallahassee. By plotting the result as $F \cos\theta$, which, as mentioned, is constant for a perfect cylinder, we find the result shown in Fig. 5.12a. The solid symbols represent first harmonics while open circles are frequencies that were identified as higher harmonics. This was the case for example for frequencies around $F \cos\theta = 700\,\mathrm{T}$ where the angle dependence resembles that of α and the mass was found to be double that of α as expected from the LK formula.

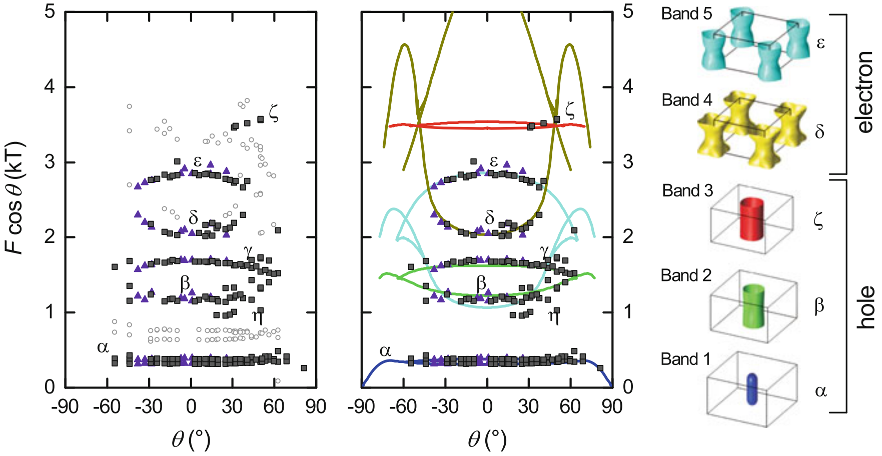

Fig. 5.12 Angle dependence of the observed oscillation frequencies of LiFeP. The *left panel* shows the obtained data. *Solid sqaures* represent extremal orbits observed in dc field. *Triangles* are obtained in pulsed magnetic field. Peaks identified as higher harmonics in the FFT are shown as *circles*. The *middle panel* shows the data superimposed by results from bandstructure calculations. The bandstructre was brought into agreement with the data using rigid bandshifts. The *right panel* shows the Fermi surface pockets obtained in calculations as guide

At low frequencies we find an almost cylindrical Fermi surface indicated as α. While two distinct frequencies are observed at $\theta = 0$ which merge into one by the higher one bending downwards and the lower one bending slightly upwards. Therefore we can identify these to originate form the same pocket representing maxima and minima orbits. As seen by data taken close to $\theta \approx 90°$ the frequency in $F \cos\theta$ is bending down showing a strong deviation form a cylindrical behaviour. This behaviour of $F(\theta)$ is shown to be in good agreement with the predicted frequency and shape of the inner hole pocket in DFT calculations. The theoretical prediction can be brought into agreement with the experimental results by applying a -65 meV rigid band shift. For orbits δ and ε we find that the angle dependence is very similar to that found in LiFeAs. We therefore assign these to the electron pockets obtained in DFT calculations. By rigid band shifts of $+20$ meV for δ and $+45$ meV for ε the DFT calculations show good agreement with experimental results. The minimum frequencies of the inner electron pocket, as predicted by theory is close to the β-orbit seen in experiments. The significantly lower variation in $F \cos\theta$ suggests this frequency to originate from a more cylindrical Fermi surface sheet. As it bends upwards we can then identify it as minimum extremal orbit. Similar behaviour but as maximum orbit is observed for γ. We therefore turn to this first and find that it is in good agreement with the middle hole pocket by shifting the band by -80 meV. This now shows that β has most likely mixed contributions from the middle hole and inner electron pocket. At angles around 30° an additional frequency is observed around $F \cos\theta \approx 1000$ T. This labelled as η shows a stronger upturn and suggests that the k_z dispersion form the inner electron pocket might be underestimated, leaving η to represent the minimum of this pocket. Additional very strong peaks were observed at high angles of $\theta \approx 51^\circ$. Those could only be observed in a small angle range but showed a very flat behaviour. This being in good proximity to the frequency expected for the outer hole pocket, we could bring the two in agreement by applying a 18 meV rigid band shift. While only very weak peaks were observed around $\theta = 0$ for this band the strong response at this angle is cause by the Yamaji effect. At this angle the shape of the Fermi surface pocket leads to the fact that maximum and minimum orbits merge into one frequency. Hence the *curvature factor* found in the LK formula causes the amplitude to become maximal.

After this identification of the Fermi surface sheets using the angle dependence of the dHvA frequencies we possess a theoretical model of the Fermi surface topology which can be used in for further analysis and possible theoretical investigations.

Taking the obtained model of the Fermi surface, we have performed cuts of the extremal orbits at the center and top of the BZ. Those are shown in Fig. 5.13 for LiFeAs and LiFeP. We find that both systems are close to fulfilling the geometrical nesting condition. This has been illustrated by plotting cuts of hole pockets (dashed lines) on top of those found for electron pockets (solid lines). Geometrical nesting is expected where shape and size of different Fermi surface sheets are congruent.

For each observed orbit we were also able to extract the effective mass by fits of the LK formula to the temperature dependence of the oscillation amplitude, see Fig. 5.14. As discussed in the context of LiFeAs all masses were taken in dc magnetic field and checked for influences of the Dingle term. We could further use the obtained model of the DFT band structure to obtain the band mass m_b. By comparing the DFT values to the experimental results we obtain the renormalization factor $\lambda = m^*/m_b - 1$, which reflects interactions such as electron-phonon and electron-electron interactions that are not captured in the LDA band structure calculation. The resulting values are summarized in Table 5.2.

For closely space frequencies such as orbit β and η we have fitted the entire data-set $\tau(T, B)$ as described for LiFeAs using the LK formula. As the band mass m_b is given as the second derivative of the energy dispersion at the Fermi level we can also relate

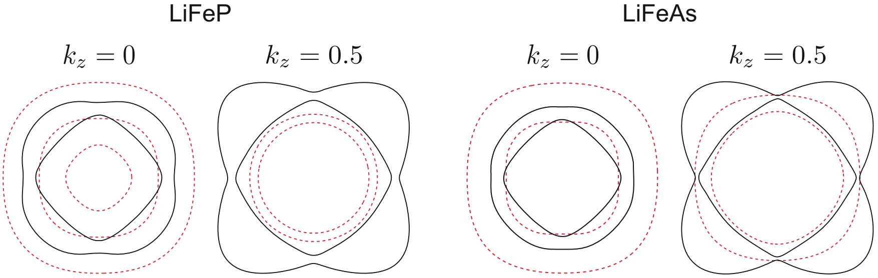

Fig. 5.13 Slices of the Fermi surface of LiFeAs and LiFeP at $k_z = 0$ and $k_z = 0.5$. The *dashed* (*solid*) *lines* represent the hole (electron) sheets after rigid band shifts as, explained in the text. The pockets where shifted in [110] direction to overlap for better comparison

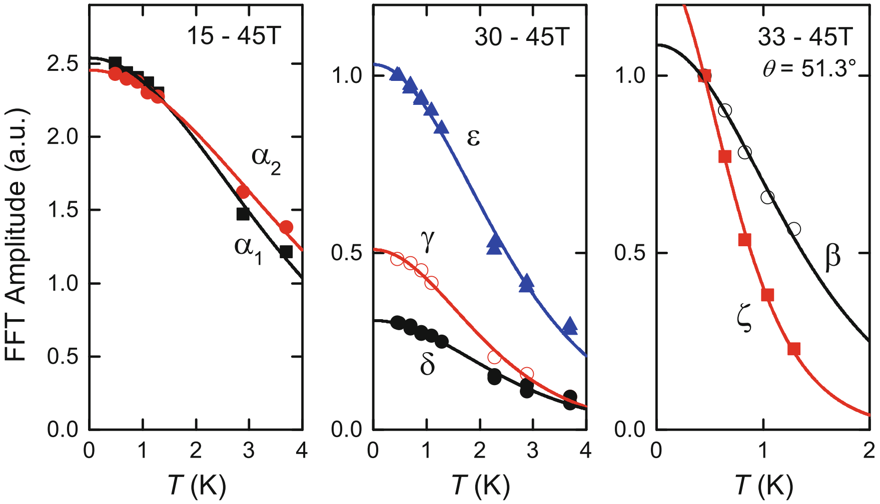

Fig. 5.14 Temperature dependence of the FFT amplitude of the observed extremal orbits in LiFeP. Field ranges are indicated in the panels respectively. The *solid lines* are fits to the data using the temperature dependence in the LK formula

it to the change of extremal area with respect to changes in the chemical potential. This is the procedure used to determine the band mass from DFT calculations. By calculating $A(E_F + \Delta E)$ and taking the first derivative we obtain m_b. For hole pockets we find that the extremal area shrinks with increasing the chemical potential, while for electron pockets the opposite is the case. Therefore we can distinguish electron and hole pockets in DFT calcluations by the sign of their band masses. We find in LiFeP three bands with negative band masses that hence correspond to hole pockets and two with positive signs, electron pockets, see Table 5.2. While we had argued in the introduction that in the presense of the third hole pocket we would expect the lifting of nodes the comparison with penetration depth shows that this seems not to hold for LiFeP.

Surprisingly while most bands in LiFeP show an enhancement of 1.4–2.3 the orbits β and γ found for the middle hole pocket show a much lower renormalization of 0.6 and 0.7. The value that was expected for electron-phonon coupling, as already mentioned, $\lambda_{ep} = 0.2$ [18]. So while the strongly k_z dependent Fermi surface sheets of inner and outer hole pocket are enhanced by a factor 10 over λ_{ep} we find for most cylindrical hole sheet only a factor 3 to 4 which is similar to those found in non superconducting $BaFe_2P_2$ [19]. As within BCS theory the superconducting gap is linked to the density of states at the Fermi level and hence to the effective mass, this finding would suggest to find the smallest superconducting gap on band 2. Hence it might be a good candidate for the formation of accidental nodes seen in magnetic penetration depth measurements [4].

In the case of LiFeAs we had argued that only two hole pockets are present, raising the question whether the absent hole in LiFeAs is the discussed third hole pocket.

Table 5.2 Measured values for LiFeP for the dHvA frequencies extrapolated to $\theta = 0$. The effective masses and bandmasses are given in units of the bare electron mass. The values marked with † are taken at an angle of $\theta = 51.3°$. Values marked with $^\sharp$ are taken on data that might possibly include contributions form different orbits

Orbit	$F_0(T)$	m_b	m^*	$\|\lambda\|$
α_1	316(2)	-0.44	1.1(1)	1.5(3)
α_2	380(2)	-0.39	1.0(1)	1.6(3)
$\beta^\dagger$	$2040(10)^\dagger$	$-1.7^\dagger$	$4.4(1)^\dagger$	$0.6(2)^\dagger$
$\beta^\sharp$	1160(10)	$+1.1$	$3.6(2)^\sharp$	$2.3(2)^\sharp$
γ	1670(10)	-1.6	2.7	0.7
$\zeta^\dagger$	$5550(10)^\dagger$	-1.8	$7.7(2)^\dagger$	$2.1(5)^\dagger$
δ	2040(20)	$+0.92$	2.2(1)	1.4(1)
ε	2840(10)	$+0.83$	2.2(2)	1.6(3)

For this we can compare our findings to more detailed calculations on the orbital character, including Wannier function [4]. The results of these calculations, see in Fig. 5.15, show the distribution of d_{xy} orbital character among the Fermi surface. Kuroki et al. [9] predicted that the *third hole pocket* would contain dominantly d_{xy} orbital character. In LiFeAs such a pocket is found and identified as the outer hole pocket. Hence it is present in this system. In LiFeP distributions of d_{xy} orbital character are found for the middle and outer hole pocket, showing a significantly different result than LiFeAs. The mixed orbital weight is caused by a degeneracy of these pockets without spin-orbit coupling. It was pointed out earlier that the orbital content has influence on the pair-scattering strength between orbits. We had argued in the introduction that the calculations by Tapp et al. [1] had shown a highly anisotropic gap on the electron pockets that was close to becoming nodal. While both LiFeAs and LiFeP are close to fulfilling the geometrical nesting condition the more detailed

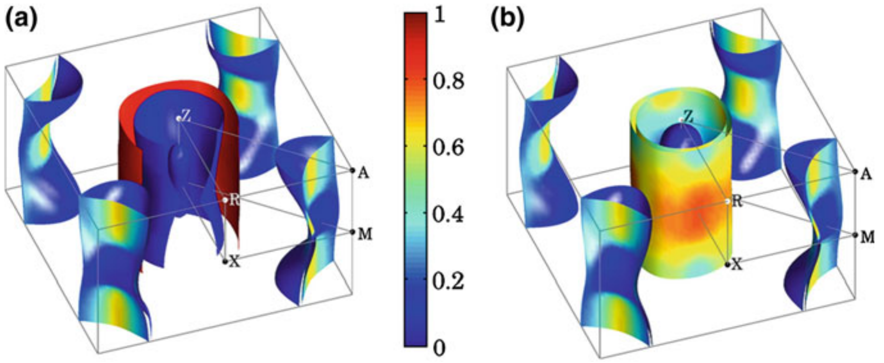

Fig. 5.15 Fermi surface of LiFeAs (**a**) and LiFeP (**b**). The Fermi surface pockets have been colored representing the orbital weight of d_{xy} orbital character. Figure taken from Ref. [4]

and possibly minor effect of a change in the orbital weight distribution could still cause the inter-band pair-scattering to reduce enough to lead to *accidental* nodes. This however would suggest the nodes to be located on the electron pockets.

Following this argument and suggestions made by Maier et al. [10], the formation of a superconducting gap in the SDW channel is favoured by good nesting of Fermi surface sheets with equal orbital character, we notice that this should hold both for the middle and outer hole pocket equally. The strong difference seen in the renormalization of the two pockets is not expected from this point of few as both are close to good nesting and contain similar orbital characters. This is even more surprising when comparing the renormalization of the inner and middle hole band. As the inner hole pocket is seen to possess a peanut-shaped topology that is caused by strong d_{z^2} orbital character at the top and bottom of the BZ it should be less susceptible to inter-band interactions than others. The renormalization however is close to that found for the outer hole pocket.

When comparing the renormalizations found for LiFeP with those for LiFeAs on the electron pockets we find a factor 2 increase for LiFeAs. This goes along with the increase in T_c from 5 to 18 K. Hence we argue that the driving mechanism for the enhancement of the quasi particle mass is the same that causes the increase in T_c. This would again favour the scenario of nodes on the middle hole pocket as this would be least coupled to this interactions.

5.4 Bandstructure Calculation

As the bandstructure of iron-based superconductors depends significantly on details in the crystal structure in this section we will take the approach to investigate changes of the pnictogen height h_{pn} and the crystal structure on the bandstructure of LiFeP by using the WIEN2k-package [7]. Starting from the lattice parameters determined by x-ray diffraction for our crystals $a = 3.6955$ Å and $c = 6.041$ Å [20]. The structure parameter are used from Tapp et al. [1].

5.4.1 Importance of the Pnictogen Height

Since the pnictogen height has been suggested to play an important role for the formation of nodes on the superconducting gap structure [4, 9] we will focus on this first. To get an idea of the changes on the band struture in LiFeP due to this, calculations for different values of the pnitogen height, leaving the lattice parameter constant, were performed. The resulting bandstruture is plotted in Fig. 5.16 for the pnictogen height according to Ref. [1] and for a 10 % change. This rather large change was used for clarity as the present study should serve to identify trends rather than quantitative results. The most important orbital content d_{xy} and $d_{xz,yz}$ are plotted separately. While for the pocket made up mainly of d_{xy}-orbital character

Fig. 5.16 Bandstructure of LiFeP obtained from experimental lattice parameters (**a**). In panel (**b**) the only parts with dominant $d_{xz,yz}$ orbital character are shown for experimental and values of the pnictogen height h_pn and for a 10 % change. The same procedure has been done for the d_{xy} orbital character in panel (**c**)

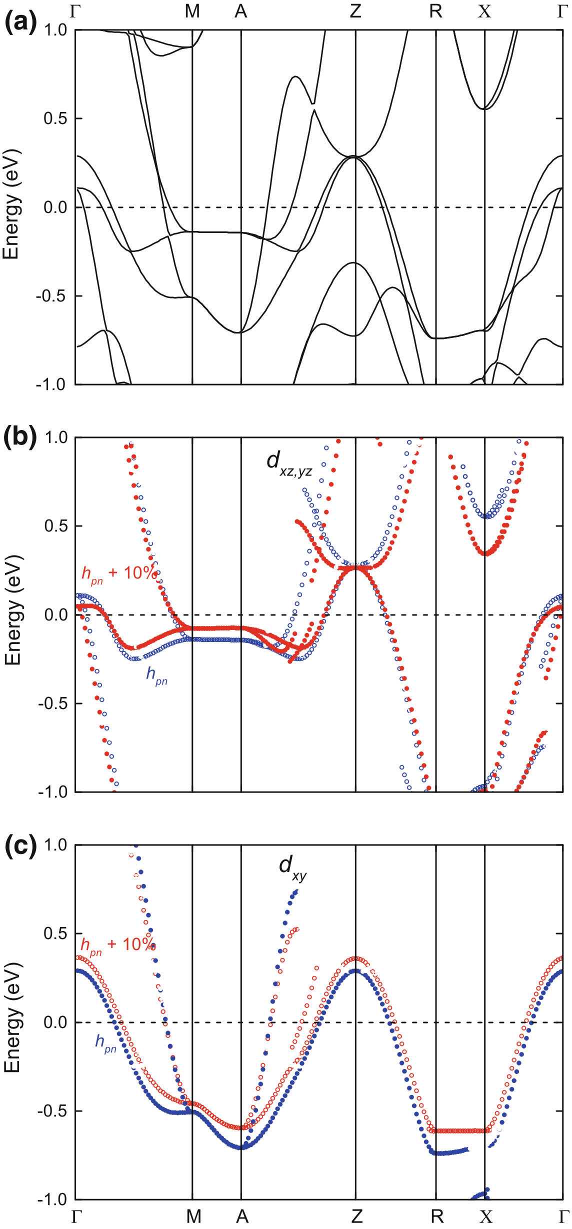

the change occurs in pocket size, the other bands are mainly effected by bandwidth. The change in the first case, d_{xy}-orbital, is consistent with the change predicted in Ref. [9], for the given parameter the bandstructure calculation predicts three hole pockets in the system. However in LaFePO Kuroki et al. [9] were able to show the disappearance of the third hole pocket, which would require a much larger change in the crystal structure of LiFeP. Further the result shows that even so rigid band shifts, as mentioned in the $\mathrm{BaFe_2(As_{1-x}P_x)_2}$ section, give good agreement with the experimental results, for bands with strong orbital mixing this procedure might not be suited.

5.4.2 *Variation in Lattice Parameter*

Single crystals of LiFeP are only available in small dimensions as mentioned before. This makes it hard to resolve the lattice parameter with high precision. As these are believed to have great influence on the bandstructure [9], calculation with varying lattice constants around the experimental values have been performed. To illustrate the changes, the extracted de Haas-van Alphen frequencies are plotted as function of angle in Fig. 5.17. The lattice parameters were varied by 3 and 5 % in both direction. The used values are indicated in the plot as $(\Delta a, \Delta c)$. Changing the parameter causes the observed pockets to change their k_z-dispersion and the size of the extremal orbits. By increasing the unit cell the system becomes more two-dimensional and promotes better nesting. Plotting the frequencies F_0 observed at $\theta = 0$ versus the change in lattice parameter, one can see that the change is not uniform among all pockets. This is again in agreement with the concept of an orbital dependent change of the Fermi surface. When plotting the bandstructure weighted for the d_{xy} orbital character we find that by changing the lattice constants the bandwidth of all orbital characters is effected. The observed changes in the nesting condition, bandwidth and k_z-dispersion with small changes in crystal structure show the need for a detailed experimental understanding of the Fermi-surface. Only a theoretical model that reflects the real *bulk* Fermi surface topology will be able to help understand the mechanism that drives superconductivity and test theories aiming to explain the nodal versus nodeless superconducting gap.

5.5 Further Development

Further work by theorists and other experimentalists including scanning tunnelling microscopy has been carried out since the publication of our results. While data obtained on LiFeP is still rather limited as available single crystals remain small, LiFeAs has proven to be of great interest to the community. Measurements using ARPES had stated the absence of nesting in the LiFeAs [8] which we could not confirm in our results. As the hole pockets up to date are not seen in LiFeAs using

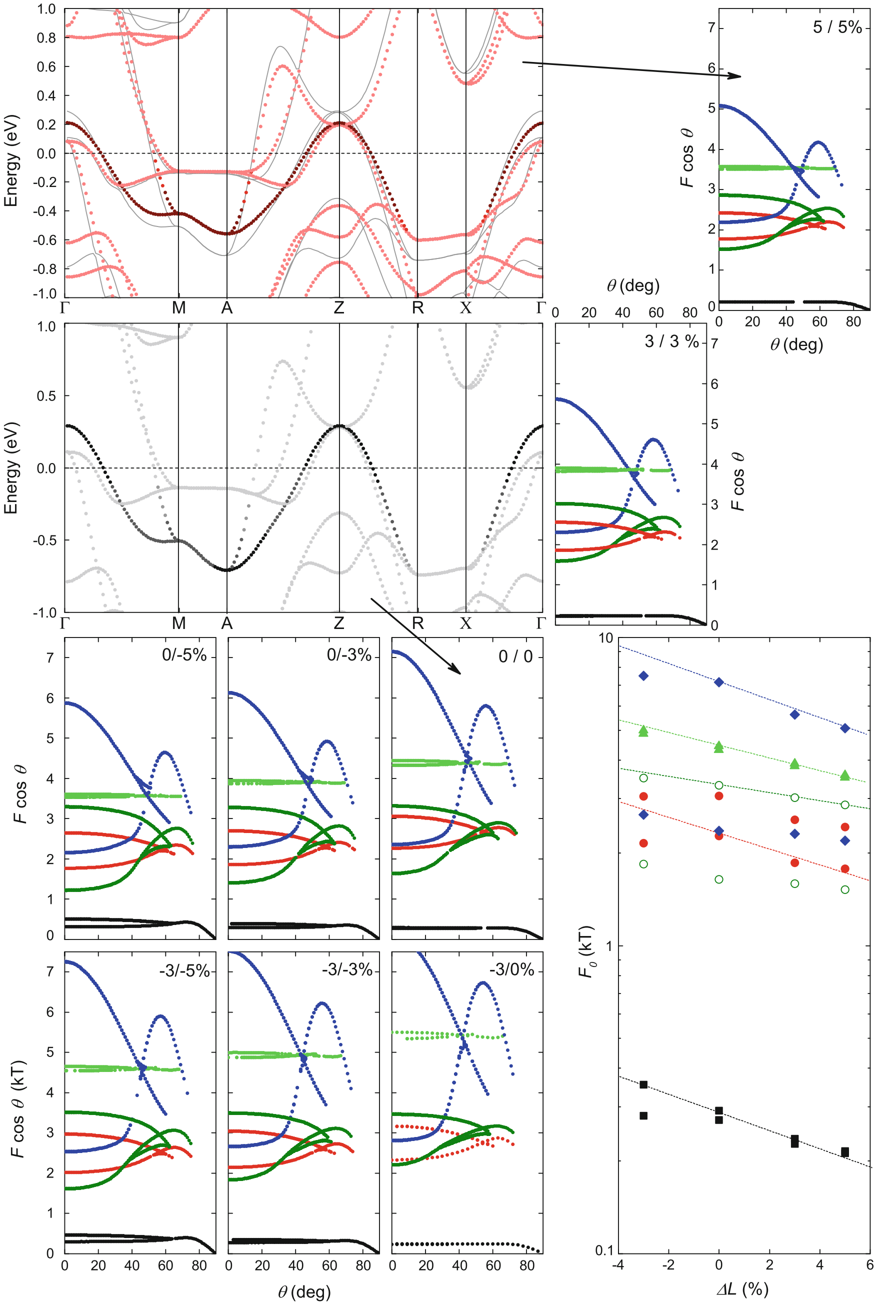

Fig. 5.17 Bandstructure calculation for 5 % increased (*top left*) and experimental (*middle left*) lattice parameter. Further the evolution of the expected dHvA frequencies are shown for a change of ±5 % in lattice parameter and the trend of F_0 in the case of $\Delta a = \Delta c$ (*bottom right*). Respective changes in lattice parameters are shown in the panels

quantum oscillations, we suggested that the presence of a pocket with $F_0 \approx 350\,\mathrm{T}$ as determined from ARPES [8] should give rise to a strong signal comparable to that observed in LiFeP. This holds even when assuming a similar behaviour as for $\mathrm{BaFe_2(As_{1-x}P_x)_2}$, where the mean free path of the hole pocket decreases strongly upon substitution of arsenide for phosphorous. In further attempts to observe signals from the hole pockets we have repeated the experiment using samples grown with a different method [21] that had shown higher residual resistivity ratios of ∼250. With these samples it was possible to reproduce our previous results, however the ratio of oscillation amplitude to paramagnetic background was smaller, suggesting that a smaller fraction of the sample contributed to the dHvA signal. Studies using STM [22] showed later that the missing hole pockets are in good agreement with the prediction made by band structure calculations. While they were not able to observe the electron pockets, this is believed to be in agreement with a higher scattering rate on the hole pockets than on the electron pockets. For comparison the area determined by STM was transferred to the minimal oscillations frequency using the Onsager relation, Eq. 2.22. The results are shown in Fig. 5.18 for the orbits determined by ARPES [8], dHvA and STM [22].

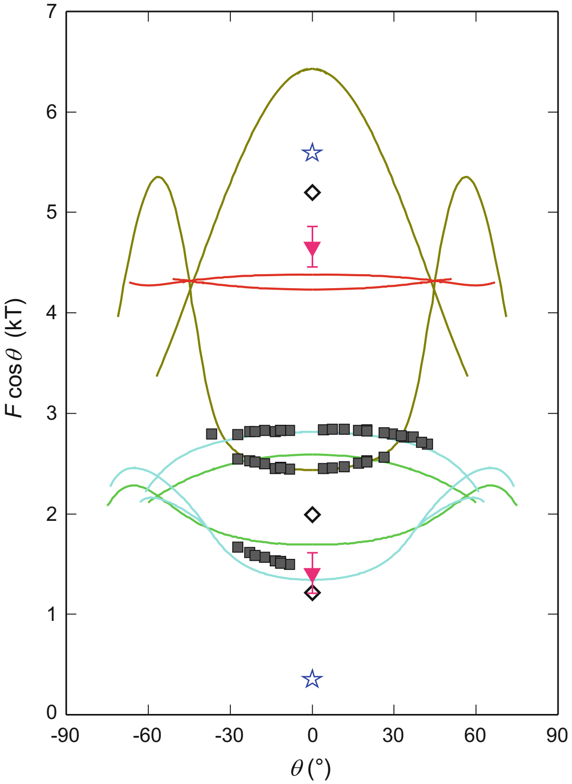

Fig. 5.18 Angle dependence of the dHvA oscillation frequency of LiFeAs. Data presented in this work (*squares*) and the bandstructure obtained by LDA calculation (*solid lines*) is compared with data taken by ARPES (*stars*, hole pockets) [8], STM (*triangles*) [22] and also LDA+DMFT calculations (*diamonds*) [23]

Ferber and co-workers have later performed calculations on the band structure of LiFeAs and LiFeP using *local density approximation + dynamic mean field theory* (LDA+DMFT) [23, 24]. They propose that the implementation of interactions not captured by LDA are responsible for the different results seen by ARPES and dHvA experiments. We have therefore added the proposed extremal orbits from Ref. [23] to Fig. 5.18 for comparison. Those values were obtained for $U = 4\,\text{eV}$ and $J = 0.8\,\text{eV}$. While they yield a significant increase in band 3 the values obtained for band 2 are in rather good agreement with dHvA and STM [22] results rather than ARPES [8]. A further increase in the Hund's coupling J would enhance the trend, but it would still not bring band 2 in agreement with the data obtained by ARPES. The same procedure was also used in Ref. [24], where the expected dHvA frequencies from LDA+DMFT were calculated for LiFeP. Only little changes to the LDA band structure were found that could neither explain the large shift of band 2 nor the low frequencies obtained on band 1 correctly. Whether the application of DMFT calculation can lead to a reconciliation of ARPES and dHvA data is therefore not clear. The observed trend is comparable to that found in Ref. [17] where the increase in Hund's rule J coupling is related to the change in lattice parameter, leading to an enhanced localization. However we believe this can only be seen as a trend, since DMFT only considers onsite interactions, while long wave-length interactions are neglected [17, 24].

This can also be seen when comparing the mass-enhancement found in dHvA measurements and DMFT calculation [23, 24], shown in Fig. 5.19. In Ref. [23] the authors had stated the mass-enhancement for different orbital character. We have therefore used the dominant orbital character to represent the enhancement factor for each orbit. We find that the quasi particle mass-enhancement in LiFeAs and LiFeP is roughly a factor two lower in LDA+DMFT than the values obtained by dHvA measurements. In LiFeP we see that the low renormalization in band 2 from dHvA is

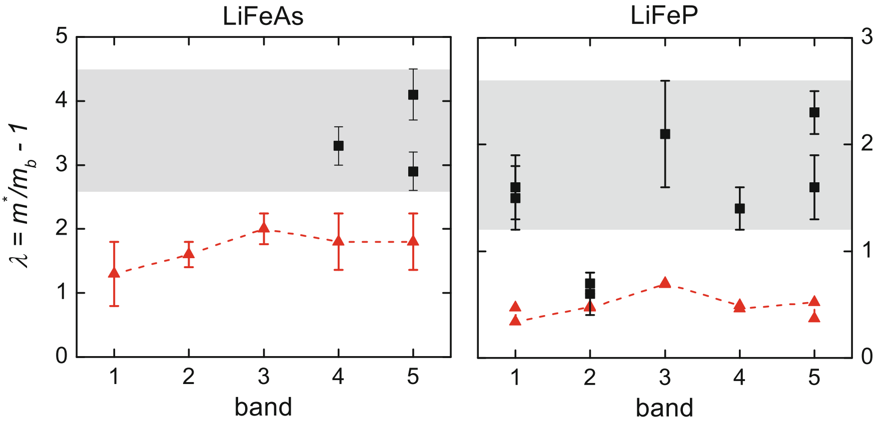

Fig. 5.19 Comparison of quasi particle mass of bands in LiFeAs and LiFeP as found by dHvA measurements (*squares*) and LDA+DMFT calculations [24] (*triangles*). Bands 1, 2 and 3 are inner, middle and outer hole band respectively, while 4 and 5 are the outer and inner electron band

the only one found to be in good agreement with the calculations. This suggests that the middle hole pocket is only coupled to onsite interactions while a non-local effect causes a further enhancement of effective mass in the other pockets. While the trend for the formation of magnetism was correctly obtained in Ref. [17] by this procedure the obtained results being close to that for non-superconducting $\mathrm{BaFe_2(As_{1-x}P_x)_2}$ suggests that superconductivity is caused by non-local effects.

A third point discussed in Ref. [24] is the possible origin of nodes in LiFeP. Following the suggestion by Kemper et al. [25], the d_{z^2} orbital content, causing the peanut-shaped inner hole pocket, might be responsible for the formation of nodes on the superconducting gap by reducing the pair-interaction. By including DMFT Ferber et al. [24] found that the inner hole pocket changes from a cigar shaped pocket to a cylindrical Fermi surface sheet. While we were not able to observe quantum oscillations at $\theta = 90°$ in LiFeP we did observe a significant down turn of the oscillation frequency in $F \cos\theta$ suggesting a significant k_z-dispersion. We must therefore conclude that the strong change to a cylindrical Fermi surface sheet of the inner hole pocket might be an artefact of the chosen U and J parameters. The proposed promotion by d_{z^2} orbital character [25] therefore still holds in LiFeP.

5.6 Conclusion

In summary we determined almost the entire Fermi surface topology of LiFeP. For LiFeAs we were able to observe both electron pockets. For both materials the experimental results were in good agreement with band structure calculations. Including results obtained by STM [22] this is also the case for the hole pockets in LiFeAs. Based on the refined Fermi surface calculations we suggest that both systems possess significant nesting. The mass-enhancement between the systems is in agreement with the increase in T_c, suggesting a relation between the mechanism causing the mass-enhancement and superconductivity. An open question remains the appearance of nodes in the superconducting gap structure of LiFeP. We found three hole pockets for this systems which, as mention, are well nested with the electron pockets. While this should lift the nodes [9], nodal behaviour was observed in penetration depth measurements [4]. Based on our results and further development three different possible scenarios were discussed that could possibly lead to the formation of nodes on the superconducting gap on different Fermi surface sheets. The most striking feature that has not been reproduced in theoretical work so far is the significant difference in mass enhancement between the different hole pockets in LiFeP. Despite the low superconducting critical temperature, LiFeP might help to understand the nature and origin of accidental nodes.

References

1. J. Tapp, Z. Tang, B. Lv, K. Sasmal, B. Lorenz, P. Chu, A. Guloy, Phys. Rev. B **78**, 060505 (2008)
2. M. Pitcher, D. Parker, P. Adamson, S. Herkelrath, A. Boothroyd, R. Ibberson, M. Brunelli, S. Clarke, Chem. Commun. (Cambridge) **45**, 5918 (2008)
3. Z. Deng, X. Wang, Q. Liu, S. Zhang, Y. Lv, J. Zhu, R. Yu, C. Jin, EPL **87**, 37004 (2009)
4. K. Hashimoto, S. Kasahara, R. Katsumata, Y. Mizukami, M. Yamashita, H. Ikeda, T. Terashima, A. Carrington, Y. Matsuda, T. Shibauchi, Phys. Rev. Lett. **108**, 047003 (2012)
5. S. Kasahara, K. Hashimoto, H. Ikeda, T. Terashima, Y. Matsuda, T. Shibauchi, Phys. Rev. B **85**, 060503 (2012)
6. S. Kasahara, K. Shibauchi, K. Hashimoto, K. Ikada, S. Tonegawa, R. Okazaki, H. Shishido, H. Ikeda, H. Takeya, K. Kirata, T. Terashima, Y. Matsuda, Phys. Rev. B **81**, 184519 (2010)
7. P. Blaha, K. Schwarz, G. Madsen, D. Kvasnicka, J. Luitz, *WIEN2K* ed. by Karl Heinz Schwarz (Technische Universität Wien, Austria, 2001)
8. S. Borisenko, V. Zabolotnyy, D. Evtushinsky, T. Kim, I. Morozov, A. Yaresko, A. Kordyuk, G. Behr, A. Vasiliev, R. Follath, B. Büchner, Phys. Rev. Lett. **105**, 076002 (2010)
9. K. Kuroki, H. Usui, S. Onari, R. Arita, H. Aoki, Phys. Rev. B **79**, 224511 (2009)
10. T. Maier, S. Graser, D. Scalapino, P. Hirschfeld, Phys. Rev. B **79**, 224510 (2009)
11. C. Platt, R. Thomale, W. Hanke, Phys. Rev. B **84**, 235121 (2011)
12. F. Pobell, *Matter and Methods at Low Temperatures*, 3rd edn. (Springer, 2007)
13. G. Pollack, Rev. Mod. Phys. **41**, 48 (1969)
14. A. Carrington, P. Meeson, J. Cooper, L. Balicas, N. Hussey, E. Yelland, S. Lee, A. Yamamoto, S. Tajima, S. Kzakov, J. Karpinski, Phys. Rev. Lett. **91**, 037003 (2003)
15. A. Carrington, Rep. Prog. Phys. **74**, 124507 (2011)
16. L. Ortenzi, E. Cappelluti, L. Benfatto, L. Pietronero, Phys. Rev. Lett. **103**, 046404 (2009)
17. Z. Yin, K. Haule, G. Kotliar, Nat. Mater. **10**, 932 (2011)
18. L. Boeri, O. Dolgov, and A. Golubov, Physica (Amsterdam) C **469**, 628 (2009)
19. B. Arnold, S. Kasahara, A. Coldea, T. Terashima, Y. Matsuda, T. Shibauchi, A. Carrington, Phys. Rev. B **83**, 220504 (2011)
20. S. Kasahara, Private communication.
21. F. Rullier-Albenque, D. Colson, A. Forget, H. Alloul, Phys. Rev. Lett. **109**, 187005 (2012)
22. M. Allan, A. Rost, A. Mackenzie, Y. Xie, J. Davis, K. Kihou, C. Lee, A. Iyo, H. Eisaki, T. Chuang, Science **336**, 563 (2012)
23. J. Ferber, K. Foyevtsova, R. Valenti, H. Jeschke, Phys. Rev. B **85**, 094505 (2012)
24. J. Ferber, H. Jeschke, R. Valenti, Phys. Rev. Lett. **109**, 236403 (2011)
25. A. Kemper, T. Maier, S. Graser, H. Cheng, P. Hirschfeld, D. Scalapino, New J. Phys. **12**, 073030 (2010)

Chapter 6
$YBa_2Cu_4O_8$

6.1 Introduction

High temperature superconductivity in copper oxides remains a challenge more than 25 years after their discovery by Bednorz and Mueller [1]. High quality single crystals in the field of iron-pnictides were available within months after their discovery, whereas it took almost 20 years until advances in crystal quality and measurement techniques in high magnetic field lead to the first observation of quantum oscillations in the cuprates [2].

While there are some similarities in the phase diagrams of cuprates and pnictides, see Fig. 6.1, there are even more differences. The similarities that led to a large interest in the pnictides and the hope that they would help towards a better understanding of cuprates was based mainly on the close proximity of superconductivity and anti-ferromagnetism (see phase diagram Fig. 6.1). However, while the pnictides possess a metallic ground state the cuprates become insulating when entering the anti-ferromagnetic state. This being due to the half filled bands in these materials, it can be understood by Mott-Hubbard-Physics [3]. Upon doping with holes or electrons the AFM state is suppressed. While for electron doped systems like $Nd_{2-x}Ce_xCuO_4$ (NCCO), with lower T_c, this leads to a superconducting state covering the QCP of the AFM state, in the hole doped systems the AFM state typically is suppressed to zero at the verge of superconductivity. At the same time a new state is found that sets in at high temperature. By optical measurements is was found that in this phase the density of states at the Fermi-level is reduced. This is known as the *pseudogap* [4]. While the orgin of this state is still under strong debate a variety of phenomena where observed in this region of the phase diagram. A change in the Hall signal from hole to electron like upon cooling was observed in $YBa_2Cu_3O_{7-\delta}$ (YBCO) [5] in the underdoped (UD) regime. Here quantum oscillations showed, in the same system, a small Fermi-surface pockets which covered only about 2 % of the BZ while in the overdoped regime a large Fermi-surface sheet was observed in $Tl_2Ba_2CuO_{6+\delta}$ (Tl2201), see Fig. 6.4 [2, 6]. ARPES experiments had previously shown the large

C.M. Putzke, *Fermi Surface and Quantum Critical Phenomena in High-Temperature Superconductors*, Springer Theses,
DOI 10.1007/978-3-319-48646-8_6

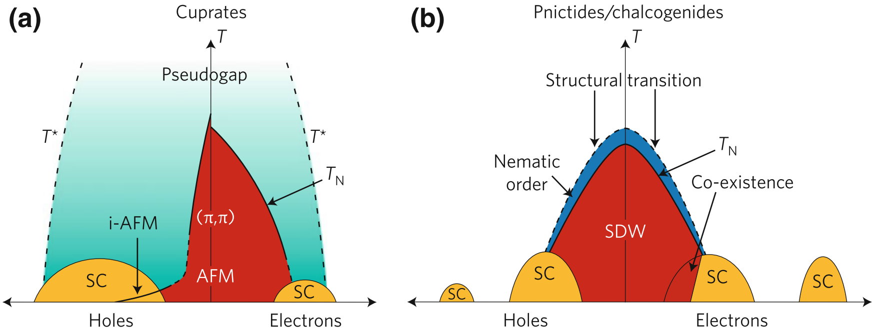

Fig. 6.1 Schematic phasediagram of cuprates (**a**) and pnictides (**b**). Taken from Ref. [7]

Fermi surface in the overdoped (OD) regime where also Fermi liquid behaviour, T^2 dependence of resistivity, was observed. In the UD regime however, ARPES only observed *Fermi arcs* [2], disconnected pieces of the original Fermi surface in the nodal direction. Those were believed to arise from a loss of density of state in the pseudogap region in the anti-nodal direction of the BZ. Therefore the observation of quantum oscillations should have not been possible.

A possible explanation was given by Seibold et al. [8], who discussed the change in spectral weight at the Fermi surface in the context of nesting leading to a formation of an incommensurate charge density wave (CDW). They found in their calculation intensity distributions very similar to those seen in ARPES experiments.

Recently the formation of an incommensurate CDW has been of great interest as it was found to exist in a variety of UD cuprates [9–11]. The onset well above the superconducting transition has been observed by resonant x-ray studies. There the authors observe that the intensity of the CDW increases when lowering the temperature but starts to drop again below T_c [9]. It is therefore interpreted as a competing order to superconductivity. When applying a magnetic field the intensity below T_c increases. Nuclear magnetic resonance [12] and ultrasound measurements [13] have found charge order in magnetic fields above 18 T. The onset temperature of the charge order in field is in good agreement with the results obtained on the Hall measurements as shown in Fig. 6.2a.

When comparing the onset temperature T_H, at which the Hall signal deviates from it extrapolated value, (see Fig. 6.2b) with the value of the onset of CDW [9] one finds that those values are in good agreement.

Further the deviation of the superconducting critical temperature from a perfect parabolic behaviour [14], shown in Fig. 6.2 and the competition found between superconductivity and CDW [9] causes speculation as to whether the CDW is the long missing building block leading to superconductivity or if its appearance hinders a higher superconducting critical temperature.

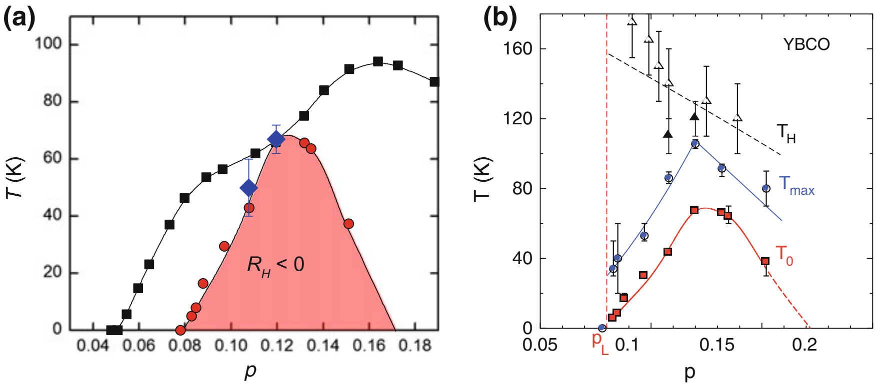

Fig. 6.2 **a** Superconducting critical temperature of YBCO (*squares*) as function of doping p [14]. The *solid circles* show the temperature T_0 below which as negative Hall signal is observed in high magnetic field [15]. Diamonds represent the temperature at which charge-order was observed in fields above 18 T by NMR [12]. **b** The temperature of sign change of the Hall signal T_0 the maximum in Hall signal T_{max} and the temperature at which the Hall coefficient starts to deviate from its predicted value T_H are shown for a variety of doping of YBCO in the UD regime [15]

6.1.1 Crystal Structure and Crystal Growth

Single crystals of $YBa_2Cu_4O_8$ (Y124) were grown by S. Adachi using a self-flux method under high pressure [16]. For this a high-pressure gas mixture of 80 % Ar - 20 % O_2 was used. The starting materials Y_2O_3, $BaCO_3$ and CuO were place in a Y_2O_3 crucible in the ration 1:8:20. After calcination a high-pressure growth using a O_2 hot isostatic pressure apparatus, single crystals of typically $0.1 \times 0.2 \times 0.05\,\text{mm}^3$ were extracted. Those crystals have *Ammm* space group, determined by x-ray diffraction [16], which is shown in Fig. 6.3.

Y124 features fully occupied copper-oxide double chains, unlike YBCO where the oxygen stoichiometry is rather unstable. This makes Y124 thermally more stable than YBCO [17]. While the oxygen content in YBCO can be changed with relatively low temperatures [18], for Y124 no changes of composition or superconducting critical temperature were observed up to 850 °C [17]. This allows us to cure electrical contacts at elevated temperatures in Y124. Also the structural transition from tetragonal to orthorhombic symmetry found in YBCO is absent in Y124. These benefits over YBCO make the system particularly interesting as the complications of different oxygen ordered states are not present in Y124.

In order to compare results obtained on Y124 to those on YBCO it is desirable to locate it on a 'general' phase diagram. When doping Y124 with Ca it was found that the superconducting critical temperature increases up to 90 K [19] and therefore Y124 should be place on the UD side of the phase diagram. A more precise value of $p = 0.14$ was given in Ref. [20], which was obtained by averaging data from T_c, the pseudogap temperature T^* and Seebeck coefficient compared to YBCO.

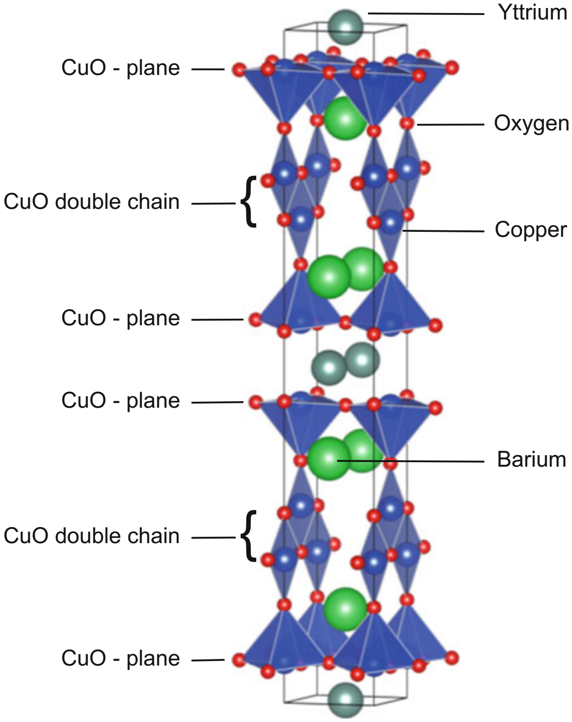

Fig. 6.3 Crystal structure of $YBa_2Cu_4O_8$

6.1.1.1 Fermi Surface in the Cuprates

The first quantum oscillations in a cuprate were observed in $YBa_2Cu_3O_{6.5}$ using Shubnikov-de Haas measurements [2]. The oscillations with frequencies of $F = 540\,\mathrm{T}$ corresponded to small Fermi-surface pockets covering only about 2 % of the BZ. see Fig. 6.4. This observation was a big surprise as ARPES measurements had suggested that UD YBCO should not have a closed Fermi surface but only contain Fermi arcs. Shortly after two groups found quantum oscillations also in Y124 with very similar frequencies $F = 660 \pm 30\,\mathrm{T}$ but slightly higher effective masses $m = 2.7 \pm 0.3$ [20, 22] than those observed in YBCO. Since those first discoveries a number of reports have shown the evolution of the effective mass and oscillation frequency in the underdoped regime in YBCO. While the effective mass is found to strongly increase, suggesting an approach to a diverging behaviour close to optimal doping, the oscillation frequency is found to increase almost linearly, see Fig. 6.5a [23]. However this only accounts for the most dominant frequency. Improvements in the measurements in pulsed magnetic fields in the last years have allowed the study these materials to even higher fields, showing the existence of two more frequencies, close to the main oscillation frequency, see Fig. 6.5b–c [23].

While in the hole doped compounds the observation of quantum oscillations close to optimal doping is difficult due to the high upper critical field, those experiments

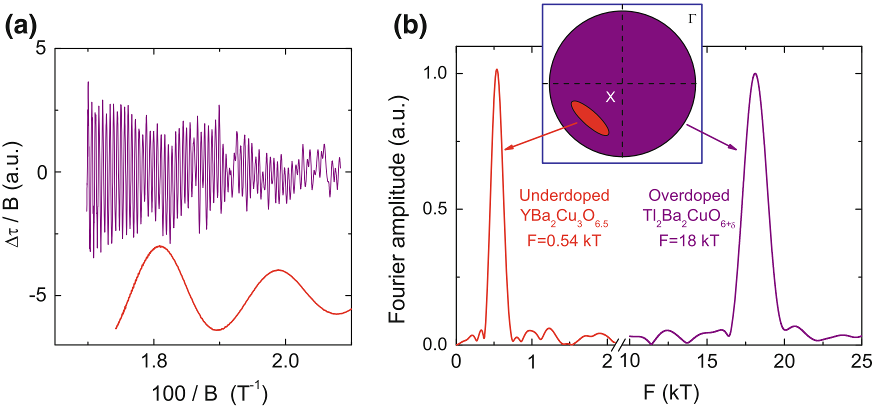

Fig. 6.4 **a** de Haas-van Alphen signal obtained for slow (YBCO) and fast (Tl2201) oscillations in high magnetic fields. The corresponding FFT spectra are shown in (**b**). Taken from Ref. [21]

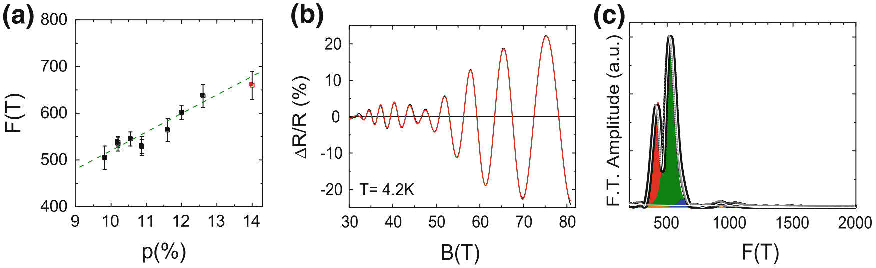

Fig. 6.5 **a** Evolution of the dominant oscillation frequency in YBCO with doping p. **b** Oscillatory component of the magnetoresistance of YBCO $p = 0.108$ at $T = 4.2\,\mathrm{K}$ in pulsed magnetic field. The FFT spectra of the oscillatory data is shown in (**c**). Taken from Ref. [23]

where possible in the electron doped materials. Here the critical temperature is much lower and the upper critical field of less than 20 T in the optimally doped samples allows the study of the normal state over the entire phase diagram. There it was found that fast and slow oscillations are observed up to optimal doping [24–26]. Using a reconstruction based on SDW as proposed by Lin and Millis [27] this behaviour can be explained by magnetic breakdown. While such a reconstruction scenario had also been discussed for the hole doped systems for a long time, recently new attention was drawn to the field with the discovery of charge order in high magnetic fields using NMR [12] and ultrasound studies [13]. Short after it was found that even in zero field a short range incommensurate CDW state exists that gets enhanced by lowering the temperatures [9]. This CDW phase coincides with the region of the Fermi surface where quantum oscillations are observed and where the Hall signal changes sign [5]. It is therefore believed that the CDW could be the mechanism which drives the reconstruction of the Fermi surface. This is supported by the finding of Tabis et al. [28] in Hg1201, where the observed frequency in quantum oscillations [29] is higher than those in YBCO but can be linked to a different incommensurate CDW wave vector. It is therefore believed that the low frequency quantum oscillations are a general feature of UD cuprates that is driven by a charge density wave that competes with superconductivity [9].

In the overdoped regime of Tl2201 quantum oscillations with a much higher frequency of $F \approx 18\,\text{kT}$ where observed, see Fig. 6.4 [6], which was in agreement with band structure calculations and ARPES measurements.

$YBa_2Cu_4O_8$ (Y124) is similar to YBCO. However it is only available in the stoichiometric form and cannot be doped by oxygen annealing. The typical transition temperature of around $T_c \approx 80\,\text{K}$ places it close to optimally doped YBCO. Slow quantum oscillations have been observed similar to YBCO [20, 22], but no charge order has yet been reported. By applying hydrostatic pressure the superconducting critical temperature in Y124 increases. This is believed to be similar to the process of hole doping as in the case of hydrostatic pressure the c-axis lattice parameter shrinks, which is similar to the effect found for oxygen annealing in YBCO [14]. While in YBCO the CuO-chains are not completely filled, they are in Y124 and hence no change in oxygen-ordering is expected, which should leave us with the pure effect of the lattice parameter changing. Our attempt is therefore to measure quantum oscillations under hydrostatic pressure to determine how the extremal orbit area and the effective mass depend on pressure. As seen in YBCO the mass becomes strongly enhanced when approaching optimal doping. Therefore a similar increase with m^* as a function of T_c is expected.

The origin of the observed Fermi surface pockets lays in the hybridized copper-oxygen bands. As seen in density of states [30] the main contribution to the density of states at the Fermi level comes from the copper atoms in the plane. Significant spectral weight close to the Fermi level is also found from the copper-atoms in the double chains, while the oxygen atoms have a minor contribution. The yttrium and barium bands are localized. While the copper-oxygen double chains contribute two one-dimensional Fermi surface sheets, the Fermi surface of the planes is quasi two-dimensional [30]. This quasi two-dimensional pocket arises from hybridization of copper $d_{x^2-y^2}$-orbitals with oxygen p-orbitals and is most likely giving rise to the observed quantum oscillations. However we need to keep in mind that these band structure calculations are performed in the tetragonal crystal structure of the system. As discussed we expect to find a reconstruction of the Fermi surface at low temperatures, as seen by Hall effect measurements [15], which is most likely caused the formation of a CDW [9].

6.2 Zero-Field Under Pressure

Measurements under pressure at zero field have been performed in a beryllium-copper pressure cell in Bristol. As the sample is only thermalized via the contact wires very slow sweep rates are required. For this the sample was stabilized at a set temperature and then held there for two minutes before reading the resistance. We

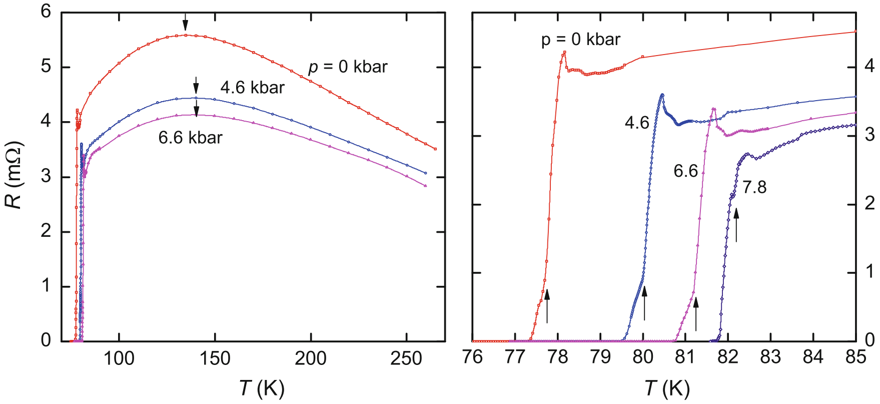

Fig. 6.6 $YBa_2Cu_4O_8$, c-axis resistance versus temperature at different hydrostatic pressures. The *right panel* shows an zoomed view on the superconducting transition

have chosen set points every 10 mK close to the transition and every 5 K between T_c and room temperature. The transition was measured by decreasing and increasing steps, to ensure no hysteresis effect. The resulting resistance versus temperature plots are shown in Fig. 6.6.

While the sample becomes more metallic at room temperature the maximum in c-axis resistance shifts to higher temperatures. The shape of the superconducting transition however remains unchanged. A strong peak is observed just before the superconducting transition. This peak, whose origin might be due to current inhomogeneity, is absent in some samples while being very pronounced in sample with small resistance values. The superconducting transition at $p = 0$ is slightly lower than previous reports but is in good agreement with T_c obtained from heat capacity measurements on a variety of samples. The *kink* in the transition, marked by the arrow in Fig. 6.6, remains constant up to a pressure of about 7 kbar where the peak above T_c disappears and a step like feature appears. We believe that this modification is due to a change in the current path through the sample.

From this we can conclude that in case where quantum oscillations are observed under pressure we will not be able to compare relative amplitude changes between different pressure and also the change of magnetoresistance with pressure can have features that might be due to inhomogeneities rather than intrinsic properties of the system.

6.3 Mass at Zero Pressure

While the effective mass in Y124 had been reported previously we have conducted experiments before using the pressure cell using magnetic fields up 70 T at the LNCMI-Toulouse. The focus on these experiments was to find good quality

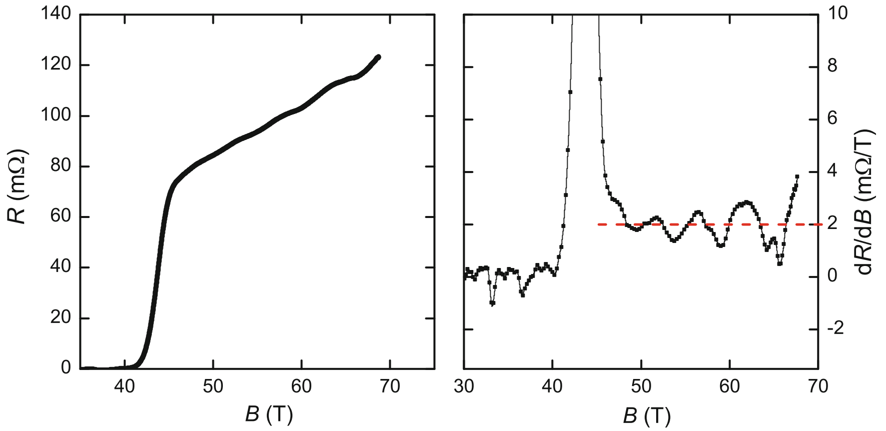

Fig. 6.7 Magnetoresistance and the derivative of a sample of YBa$_2$Cu$_4$O$_8$ at $T = 1.5$ K. The *dashed line* in the *right panel* is a guide to the eye for a linear magnetoresistance

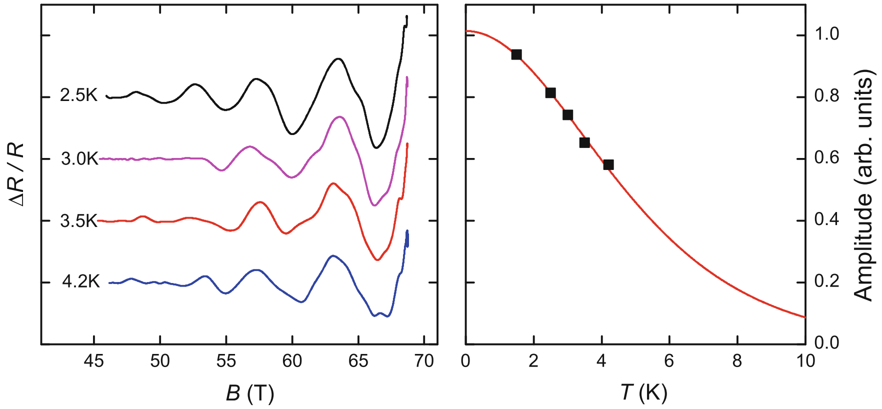

Fig. 6.8 Oscillatory part of the magnetoresistance of YBa$_2$Cu$_4$O$_8$ at various temperature (*left panel*) and the extracted oscillation amplitude versus temperature as extracted by fits of the LK formula to the data (*right panel*). The *solid line* is a fit of the temperature dependent part the LK formula to the data and holds an effective mass of $m^* = (2.0 \pm 0.3)\ m_e$

single crystals and to determine the effective mass prior to using the pressure cell. As the sample in this setup is submerged in liquid helium we have a good knowledge of the sample temperature. Hence we can compare to results at zero-pressure inside the cell for consistency (Fig. 6.7).

In Fig. 6.8 (left) the magnetoresistance of Y124 at a temperature of 2.5 K is shown. When taking the first derivative of this data we obtain the data shown in Fig. 6.8 (right). The dashed line is given as guide to the eye showing that the magnetoresistance does not follow a B^2 dependence but is rather linear in B. By subtracting a smooth background from the raw data we are able to obtain the oscillatory part only.

The data is shown in Fig. 6.6. By fitting the data using the LK formula we are able to track the amplitude dependence with temperature, resulting in the data shown in Fig. 6.6 (right). The solid line represents a fit to the data as given by the LK formula. This gives an effective mass $m^* = (2.0\pm 0.3)m_e$ lower than the previous reports [20]. This result was obtained independently on a second sample. The observed frequency of $F = (650 \pm 30)$ T is consistent with the previous report [20].

6.4 Magnetoresistance Under Pressure

Under hydrostatic pressure the superconducting critical temperature increases. At the same time we observe an increase in the irreversible field, which in accordance to Ref. [31] is defined as the onset of a finite resistance. In Fig. 6.9 the magnetoresistance is shown for one sample at different applied pressure. We find a strong variation of the magnetoresistance at low pressure values. On first sight this in agreement with the drop in resistance in zero-field cool. We remember that in the two-carrier model the magnetoresistance $\Delta\rho \propto \rho_0^{-1}$. This means that for a lower residual resistance ρ_0 we expect a higher response of the resistance in field. This holds up to about $p = 5$ kbar where the magnetoresistance starts to drop again, see Fig. 6.10a. At the same time the derivative of the magnetoresistance saturates as shown in Fig. 6.10b. In the case of YBCO the effect of an increase in T_c is caused by doping which changes the c-axis parameter of the system [14], such that $c \propto p^{-1}$. If we were to assume the same scenario here, which is likely as the hydrostatic pressure could reduce the lattice parameter, the c-axis hopping term $t_\perp$ would increase which leads

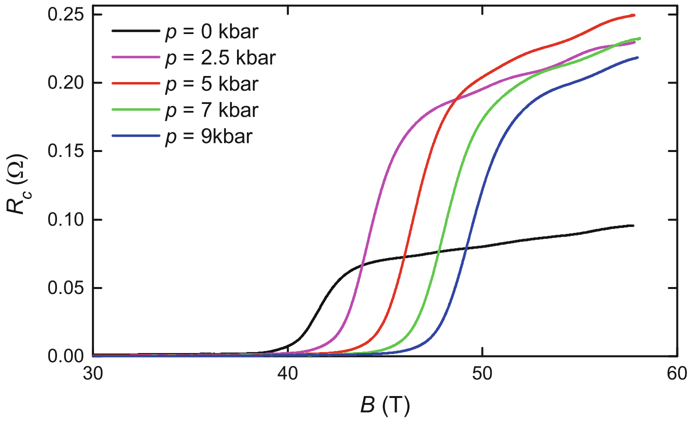

Fig. 6.9 Magnetoresistance of $YBa_2Cu_4O_8$ at $T = 1.5$ K under hydrostatic pressure. A strong increase in the magnetoresistance is found for low pressure values. A increase in the upper critical field with applied pressure is found

Fig. 6.10 **a** Evolution of the magnetoresistance value at $B = 57\,\mathrm{T}$ of $YBa_2Cu_4O_8$. After a strong increase at low pressure of the resistance value a slow decrease is observed in pressure above 5 kbar. The slope of the magnetoresistance saturates at the pressure where the maximum resistance value is observed (**b**)

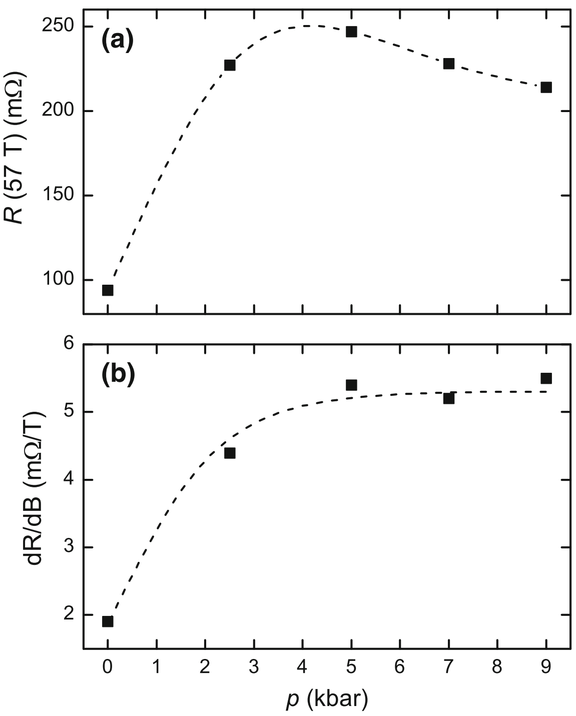

to a decrease in magnetoresistance [32]. While the two effects would constructively lower the zero-field resistance, they would counteract each other under magnetic field.

Further it should be pointed out that the same strong increase in magnetoresistance was observed in a second sample which makes us believe that it is not caused by a change in the current path in the sample. Further the Shubnikov-de Haas oscillations, which will be discussed in the next section show a rather constant amplitude in $\Delta R/R$ for all pressures, suggesting that we do not probe a different part of sample.

6.5 Fermi Surface Evolution Under Pressure

We now turn to the evolution of the Fermi surface. Since we start out with a stoichiometric material, we do not expect any sudden changes when applying pressure. Such changes that could in principle be caused by reorganizing the partial chain filling in YBCO should be absent here. As we mentioned before, both the expected shrinking of the crystal lattice [14] with hydrostatic pressure, as the increase in T_c suggest that the application of pressure has similar effects as hole-doping the system.

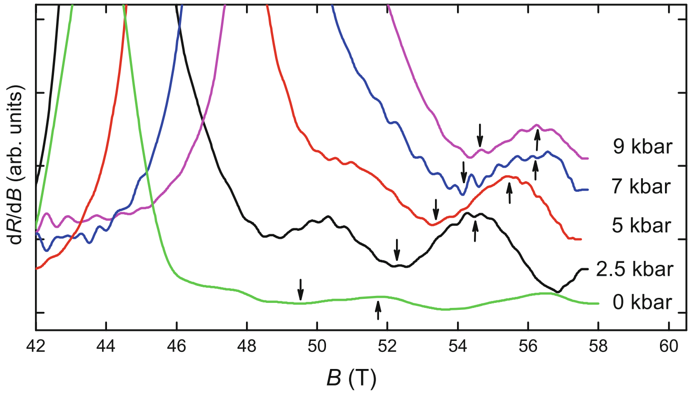

Fig. 6.11 Differential magnetoresistance of $YBa_2Cu_4O_8$ at $T = 1.5$ K. The arrows point at position of maximum and minimum values in the oscillatory part of the signal. A clear phase shift is observed, indicating a shift in oscillation frequency

We will first turn to the frequency of the observed Shubnikov-de Haas oscillations. In Fig. 6.11 the differential of the magnetoresistance is shown for a temperature of 1.5 K at different pressure. The data has been offset for clarity. We see that the observed maxima and minima are shifted in field. This most likely being caused by a change in oscillations frequency, we will try to track the evolution of F with pressure. For pressures of 7 and 9 kbar the limited normal state field window does not allow for a very precise determination and hence the obtained result can only be seen as a trend. In Fig. 6.12a the obtained frequencies, from LK fits to the data, are shown. While the results would allow for a rather constant extremal orbit size with pressure, the strong change seen in Fig. 6.11 does not support this scenario. The date rather suggest a small continuous increase in orbit size with pressure, which is consistent with the assumption that the application of pressure is similar to hole doping [6, 21]. For the highest pressures of 9 kbar very little change in the maximum position is seen compared to that of 7 kbar. This could be interpreted as a saturation in frequency at this point. In the previous section we saw that the slope of the magnetoresistance becomes roughly constant in this pressure range. For a *barrel-shaped* Fermi surface like present in the cuprates we expect for the magnetoresistance $\Delta\rho(B) \propto k_F B/t_\perp m^*$ [33]. In this we need to assume that the decrease in zero-field resistance is caused by an increase in the c-axis hopping parameter $t_\perp$ while the scattering rate τ is in first approximation unaffected. We then conclude that for the $d\rho/dB$ being constant the term $k_F B/t_\perp m^*$ to be constant. As $t_\perp$ is expected to be proportional to p for constant k_F a reduction of m^* is expected. In fact, we do observe a trend towards a lower effective mass at high pressure, see Fig. 6.12b. Those masses were extracted from LK fits with a smooth background to the derivative shown in Fig. 6.11 at different temperatures between 1.5 and 4.2 K. The obtained amplitudes were then used to fit the temperature dependent part of the LK formula to deduce the effective mass. This reduction in the effective mass seems to be in contrast to the increase in the

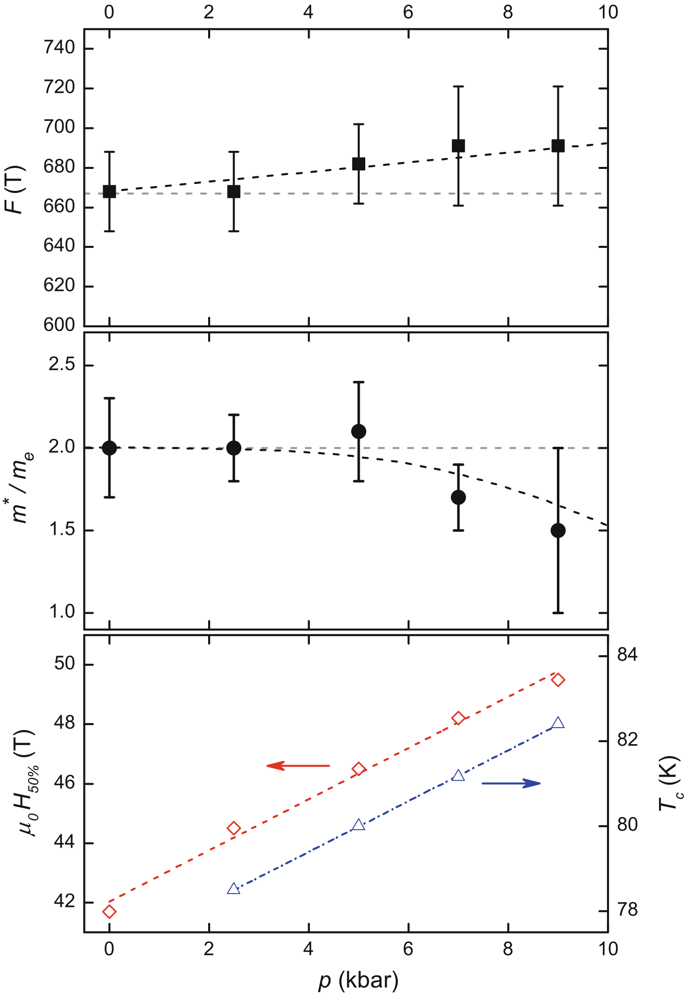

Fig. 6.12 Evolution of the extracted parameter F, effective mass m^*, superconducting-normal conducting transition of $YBa_2Cu_4O_8$ in field and the critical temperature under pressure. The *dashed lines* are guides to the eye

superconducting critical temperature and upper critical field. However while both of these are connected to the effective mass, in BCS theory, the assumption of an isotropic gap is not valid for the cuprates. The gap in this class of materials possesses *d-wave* symmetry which mean the gap-function $\Delta_{kk'}$ is a function of k. This being caused by a k-dependent interaction potential $V_{kk'}$ could lead to *hot-spots* on the Fermi surface, points where the mass is enhanced over the average value. In the SdH experiment we are only sensitive to an average over the entire Fermi surface sheet and hence while some parts might be strongly enhance, we could still find a slight decrease or roughly constant mass as indicated in Fig. 6.12b as dashed lines.

Another possible scenario that we can not rule out at this stage, is the evolution due to a change in harmonic content. As pointed out in the introduction the oscillation spectrum for YBCO contains additional frequencies from other extremal orbits, that modulate the amplitude. This likely also being the case in Y124, could lead to changes in the dominant frequency and hence the strong phase shift observed under pressure.

6.6 Conclusion

In conclusion we have performed measurements on the evolution of the quasi particle mass under hydrostatic pressure. An increase in the oscillation frequency was found that is in good agreement with that found in YBCO [21] in the case of hole-doping. This is also in agreement with the assumption of Y124 being located at $p = 0.14$ in the phase diagram of YBCO. The increase in the superconducting critical temperature, as observed previously for Y124 under pressure [34] resembles the increase in YBCO with doping and used in this experiment to determine the applied pressure.

While for an analogy of pressure and hole doping also an increase in quasi particle mass would be expected, using Shubnikov-de Haas measurements in high magnetic field we found a rather constant effective mass, that tends towards a suppression at applied pressure above 5 kbar. Here we can not rule out hot-spots on the Fermi surface that lead to the formation of a larger gap at these k-values. However the agreement of extremal orbit, critical temperature and c-axis resistivity evolution with that expected from a general picture raises the question why the strong mass enhancement observed is not reproduced.

Further we have found, in measurements up to 70 T at ambient pressure, a significantly lower effective mass than reported previously. As the change in quasi particle mass might be smaller than the observed difference between reported values and our findings, additional measurements at zero-pressure are necessary.

At this stage we can not draw any final conclusion as further measurements at high pressure need to be carried out to verify our results. For this the design of a new pressure cell for use in fields up to 70 T is currently under development. This will hopefully allow us to determine the oscillation frequency and quasi particle mass more reliably under hydrostatic pressure up 10 kbar. Further the use of higher field would possibly help to understand the harmonic content evolution that could also have influence on the evolution of the effective mass.

References

1. J. Bednorz, K. Mueller, Zeitschrift für Physik B **64**, 189 (1986)
2. N. Doiron-Leyraud, C. Proust, D. LeBoeuf, J. Levallois, J. Bonnemaison, R. Liang, D. Bonn, W. Hardy, L. Taillefer, Nature **447**, 565 (2007)
3. C. Weber, K. Haule, G. Kotliar, Nat. Phys. **6**, 574 (2010)
4. D. Basov, R. Liang, B. Dabrowski, D.A. Bonn, W.N. Hardy, T. Timusk, Phys. Rev. Lett. **77**, 4090 (1996)
5. D. LeBoeuf, N. Doiron-Leyraud, J. Levallois, R. Daou, J. Bonnemaison, N. Hussey, L. Balicas, B. Ramshaw, R. Liang, D. Bonn, W. Hardy, S. Adachi, C. Proust, L. Taillefer, Nature **450**, 533 (2007)
6. B. Vignolle, A. Carrington, R. Cooper, M. French, A. Mackenzie, C. Jaudet, D. Vignolles, C. Proust, N. Hussey, Nature **455**, 952 (2008)
7. D. Basov, A. Chubukov, Nat. Phys. **7**, 272 (2011)
8. G. Seibold, F. Becca, F. Bucci, C. Castellani, C. DiCastro, M. Grilli, Eur. Phys. J. B **13**, 87 (2000)
9. J. Chang, E. Blackburn, A. Holmes, N. Christensen, J. Larsen, J. Mesot, R. Liang, D. Bonn, W. Hardy, A. Watenphul, M. Zimmermann, E. Forgan, S. Hayden, Nat. Phys. **8**, 871 (2012)
10. E. Blackburn, J. Chang, M. Hücker, A. Holmes, N. Christensen, R. Liang, D. Bonn, W. Hardy, U. Rütt, O. Gutowski, M. Zimmermann, E. Forgan, S. Hayden, Phys. Rev. Lett. **110**, 137004 (2013)
11. S. Blanco-Canosa, A. Frano, T. Loew, Y. Lu, J. Porras, G. Ghiringhelli, M. Minola, C. Mazzoli, L. Braicovich, E. Schierle, E. Weschke, M. LeTacon, B. Keimer. Phys. Rev. Lett. **110**, 187001 (2013)
12. T. Wu, H. Mayaffre, S. Krämer, M. Horvatic, C. Berthier, W. Hardy, R. Liang, D. Bonn, M. Julien, Nature **477**, 191 (2011)
13. D. LeBoeuf, S. Kräner, W. Hardy, R. Liang, D. Bonn, C. Proust, Nat. Phys. **9**, 79 (2013)
14. R. Liang, D.A. Bonn, W.N. Hardy, Phys. Rev. B **73**, 180505 (2006)
15. D. LeBoeuf, N. Doiron-Leyraud, B. Vignolle, M. Sutherland, B. Ramshaw, J. Levallois, R. Daou, F. Laliberte, O. Cyr-Choiniere, J. Chang, Y. Jo, L. Balicas, R. Liang, D. Bonn, W. Hardy, C. Proust, L. Taileffer, Phys. Rev. B **83**, 054506 (2011)
16. S. Adachi, K. Nakanishi, K. Tanabe, K. Nozawa, H. Takagi, W. Hu, M. Izumi, Phys. C **301**, 123 (1998)
17. J. Karpinski, E. Kaldis, E. Jilek, S. Rusiecki, B. Bucher, Nature **336**, 660 (1988)
18. M. Zimmerman, J. Schneider, T. Frello, N. Andersen, J. Madsen, M. Käll, H. Poulsen, R. Liang, P. Dosanjh, W. Hardy, Phys. Rev. B **68**, 104515 (2003)
19. T. Miyatake, S. Gotoh, N. Koshizuka, S. Tanaka, Nature **341**, 41 (1989)
20. A. Bangura, J. Fletcher, A. Carrington, J. Levallois, M. Nardone, B. Vignolle, P. Heard, N. Doiron-Leyraud, D. LeBoeuf, L. Taillefer, S. Adachi, C. Proust, N. Hussey, Phys. Rev. Lett. **100**, 047004 (2008)
21. B. Vignolle, D. Vignolles, D. LeBoeuf, S. Lepault, B. Ramshaw, R. Liang, D. Bonn, W. Hardy, N. Doiron-Leyraud, A. Carrington, N. Hussey, L. Taillefer, C. Proust, Physique C.R., **12**, 446 (2011)
22. E. Yelland, J. Singleton, C. Mielke, N. Harrison, F. Balakirev, B. Dabrowski, J. Cooper, Phys. Rev. Lett. **100**, 047003 (2008)
23. B. Vignolle, D. Vignolles, M. Julien, C. Proust, Physique C.R., **14**, 39 (2013)
24. T. Helm, M. Kartsovnik, M. Bartkowiak, N. Bittner, M. Lambacher, A. Erb, J. Wosnitza, R. Gross, Phys. Rev. Lett. **103**, 157002 (2009)
25. T. Helm, M. Kartsovnik, I. Sheikin, M. Bartkowiak, F. Wolff-Fabris, N. Bittner, W. Biberacher, M. Lambacher, A. Erb, J. Wosnitza, R. Gross, Phys. Rev. Lett. **105**, 247002 (2010)
26. M. Kartsovnik, T. Helm, C. Putzke, F. Wolff-Fabris, I. Sheikin, S. Lepault, C. Proust, D. Vignolles, N. Bittner, W. Biberacher, A. Erb, J. Wosnitza, R. Gross, New J. Phys. **13**, 015001 (2011)

27. J. Lin, A. Millis, Phys. Rev. B **72**, 214506 (2005)
28. W. Tabis, Y. Li, M. LeTacon, L. Braicovich, A. Kreyssig, M. Minola, G. Dellea, E. Weschke, M. Veit, M. Ramazanoglu, A. Goldman, T. Schmitt, G. Ghiringhelli, N. Barisic, M. Chan, C. Dorow, G. Yu, G. Yu, X. Zhao, B. Keimer, M. Greven (2014). arXiv:1404.7658
29. N. Barisic, S. Badoux, M. Chan, C. Dorow, W. Tabis, B. Vignolle, G. Yu, J. Beard, X. Zhao, C. Proust, M. Greven, Nat. Phys. **9**, 761 (2013)
30. J. Yu, K. Park, A. Freeman, Phys. C **172**, 467 (1991)
31. O. Grissonnanche, G. Cry-Choiniere, F. Laliberte, S. Rene de Cotret, A. Juneau-Fecteau, S. Dufour-Beausejour, M. Delage, D. LeBoeuf, J. Chang, B. Ramshaw, D. Bonn, W. Hardy, R. Liang, S. Adachi, N. Hussey, B. Vignolle, C. Proust, M. Sutherland, S. Krämer, J. Park, D. Graf, N. Doiron-Leyraud, L. Taillefer, Nat. Commun. **4**, 280 (2014)
32. M. French, Angle dependent magnetoresistance in $\mathrm{tl}_2\mathrm{ba}_2\mathrm{cuo}_{6+\delta}$, Ph.D. dissertation, University of Bristol (2009)
33. A. Schofield, J. Cooper, Phys. Rev. B **62**, 10779 (2000)
34. B. Bucher, J. Karpinski, E. Kaldis, P. Wachter, Phys. C **157**, 478 (1989)

Appendix A
Numerical Phase Sensitive Detection in Matlab

```
function result = Lockin(data,tcol,ycol,refcol,fcut,phase,time,harmonic)
%% function result = Lockin(data,tcol,ycol,refcol,fcut,phase,timeconst,harmonic)
%
%       data:       matrix of data
%       tcol:       column number of time
%       ycol:       column of sample voltage
%       refcol:     column of reference signal
%       fcut:       cut of frequency for low pass filter f = 1/(2*pi*t)
%       time:       sampling time
%       harmonic:   select the harmonic order

if ~exist('harmonic')
    harmonic = 1;
end

yref = data(:,refcol);
ysample = data(:,ycol);
x = data(:,tcol);

% find 1st harmonic frequency
fftdata = myfft([x,yref],1,2,50,false);
[m,i] = max(fftdata(:,2));
f = fftdata(i,1);
sinus = @(p,x) p(1).*sin(2*pi.*x.*f+p(2));
start = [1 0];
if length(data) > 500e3
    coef = nlinfit(x(1:1000),yref(1:1000),sinus,start);
else
    coef = nlinfit(x(1:10000),yref(1:10000),sinus,start);
end

% save reference parameter
result.ref_freq = f;
result.ref_ampl = coef(1);
result.ref_phase = coef(2)*180/pi;
result.harmonic = harmonic;

% select harmonic
f = f * harmonic;

% create numerical reference signal
sinus = @(p,x) p(1).*sin(2*pi.*x.*f+p(2));
coef(2) = coef(2) + phase*pi/180;
coef(1) = 1;
yref_in = sinus(coef,x);
coef(2) = coef(2) + pi/2;
```

C.M. Putzke, *Fermi Surface and Quantum Critical Phenomena in High-Temperature Superconductors*, Springer Theses,
DOI 10.1007/978-3-319-48646-8

```
yref_out = sinus(coef,x);

% multiplication of signal and reference
ydsp_in = ysample.*yref_in;
ydsp_out = ysample.*yref_out;

% create filter parameter for butterworth filter
pts = round(1/fcut/(x(2)-x(1)));
fniq = 1/(x(2)-x(1))/2;
[b1,a1] = butter(4,fcut/fniq,'low');

% perform butterwort filter forward and backward
yresult_in = filtfilt(b1,a1,ydsp_in);
yresult_out = filtfilt(b1,a1,ydsp_out);
yresult_in = yresult_in.*2;
yresult_out = yresult_out.*2;

% save results
result.X = yresult_in;
result.Y = yresult_out;

disp('------------ LIA Reference Parameter -------------');
disp(['Frequency: ' num2str(result.ref_freq) ' Hz']);
disp(['Amplitude: ' num2str(result.ref_ampl) ' V']);
disp('--------------------------------------------------');
end
```